

Université de Lille

Ecole doctorale : Sciences pour l'ingénieur

Institut d'Electronique, Microélectronique et Nanotechnologie

THESE

Présentée par

Jean-Marc BOUCAUD

Pour obtenir le grade de

Docteur de l'Université

Spécialité électronique, microélectronique, nanoélectronique et micro-ondes

Electrical and Optical Interposer on a Glass Substrate for the Packaging of Optical Transceivers based on Silicon Photonic Technology

Evaluation d'un interposer électro-optique sur substrat de verre pour interconnexions optiques 400 Gb/s à base de technologie photonique sur silicium

Soutenue le 26/06/2020, devant le jury composé de :

Pr. Delphine MARRIS-MORINI, <i>Professeur, C2N</i>	Rapporteur
Dr. Taha BENYATTOU, <i>Directeur de recherche CNRS, INL</i>	Rapporteur/Président
Dr. Sylvie MENEZO, <i>CEO, SCINTIL Photonics</i>	Examineur
Dr. Moritz SEYFRIED, <i>Manager R&D, FiconTEC</i>	Examineur
Dr. Peter O'BRIEN, <i>Directeur de recherche, Tyndall National Institute</i>	Examineur
Dr. Cédric DURAND, <i>Ingénieur R&D, STMicroelectronics</i>	Encadrant industriel
Dr. Davide BUCCI, <i>Maître de conférences, Grenoble INP</i>	Encadrant académique
Dr Jean-François ROBILLARD, <i>Assistant professeur, IEMN/YNCREA</i>	Invité
Pr. Jean-Emmanuel BROQUIN, <i>Professeur, Grenoble INP</i>	Co-directeur de thèse
Dr. Emmanuel DUBOIS, <i>Directeur de recherche CNRS, IEMN</i>	Directeur de thèse

Acknowledgements

Cette thèse CIFRE, collaboration entre STMicroelectronics, l'IMEP-LaHC et l'IEMN, a été une formidable aventure qui m'a permis de côtoyer de nombreuses personnes d'horizons différents et de m'enrichir de cela. Je voudrais leur adresser mes remerciements pour leur contribution directe ou indirecte à ce travail dans ce paragraphe.

Tout d'abord, un grand merci à mes encadrants de thèse. Merci Emmanuel, pour m'avoir transmis autant une partie de tes connaissances et compétences que de ton enthousiasme. Jean-Emmanuel, pour la pertinence de tes contributions tout au long de la thèse, Davide, pour nos longues discussions à propos de l'optique guidée mais pas que, Fred, pour ton soutien officieux et enfin Cédric, pour les opportunités que tu m'as données et ton encadrement qualitatif et soutenu depuis longtemps.

Merci aux membres de l'équipe MicroE de l'IEMN : Jean-François, Jean-Michel D., Florence, Arun, Justine, Matthieu, Jun, Di, Tianqi, Stanislav pour leur accueil chaleureux. Mentions spéciales à Thierno, pour m'avoir supporté dans non pas un mais deux bureaux pendant toute la thèse, ainsi qu'à Quentin qui m'a beaucoup coaché à mon arrivée. Merci à Kathia pour son stage de qualité, duquel proviennent certains résultats importants de ce travail.

Je remercie également tous les collègues de l'IEMN qui m'ont partagé leur expertise dans leur domaines respectifs : Flavie, Pascal, François, Christophe, Vanessa, Marc, Jean-Michel M., sans oublier Sylvie et son inépuisable énergie.

Merci également à tous les membres de l'équipe RFSS de ST que j'ai pu côtoyer durant ces années d'apprentissage puis de thèse (7 ans quand même !), en particulier Simon et Joao.

Petit clin d'œil à la team escalade. Cybelle, Mélanie, Théo, Kévin merci pour ces moments passés ensemble au labo et à la salle.

Je terminerai en remerciant ma famille pour tout ce qu'elle a fait pour moi.

A mon Père

Table of contents

ACKNOWLEDGEMENTS	3
TABLE OF CONTENTS	7
GENERAL INTRODUCTION	11
I TOWARDS 400 GB/S SILICON PHOTONICS BASED TRANSCEIVERS AND BEYOND	13
1 <i>OPTICAL FIBER COMMUNICATIONS</i>	15
1.1 Brief Historical Background	15
1.2 Transmission Scheme.....	16
1.2.1 Optical Transmitter	17
1.2.2 Optical Fiber.....	18
1.2.3 Optical Receiver.....	19
1.3 Data Center Short-Reach Optical Interconnect	20
2 <i>SILICON PHOTONIC TECHNOLOGY</i>	22
2.1 Silicon Photonic Integrated Circuits.....	22
2.2 Electro-optical Modulation and Detection	24
2.2.1 Mach-Zehnder Modulator	24
2.2.2 Photodetectors.....	25
2.3 Coupling devices	26
2.3.1 The challenge of coupling into silicon photonics devices	26
2.3.2 Grating coupler	26
2.3.3 Lateral spot size converters	27
3 <i>SILICON PHOTONIC BASED ELECTRO-OPTIC TRANSCEIVERS</i>	29
3.1 100G implementations and beyond	29
3.1.1 100 Gb/s Parallel Single Mode 4 (PSM4)	29
3.1.2 100 Gb/s CWDM4.....	30
3.2 Electrical and Optical Interposers.....	31
3.2.1 Electrical interposers.....	31
3.2.1.1 Silicon interposer.....	32
3.2.1.2 Organic interposer	33
3.2.1.3 Glass interposer.....	34
3.2.1.4 Synthesis on electrical interposer technologies	34
3.2.2 Optical technologies on a glass substrate	34
3.2.2.1 Ion-exchange.....	35
3.2.2.2 Direct Femtosecond Laser Writing	35
3.2.2.3 Silica-based PLCs	35
3.2.2.4 Polymer waveguides	36
3.2.2.5 Synthesis on optical technologies on a glass substrate	38
4 <i>STATE-OF-THE-ART SYNTHESIS AND DEFINITION OF THE OBJECTIVES</i>	39
5 <i>CONCLUSION</i>	41
II INTERPOSER DESIGN & SIMULATIONS	43
1 <i>OPTICAL WAVEGUIDES</i>	44
1.1 2D Slab Waveguide	44

1.2 3D Waveguides	48
1.2.1 Effective Index Method	48
1.2.2 Rib Waveguide	50
1.2.3 FDE Simulations	52
1.3 Lateral Coupling Efficiency with Optical Fiber	54
1.3.1 Coupling Efficiency	54
1.3.2 Coupling Efficiency Simulations	55
2 RF OPTIMIZATIONS.....	57
2.1 Interposer Transmission Lines	57
2.1.1 Coplanar Waveguides	57
2.1.2 ADS simulations	60
2.1.3 Interposer Stack Modeling.....	62
2.2 PIC25G Modulator electrodes optimization	63
3 PIC TO INTERPOSER COUPLING.....	66
3.1 Proposed coupling scheme and 1 st order approximation	67
3.2 FDTD Simulation & Modeling Methodology	68
3.3 PIC25G Grating Coupler Simulation	69
3.4 PIC to Interposer Coupling.....	70
3.4.1 2D Simulations.....	70
3.4.2 3D Simulations.....	72
4 CONCLUSION	72
III INTERPOSER FABRICATION	73
1 POLYMER OPTICAL WAVEGUIDES.....	74
1.1 Polymer/Glass surface waveguides	74
1.1.1 Femtosecond Laser Direct Writing	74
1.1.2 Etching in Hydrofluoric Acid.....	76
1.1.3 Dry film lamination.....	77
1.1.4 Chemical Mechanical Polishing.....	79
1.2 Waveguides by laser lithography	80
1.2.1 Liquid resins spin-coating	81
1.2.2 Laser lithography.....	82
1.2.3 Dimensional Characterizations.....	83
1.2.4 Optimization for single mode operation	85
1.3 Waveguides by laser ablation	86
1.3.1 Dry films for organic stack.....	88
1.3.2 Refractive index measurements.....	88
1.3.3 Optical Transmission.....	89
1.3.4 Laser trenches.....	93
1.3.5 Rib waveguides with photosensitive resins	96
1.4 Waveguide technologies comparison.....	97
2 ELECTRICAL-OPTICAL HYBRIDIZATION.....	98
2.1 Electrical and optical glass interposer fabrication process	99
2.2 Copper deposition	100
2.2.1 Copper plating of glass substrates	100
2.2.2 Sputtered thickness calibration.....	101
2.2.2.1 Titanium buffer layer.....	101
2.2.2.2 Copper layer	101

2.3 Copper structuration	102
2.3.1 Chemical etching.....	102
2.3.2 Selective femtosecond laser ablation.....	104
2.4 Laser ablated rib waveguides	105
2.5 Laser ablation of polymer layers for flip-chip bonding and probing	106
2.6 Total Internal Reflection (TIR) mirror	107
3 PIC/INTERPOSER FLIP-CHIP ASSEMBLY AND DEMONSTRATOR.....	109
3.1 PIC25G test IC.....	109
3.2 Interposer layout & alignment strategy	110
3.3 Flip-chip bonding.....	114
4 CONCLUSION	116
IV CHARACTERIZATIONS	117
1 INTERPOSER.....	118
1.1 Polymer waveguides characterization.....	118
1.1.1 Mode profile	118
1.1.1.1 Principle	118
1.1.1.2 Polymer/glass surface waveguides	119
1.1.1.3 Waveguides by laser lithography.....	120
1.1.1.4 Waveguides by laser ablation.....	124
1.1.2 Propagation & coupling losses	126
1.1.2.1 Principle	126
1.1.2.2 Polymer/glass surface waveguides	127
1.1.2.3 Waveguides by laser lithography.....	128
1.1.2.4 Waveguides by laser ablation	128
1.2 RF/mmW characterizations	129
1.2.1 Characterization setup.....	129
1.2.2 CPW measurements and deembedding structures.....	130
1.3 Total internal reflection mirror.....	133
1.3.1 Measurement bench.....	133
1.3.2 Angle measurement.....	134
2 ASSEMBLY	136
2.1 RF/mmW characterizations	136
2.1.1 RF/mmW path	136
2.1.2 Modulators reflection coefficient.....	137
2.2 Optical path characterization.....	139
2.2.1 Mode Profile	139
2.2.2 Losses	140
2.3 Optical coupling measurement through embedded photodetector.....	141
2.3.1 Principle	141
2.3.2 Results.....	143
3 CONCLUSION	144
V GENERAL CONCLUSION & PERSPECTIVES	145
1 ACHIEVEMENTS VERSUS OBJECTIVES.....	145
2 PERSPECTIVES	147
2.1 Short-term perspectives.....	147
2.2 Long-term perspectives.....	148

ANNEX A: MATLAB SCRIPT FOR RECTANGULAR WAVEGUIDE MODES COMPUTATION	149
ANNEX B: EXAMPLE OF A DETAILED PROCESS SHEET	153
REFERENCES	155
LIST OF RELATED PUBLICATIONS.....	163
LIST OF FIGURES.....	165
LIST OF TABLES	175
LIST OF ACRONYMS	177
RESUME.....	181
ABSTRACT.....	183

General Introduction

The past decades have brought major changes in the way we communicate. The advent of smartphones, social medias, streaming platforms, etc., exponentially increased the amount of data we exchange through telecommunication. In 1997, the global internet traffic was about 100 GB per hour. Twenty year after, in 2017, it grew up to 47 TB per second [1]. A large number of services being now cloud-based, the data traffic within data centers (DCs) has no choice but to keep up the same pace. In order to handle the more than 20.6 ZB of DC traffic that is forecasted for the year 2021[2], DCs are constantly under pressure to improve their capacity, speed and latency. To meet this stringent demand, interconnections within DCs moved from copper cables to optical fibers. During this transition, many different technologies emerged to perform optical telecommunications.

Among the most recent ones, silicon photonics (SiPh), an electro-optical technology derived from standard CMOS technologies, appears as a promising solution to reduce costs, lower power consumption and enhance data rates of optical links. Despite leveraging most of the developments around the CMOS platform, SiPh presents additional packaging constraints related to the interfacing of its optical part. These packaging constraints increase the cost of silicon photonics based optical transceivers and complicates the implementation of technologies such as coarse wavelength division multiplexing (CWDM).

The purpose of this thesis is to investigate the possibility to develop a low-cost electrical and optical interposer fabricated on a glass substrate to solve the packaging issues of SiPh. This work is divided in 4 chapters:

The goal of the first chapter is to introduce in details the context of this work. First, the basics of modern optical telecommunications in DCs are presented. We subsequently review the SiPh technology and its essential components in order to highlight its specificities. In a third part, the current implementations of 100Gb/s and 400 Gb/s silicon photonics transceivers and the potential solutions to further improve data rates are investigated. This points out the packaging issue of this technology and allows us to discuss the concept of electrical and optical interposers. Finally, we synthetize the previously detailed state-of-the-art and set the objectives of this work.

The second chapter is dedicated to the design and simulation of the interposer and its components. The first part details the theory and simulations of 2D, 3D and Rib dielectric waveguides, in order to determine the ideal physical properties of the waveguides in the interposer. In the second part of the chapter, we review coplanar waveguide (CPW)

transmission lines and optimize Mach-Zehnder modulators (MZMs) electrodes for the transmission of high data rate signals in the interposer and in the SiPh IC, respectively. Finally, the design strategy and simulations of the vertical coupling between the interposer and the SiPh IC are presented.

In the third chapter, we review the experiments that allowed us to develop a process enabling the fabrication of an electrical and optical interposer. First, three different fabrication processes for the polymer waveguides are investigated and compared, namely, polymer/glass surface waveguides, rectangular waveguides by laser lithography and rectangular/rib waveguides by laser ablation. Then, the method used to associate the electrical and optical parts is presented. Finally, the PIC25G test chip and its functions are detailed as well as the corresponding interposer layout and the alignment strategy used for the flip-chip bonding between both chips.

Chapter IV presents the characterizations carried out during and after the fabrication of the interposer. In a first time, we review the optical characterizations of the three polymer waveguide technologies studied previously, the RF/mmW characterization of the interposer transmission lines and the optical characterizations of the total internal reflection mirror. In a second time, we present the characterizations performed on the assembled demonstrator including the validation of RF/mmW paths and the demonstration of the optical coupling between the interposer and the SiPh IC by both characterizing an optical signal passing through the SiPh IC and another one feeding SiPh IC-integrated photodetectors.

I Towards 400 Gb/s Silicon Photonics Based Transceivers and Beyond

The goal of the first chapter is to introduce in details the context of this work. First, the basics of modern optical telecommunications in data centers are presented. As it seems to be a promising solution to further decrease the cost of high data rate optical links, we then review silicon photonic technologies and particularly STMicroelectronics' PIC25G technology as well as its essential components in order to highlight its specificities. In a third part of the chapter, the current implementation of 100Gb/s optical transceivers based on PIC25G and the potential solutions to further improve their data rates are investigated. This points out the packaging issue of this technology and allows us to discuss the concept of electrical and optical interposers. Finally, we synthesize the previously detailed state-of-the-art and set the objectives of this work.

<i>1 OPTICAL FIBER COMMUNICATIONS</i>	15
1.1 Brief Historical Background	15
1.2 Transmission Scheme.....	16
1.2.1 Optical Transmitter	17
1.2.2 Optical Fiber.....	18
1.2.3 Optical Receiver.....	19
1.3 Data Center Short-Reach Optical Interconnect	20
<i>2 SILICON PHOTONIC TECHNOLOGY</i>	22
2.1 Silicon Photonic Integrated Circuits.....	22
2.2 Electro-optical Modulation and Detection	24
2.2.1 Mach-Zehnder Modulator	24
2.2.2 Photodetectors.....	25
2.3 Coupling devices.....	26
2.3.1 The challenge of coupling into silicon photonics devices	26
2.3.2 Grating coupler	26
2.3.3 Lateral spot size converters	27
<i>3 SILICON PHOTONIC BASED ELECTRO-OPTIC TRANSCEIVERS</i>	29
3.1 100G implementations and beyond	29
3.1.1 100 Gb/s Parallel Single Mode 4 (PSM4)	29
3.1.2 100 Gb/s CWDM4.....	30
3.2 Electrical and Optical Interposers.....	31
3.2.1 Electrical interposers.....	31
3.2.1.1 Silicon interposer.....	32
3.2.1.2 Organic interposer	33
3.2.1.3 Glass interposer.....	34

3.2.1.4 Synthesis on electrical interposer technologies	34
3.2.2 Optical technologies on a glass substrate	34
3.2.2.1 Ion-exchange.....	35
3.2.2.2 Direct Femtosecond Laser Writing	35
3.2.2.3 Silica-based PLCs	35
3.2.2.4 Polymer waveguides	36
3.2.2.5 Synthesis on optical technologies on a glass substrate.....	38
<i>4 STATE-OF-THE-ART SYNTHESIS AND DEFINITION OF THE OBJECTIVES.....</i>	<i>39</i>
<i>5 CONCLUSION</i>	<i>41</i>

1 Optical Fiber Communications

1.1 Brief Historical Background

The idea of using light as a very high frequency carrier to transmit data over an optical cable was imagined as early as 1950s [3], however the coherent light source and the low-loss transmission medium needed were not available at that time. Optical communications over fibers really emerged in the 70s thanks to the demonstration of coherent light generation using a ruby laser in 1960 by T. H. Maiman [4] and, ten years later, GaAs semiconductor lasers operating continuously at room temperature [5]. In the meantime, the drastic reduction of optical losses in optical fibers following the work of C. K. Kao [6] made them appear as a suitable transmission medium and led to the development of the first Optical Fiber Communications (OFCs).

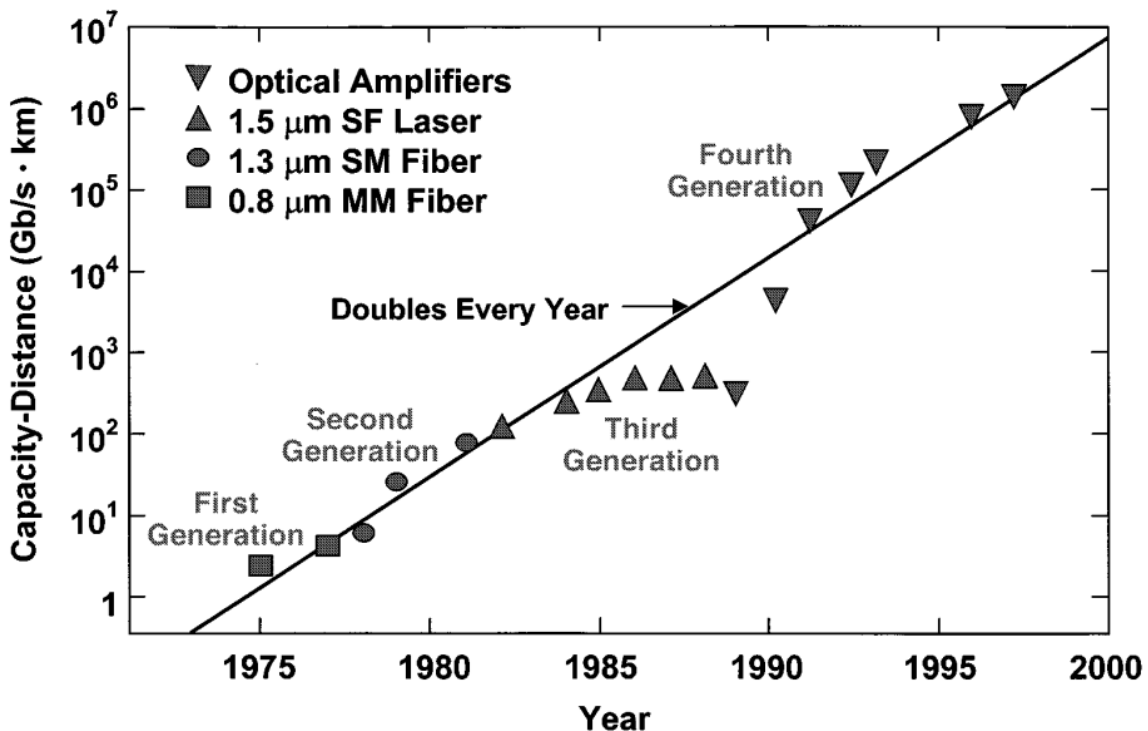


Figure 1: Exponential growth of the bit rate · distance product [7]

Over the next 30 years, the bit rate · distance product doubled every year. As shown in

Figure 1 [7], four different generations are distinguishable:

- The first generation, on which is based the first commercial OFC [8], is transmitting data at a bit rate of 45 Mb/s over a 10-kilometer long multimode fiber (MMF) using a 0.8 μm GaAs laser.

- The second generation solves the modal dispersion problem of the first generation by using 1.3 μm InGaAsP semiconductor lasers and single mode fibers (SMF).
- Silica SMFs show minimum losses around 1.55 μm but chromatic dispersion is also higher around this wavelength. The third generation of OFCs allows to compensate the chromatic dispersion at 1.55 using dispersion-shifted SMFs and InGaAsP lasers oscillating in a single longitudinal mode to decrease the spectral width of the signal.
- The latest major improvement of these years of fast OFCs development came from the use of erbium-doped fiber amplifiers [9] and Wavelength Division Multiplexing (WDM) which consists in transmitting multiple data stream using different wavelengths in a single fiber.

Since then, data rates have continued to progress, thanks to the improvement on WDM systems and the use of more complex modulation formats enabled by the introduction of coherent transmissions.

Aside of data rates and communication distance, there was, and there still is, room for improvement in several areas, such as integration, power consumption and cost reduction. Indeed, after being used only over very long distances, OFCs gradually integrated shorter links as their cost decreased, increasing at the same time their competitiveness in comparison with copper cable links. In the recent years, OFCs have become a major interconnection technology within data centers, covering distances from a few kilometers to a few tens of meters [10].

1.2 Transmission Scheme

An optical fiber communication system is made of three parts:

- The optical transmitter
- The optical fiber
- The optical receiver

Each part and the associated main characteristics are presented in this section.

A generic representation of an optical link is depicted in Figure 2:

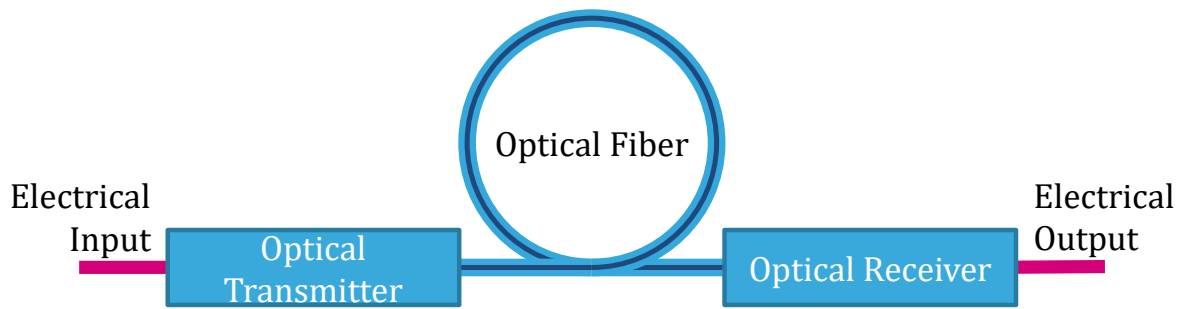


Figure 2: Schematic diagram of a generic optical link

In most cases, optical communications are full duplex which is why we generally find both the receiver and the transmitter put together in a single assembly at each end of the fiber: the optical transceiver.

1.2.1 Optical Transmitter

The function of the optical transmitter is to convert an electrical signal into an optical signal carrying the same data. In high speed systems, where a laser source is employed, two different topologies are employed to fulfill this purpose (Figure 3):

- Directly Modulated Laser (DML): the electrical signal is encoded and amplified in an electronic circuit that directly drives a laser [3].
- Externally Modulated Laser (EML): this method uses a laser operating continuously and a specific circuit to do the conversion: an electro-optical modulator. In Figure 3 (b), even though the encoding and amplification of the electrical signal that drives the modulator and the laser driving are dissociated, the same circuit can perform both functions [3].

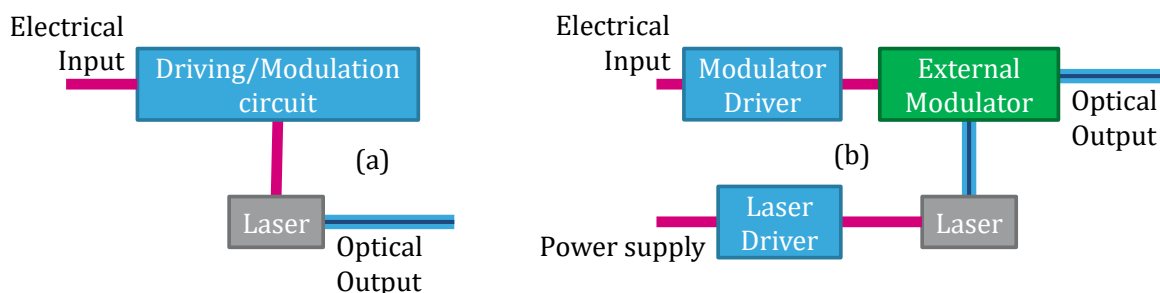


Figure 3: Block Diagram of optical transmitters using (a) a Directly Modulated Laser (DML) and (b) an Externally Modulated Laser (EML) [3]

Optical transmitters are characterized by a lot of different parameters, such as: optical output power, modulation format, multiplexing type, number of channels, operating

temperatures and power consumption. The aforementioned transmitter topologies are more deeply compared in section 1.3.

Simple modulation formats consist in light intensity modulation. The most used ones are: Non-Return to Zero (NRZ) and Pulse Amplitude Modulation, generally on 4 levels (PAM4). The first uses 2 intensity levels to transmit one bit per sampling period (Figure 4 (a)) whereas the second employs 4 intensity levels to transmit 2 bits per sampling period (Figure 4 (b)).

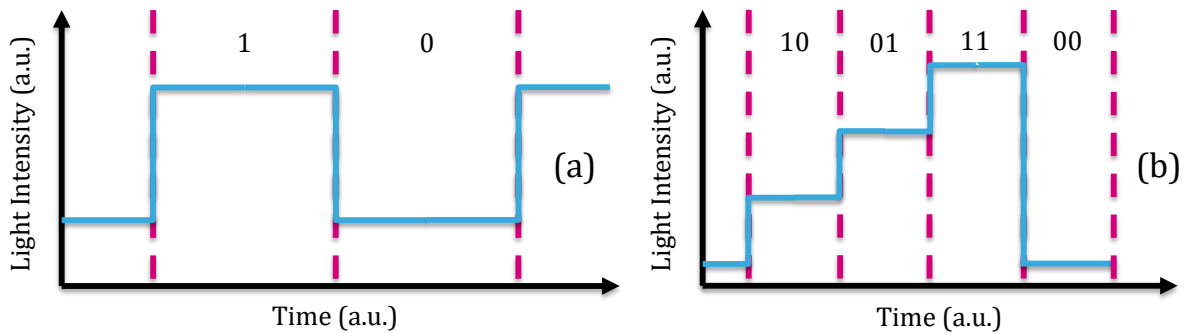


Figure 4: NRZ (a) and PAM4 (b) modulation formats

Also, WDM generally divides into two categories: Coarse WDM (CWDM) whose carrier wavelength spacing is 20 nm [11] and Dense WDM (DWDM) whose carrier wavelength spacing is shorter and typically varies from 0.8 to 0.1 nm [12].

1.2.2 Optical Fiber

Optical fibers are the transmission medium of OFCs. Their role is to transmit an optical signal from the transmitter to the receiver without losing the information it carries. Like many other waveguiding structures, optical fibers rely on the difference of refractive index between dielectric materials in order to spatially confine light. In their simplest form, standard SMFs are cylindrical parts made of two layers of silica: the core layer inside and the cladding layer around it (Figure 5). These layers can be doped to increase or decrease their respective refractive indices in order to confine light inside an inner cylinder of a few micrometers.

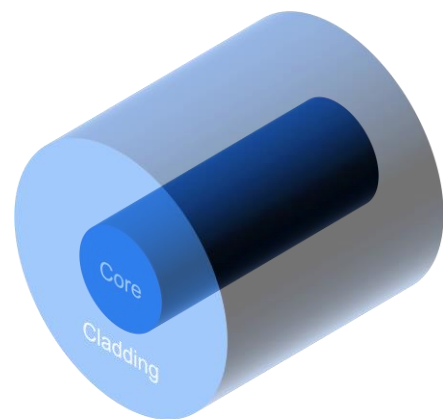


Figure 5: Core and cladding layers of an optical fiber

Two important optical fiber parameters are, on one hand the attenuation, which is the decrease in light intensity due to various phenomena, such as absorption in the material

or imperfection of the guiding structure, usually expressed in dB/km; dispersion, on the other hand is the variation of light waves velocity as a function of the wavelength, expressed in ps/nm.km. Both play a major role in the transmission distance that can be achieved. Fibers are categorized following their propagation type and operating wavelength. Moreover, when the index transition between the core and the cladding is a clearly defined surface, they are called step-index fibers. When the transition is gradual, they are referred as graded-index fibers. Table 1 shows a few examples of optical fiber and their characteristics.

Table 1: Main characteristics of three different optical fibers

Fiber name	Propagation type	Index type	Operating Wavelengths	Attenuation	Source
SMF28	Single Mode	Step-index	1310 nm 1550 nm	0.18 dB/km @ 1550 nm	[13]
HI1060	Single Mode	Step-index	980 nm 1060 nm	1.5 dB/km @1060 nm	[14]
OM4	Multimode	Graded-index	850 nm	2.3 dB/km @ 850 nm	[15]

1.2.3 Optical Receiver

The receiver is in charge of converting back the optical signal to an electric signal. In most simple situations, direct detection is used. This includes a photodetector, which usually is a photodiode generating a current proportional to the optical power it receives, and its driving circuitry, as well as an electrical demodulator (Figure 6).

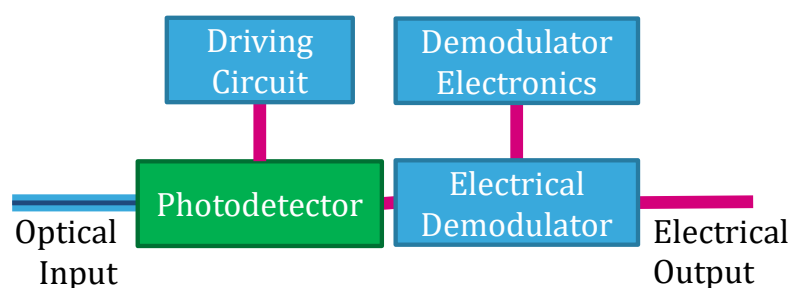


Figure 6: Block diagram of an optical receiver [3]

The use of more complex modulation formats like phase and frequency shift keying, changes the architecture of the receiver. In a similar manner to what is done for radio frequencies, homodyne and heterodyne detection of an optical signal is possible by adding a laser in the receiver who plays the role of a local oscillator. The main difference is that the signal and local oscillator being optical, the mixing needs dedicated optical circuitry

[3]. Nonetheless, most optical transceivers used in data center are, as we will see in the next section, based on intensity modulation and direct detection.

1.3 Data Center Short-Reach Optical Interconnect

Data center optical interconnects are OFCs covering a wide range of distances and data rates. Several standards are used in the industry depending on the application. The IEEE 802.3 working groups define the ethernet standards in terms of physical layer specifications for optical transceivers such as transmission reach, data rate, electrical interface, type and number of fibers, multiplexing methods, etc [16].

Table 2: 100Gb/s Ethernet Standards [16]

Standard name	Number of fibers	Fiber type	Multiplexing type	Wavelength	Reach	No of channels Modulation format
100GBASE-SR10	10	MMF	SDM	850 nm	150 m	10x10Gb/s NRZ
100GBASE-SR4	4	MMF	SDM	850 nm	100 m	4x25Gb/s NRZ
100GBASE-SR2	2	MMF	SDM	850 nm	100 m	2x50Gb/s PAM4
100GBASE-DR	1	SMF	n.a.	1310 nm	500 m	1x100Gb/s PAM4
100GBASE-LR4	1	SMF	CWDM, 4 λ	1310 nm	10 km	4x25Gb/s NRZ
100GBASE-ER4	1	SMF	CWDM, 4 λ	1310 nm	40 km	4x25Gb/s NRZ

Table 2, above, and Table 3, below, present the active ethernet standards for 100 Gb/s and 400 Gb/s. One can observe that data rates and reach are conditioning the technologies used for the link. For very short distances (100m), MMFs are used and data rates are increased by multiplying the number of fibers, this a technique belonging to the Space Division Multiplexing (SDM) methods. As the reach goes farther, MMFs are replaced by SMFs. However, the longer the distance, the bigger is the part of fibers in the total cost of the link. This is why this type of SDM is being abandoned in favor of WDM over very long distances. In a word, this is a tradeoff between the cost of fibers and transceivers.

Table 3: 400 Gb/s Ethernet Standards

Standard name	No of fibers	Fiber type	Multiplexing type	Wavelength	Reach	No of channels Modulation format
400GBASE-SR16	16	MMF	SDM	850 nm	100 m	10x10Gb/s NRZ
400GBASE-DR4	4	SMF	SDM	1310 nm	500 m	4x100Gb/s PAM4
400GBASE-FR8	1	SMF	WDM, 8 λ	1310 nm	2 km	8x50Gb/s PAM4
400GBASE-LR8	1	SMF	WDM, 8 λ	1310 nm	10 km	8x50Gb/s PAM4

Yet, Ethernet standards leave a part of freedom regarding the physical implementation of optical transceivers. To avoid incompatibilities between data center devices due to the number of players in the industry, Multi-source Agreements (MSA) have been set up by several groups of companies to provide interoperable transceivers. Table 4 provides the names of the four 100G MSAs and some of their specifications [17]. It is worth noting that almost all standards for 100G and 400G make use of 2 to 16 channels (either via SDM or

WDM), the modulation bandwidth per channel of industrially available technologies being limited to 50 Gb/s NRZ – 100 Gb/s PAM4.

Table 4: 100 Gb/s Multi-Source Agreement standards for short-reach interconnects

MSA name	No of fibers	Multiplexing type	Wavelength	Reach	Link Budget
PSM4	4	SDM	1310 nm	500 m	3.26 – 14.66 dB
CWDM4	1	CWDM, 4λ	1310 nm	2km	5.0 – 14.0 dB
CLR4	1	CWDM, 4λ	1310 nm	1-2km	3.5 – 12.5 dB
OpenOptics	1	DWDM	1550 nm	2km+	> 5 dB

Several transceiver technologies support the different standards.

Figure 7 provides an overview of the different optical transceiver technologies for data centers by reach and loss budget. This takes into account lower data rates (10 and 40 Gb/s) links. For communications over MMF, the transceiver is based on a directly modulated multimode Vertical Cavity Surface Emitting Laser (VCSEL). For communications over SMF, DMLs are competing with EMLs. Both use Indium Phosphide (InP) Distributed Feedback (DFB) lasers as a light source and provide the same data rate per channel. While it is obviously simpler and cheaper to use DMLs for single channel transceivers, it is a different story for multi-channel transceivers, which, are very often the solution of choice for 100G and 400G links [18].

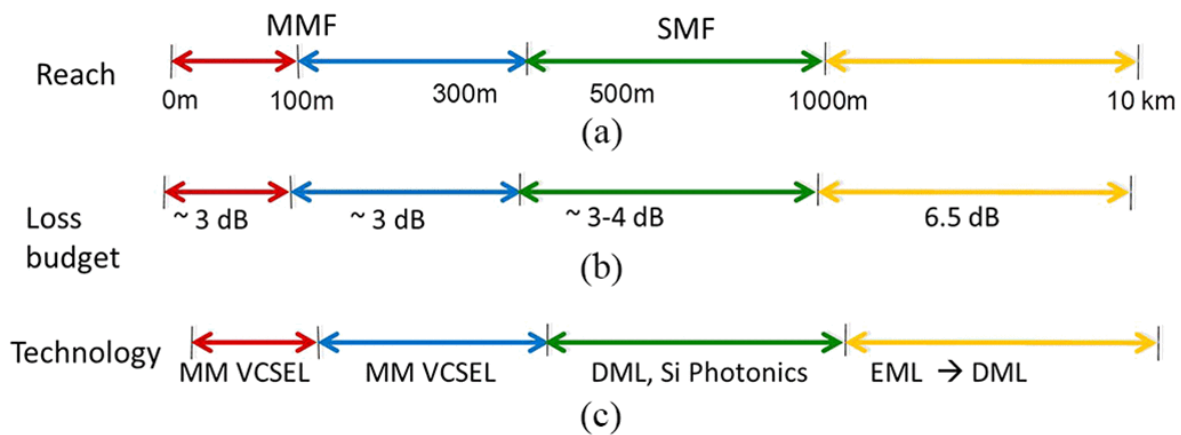


Figure 7: Application space in current data centers based on (a) transmission reach and fiber type, (b) loss budget, or (c) technology [18]

In an SDM scheme, a single laser can be used for all channels, greatly reducing the cost and making EMLs an economically viable solution.

In a WDM scheme, one laser per wavelength is required. Nevertheless, if the technology of the chip performing the multiplexing is also capable of performing the modulation, it will facilitate the packaging of EMLs over DML and consequently reduce costs.

Both approaches can benefit from the predictability, reliability and high yields of a CMOS-based manufacturing process. This is the promise of silicon photonics. In the next section, assets and drawbacks of silicon photonic technology's main functions are presented.

2 Silicon Photonic Technology

2.1 Silicon Photonic Integrated Circuits

Silicon photonics (SiPh) is a technology derived from a standard CMOS process optimized to integrate optical components at telecom wavelengths (1300 – 1500 nm). STMicroelectronics has developed a silicon photonic technology known as PIC25G. We will take PIC25G as the main example to show the specificities of SiPh technologies.

First of all, the development of a photonic integrated circuit (PIC), started by the manufacturing of an optical waveguide (WG). WGs confine light inside a structure in the same way as optical fibers. This is possible on silicon-on-insulator (SOI) wafers thanks to the excellent optical transmission coefficient of silicon (Si) and silicon dioxide (SiO₂) in the near infrared, as well as the strong index difference between these materials: $n_{Si} = 3.503$ and $n_{SiO_2} = 1.447$ at a wavelength of 1310 nm [19][20].

To this purpose, the manufacturing process depicted in Figure 8 is followed [21]: the top Si layer of a SOI wafer is partially removed in some areas by a first Hard Mask (HM) deposition, lithography and etching step. Immediately after, a second lithography and etching remove other areas. Then, etched areas are filled with SiO₂ and the wafer is planarized. This allows creating the waveguiding structure that is known as rib waveguide, whose cross-section is represented in Figure 9. The rib topology helps the reduction of waveguide losses by lowering the impact of sidewalls roughness thanks to the partial silicon etch.

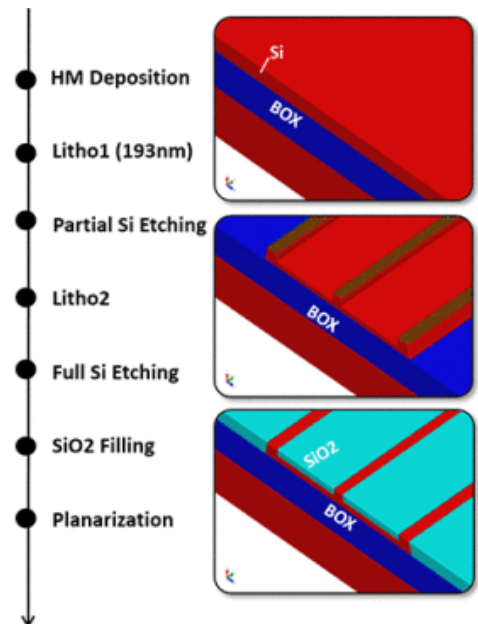


Figure 8: Manufacturing process of SOI rib waveguides [Boeuf et al. 2016]

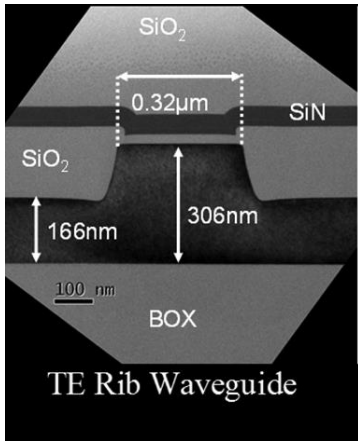


Figure 9: TEM cross section of a SOI rib waveguide

Single Mode Waveguides (SMWGs) are available for 1310 nm, 1490 nm and 1550 nm with propagation losses of 1.6 dB/cm, 1.38 dB/cm and 1.2 dB/cm respectively [22]. Due to the important refractive index difference between their core and cladding, SOI WGs can be birefringent. In PIC25G, WGs have been optimized for transverse electric (TE) propagation and consequently exhibit comparatively high losses for the transverse magnetic (TM) mode. Besides guiding light in a straight line, the waveguides created by this process are capable of routing light via bent waveguides, power splitting and combining via 2 passive components

shown in Figure 10. The directional coupler performs power splitting and combining with a variable ratio depending on the coupling length between the 2 waveguides that compose the device. Symmetric Y junctions can only perform power splitting via a tapered waveguide connected to two SMWGs.



Figure 10: Schematic of (a) a directional coupler and (b) a Y junction

However, the main functions of silicon photonics in optical transceivers are electro-optical modulation and photodetection, as we will see in the next section.

2.2 Electro-optical Modulation and Detection

2.2.1 Mach-Zehnder Modulator

The modulation of light can be done by a component based on the Mach-Zehnder interferometer principle [23]. A coherent light source is divided to follow two different optical paths inducing a phase shift between them. Both paths are then recombined and this generates constructive or destructive interference depending on the phase shift. In silicon photonics, the phase shift is obtained using the carrier depletion phenomenon occurring at the PN junction of a diode. Indeed, applying a reverse bias to a diode enlarges the depletion layer and changes Si refractive index which is, as shown in [24], sensitive to free-carrier concentration. These diodes are fabricated following the process depicted Figure 11: after the fabrication of a waveguide with unetched silicon at each end of the slab region, P and N regions of the diode junction are defined, as shown in Figure 12. The waveguide is then covered by a protective layer against silicidation that may happen during the self-aligned silicide process coming next and which allows making the diode contacts. Mach-Zehnder modulators use several of these diodes called high-speed phase modulators (HSPM) in series to form a modulator branch. One is present on each optical path of the interferometer.

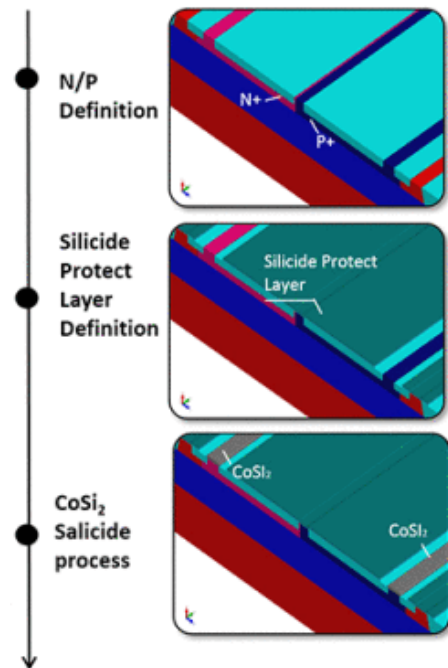
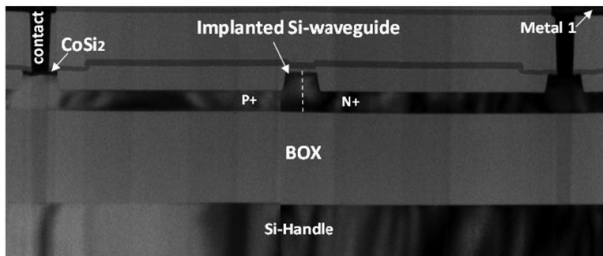


Figure 11: Fabrication process of high-speed phase modulators [Boeuf et al. 2016]



Integrated P/N junction depletion mode High Speed Phase Modulator.

Figure 12: TEM cross section of a HSPM [21]

Their figures of merit are optical losses (dB/cm) and $V\pi$ (V.cm), the voltage needed to obtain a phase shift of 180° using a 1 cm-long branch. PIC25G HSPMs exhibit 6 dB/cm of optical losses and a $V\pi$ of 2.6 V.cm [21]. Using drivers in a BiCMOS 55 nm [25] technology and traveling wave electrodes, PIC25G

Mach-Zehnder modulators demonstrated a NRZ amplitude modulation of light at a 56 Gb/s bit rate, with an extinction ratio of 2.3 dB [26].

2.2.2 Photodetectors

In silicon photonics, light detection is relying on the photogeneration effect: the absorption of a photon in the depletion layer of a diode junction generates a current directly proportional to the incident optical power because of the creation of electron/hole pairs. At a wavelength of 1.31 μm , the photon energy is about 0.95 eV, which is lower than silicon bandgap (1.12 eV) [27]. Therefore, another material is needed to form electron/holes pairs. This material is germanium and its bandgap is 0.6 eV [27]. After waveguides planarization, a cavity is etched in a large waveguide. Ge is grown by epitaxy inside the cavity and protected by a silicon nitride layer. Then, P and N regions are defined as well as contacts above them (process Figure 13). This makes a waveguide Ge PIN photodiode also called high-speed photodiode (HSPD) (Figure 14).

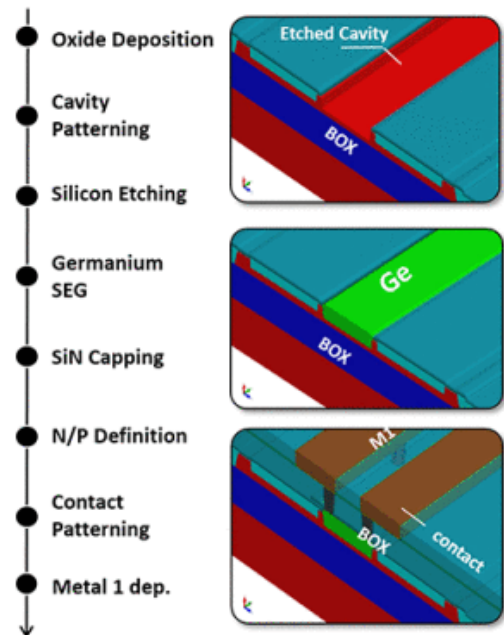


Figure 13: Fabrication process of an integrated waveguides Ge photodiode [Boeuf et al. 2016]

Photodiodes are characterized by their dark current (the remaining current without exposure to light) in A, their responsivity in A/W and their bandwidth in GHz. In PIC25G, HSPDs have demonstrated a dark current of 10 nA, a responsivity of 0.98 A/W and bandwidth larger than 20 GHz under a 1V reverse bias and at a wavelength of 1310 nm

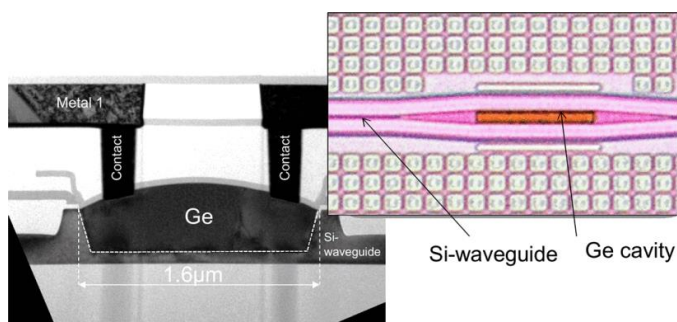


Figure 14: TEM cross section and top view of a Ge HSPD

[21]. Such performance allows the detection of modulated signals up to 28 Gb/s. Waveguide Ge-photodiodes have been reported with a bandwidth higher than 50 GHz using a similar technology, enabling 40 Gb/s signal detection at the cost of a lower responsivity [28].

2.3 Coupling devices.

2.3.1 The challenge of coupling into silicon photonics devices

As already discussed, SiPh ICs are capable to guide, modulate and detect light at the wavelengths used for optical communications over SMFs in data centers. At this point, we need a way to couple light in and out of the PIC. Unfortunately, here lies the main drawback of the high index contrast SMWGs: the complexity to couple light to low index contrast waveguiding structures without excessive optical loss. A high refractive index contrast between the core and cladding of a waveguide results in smaller dimensions for the latter to ensure a single mode propagation. The mode field diameter (MFD) of an SOI SMWG is approximately 300 nm while the MFD of SMF is approximately 10 μm . Figure 15 depicts a SOI rib waveguide in front of a SMF core with dimensions proportional to reality. The coupling efficiency between both components is directly linked to the overlapping area of their respective modal field distribution (this point will be detailed in chapter II). Consequently, directly coupling a SMF to a SOI waveguide by the edge (called in-plane, end-fire or butt-coupling) results in optical loss over 20 dB [29]. To cope with this drawback, two main paths have been followed: the vertical coupling by means of a grating coupler (GC) and butt-coupling using spot size converters. Both are detailed thereafter.

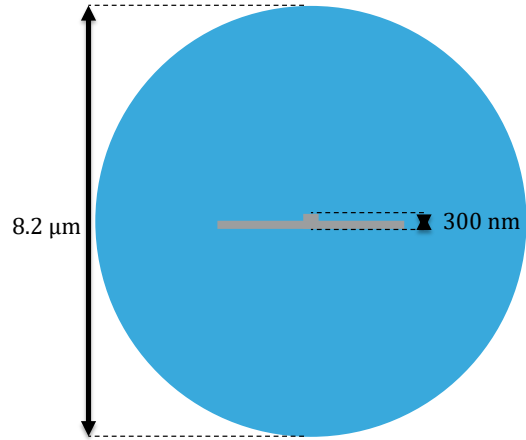


Figure 15: Schematic of a SOI rib waveguide in front of an SMF core

2.3.2 Grating coupler

GCs are diffraction gratings specifically designed to enable a high coupling efficiency between a vertically placed fiber and a SOI waveguide. GCs are based on a periodic and subwavelength variation of the refractive index inside a guiding structure. A GC whose index variation is along a single dimension (1D) follows Bragg's condition, which links the incident wave to the diffracted waves [30]:

$$k_{m,z} = \beta - m \frac{2\pi}{\Lambda}$$

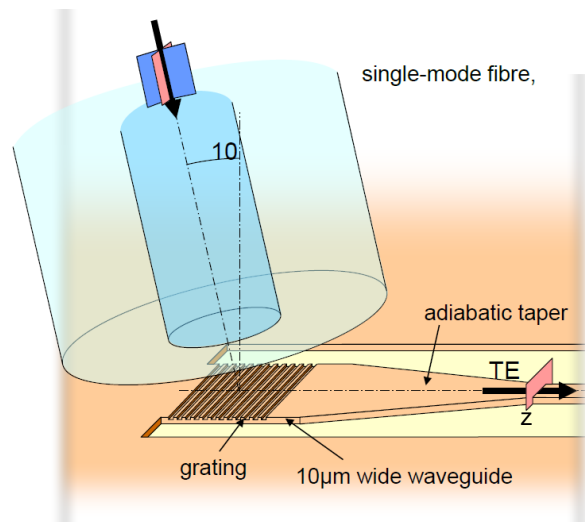


Figure 16: Grating coupler - SMF coupling scheme [122]

where $k_{m,z}$ is the wavevector component of the m^{th} diffraction order along the propagation direction of the incident wave in the waveguide. β is the propagation constant of the latter while Λ is the period of the refractive index variation. In practice, the refractive index variation is introduced through an etching of shallow trenches in a widened waveguide, as depicted by Figure 16. Because of their working principle, GCs are strongly dependent on wavelength and polarization. While output GC have to handle only TE polarization coming from the SOI waveguide, input grating couplers have to manage the unknown polarization state of the light coming from the fiber. As a consequence, two types of grating couplers are used in PIC25G. Single polarization grating couplers (SPGC) are 1D GCs for coupling light out of the PIC with coupling losses as low as 2.2 dB at 1310 nm only for the TE polarization. Polarization splitting grating couplers (PSGC) are 2D GCs that perform the coupling with the TE and TM components of the fiber output light and convert the TM component in TE to be coupled to PIC25G WGs, achieving total losses of 3.2 dB at 1310 nm [21]. Both of them are represented in Figure 17.

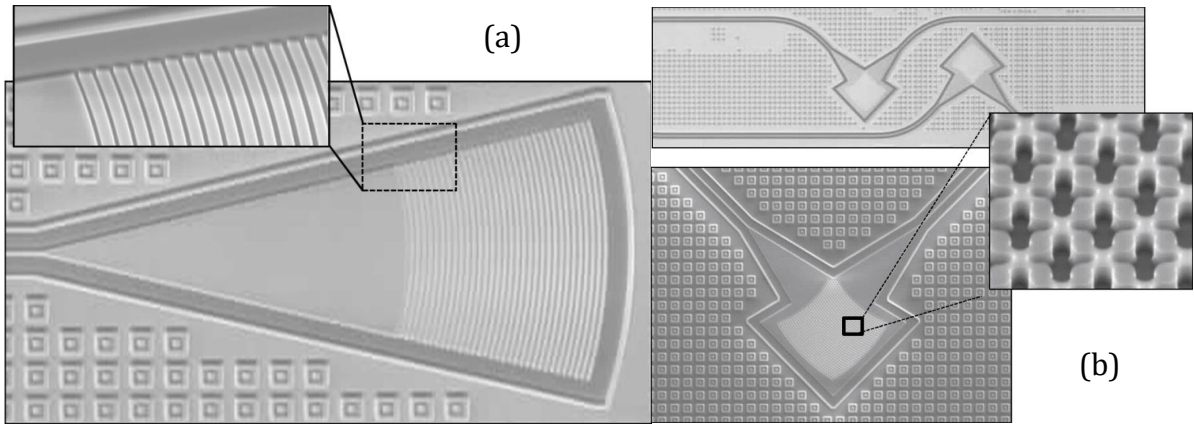


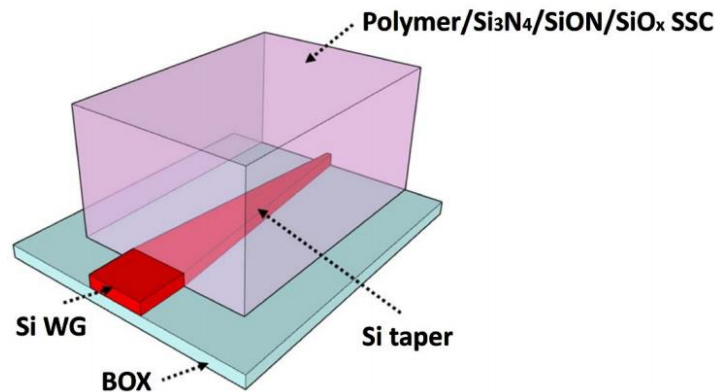
Figure 17: SEM top views of (a) an SPGC and (b) a PSGC [22]

As mentioned above, the GCs coupling efficiency (CE) is very sensitive to wavelength and the result is a 1-dB bandwidth of less than 20 nm. This makes GCs unsuitable for carrying CWDM signals. However, it has been demonstrated that using layout variations, GCs peak wavelength can be adjusted to handle a particular wavelength in the 1270-1330 nm range with a peak loss difference between the GCs below 1 dB [31]. Last but not least, GCs offer an excellent on-wafer probing capability, which is a strong asset for a large-scale industrialization.

2.3.3 Lateral spot size converters

On the other hand, multiple solutions have been investigated to fabricate wideband, polarization insensitive and efficient edge couplers (EC). Most of them rely on the progressive widening of the MFD at the end of an SOI waveguide by a spot size converter (SSC). The first straightforward method is to use an inverted taper in an SOI waveguide to

decrease the confinement of light in the horizontal direction while expanding the mode vertically using a lower index contrast waveguiding structure (Figure 18). Polymers [32] [33] [34], silicon oxynitrides (SiO_xN_y) [35] and silicon-rich oxides (SiO_x) [36] have been used to create SSCs. They manage to increase the MFD to 4.3, 2.5, 4.2, 4.3 and 3 μm , respectively. This is enough to achieve very low loss when coupling with expensive ultra-high numerical aperture (UHNA) and lensed fibers. However, the CE with standard SMFs remains low. Small MFD fibers also bring a higher sensitivity to misalignment. Typical tolerances are around -1 dB for a 1 μm shift



The replacement of solid silicon tapers by metamaterials allows increasing more the MFD, hence the CE with standard SMFs. The principle is to decrease the effective index by periodically alternating the core and cladding materials along the waveguide propagation axis (Figure 19). The period must be even lower than those used for GCs to avoid any diffraction. This method shows a CE with a SMF28 fiber of -1.3 dB at 1310 nm with a 1-dB bandwidth greater than 100 nm and polarization dependent losses down to 0.6 dB [37].

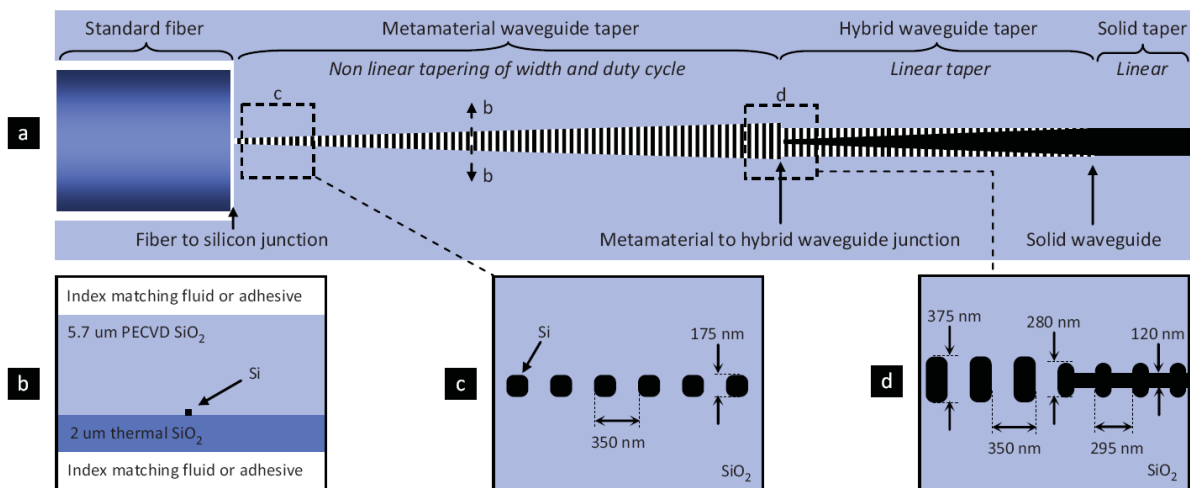


Figure 19: Optical design of the metamaterial fiber interface. (a) Schematic top view of the three sections of the mode size converter. (b) Cross-sectional diagram of the metamaterial waveguide. PECVD stands for plasma-enhanced chemical vapor deposition. The refractive index of the fluid or adhesive must be under 1.445 at 1310 nm. (c) Detailed top view of the metamaterial fiber coupler. (d) Detailed top view of the transition from a metamaterial to a hybrid waveguide.[37]

Nevertheless, this solution brings a few drawbacks. An opening is etched through the entire SiPh Integrated Circuit (IC) back-end layers that can cause thermo-mechanical reliability issues [38]. The on-wafer probing is more difficult and a polarization splitting-rotator [39] is needed in technologies where only one polarization is supported. For all these reasons, none of these components have been implemented in PIC25G. Table 5 sums up the main different optical fiber/SOI waveguide coupling strategies.

Table 5: Summary of the main SiPh IC coupling strategies

	Coupling loss	MFD	Tolerance (-1 dB)	On-wafer probing
Grating coupler	2.2/3.2 dB	$\approx 10 \mu\text{m}$	$\pm 4 \mu\text{m}$	✓
Polymer SSCs	<1 dB	$\leq 4.3 \mu\text{m}$	$\approx 1 \mu\text{m}$	X
Metamaterial	1.3 dB	$\approx 10 \mu\text{m}$	Not Available	X

3 Silicon Photonic based Electro-optic Transceivers

3.1 100G implementations and beyond

3.1.1 100 Gb/s Parallel Single Mode 4 (PSM4)

Capabilities of silicon photonics that have been detailed in the previous section have been used in several kinds of optical transceivers and especially in 100G PSM4 transceivers. Figure 20 depicts the assembly strategy of such a transceiver with PIC25G technology.

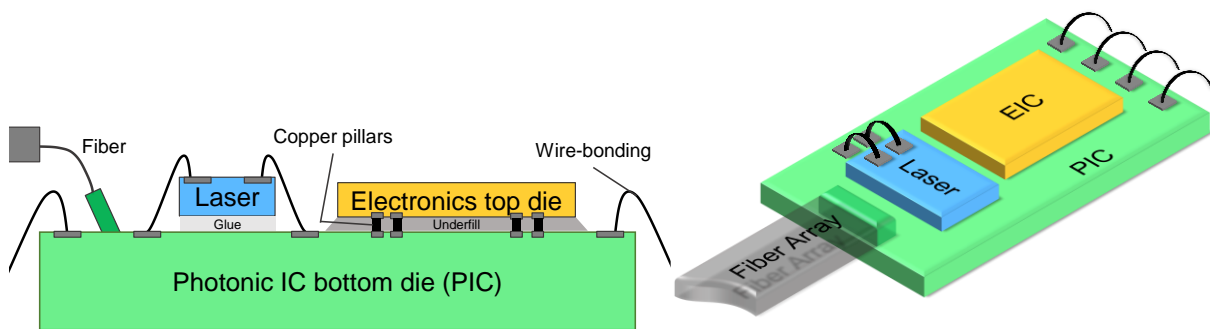


Figure 20: Assembly strategy of a 100G PSM4 silicon photonic transceiver [22]

In this approach, the SiPh IC is used as an interposer. It performs electro-optical modulation, light detection as well as optical and high frequency routing.

On the transmitter side, the light source is a micro-packaged InP laser glued and wire-bonded on top. Light is coupled via a GC. An Electronic IC (EIC) in a BiCMOS or CMOS technology is assembled by flip-chip on the interposer to drive the MZM efficiently. Light is then coupled to a glued fiber by another GC. On the receiver side, light is directly

detected by the photodiode after the fiber/GC coupling. The electric signal is then processed by the electronic IC.

Since a few years now, such silicon photonic transceivers are commercially available. With photodiodes and modulators able to detect and modulate at 50 Gb/s bit rate and Pulse Amplitude Modulation over 4 levels (PAM4), this assembly scheme can be used for the next generation 400G optical links. Yet, the drawbacks present today will not be overcome easily. Those include, first, a high packaging cost due to the unconventional assembly of the fiber that requires an active alignment. Indeed, GCs have a 1-dB tolerance of 4 μm to lateral misalignment and a 3-dB tolerance for an angle shifted from 1° [40]. This cannot be done by high throughput placing machines. Second, this scheme uses multiple fibers. The longer the link is, the more important the part of fibers in the total cost is. As a consequence, this approach cannot compete for long optical reach (> 2 km) with transceivers requiring only one fiber. A possible solution for cost reduction and for reaching longer distances would be to use CWDM but the GC 1-dB bandwidth of 20 nm impedes this solution, the CWDM 4 λ wavelengths range being 60 nm wide.

Changing the assembly strategy may allow to solve both problems by the use of an external multiplexing/demultiplexing device in a low-cost package.

3.1.2 100 Gb/s CWDM4

In order to enable CWDM, one proposed solution has been to consider the addition of an external multiplexer to the assembly scheme above [41]. Kaiam developed a silica planar lightwave circuit (PLC) with an integrated CWDM multiplexer and facet polished with an angle allowing the coupling with GCs. The PIC25G chip is still an interposer with the electronic IC on top but the PLC comes between the SiPh IC and the fibers/lasers (Figure 21).

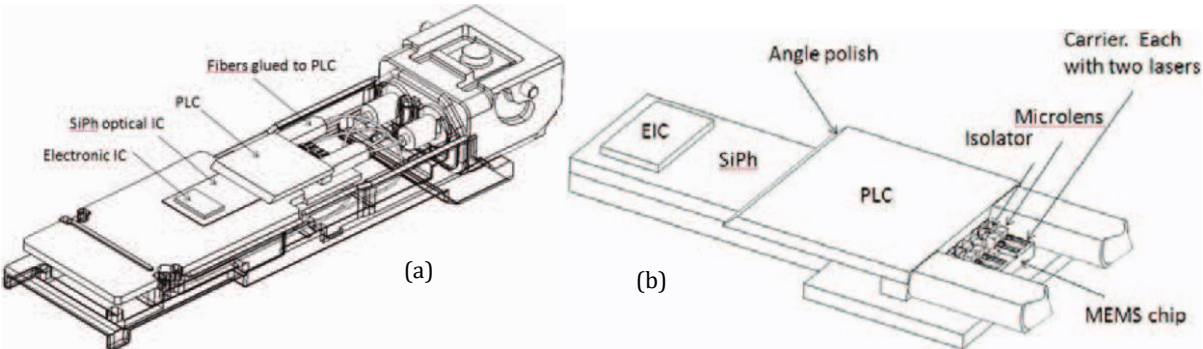


Figure 21: CWDM Transceiver in housing without lid (a). Enlargement of the optical engine (b) [41]

The 2 fibers in ferrules are aligned and glued at the other end of the PLC and the 4 lasers are aligned in front of the same facet using Microelectromechanical systems (MEMS) levers. This approach is able to deliver an optical signal compliant with CLR4 MSA

specifications and achieve a CWDM4 MSA compliant bit error ratio for an optical modulation amplitude greater than -7 dBm. Unfortunately, this is done at the cost of the addition of a silica PLC, a MEMS chip and a more complex package, all resulting in a direct increase of the transceiver cost.

At this point, the added value of a single low-cost interposer platform to manage all the interconnections (electrical and optical), containing optical multiplexer/demultiplexer and using conventional assembly techniques is revealed.

3.2 Electrical and Optical Interposers

3.2.1 Electrical interposers

The sharp increase in the operating frequency and I/O density of the processors and memories has created a bottleneck at the level of the electrical interconnections between these two types of integrated circuits that constrains the performance of the system. This led to the development of high-density interconnect (HDI) interposers. From an electrical point of view, an interposer is a chip capable to interconnect multiple ICs between them with a shorter interconnection distance and higher I/O density than the printed circuit board (PCB) underneath allows. To fulfill that condition, it contains several redistribution layers (RDLs) and solder balls on both sides as well as through package vias (TPVs) in its core material to connect the ICs to the PCB. It is even possible to vertically connect an IC placed between the interposer and the PCB, as shown in Figure 22. A few technologies have been deployed at large scale for high performance applications. An important criterion regarding the electrical and optical interposer is its cost which is defined by its materials, process and assembly costs as well as the scale of its deployment. Consequently, leveraging interposer technologies for high performance applications to develop an electrical and optical interposer is a good way to keep costs low. Three main interposer types, depending on the substrate material, are distinguishable: organic, glass and silicon. We will now review each material regarding our application.

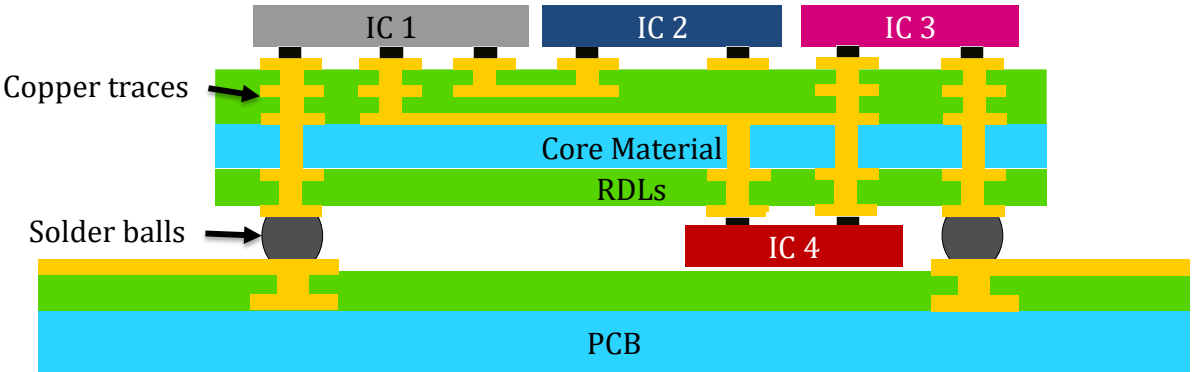


Figure 22: Generic schematic of an electrical interposer

3.2.1.1 Silicon interposer

Silicon interposers are fabricated following the same process as ICs' back-end-of-line (BEOL) and are already in use in several high-end and high-volume electronic products such as some AMD GPUs and Xilinx FPGAs [42][43]. The BEOL dual damascene (Figure 23) process makes them able to show very aggressive design rules: typical line width and spacing (L/S) is below $1\ \mu\text{m}/1\ \mu\text{m}$ [44]. Also, sharing the same material between the IC and the interposer has the benefit to make reliable assemblies thanks to the perfectly matched coefficients of thermal expansion (CTE) and the high thermal conductivity of silicon compared to glass and organic materials.

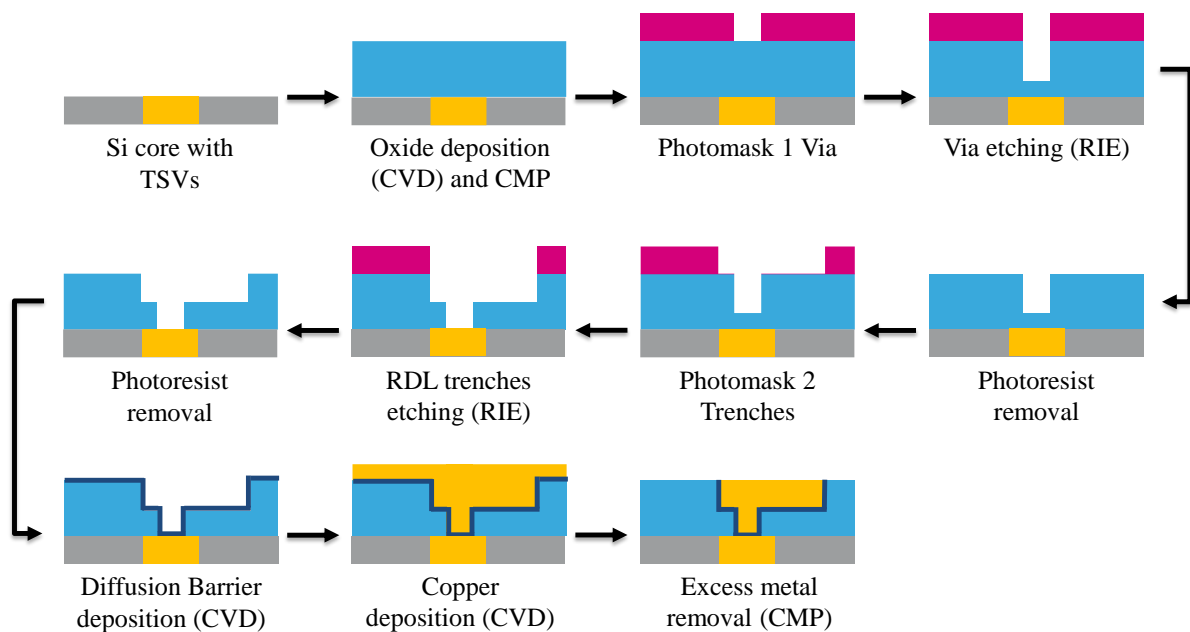


Figure 23: Dual Damascene process [45]

However, the intrinsic electrical performance of silicon interposers are far from ideal especially that of the through silicon via (TSV) [46] [47] due to the low resistivity of silicon. In addition, the cost of silicon interposers remains high because they require wafer manufacturing infrastructure and a costly TSV fabrication scheme (Figure 24) [48]. Regarding our application, the mechanical and thermal reliability is an asset but the cost structure of silicon interposers confines them to very high-end products which is not the case of the targeted optical transceivers market.

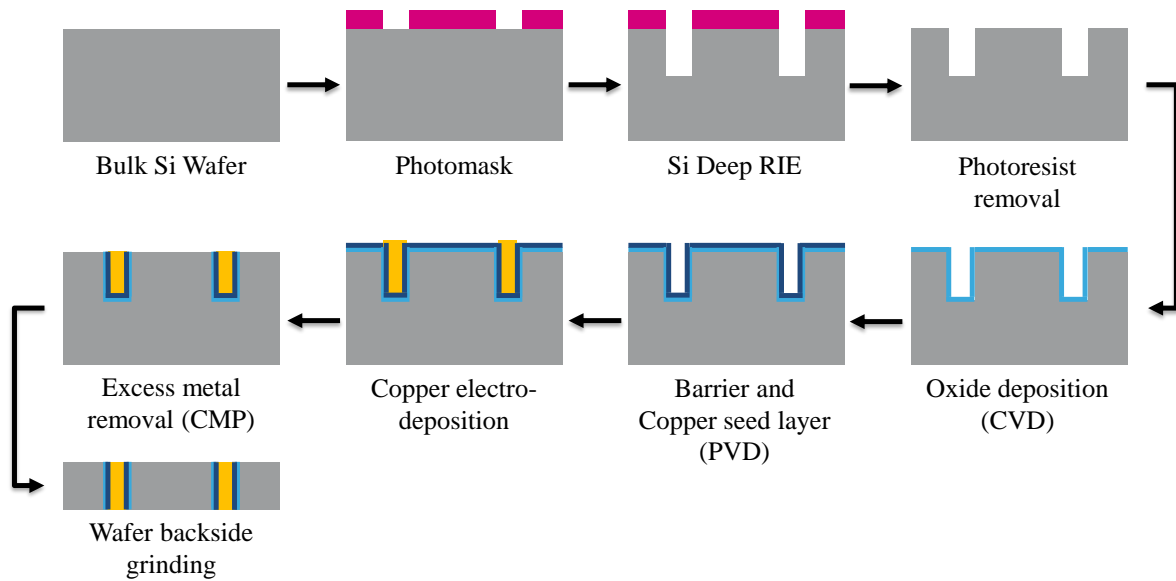


Figure 24: TSV fabrication process [49]

3.2.1.2 Organic interposer

Organic interposers seem to be a valuable alternative to silicon. Indeed, the widely used semi-additive process (SAP) allows a panel manufacturing of L/S up to $2\ \mu\text{m}/2\ \mu\text{m}$ RDLs ensuring low-cost production [50] and excellent RF performance on low-dissipation factor substrates [51]. A typical fabrication process of high-density interposers is described in Figure 25.

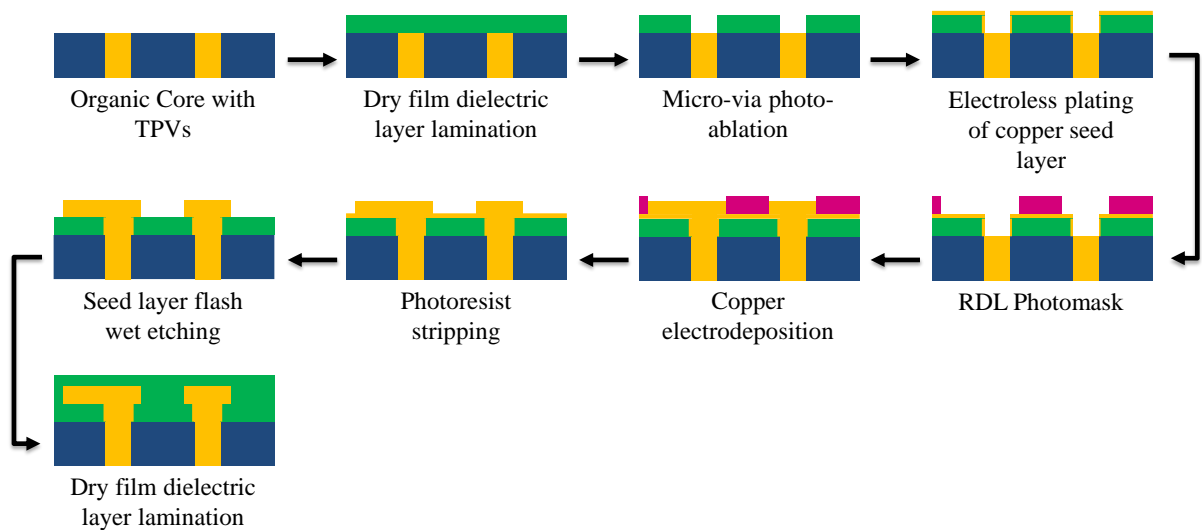


Figure 25: Semi-additive process on organic substrate [50]

However, such aggressive design rules necessitate a specific substrate with a high glass transition temperature (T_g) to minimize misalignment between RDLs during fabrication and a very low CTE to minimize mechanical mismatch with the IC during temperature variations. This can result in the debonding of the silicon IC. Ultimately, these constraints

increase the fabrication cost of the core material to obtain the same performance of glass, as we will see thereafter.

3.2.1.3 Glass interposer

In order to overcome the high fabrication cost of silicon interposer and low reliability of organic substrates, electrical interposers using a glass substrate have been developed in recent years. The electrical performance of glass interposers is superior to those of silicon interposers, as shown in [52] and on par with organic interposers, notably thanks to the low dielectric constant and dissipation factor of glass. In addition, the flatness and mechanical rigidity of the glass allow to obtain a higher integration density than conventional organic substrates by using the same panel manufacturing SAP, as demonstrated in [53]. Last but not least, large glass panels are available in high volumes at a very low cost from the display industry and their CTE can be matched to Si CTE at fabrication. Still, semiconductors foundries and Outsourced Semiconductor Assembly and Test (OSATs) do not provide glass interposers in high volumes for the time being.

3.2.1.4 Synthesis on electrical interposer technologies

Silicon, organic and glass interposers have been presented. The two first technologies benefit from an already deployed supply chain but suffer from a few drawbacks. Silicon interposer fabrication cost is high and its electrical performance is limited. Organic substrates suffer from mechanical assembly issues when using aggressive design rules, unless an expensive substrate is used.

Therefore, from the electrical and packaging point of view, glass seems to be a promising candidate for the core material of the electrical and optical interposer thanks to its mechanical and RF properties. The only issue is the industrial availability. However, as it is foreseen to be the next technology for high performance applications in high volumes, some OSATs already propose prototyping over glass substrates [54]. In the next section, we will move to the optics side and review the different optical technologies available on a glass substrate.

3.2.2 Optical technologies on a glass substrate

A large number of optical technologies have been developed over time for an equally large number of applications. For the purpose of SiPh ICs packaging using a glass substrate, the required optical technology has to provide SMWGs at the telecom wavelengths used in CWDM (1270-1330 nm), a multiplexer, a device allowing the vertical coupling with the SiPh IC and a lateral coupling with a fiber using V-grooves for example. Two approaches can be considered: the integration of the optical technology inside the glass substrate or on top of it. In the first category, ion-exchanged waveguides and direct femtosecond laser writing in glass are potential technologies.

3.2.2.1 Ion-exchange

SMWG with losses down to 0.1 dB/cm at 1.3 μm [55] [56] [40], multiplexers/demultiplexers [57] μm , [58] and mirrors for vertical coupling [59] have been demonstrated using ion-exchange in glass. The fabrication process (Figure 26) consists in exposing a glass substrate to a mix of melted silver nitrate and sodium nitrate salts through an aluminum or alumina hard mask. Ag^+ ions replace Na^+ ions at the glass surface. Then, the aluminum mask is removed and Ag^+ ions are moved deeper inside the substrate using an electrical field. This migration allows to locally increase the refractive index of glass.

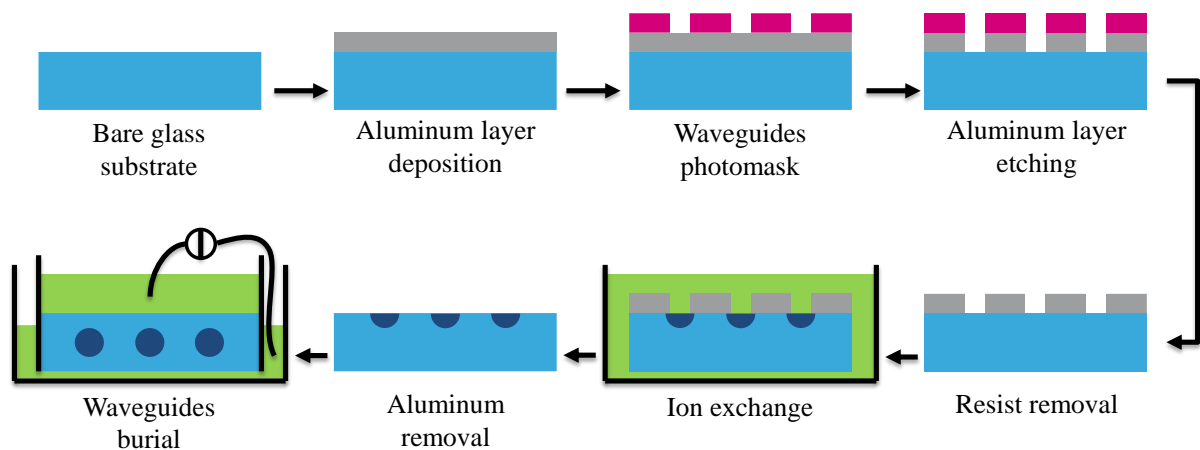


Figure 26: Ion-exchanged waveguides process

This technology has been demonstrated at PCB level for board-to-board optical interconnections alongside electrical interconnections [123].

3.2.2.2 Direct Femtosecond Laser Writing

Direct laser writing of waveguides relies on the non-linear absorption phenomenon occurring in glass exposed to ultra-short & high-energy laser pulses [60]. At energies below the glass ablation threshold, this absorption results in a local increase of glass density and refractive index due to structural modifications [61]. Using this method, SMWGs at 1.55 μm with losses of 0.5 dB/cm have been reported [62]. More recently, arrayed waveguide grating have been fabricated in the visible [63]. The same technique as in [59] [64][40] can be used to implement the mirror.

3.2.2.3 Silica-based PLCs

In the second category, namely the optical technologies deposited on a glass substrate, we find PLCs based on silica and polymer waveguides either created by photolithography or by laser ablation.

Silica-based PLCs are created following the fabrication process of Figure 27: layers of pure silica and $\text{SiO}_2\text{-GeO}_2$ are deposited on the substrate by flame hydrolysis deposition (FHD).

Both layers being porous, a high temperature annealing follows. Waveguides are then defined by reactive ion etching (RIE) of the SiO₂-GeO₂ layer through a photomask. Waveguides cores are finally encapsulated in a second layer of pure SiO₂. The core refractive index depends on the GeO₂ concentration.

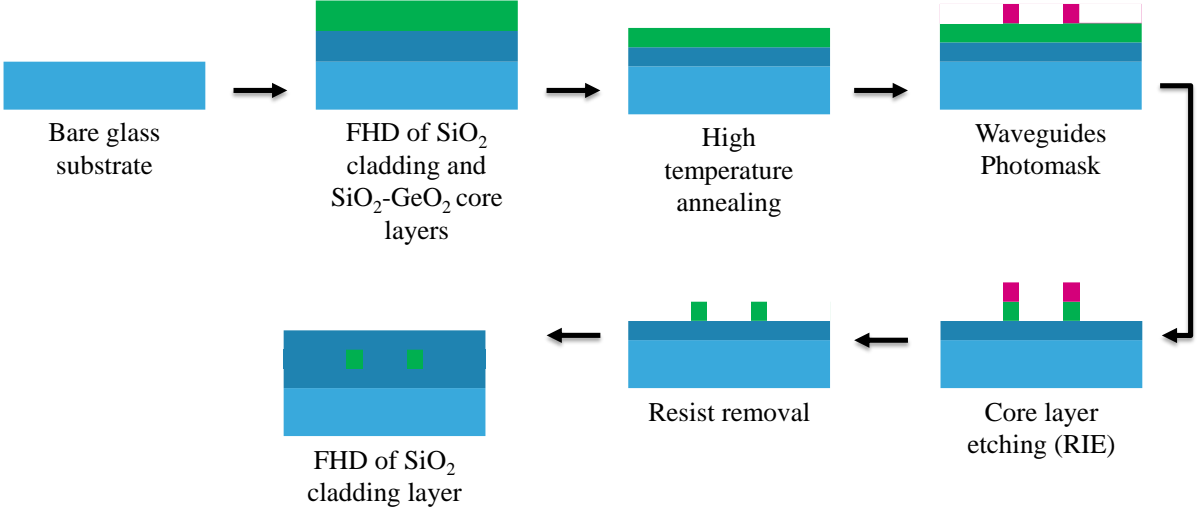


Figure 27: Silica PLC fabrication process [65]

Silica PLCs have been a material of choice for passive integrated optics for years, especially in the domain of telecommunications. Therefore, numerous circuits have been developed, including of course multiplexers such as the one described in [41]. SMWGs have shown very low loss in this technology: down to 1.7 dB/m at 1.5 μm [66].

3.2.2.4 Polymer waveguides

Widely used in electronics fabrication, from ICs (photomask) to PCB (both photomask and dielectric layers), polymer materials are versatile materials in terms of physical properties and patterning techniques. Some polymers showing a low optical absorption in the telecom range, the idea came to fabricate waveguides with these materials. Their availability in the form of dry films make them suitable for panel manufacturing [67]. Two fabrication processes have been commonly used: photolithography (Figure 28) and laser ablation (Figure 29).

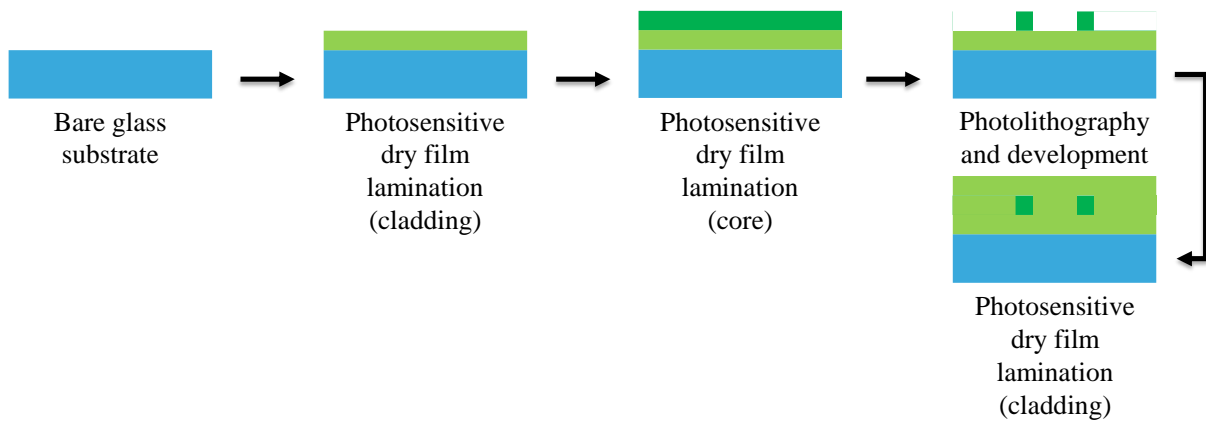


Figure 28: Fabrication of polymer waveguides by photolithography

In the first case, negative photosensitive resins are used. A first cladding layer is laminated on the glass substrate, exposed to UV light and baked. Then, the core layer is laminated, exposed to UV, developed and cured just as it would have been the case for the fabrication of a photomask, the difference lying in the fact that the resin is not removed afterward as it serves as the core of the waveguide. Finally, the core is encapsulated by the lamination of a second cladding layer. The fabrication of single mode waveguides with propagation losses below 1 dB/cm at 1.3 μm using dedicated and commercially available epoxy-based and siloxane-based polymers has been demonstrated [68] [69]. These materials also allow the fabrication of integrated passive devices such as Mach-Zehnder interferometers and consequently multiplexers. Unfortunately, similar materials in the form of dry films are not, to our knowledge, commercially available.

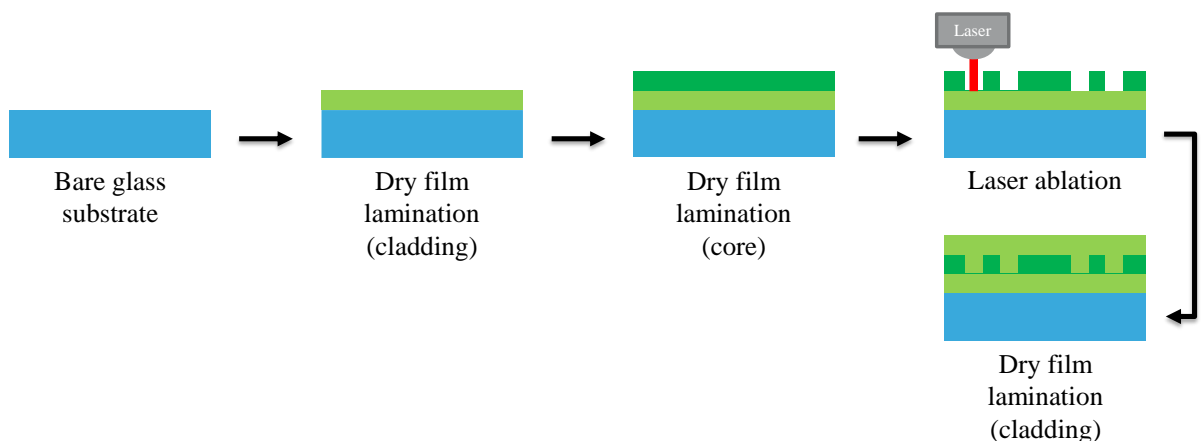


Figure 29: Fabrication process of polymer waveguides by laser ablation

In the second case, the fabrication process is very similar but the waveguide core is formed by the laser ablation of trenches inside the core layer. Laser-ablated polymer waveguides have been fabricated using different laser types such as CO₂, Nd-YAG and excimer [70].

Several of these technologies have been used, inter alia, as an interposer in order to solve the two problems of grating couplers mentioned in section 3.1.1 [71] [72]. Vertical coupling solutions, such as integrated micromirrors [73] or the angled polishing of the interposer slice [72] have been demonstrated for coupling to the PIC. Passive alignment structures in U or V shape for the coupling between the fiber and the interposer waveguide have also been fabricated [74].

3.2.2.5 Synthesis on optical technologies on a glass substrate

Among the technologies listed above, ion-exchange and silica-based PLCs waveguide fabrication processes are very different from those of electric glass interposers. Indeed, the first requires a mask followed by a contact at high temperature with silver salts, in order to proceed to ion exchange and the second uses unconventional material deposition and etching methods for packaging substrates: FHD and RIE. Despite, their apparent viability, the large-scale deployment of these technologies is not guaranteed since tooling and processes are not used among the main substrate manufacturers.

The manufacturing of polymer waveguides by photolithography uses materials similar to those used as dielectrics between the electrical RDLs of glass interposers, such as epoxy. However, dry films exploited in the literature to fabricate the core and the cladding of waveguides in [67] were not commercially available at the beginning of this work, to the best of our knowledge. These resins are available in a liquid form for spin-coating but this involves the use of glass wafers and therefore a more expensive manufacturing than that of electrical interposers which uses glass panels, on which the polymer is deposited by lamination. Granted the availability of optical epoxy dry films for the manufacturing of SMWG, polymer waveguides by photolithography or laser ablation would make a perfect candidate for the electrical and optical interposer since the material can be structured at a low-cost and since the tooling is already in use in the industry. As we will see in the next sections, we mainly considered two approaches: the laser ablation of traditional polymer dry films and the laser lithography of dedicated spin-coated epoxy resins.

Finally, the waveguides defined by exposure to the femtosecond laser seem a viable alternative, even if, in the long term, the electric RDLs will separate them from the photonic chip which will complicate the coupling with the latter.

4 State-of-the-art synthesis and definition of the objectives

In the previous sections, we showed that silicon photonics is potentially interesting for data centers high-speed optical links which are using several channels and over distances that cannot be achieved using multimode fibers. Yet, PIC25G SiPh transceivers are held back by the complexity and constraints of the vertical coupling scheme between SMFs and SiPh ICs. Indeed, the grating coupler bandwidth and assembly cost makes SiPh unable to compete with solutions that are using CWDM. Several edge-couplers have been developed to enable a broadband edge-coupling at the cost of the loss of on-wafer probing and a more complex fabrication process generating thermo-mechanical stress. To keep grating couplers in the same SiPh technology, we then highlighted that exploiting an interposer, integrating both passive optics and RF RDLs, would help to solve the problem of the GC bandwidth using frequency specific GCs and a multiplexer integrated in the interposer while reducing the assembly cost by the use of traditional flip-chip bonding.

We reviewed three electrical interposer technologies, namely silicon glass and organic interposers and determined that, despite a non-existing supply chain, glass interposer offers most of the requirements needed for this application, i.e. a low cost, a good RF performance, a decent wiring density and reliable assembly (Table 6). Besides, the lack of supply chain may be mitigated in the coming years since this interposer type has been extensively studied as a replacement for its silicon counterpart. An optical technology compatible with these recent developments should be easier to deploy at a large scale.

Table 6: Comparison of interposer core materials

	Density	CTE mismatch	RF performance	Cost	Supply Chain	Total Score
Silicon	++	++	-	-	+	4
Glass	+	+	++	++	-	6
Organic	-	-	++	+	+	5

The interposer core material being set, we reviewed several optical technologies that allow the fabrication of SMWGs on a glass interposer. Here, polymer-based solutions stand out because the materials are already in use in the back-end of electrical interposers. This would allow to get the interposer waveguide to be as close as possible to the SiPh, thus facilitating the coupling between both chips. Table 7 sums-up the comparison between optical technologies on a glass substrate.

Table 7: Comparison of optical technologies on a glass substrate

	Integration	SMWG	Loss	Vertical coupling	Multiplexer	Refs
Ion-Exchange	Inside substrate	1.3/1.5 μm	0.1 dB/cm	✓	✓	[55] [56] [40] [57][58][59]
Femtosecond Laser Writing	Inside substrate	1.5 μm	0.5 dB/cm	(✓)	✓	[62] [63] [59] [64][40]
Silica PLC	On substrate	1.3/1.5 μm	1.7 dB/m	✓	✓	[66] [41]
Polymer Litho	In back-end	1.3/1.5 μm	<1 dB/cm	✓	✓	[68] [69]
Polymer Laser	In back-end	X	?	✓	?	[70]

The objective of this thesis is to investigate the feasibility of a new approach making of using an electrical and optical interposer to connect the photonic silicon chip to a single-mode optical fiber (see Figure 30 and Figure 31).

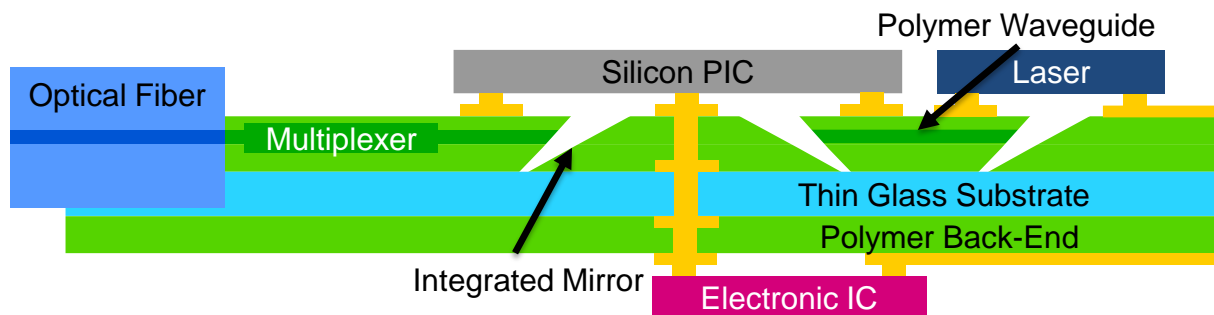


Figure 30: Electrical and Optical Interposer Approach for silicon photonic transceivers

In this approach, the electrical and optical interposer would integrate:

- An organic back-end with copper RDLs with a high density to interconnect the silicon photonic chip, the CMOS/BiCMOS chip and board and transmit 50 Gb/s signals

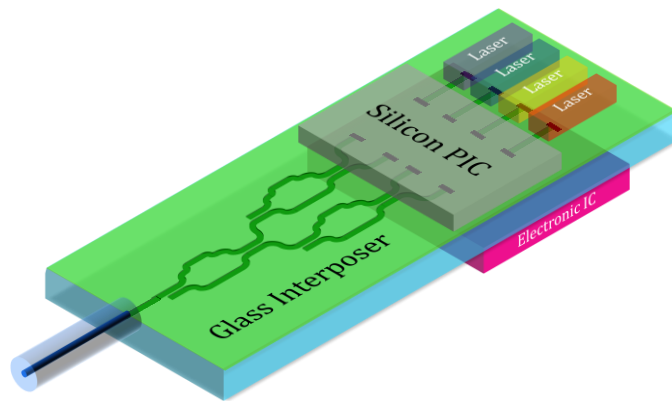


Figure 31: 3D view of the electrical and optical interposer proposed approach

- An optical technology integrated in the back-end using compatible polymer materials to enable SMWG and de/multiplexers for CWDM
- Broadband optical interfaces coupled on the side to ensure low-loss connections with passively aligned fibers using the principle of v-grooves, as it is done in fiber arrays.
- A solution for optically connecting the SiPh IC (containing grating couplers) and the lasers to the interposer.

With such an interposer, the SiPh and CMOS/BiCMOS ICs can be assembled using a conventional flip-chip technique. This, together with the passively aligned fibers, could enable 4x100 Gb/s CWDM 4 λ optical transceivers using the same SiPh technology and PAM4 modulation at very low cost. Moreover, several of the constituting blocks of this interposer have already been demonstrated separately.

The objective of this work is to develop an optical coupling between an electrical/optical interposer and an existing SiPh IC in PIC25G technology and demonstrate light detection and modulation through this system. This includes three steps:

- The design of the interposer and its components:
 - Single mode polymer waveguides with low coupling losses to butt-coupled SMFs and low propagation losses (1 dB/cm). The development of the multiplexer will not be tackled in this work.
 - A slanted mirror optimized for interposer/SiPh IC coupling. The coupling efficiency has to be equivalent to a fiber/grating coupling.
 - RF transmission lines able to transmit 50 Gb/s signals over a few millimeters. We target insertion losses below 3-dB/mm at 75 GHz.
- The fabrication of an interposer using standard equipment with regards to the fabrication of electrical interposers. It shall allow to perform the characterization of test structures embedded in the PIC25G IC bonded by flip-chip on the interposer.
- The characterization of the assembly, including: insertion loss measurement of waveguides and transmission lines, coupling efficiency and modulation bandwidth.

All three points are the subject of the next chapters.

5 Conclusion

In a nutshell, we presented OFCs to show that 400G is the next step of data centers optical interconnections using WDM and PAM4 modulation for communication longer than 500 meters over SMFs. Then, the SiPh technology developed by STMicroelectronics was presented. It is capable of light modulation and detection near 50 Gb/s, but the coupling with SMFs suffers from high assembly costs and a narrow bandwidth regarding CWDM requirements. We compared subsequently different electrical interposers and optical technologies to highlight that a passive, low-cost, electrical/optical glass interposer has the potential to provide 4x100 Gb/s CWDM 4 λ transceivers based on SiPh. Finally, the objectives of this work have been presented.

II Interposer Design & Simulations

The second chapter is dedicated to the design and simulation of the interposer and its components. The first part details the theory and simulations of 2D, 3D and Rib dielectric waveguides, in order to determine the ideal physical properties of the waveguides embedded in the interposer. In the second part of the chapter, we review coplanar transmission lines and optimize MZM electrodes for the transmission of high data rate signals in the interposer and in the SiPh IC, respectively. Finally, the design and simulations of the vertical coupling between the interposer and the SiPh IC are presented.

<i>1 OPTICAL WAVEGUIDES</i>	44
1.1 2D Slab Waveguide	44
1.2 3D Waveguides	48
1.2.1 Effective Index Method	48
1.2.2 Rib Waveguide	50
1.2.3 FDE Simulations	52
1.3 Lateral Coupling Efficiency with Optical Fiber	54
1.3.1 Coupling Efficiency	54
1.3.2 Coupling Efficiency Simulations	55
<i>2 RF OPTIMIZATIONS</i>	57
2.1 Interposer Transmission Lines	57
2.1.1 Coplanar Waveguides	57
2.1.2 ADS simulations	60
2.1.3 Interposer Stack Modeling	62
2.2 PIC25G Modulator electrodes optimization	63
<i>3 PIC TO INTERPOSER COUPLING</i>	66
3.1 Proposed coupling scheme and 1 st order approximation	67
3.2 FDTD Simulation & Modeling Methodology	68
3.3 PIC25G Grating Coupler Simulation	69
3.4 PIC to Interposer Coupling	70
3.4.1 2D Simulations.....	70
3.4.2 3D Simulations.....	72
<i>4 CONCLUSION</i>	72

1 Optical Waveguides

In this section, we describe the working principles of a slab waveguide from ray optics and electromagnetic point of views, respectively, as this structure is used to approximate the operation of two other structures we consider for the optical waveguide of the interposer. Then, we study the impact of the waveguide physical properties regarding the coupling efficiency with a single mode optical fiber.

1.1 2D Slab Waveguide

When dealing with optical waveguides, light trapping can be explained by ray optics using the concept of total internal reflection. Though ray optics is a huge simplification of the electromagnetism that is only valid for structures that are much larger than the wavelength, it helps understanding some basic characteristics of the slab waveguide [75]. The assumption is made that a ray of light that moves in a straight line in a material of index n_1 is split in 2 rays when arriving at the interface between 2 materials of refractive indices n_1 and n_2 , respectively. One is reflected whereas the other is refracted (Figure 32). The refractive index of a given material is defined as $n = \frac{c}{v}$, where c is the speed of light in vacuum and v the phase velocity of light in the material. According to the Snell-Descartes law, the relation between the angle of the incident ray $\theta_{incident}$ and the angle of the refracted ray $\theta_{refracted}$ is:

$$n_1 \cdot \sin(\theta_{incident}) = n_2 \cdot \sin(\theta_{refracted}) \quad (1)$$

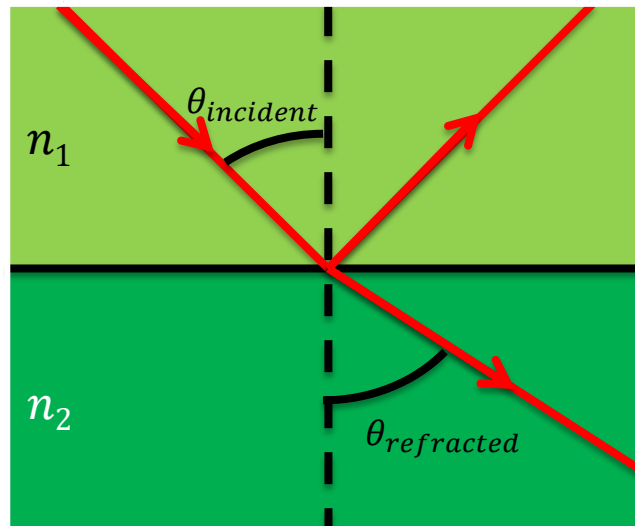


Figure 32: Schematic of the refraction principle

However, the maximum angle for which the refracted ray crosses the interface is 90° . We can deduce a maximum angle of the incident ray for which the refracted ray exists. This one, called critical angle, is: $\theta_c = \arcsin\left(\frac{n_2}{n_1}\right)$

For larger angles, the incident ray is not divided in two and is, as a consequence, totally reflected. This phenomenon is called the total internal reflection and is used to guide the light into waveguides.

The principle of waveguides is to guide the light waves in a material of high refractive index n_{core} surrounded by a material of lower refractive index n_{clad} (as in Figure 33) so that the rays contained in the inner material are incident at the interfaces with an angle higher than the critical angle and consequently, keep being reflected inside the structure.

However, this picture does not allow to obtain a complete description of the electromagnetic fields in the structure. Indeed, as light waves are electromagnetic (EM) waves, Maxwell's equations should be used to describe thoroughly the propagation of light in a two-dimensional step-index slab waveguide that is infinite along the y dimension, as shown in Figure 33.

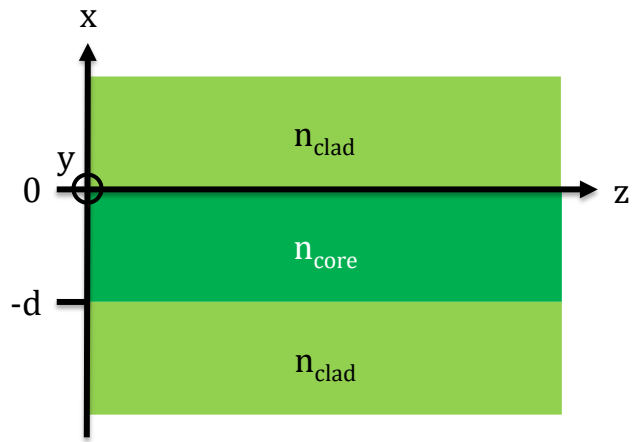


Figure 33: Schematic of a 2D slab WG cross-section

As we are searching for waves travelling in the z direction, we will study the field solutions of Maxwell equations in the three regions and impose continuity at the interfaces to determine if a wave can be guided within the structure and its propagation constant. Maxwell equations inside a homogeneous non-magnetic dielectric material of refractive index n can be written:

$$\left\{ \begin{array}{l} \vec{\nabla} \wedge \vec{E} = -\mu_0 \frac{\partial \vec{H}}{\partial t} \\ \vec{\nabla} \wedge \vec{H} = n^2 \epsilon_0 \frac{\partial \vec{E}}{\partial t} \\ \vec{\nabla} \cdot \vec{E} = \frac{\sigma}{\epsilon_0} \\ \vec{\nabla} \cdot \vec{H} = 0 \end{array} \right. \quad \begin{array}{l} (2) \\ (3) \\ (4) \\ (5) \end{array}$$

Where \vec{E} is the electric field vector, \vec{H} the magnetic field vector, μ_0 the vacuum permeability, ϵ_0 the vacuum permittivity and σ the electric charge density.

Let us consider the general form of the complex electric and magnetic fields of a monochromatic traveling wave with a pulsation ω and a propagation constant β propagating in \vec{z} direction:

$$\begin{cases} \vec{E} = (E_x\vec{x} + E_y\vec{y} + E_z\vec{z}) = \vec{E}(x, y)e^{i(\omega t - \beta z)} \\ \vec{H} = (H_x\vec{x} + H_y\vec{y} + H_z\vec{z}) = \vec{H}(x, y)e^{i(\omega t - \beta z)} \end{cases} \quad (6)$$

Since we are considering an identical and infinite structure along the y axis, there no y -dependency of \vec{E} and \vec{H} fields. Hence, $\frac{\partial \vec{E}}{\partial y} = \frac{\partial \vec{H}}{\partial y} = 0$ and after substituting (6) in (2) and (3), we obtain a system with two independent group of 3 equations. With variables substitution within the respective groups of equations, two identical equations, called wave equations, are obtained (one as a function of E_y and the other as a function of H_y). Waves satisfying these equations are called propagation modes. The wave equation, presented below, is a second order partial differential equation, where Ψ may be either E_y or H_y :

$$\frac{\partial^2 \Psi}{\partial x^2} + k_0^2(n^2 - n_0^2)\Psi = 0 \quad (7)$$

With, $n_0 = \frac{\beta}{k_0}$ the effective index of the propagation mode and $k_0 = \frac{\omega}{c}$

Therefore, 2 cases have to be considered: the TE mode and TM mode, depending on the variable that is chosen (E_y or H_y). In the TE case, we have $E_z = E_x = H_y = 0$. In the case TM, we have $H_x = H_z = E_y = 0$. From now on, we will only consider TE but the solving is similar for TM. Equation (7) admits different general solutions following the value of the discriminant Δ of its characteristic equation: $\Delta = -4 \cdot k_0^2(n^2 - n_0^2)$

Regarding our problem, 3 cases are distinguishable:

- $0 < n_0 < n_{clad}$
- $n_{clad} < n_0 < n_{core}$
- $n_0 > n_{core}$

The solutions of interest are: $n_{clad} < n_0 < n_{core}$. These solutions are called guided modes and correspond to modes whose fields oscillate in the core region and exponentially decrease in the cladding region, as we will see thereafter.

Given the n_0 range, the general solutions of equation (7) are:

- For $x \geq 0$, $n = n_{clad}$, $\Delta > 0$:

$$E_y(x) = a_1 e^{k_0 \sqrt{n_0^2 - n_{clad}^2} x} + a_2 e^{-k_0 \sqrt{n_0^2 - n_{clad}^2} x} \quad (8)$$

The boundary conditions dictate $\lim_{x \rightarrow +\infty} E_y = 0$ and so $a_1 = 0$

- For $-d \leq x \leq 0, n = n_{core}, \Delta < 0$:

$$E_y(x) = b_1 \cos\left(k_0 \sqrt{n_{core}^2 - n_0^2} x\right) + b_2 \sin\left(k_0 \sqrt{n_{core}^2 - n_0^2} x\right) \quad (9)$$

- For $x \leq -d, n = n_{clad}, \Delta > 0$:

$$E_y(x) = c_1 e^{k_0 \sqrt{n_0^2 - n_{clad}^2} x} + c_2 e^{-k_0 \sqrt{n_0^2 - n_{clad}^2} x} \quad (10)$$

The boundary conditions dictate $\lim_{x \rightarrow -\infty} E_y = 0$ and so $c_2 = 0$

We assumed at the beginning that the waveguide core is separated from the cladding by 2 interfaces. At these interfaces, it is demonstrated in that, in a dielectric material, tangential components of the EM fields are continuous. Regarding the 2D waveguide problem, this results in the following conditions at each interface:

$$\begin{cases} E_{y_{core}} = E_{y_{clad}} \\ \frac{\partial E_{y_{core}}}{\partial x} = \frac{\partial E_{y_{clad}}}{\partial x} \end{cases} \quad (11)$$

Using these conditions applied in $x = 0$ and $x = -d$, we obtain a system that can be reduced to 2 equations with 2 unknowns which admits non-trivial solutions for a determinant equal to 0:

$$\tan\left(k_0 \sqrt{n_{core}^2 - n_0^2} d\right) + 2 \cdot \frac{\left(k_0^2 \sqrt{n_{core}^2 - n_0^2} \sqrt{n_0^2 - n_{clad}^2}\right)}{k_0^2 (n_{clad}^2 - n_{core}^2)} = 0 \quad (12)$$

This can be rewritten as:

$$2 \cdot \arctan\left(\frac{k_0 \sqrt{n_0^2 - n_{clad}^2}}{k_0 \sqrt{n_{core}^2 - n_0^2}}\right) - k_0 d \sqrt{n_{core}^2 - n_0^2} + m\pi = 0 \quad (13)$$

This equation is the dispersion equation of a symmetrical slab waveguide and implies that there are only discrete values n_0 for given waveguide thickness d refractive indices n_{core} and n_{clad} . Using this equation and the following method, we can determine the number of propagation modes inside the structure and their effective indices:

- For $m = 0$, if a solution is found, there is a fundamental mode, otherwise, nothing is propagated inside the waveguide and it is useless to go further.
- For $m = 1$, if a solution is found, the waveguide has 2 guided modes: the fundamental mode and a secondary guided mode. Otherwise, there is only the fundamental mode and no more guided wave.

- For $m = 2$, if a solution is found, the waveguide has 3 guided modes: the fundamental mode and two other guided modes. Otherwise, there are only the 2 previous modes and there are no more solutions.
- And so on ...

This method enables to determine whether a waveguide is multimode or single mode in 2 dimensions. For a single mode waveguide, the fields distribution, as well as the propagation constant is known and unique, which is not the case for multimode waveguides. This has the advantage to prevent modal dispersion that occurs in multimode waveguides due to multiple propagation constants.

1.2 3D Waveguides

1.2.1 Effective Index Method

For a 3-dimensions rectangular waveguide, whose cross-section is depicted in Figure 34, the problem becomes more complex to solve, since the fields derivative along the third dimension cannot be considered equal to 0 anymore. Therefore, different methods have been used by Marcatili [76], Kumar [77] and Knox and Toulous [78] to approximate the 3D problem using a superposition of 2D problems.

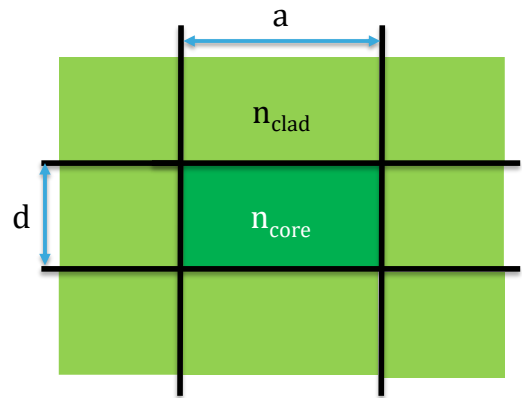


Figure 34: 3D Rectangular waveguide cross section

In weakly guiding condition, i.e. when $n_{core} \cong n_{clad}$, the approximation can be made that the longitudinal components E_z and H_z of the EM fields are small compared to the transverse components. It is then possible to consider two groups of solutions by neglecting one transverse component with respect to the other. By analogy with the slab waveguides, the groups of solution are named quasi-TE and quasi-TM modes. Expressed using the H field formulation, we have, on one hand, $H_x = 0$ and the wave equation is:

$$\frac{\partial^2 H_y}{\partial x^2} + \frac{\partial^2 H_y}{\partial y^2} + k_0^2(n^2(x, y) - n_0^2)H_y = 0 \quad (14)$$

On the other hand, $H_y = 0$, and the wave equation is:

$$\frac{\partial^2 H_x}{\partial x^2} + \frac{\partial^2 H_x}{\partial y^2} + k_0^2(n^2(x, y) - n_0^2)H_x = 0 \quad (15)$$

In the effective index method developed by Knox and Toulous, the assumption is made that $H(x, y) = X(x)Y(y)$. As a consequence, (14) and (15) can be rewritten as:

$$\frac{1}{X} \frac{\partial^2 X}{\partial x^2} + \frac{1}{Y} \frac{\partial^2 Y}{\partial y^2} + k_0^2(n^2(x, y) - n_0^2) = 0 \quad (16)$$

Furthermore, (16) can be split into two independent equations by adding and subtracting the y-independent value $k_0^2 n_{eff}^2(x)$, $n_{eff}^2(x)$ is an intermediate effective index that reflects the effective index of horizontal waveguides describing the vertical confinement in each horizontally homogeneous part of the waveguide:

$$\begin{cases} \frac{1}{X} \frac{\partial^2 X}{\partial x^2} + k_0^2(n_{eff}^2(x) - n_0^2) = 0 \\ \frac{1}{Y} \frac{\partial^2 Y}{\partial y^2} + k_0^2(n^2(x, y) - n_{eff}^2(x)) = 0 \end{cases} \quad (17)$$

As a result, an approximation of the guided modes propagating in a rectangular waveguide is obtained by solving the horizontal slab waveguide problems that determine the different values of the intermediate effective index $n_{eff}(x)$ used in place of refractive indices in a vertical slab waveguide problem. In the case of the rectangular waveguide described in Figure 34, this is equivalent to the two independent slab waveguides depicted in Figure 35:

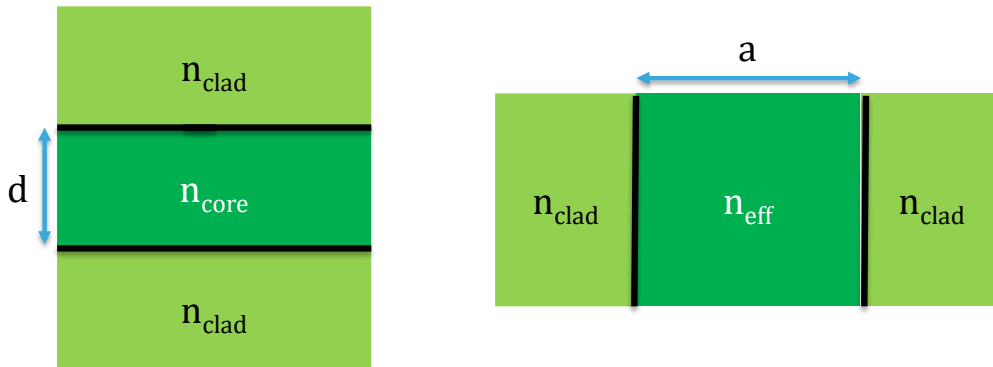


Figure 35: Effective index method for a rectangular waveguide with a unique cladding material

With this method, we can get a first glimpse of the single mode condition of the interposer waveguide. As a starting point, we will assume that the best fiber/waveguide coupling efficiency is obtained for waveguide dimensions (a and d) and refractive index difference (Δn) between core and cladding close the fiber: $\Delta n = 0.0052$ and $diameter = 8.2 \mu m$ [79]. This will be verified in section 1.3.2.

Using a MATLAB script (Annex A), we implemented the effective index method to determine indices of the guided modes inside an $8 \mu m \times 8 \mu m$ square waveguide in function of Δn for a wavelength of $1.31 \mu m$. We set $n_{clad} = 1.56$ since epoxy-based polymers refractive index is close to this value so that $n_{core} = n_{clad} + \Delta n$. Figure 36 displays the results of this analysis.

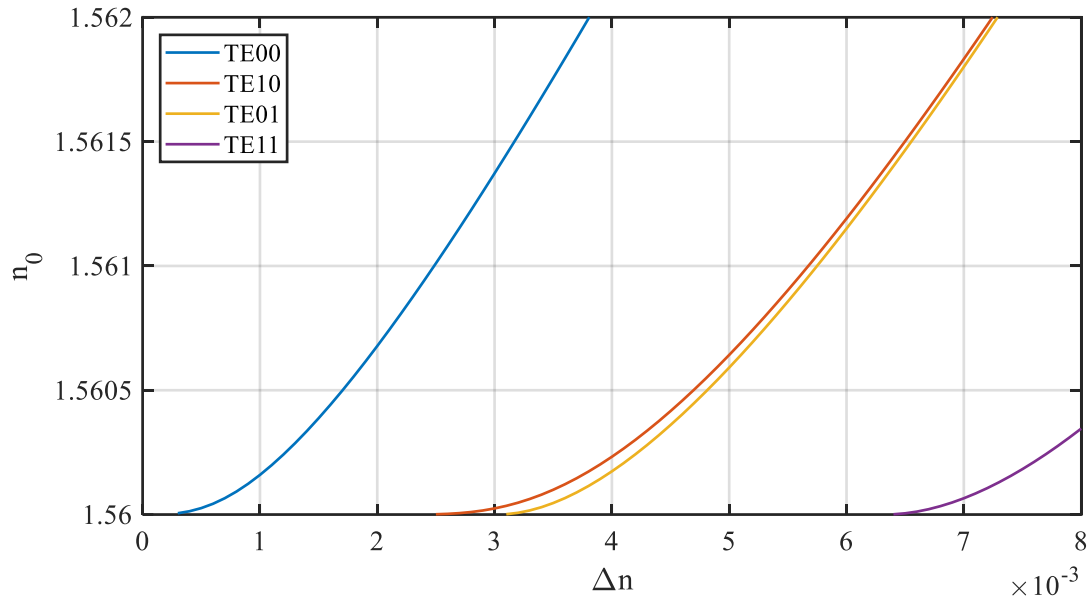


Figure 36: Computation of modes index n_0 vs refractive index difference Δn in an $8 \mu\text{m} \times 8 \mu\text{m}$ waveguide using the effective index method

As a first approximation, we can consider that such a waveguide is single mode for $5 \cdot 10^{-4} < \Delta n < 3 \cdot 10^{-3}$. In section 1.2.3, we will see that the real maximum index limit is slightly higher.

1.2.2 Rib Waveguide

In addition to rectangular waveguides, other structures are viable to guide light waves. An interesting one is the rib waveguide, which consists in a core in two parts, a slab part and a rib, between two cladding layers (Figure 37). As briefly outlined in the previous chapter and demonstrated in [80], this topology reduces losses by decreasing sensitivity to side walls roughness.

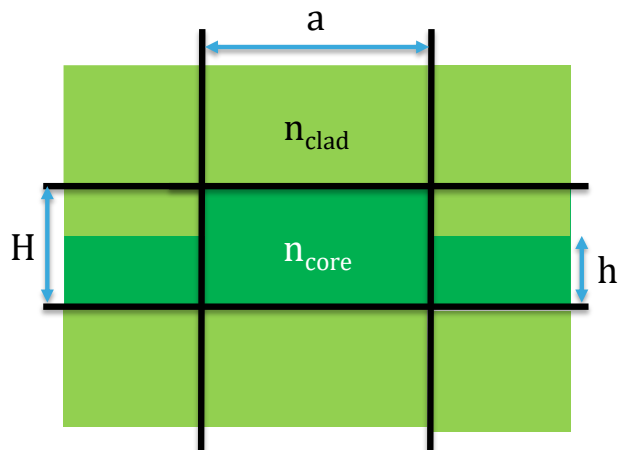


Figure 37: Rib waveguide cross-section

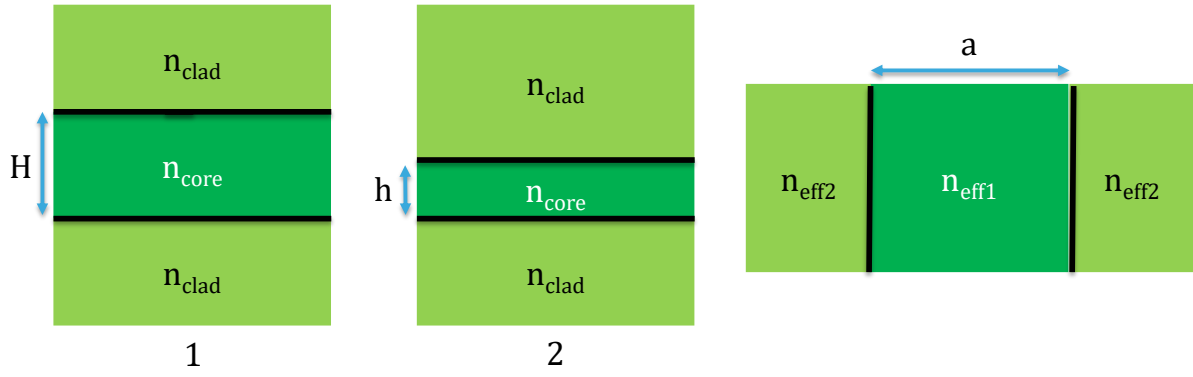


Figure 38: Effective index method applied to a rib waveguide topology

Another very interesting feature has been demonstrated in the work of [81] and [82]. For the same Δn , rib waveguides allow single mode operation with wider dimension than their rectangular counterparts. Effective index method can be used to determine guided modes inside a rib waveguide. First, the 1D horizontal slab waveguide problem number two, shown in Figure 38 and representing the areas close to the rib, is solved. Parallely, a second horizontal slab waveguide associated to the rib part is also solved. Assuming that both admit guided modes, at least one effective index n_{eff1} and one n_{eff2} is found for each geometry. It is therefore possible to define a third vertical slab waveguide with n_{eff1} and n_{eff2} as the core and cladding refractive indices, respectively. S. P. Pogossian [82] showed, using experimental data from [83], that the single mode condition resulting from the effective index method is accurate enough for design purpose. In our case, this condition takes the form of two equations:

$$r > 0.5 \quad (18)$$

$$t - \frac{r}{\sqrt{1-r^2}} - c < 0 \quad (19)$$

With:

$$r = \frac{h + \frac{2}{k_0 \sqrt{n_{core}^2 - n_{clad}^2}}}{H + \frac{2}{k_0 \sqrt{n_{core}^2 - n_{clad}^2}}} \quad (20)$$

$$t = \frac{a + \frac{2}{k_0 \sqrt{n_{core}^2 - n_{clad}^2}}}{H + \frac{2}{k_0 \sqrt{n_{core}^2 - n_{clad}^2}}} \quad (21)$$

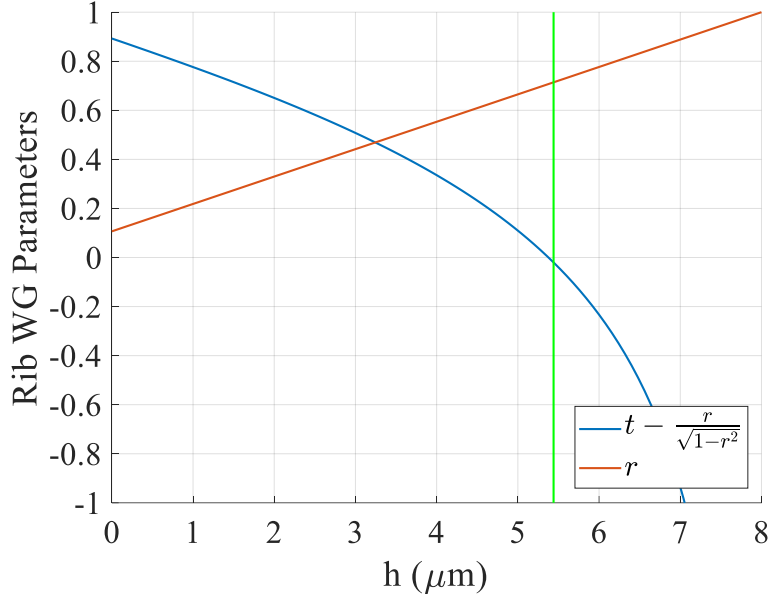


Figure 39: r and t parameters in function of WG slab part h . Single mode conditions are verified for $r > 0.5$ equation (18) and eq (19) whose lower limit is represented by the green line.

When applying conditions (15) and (16), with $c = 0$, on a rib waveguide with $a = 8 \mu\text{m}$, $H = 8 \mu\text{m}$, $\Delta n = 6 \cdot 10^{-3}$, and h varying from 0 to $8 \mu\text{m}$, we can see that single mode operation is still possible if the slab part thickness $h > 5.44 \mu\text{m}$. Indeed, (15) is verified for $h > 3.5 \mu\text{m}$ and (16) for $h > 5.44 \mu\text{m}$. On Figure 39, the theoretical single mode cut-off is represented by the vertical green line. Left to this line lies the multimode space and right to it is the single mode space.

1.2.3 FDE Simulations

We performed numerical simulations using the Finite-Difference Eigenmode solver (FDE) from Lumerical in order to assess theoretical calculations. This solver is based on the full-vectorial finite-difference analysis developed by [84] that uses a 2D mesh structure [85] and a refractive index averaging technique to determine modes for a given structure. Waveguides are modelled by dielectric materials with constant refractive indices with respect to wavelength. The simulation area is a $40 \times 40 \mu\text{m}^2$ surface with Perfectly Matched Layers (PMLs) as boundary conditions (Figure 40). With several iterations of the dichotomy method while varying the refractive

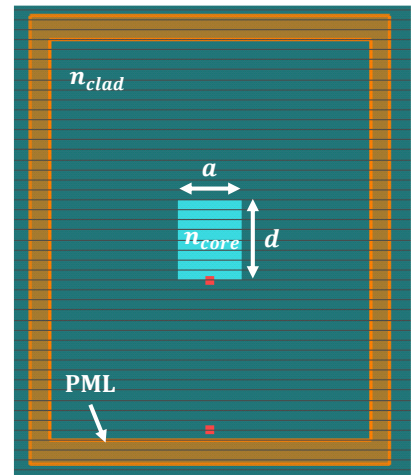


Figure 40: Cross section of the simulated rectangular waveguide in the simulation plane with PML boundaries

index difference, we determined that the higher order modes TE_{01} and TE_{10} appear for $\Delta n > 4 \cdot 10^{-3}$ for an $8 \mu\text{m} \times 8 \mu\text{m}$ rectangular waveguide. Figure 41 shows the E field

distribution of TE_{00} , TE_{01} and TE_{10} mode across the waveguide cross section for Δn of $4 \cdot 10^{-3}$, $4.1 \cdot 10^{-3}$ and $4.1 \cdot 10^{-3}$, respectively, at a wavelength of 1310 nm.

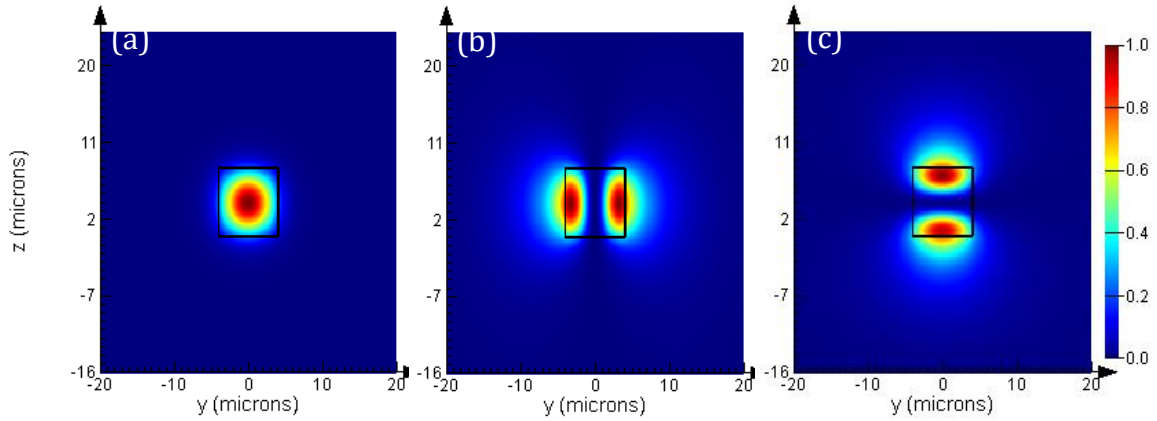


Figure 41: (a) TE_{00} , (b) TE_{01} , (c) TE_{10} modes E field distribution across the waveguide cross section

At $\Delta n = 3 \cdot 10^{-3}$, the TE_{00} mode index given by the effective index method is $n_{0_{EIM}} = 1.561373$ whereas the index given by simulation is $n_{0_{FDE}} = 1.561311$.

Regarding the rib waveguide described in section 1.2.2, i.e. $a = H = 8 \mu m$ and $\Delta n = 6 \cdot 10^{-3}$ (Figure 42), our FDE simulation results differ from calculations following the effective index method. Using the same iterative method but h as a variable, we obtained upper and lower single mode limits for slab thickness. We determined that this rib waveguide is single mode for $2.9 \mu m < h < 6.4 \mu m$. Below $3 \mu m$, the lateral TE_{01} mode is guided. Above $7 \mu m$, it is the vertical TE_{10} mode that is starting to be guided. Figure 43 presents the E field distribution of TE_{00} ($h = 4 \mu m$), TE_{01}

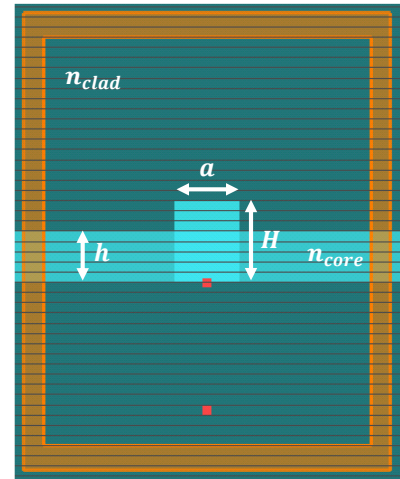


Figure 42: Cross section of the simulated rib waveguide in the simulation plane with PML boundaries

($h = 2.9 \mu\text{m}$) and TE_{10} ($h = 6.4 \mu\text{m}$) mode across the waveguide cross section.

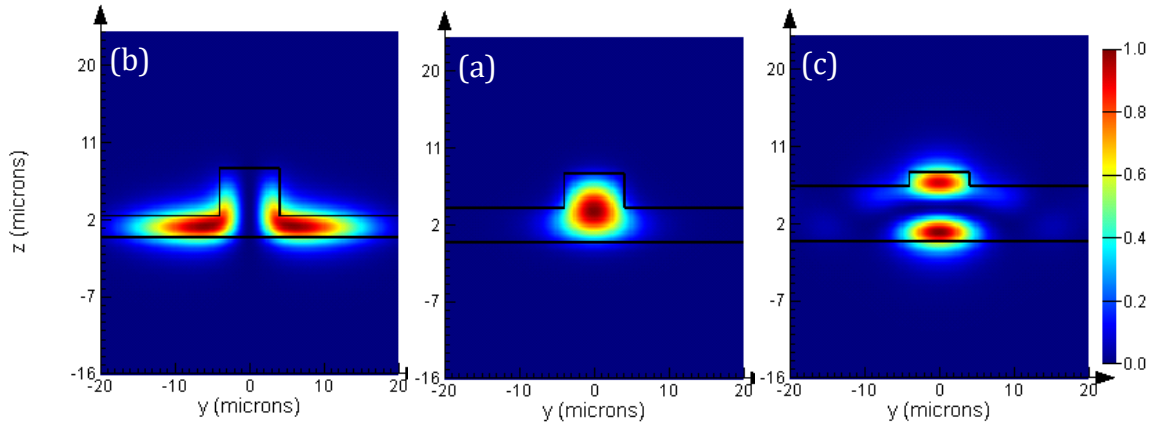


Figure 43: (a) TE_{00} , (b) TE_{01} , (c) TE_{10} modes E field distribution across rib waveguides cross section with a height H of $8 \mu\text{m}$, a width a of $8 \mu\text{m}$ and respective slab thicknesses h of 4 , 2.9 and $6.4 \mu\text{m}$

At this point, we have theoretically studied and simulated the single mode condition for rectangular and rib waveguides of $8 \mu\text{m} \times 8 \mu\text{m}$ in terms of refractive index difference and slab thickness respectively. We supposed that the best optical coupling with SMF would be obtained with such dimensions. We will now verify this assumption.

1.3 Lateral Coupling Efficiency with Optical Fiber

1.3.1 Coupling Efficiency

An important feature is to provide the ability to couple light between the fiber and the interposer. For that purpose, we have to determine the coupling efficiency between the fiber and the waveguide fundamental mode. First, we define the coupling efficiency as the ratio between the power transmitted to the waveguide fundamental mode P_{WG_0} , for a given input power P_{in} , and the latter:

$$CE = \frac{P_{WG_0}}{P_{in}} \quad (22)$$

The amount of power carried by an electro-magnetic field is given by the Poynting vector which can be written as follows for the power passing through a surface:

$$P_{in} = \frac{1}{2} \text{Re} \left\{ \int \vec{E}_{in} \wedge \vec{H}_{in}^* \cdot d\vec{S} \right\} \quad (23)$$

Knowing that tangential components of EM fields are continuous, we neglect the reflections at the interface, and obtain:

$$\begin{aligned} \vec{E}_{in} &= \vec{E}_{out} \\ \vec{H}_{in} &= \vec{H}_{out} \end{aligned} \quad (24)$$

Moreover, it has been demonstrated in that any field can be expressed using a basis of orthogonal modes. In the output guiding structure, the fields decomposition is as follows:

$$\begin{aligned}\vec{E}_{out} &= \sum a_i \vec{e}_i \\ \vec{H}_{out} &= \sum b_i \vec{h}_i\end{aligned}\quad (25)$$

Here, \vec{e}_i and \vec{h}_i are the E and H fields of the i^{th} mode of the output guiding structure and a_i and b_i are the coordinates of \vec{E}_{out} and \vec{H}_{out} associated to the i^{th} mode, respectively.

Finally, we can express the coupling ratio in the form:

$$\frac{P_{WG_i}}{P_{in}} = Re \left\{ \frac{\int \vec{e}_i \wedge \vec{H}_{in}^* \cdot d\vec{S} \int \vec{E}_{in} \wedge \vec{h}_i^* \cdot d\vec{S}}{\int \vec{e}_i \wedge \vec{h}_i^* \cdot d\vec{S}} \right\} \frac{1}{Re \{ \int \vec{E}_{in} \wedge \vec{H}_{in}^* \cdot d\vec{S} \}} \quad (26)$$

Which can also be written:

$$CE = \frac{[\iint \Psi_{in} \Psi_{out}^* dx dy]^2}{[\iint \Psi_{in} \Psi_{in}^* dx dy][\iint \Psi_{out} \Psi_{out}^* dx dy]} \quad (27)$$

Where Ψ_{in} and Ψ_{out} represent the fiber input and waveguides output electrical fields, respectively.

This equation allows the computation of the CE between the i^{th} mode of a waveguide and any input field. However, this is an approximation based on the assumption that there is no reflection at the interface which is the case when refractive indices of both guiding structures are almost identical.

1.3.2 Coupling Efficiency Simulations

The simulations presented in this paragraph were made using the overlap analysis of the Lumerical MODE simulation software. This tool provides a computation of the CE and a more accurate power coupling ratio that takes into account the reflected wave. For a better readability, it will be represented in dB. This coefficient gives a good idea of the power ratio transmitted to the waveguide when illuminated by a SMF.

We modeled a Corning SMF-28e (Figure 44) fiber to determine its fundamental mode using FDE and used it as the input field.

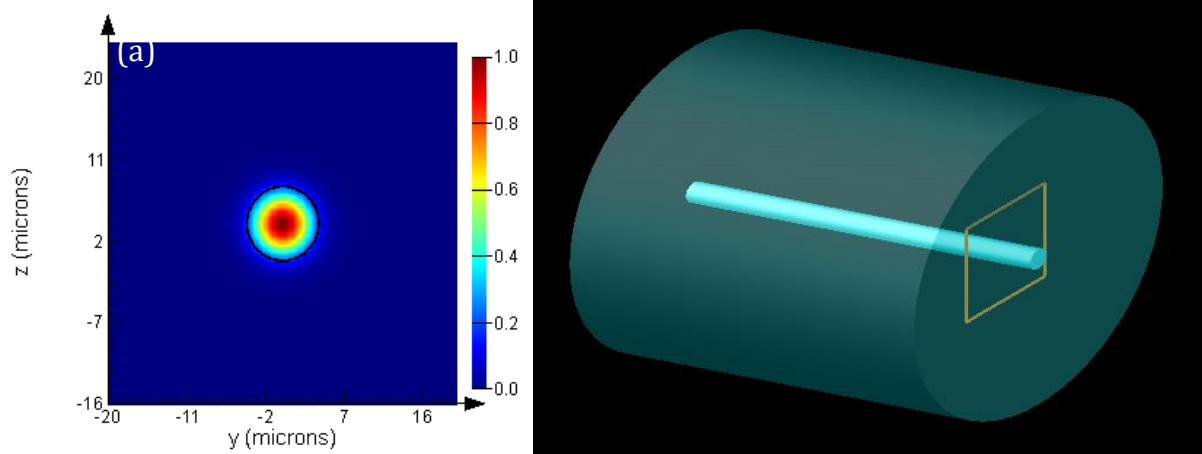


Figure 44: Fundamental mode E field distribution (a) of the simulated SMF28 fiber (b)

Then, we simulated a wide range of rectangular and rib waveguides to verify the assumption made in section 1.2.1 on the waveguide dimensions regarding the coupling efficiency.

The height and width of the rectangular waveguide was varied from $6 \mu\text{m}$ to $10 \mu\text{m}$ by steps of $1 \mu\text{m}$ while keeping an aspect ratio of 1:1. This was performed for four different values of Δn , ranging from $2 \cdot 10^{-3}$ to $5 \cdot 10^{-3}$ with a $1 \cdot 10^{-3}$ step.

Regarding the rib waveguide, we kept a Δn of $6 \cdot 10^{-3}$ and dimensions of $8 \mu\text{m}$ for both a and H and we varied the slab part thickness in the single mode range, from $3 \mu\text{m}$ to $6 \mu\text{m}$, to study its impact on the CE. In the following, the results in terms of power coupling for each configuration are shown (Figure 45).

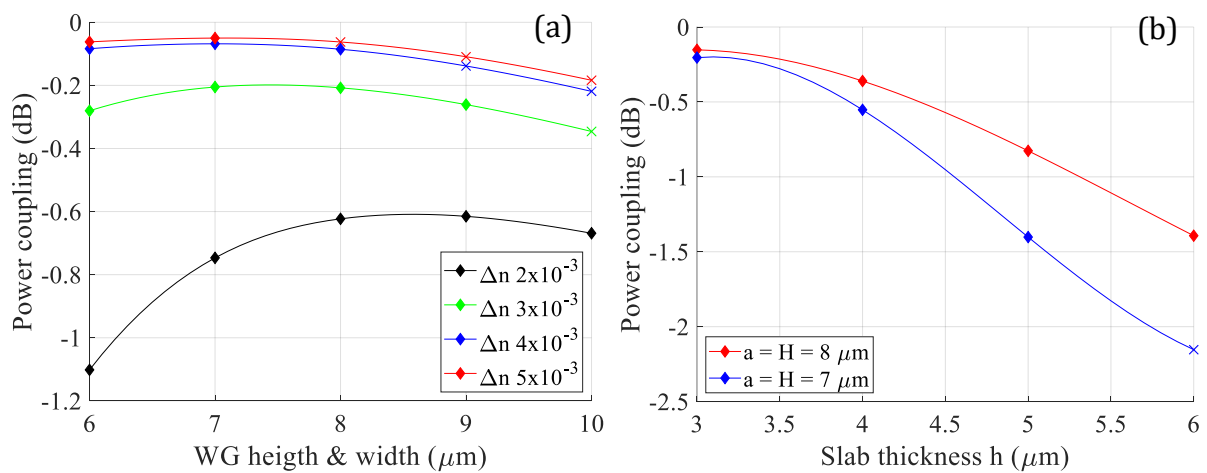


Figure 45: Power coupling ratio vs (a) WG width and height for a rectangular waveguide and (b) slab thickness for a rib waveguide. Values represented by a cross indicate a multimode behavior

The main point that we can draw from these results is that an optimum power coupling with SMFs of -0.05 dB is obtained for dimensions of the core of a rectangular guide of the

order of $7 \times 7 \mu\text{m}^2$ and for an index difference of about 0.005. These are values close to those of the fiber ($\Delta n = 0.0052$ and diameter of $8.2 \mu\text{m}$). However, such a waveguide is close to being multimode and a decrease of Δn by $1 \cdot 10^{-3}$ still gives CEs higher than -0.1 dB.

Another interesting phenomenon is that single mode rib waveguides with a higher Δn and CEs above -0.5 dB with fibers are possible if the slab part remain thinner than $4 \mu\text{m}$. These results give us an overview of possible dimensional specifications for the polymer waveguides of the interposer. In the next section, we will study the RF performance of the assembly and focus on 2 particular levers: interposer transmission lines and PIC25G electro-optical modulator electrodes.

2 RF Optimizations

2.1 Interposer Transmission Lines

2.1.1 Coplanar Waveguides

Transmission lines are waveguiding structures used for the transmission of high frequency signals. Generally, they are composed of metallic conductors separated by a dielectric material. Several topologies have been used in the domain of ICs, the most well-known being: striplines, microstrips and CPWs. Each of them admits one or more variants. The stripline is a metallic line in a dielectric material sandwiched between two ground planes. Microstrip are transmission lines placed on top of a dielectric placed above a ground plane. In the third case, namely CPW, the ground plane and line are on the same level above the dielectric.

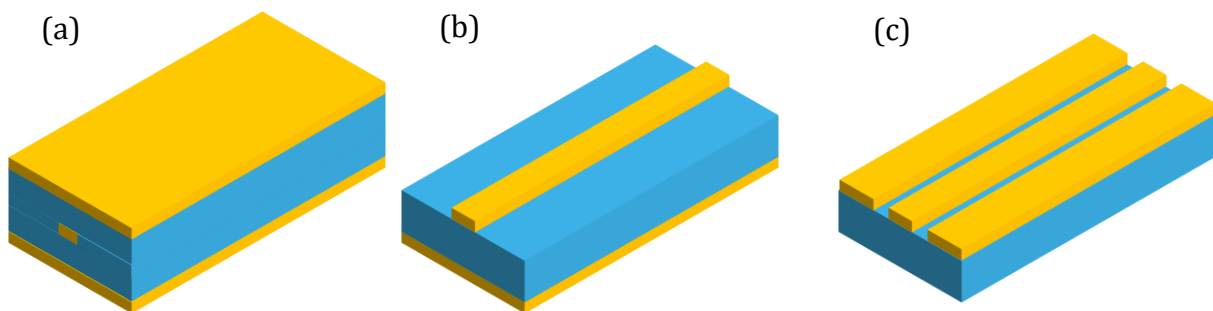


Figure 46: 3D schematic of (a) a stripline, (b) a microstrip and (c) a CPW

As set in the first chapter of this work, the demonstrator must include transmission lines able to transmit 50 Gb/s signals over a few millimeters. Considering that only one redistribution layer was required for routing, we decided to stick with CPW. This simplifies the fabrication process described in chapter III.

Electrically speaking, transmission lines are generally modeled using an equivalent RLCG model that employs per unit length constants of resistance R (Ω/m), inductance L (H/m), capacitance C (F/m) and conductance G (S/m) [86]. The equivalent circuit for an infinitesimal Δz -long transmission is drawn in Figure 47 below:

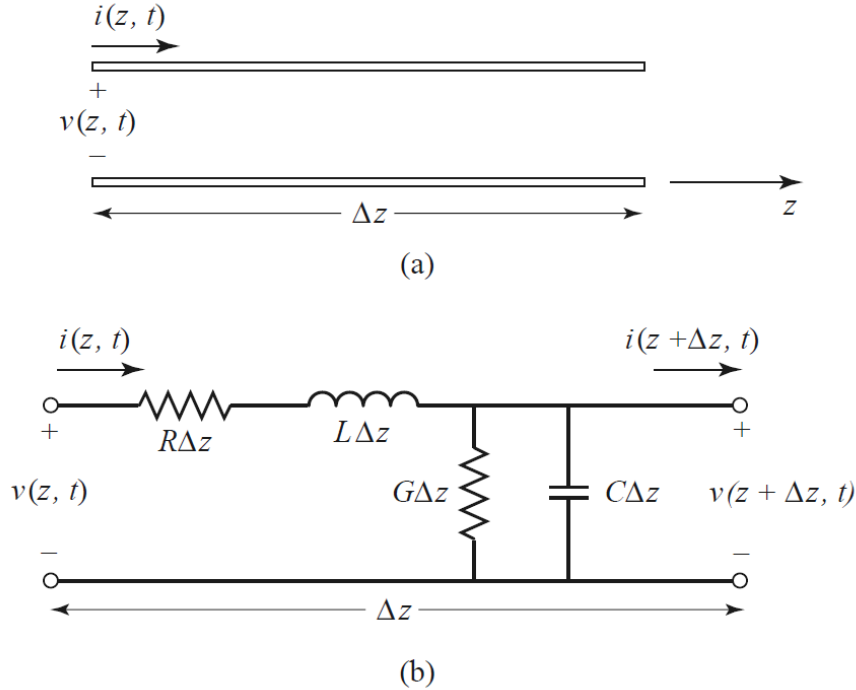


Figure 47: Voltage and current definitions and equivalent circuit for an incremental length of transmission line. (a) Voltage and current definitions. (b) Lumped-element equivalent circuit. [86]

Applying Kirchhoff's laws to this equivalent circuit, in the frequency domain and with $\Delta z \rightarrow 0$, gives a set of 2 differential equations depending on $V(z)$ and $I(z)$, the phasors corresponding to $v(z, t)$ and $i(z, t)$, respectively:

$$\frac{dV(z)}{dz} = -(R + jL\omega)I(z) \quad (28)$$

$$\frac{dI(z)}{dz} = -(G + jC\omega)V(z) \quad (29)$$

Replacing (25) in (24) and conversely, we obtain:

$$\frac{d^2V(z)}{dz^2} - \gamma^2V(z) = 0 \quad (30)$$

$$\frac{d^2I(z)}{dz^2} - \gamma^2I(z) = 0 \quad (31)$$

With γ , the propagation constant of the transmission line defined as:

$$\gamma = \alpha + i\beta = \sqrt{(R + jL\omega)(G + jC\omega)} \quad (32)$$

Indeed, (26) and (27) admits general solutions in the form of the sum of forward and backward traveling waves:

$$V(z) = V_0^+ e^{-\gamma z} + V_0^- e^{\gamma z} \quad (33)$$

$$I(z) = I_0^+ e^{-\gamma z} + I_0^- e^{\gamma z} \quad (34)$$

Back in the time domain, $v(z, t)$ can be written:

$$v(z, t) = |V_0^+| \cos(\omega t - \beta z + \phi^+) e^{\alpha z} + |V_0^-| \cos(\omega t + \beta z + \phi^-) e^{-\alpha z} \quad (35)$$

We can observe that α is responsible for the attenuation of both waves and is thus called the attenuation coefficient. For transmission lines to be efficient, this coefficient has to be as small as possible. It can be split in two contributions: α_c the conductor losses and α_d the dielectric losses.

In addition to the attenuation coefficient, the minimization of the backward propagating wave is also a key point in RF transmissions. To evaluate this criterion, it is necessary to study a transmission line loaded by a load Z_L , as in Figure 48. First, we define Z_0 the characteristic impedance of the transmission line, as:

$$Z_0 = \frac{\gamma}{G + jC\omega} \quad (36)$$

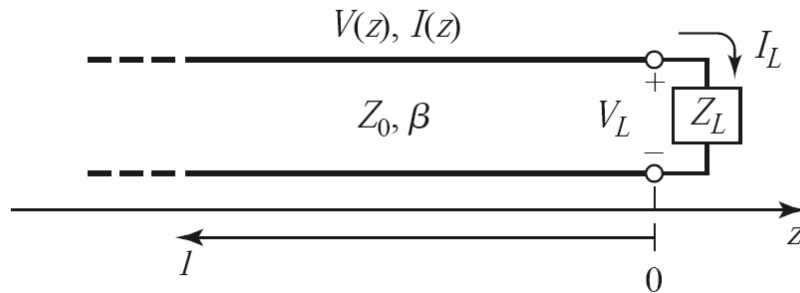


Figure 48: A transmission line terminated in a load impedance Z_L [86]

Then, at $z = 0$, we have:

$$Z_L = \frac{V(0)}{I(0)} = Z_0 \frac{V_0^+ + V_0^-}{V_0^+ - V_0^-} \quad (37)$$

This can be written:

$$V_0^- = \frac{Z_L - Z_0}{Z_L + Z_0} V_0^+ = \Gamma_0 V_0^+ \quad (38)$$

Where Γ_0 is called the voltage reflection coefficient at the load. At a distance z from the load, we have:

$$\frac{V_0^- e^{\gamma z}}{V_0^+ e^{-\gamma z}} = \Gamma_0 e^{2\gamma z} = \Gamma(z) \quad (39)$$

As a consequence, the backward propagating wave is zero for $Z_L = Z_0$ and the load is said to be matched to the line. It is common to design transmission lines with a characteristic impedance of 50Ω in order to be compatible with a vast majority of RF systems.

Like their optical counterparts, transmission lines behavior can be described by solving the Maxwell equations presented in section 1.1. These equations establish a relationship between γ , Z_0 and the physical properties of the line. In the same way as the optical waveguide, it is possible to define ϵ_r , the dielectric constant of dielectric material as $\sqrt{\epsilon_r} = n$, and ϵ_{eff} , the effective dielectric constant for a propagation mode: $\epsilon_{eff} = \frac{\beta^2}{k_0^2}$.

2.1.2 ADS simulations

In this section, we coarsely dimension the transmission lines using a simulation software. Reference [87] proposed a model for CPWs with finite dimensions using a conformal mapping technique. Further enhanced to take into account the thickness of the conductors [88], conductor losses α_c [89] and dielectric losses α_d , this model gives computation formulae for Z_0 , ϵ_{eff} and α of a CPW such as the one described by Figure 49. ρ is the resistivity of the metallic conductor and $\tan \delta$ is the dielectric-loss tangent. Both are material properties required for the calculation of α_c and α_d respectively.

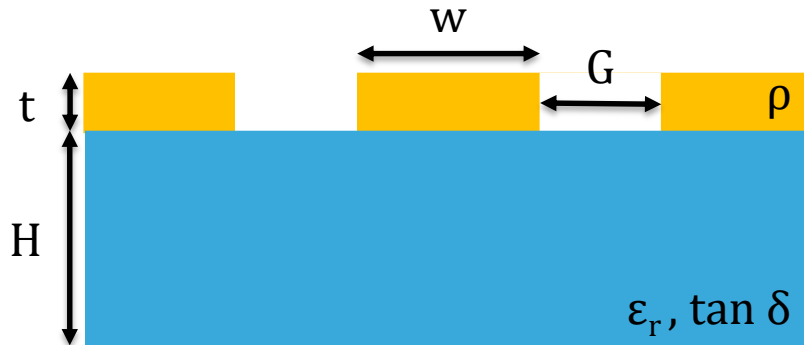


Figure 49: Cross-section schematic of a CPW with ADS CPW model parameters

This model is integrated in the LineCal tool from Keysight's Advanced Design System (ADS) simulator which can calculate Z_0 for given physical parameters and synthesize physical properties from given electrical constants.

The materials considered for the interposer are copper with a resistivity of $\rho_{copper} = 1.68 \cdot 10^{-8} \Omega \cdot m$ [90] for the conductors and a 500 μm -thick AF-32 glass wafer from Schott with a relative dielectric permittivity $\epsilon_r = 5.1$ at 24 GHz and a loss tangent $\tan \delta = 9 \cdot 10^{-3}$ at the same frequency [91]. Due to process constraints that will be explained in

the next chapter, we also set G to $15 \mu\text{m}$ and t to $3 \mu\text{m}$. With these parameters, the synthesized 50Ω CPW has a width $w_{50\Omega}$ of $71.76 \mu\text{m}$. This gives a first idea of the interposer CPW dimensions.

To push the study a little bit further, we performed a S-parameter simulation of a 1 cm-long CPWs with different widths, namely $80 \mu\text{m}$, $71.76 \mu\text{m}$, $60 \mu\text{m}$ and $10 \mu\text{m}$, using this CPW model and ports terminated with a 50Ω load at both ends. S-parameters are defined as [86]:

$$S_{ij} = \left. \frac{V_i^-}{V_j^+} \right|_{V_k^+ = 0 \text{ for } k \neq j} \quad (40)$$

Where V_i^- is the backward propagating voltage wave at the i^{th} port of the device in response to a forward propagating voltage at the j^{th} port with all other forward voltage wave set to 0. However, the link with the transmission line parameters is simpler using the transfer matrix ABCD, which is defined, for a two-port device as:

$$\begin{bmatrix} V_1 \\ I_1 \end{bmatrix} = \begin{bmatrix} A & B \\ C & D \end{bmatrix} \begin{bmatrix} V_2 \\ -I_2 \end{bmatrix} \quad (41)$$

Indeed, it can be demonstrated that [86]:

$$\gamma = \frac{1}{l} \text{acosh}(A) \quad (42)$$

$$Z_0 = \frac{B}{\sinh(\gamma l)} \quad (43)$$

Therefore, after the S-parameters to ABCD-parameters transformation, we compared the attenuation coefficient α , expressed in dB/cm, and the real part of the characteristic impedance of each CPW.

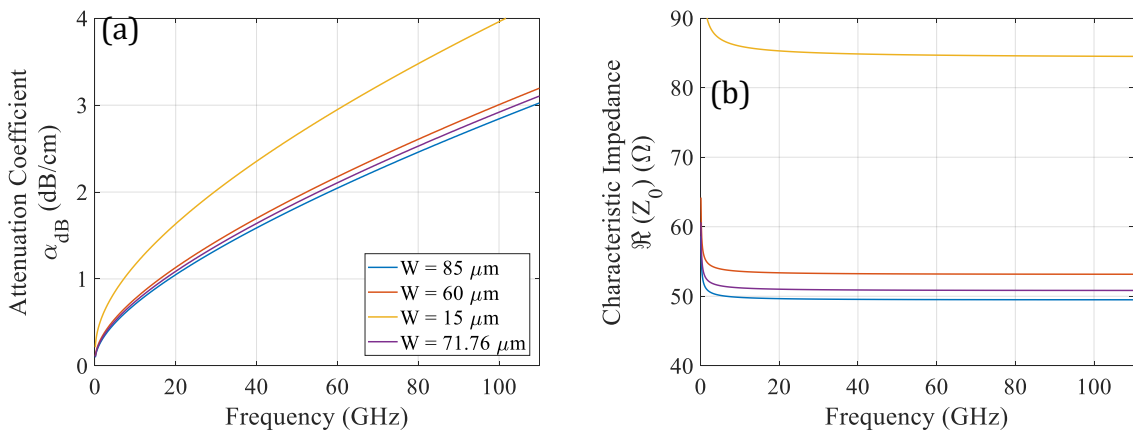


Figure 50: Attenuation coefficient in dB/cm (a) and real part of the characteristic impedance (b) of 4 CPWs simulated using ADS model with widths varying from $15 \mu\text{m}$ to $85 \mu\text{m}$

The results shown in figure (Figure 50) confirm that, given the constraints on materials and dimensions mentioned earlier, 50 Ω CPWs with loss below 3 dB/cm at 90 GHz are theoretically achievable. In addition, a $\pm 10 \mu\text{m}$ variation of the width does not dramatically change the line properties. Nonetheless, this model assumed that the CPW is placed on the substrate without any topping material. This will not be the case in reality.

2.1.3 Interposer Stack Modeling

The cointegration of polymer optical waveguides with CPW transmission lines necessitates to take into account the impact of the polymer topping layers. To facilitate the optical coupling, we decided to place the polymer layers on top of the transmission lines as depicted in Figure 51.

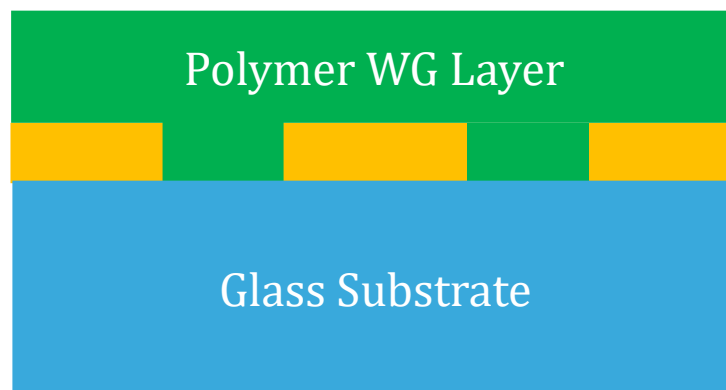


Figure 51: Cross section of the CPW with polymer layers.

The ADS integrated model does not account for a top layer. As a consequence, we performed EM simulations using the software ANSYS HFSS, which is based on a finite element method. Unfortunately, we do not have the dielectric constant and loss tangent for the photosensitive resins that will be used to fabricate the waveguides so we used the parameters of an epoxy-based polymer dry film that is used in organic back-end fabrication: Ajinomoto's ABF GY11. Its $\epsilon_r = 3.2$ and $\tan \delta = 0.0042$ at 5.8 GHz. We simulated a CPW with the same dimensional parameters as the previous 50 Ω CPW and compared it to the latter in FIG.

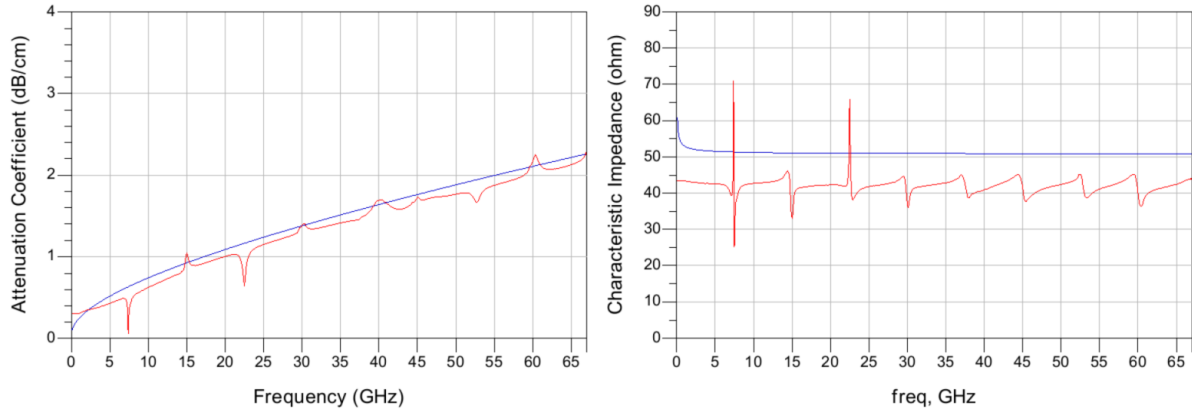


Figure 52: Attenuation coefficient and real part of the characteristic impedance of the ADS model (blue line) and HFSS simulated (red line) CPWs

We can observe that the addition of a top polymer layer lowers the characteristic impedance of the line. As a consequence, we fabricated CPW with different widths in order to approximate the dielectric constant of the polymer resins used for the waveguide’s fabrication.

2.2 PIC25G Modulator electrodes optimization

Prior to this work, we have been involved in the RF optimization of the Mach-Zehnder modulators that were embedded in the PIC25G IC assembled onto the glass interposer. The MZM topology used in a former design was based on travelling wave electrodes such as the one depicted in Figure 53:

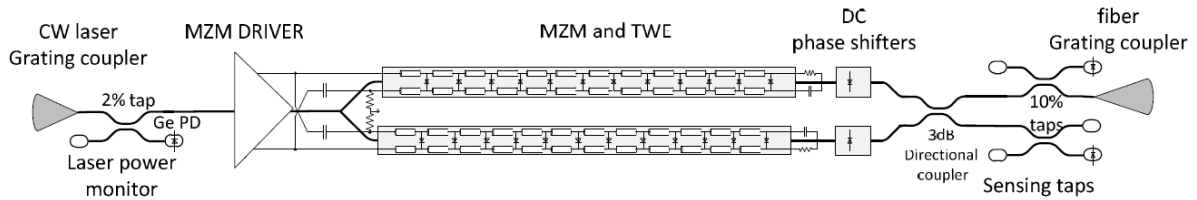


Figure 53: MZM differential travelling wave electrodes (TWE) and differential drive [26]

While optimizing the system for the highest possible bite rate, high frequency design rules must be taken into account in the electrode design. Typically, parasite effects determine the maximum working frequency and hence the maximum achievable modulation speed. It is therefore necessary to adapt the transmission line feeding the electrodes of the HSPM in a wide band manner in order to minimize the associated losses and maximize the phase shift of the optical signal sufficiently in order to have the largest possible difference in light intensity between the state 1 and the state 0 at the exit of the modulator: the Extinction Ratio (ER).

$$ER = 10 \cdot \log \frac{P_{state0}}{P_{state1}} \quad (44)$$

The electrodes are divided into 100 μm long elementary cells and each cell is connected to a diode. Electrodes are modeled by a RLCG transmission line from ST PIC25G design kit with the RF model of the diode coming from the same design kit in parallel:

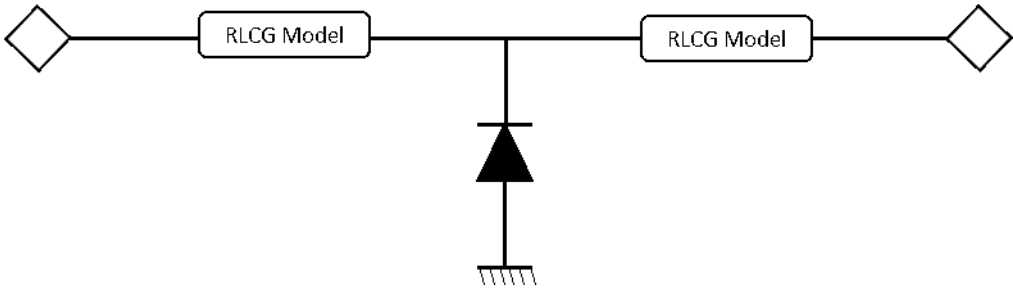


Figure 54: Modeling a line section of the form modulator electrode

Part of the problem is that the diode behaves like a large capacitor and acts as a low pass filter. The best trade-off that we found for the adaptation of the line was to add an inductor to each line section and to terminate it by an impedance of 35Ω . The inductor was first assimilated to a perfect inductor to find the optimal inductance value. Then, we used an inductor model from the design kit of a similar technology since no scalable model of inductors was available in PIC25G design kit at that time. Finally, we simulated the inductor with PIC25G back-end using HFSS. We obtain the following modeling of a line section:

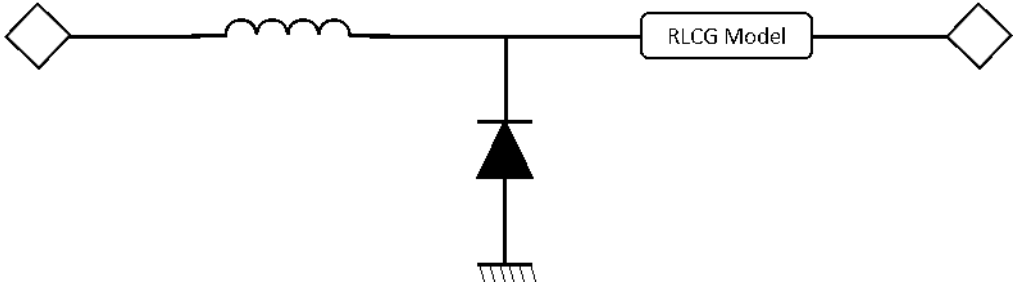


Figure 55: Modeling of a line section of the modulator with an inductor

With this new modeling approach, the return and insertion losses presented in Figure 56 are obtained for 3 mm long modulators with and without inductors. We can observe that the adaptation was greatly improved, from 0 to 60 GHz, despite generating higher insertion loss using inductors.

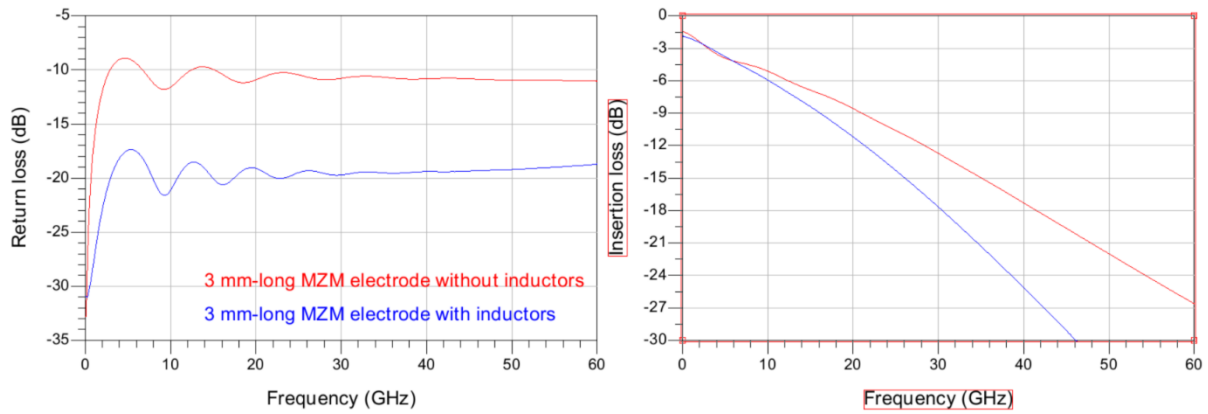


Figure 56: Return loss (a) and insertion loss (b) of MZM electrodes terminated by a 35Ω load with and without discrete inductors

However, this step is not enough to determine the extinction ratio. Simulating both electrical and optical aspects becomes necessary. After adding elements to simulate the optical part (optical models of diodes, optical source and photodetector), we applied a PRBS signal (Pseudo Random Binary Sequence) to the transmission lines.

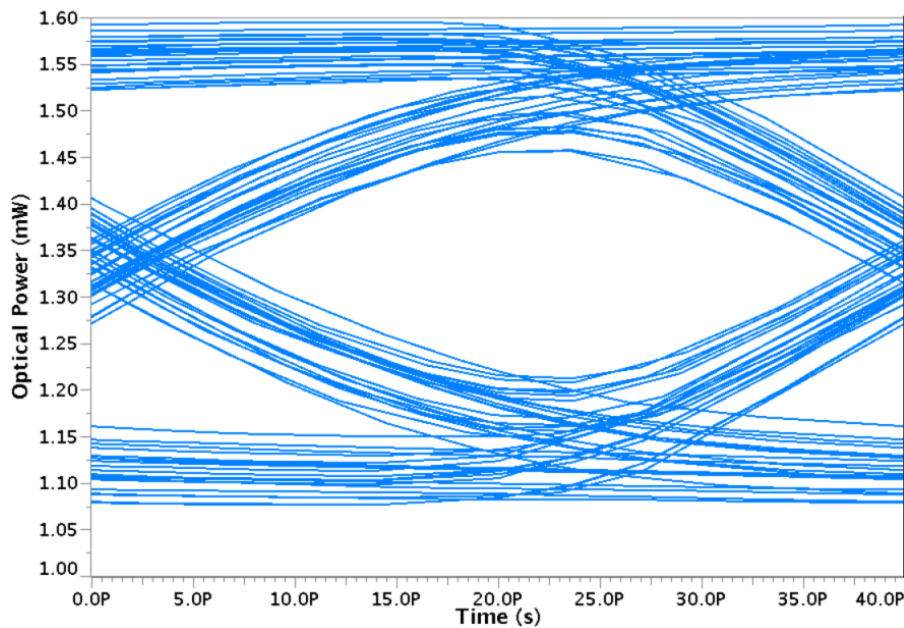


Figure 57: Simulation of an optical eye diagram at the output of a 2.8 mm long modulator with inductors in response to a $25 \text{ Gb} \cdot \text{s}^{-1}$ PRBS with 2.5 V between the 1 and 0 state.

By superimposing the signal received at the output of the photodetector on itself with the same period as that of a bit of the sequence, it is possible to draw a diagram called the “eye-diagram” from which the extinction ratio is determined. The extinction ratio is the ratio in optical powers between the top and bottom of the eye in the center of it.

On one hand, the longer the modulator, the higher the electrode losses (electrical and optical). On the other hand, the shorter the modulator, the smaller the phase shift. In order to find the best trade-off between the losses and the associated maximum phase shift, 4 modulators of different lengths were designed: 2.1, 2.8, 3.5 and 4.2 mm.

They all share the same basic cell corresponding to the model with inductance below:

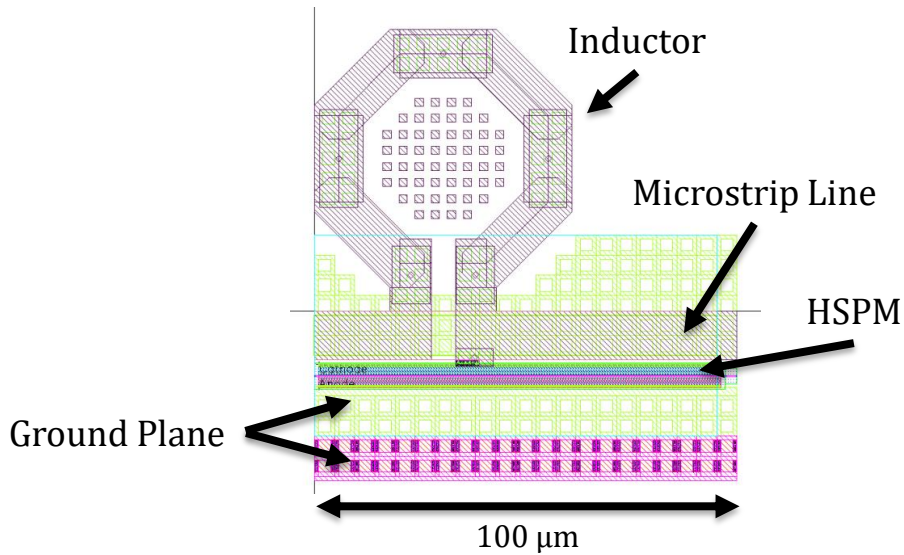


Figure 58: Elementary cell of the MZM with inductors

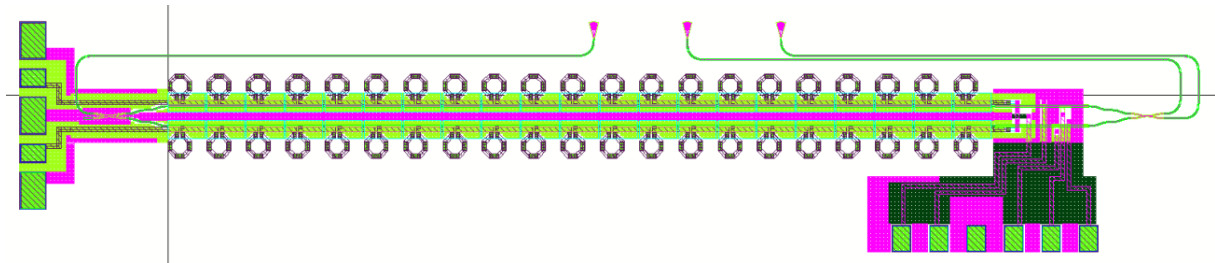


Figure 59: 2.1mm MZM with inductors

These MZM have been embedded in the PIC25G IC used in this work and the 3.5mm long modulator can be tested through the interposer.

3 PIC to Interposer Coupling

In this section, we propose an optical coupling between a polymer waveguide and a SOI waveguide relying on a total internal reflection mirror in the polymer layers and a grating coupler on the silicon chip. After a first approximation, consisting in ray optics calculations, we perform EM simulations to determine optimal angle and position for the mirror.

3.1 Proposed coupling scheme and 1st order approximation

The approach taken in this work assumes that the coupling between the interposer and the silicon PIC is performed with a mirror and a grating coupler as described in Figure 60, whereas, in the existing silicon PIC technology, grating couplers have been optimized for coupling with an optical fiber [92] making an angle (θ_{GC} in Figure 60) of 8° with the normal of the chip surface where it is glued. Therefore, light also propagates through the air and the polymer cladding. Assuming that the PIC BEOL is a homogenous material whose refractive index is the same as SiO_2 and using Snell-Descartes's law, we can determine the angle θ_m of the mirror for which the light illuminates the grating coupler with the same incidence angle θ_{GC} as in the fiber/grating coupling scheme. In section 1.2, we set the cladding polymer refractive to 1.56. We keep the same value here. This angle is:

$$\theta_m = \frac{1}{2} \left(90^\circ - \frac{\text{asin}(n_{\text{SiO}_2} \sin \theta_{GC})}{n_{\text{polymer}}} \right) \approx 41.3^\circ \quad (45)$$

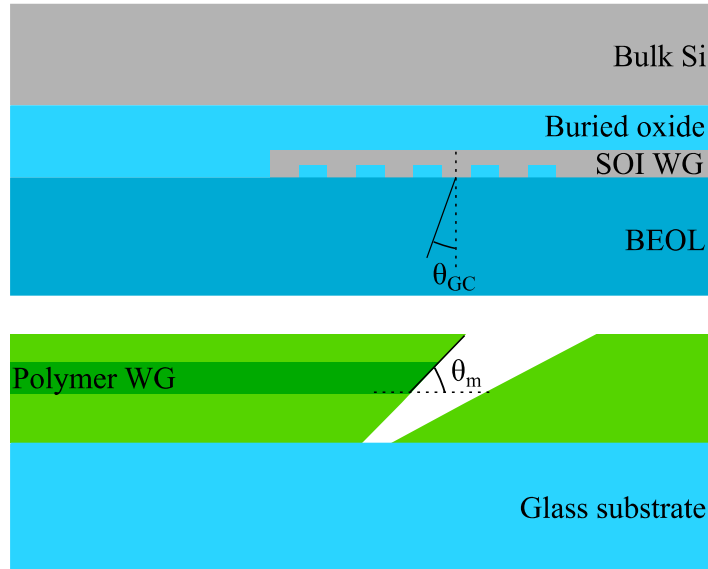


Figure 60: Coupling scheme between a polymer waveguide and a silicon-on-insulator waveguide

Moreover, at the interface between the core material and the air, the critical angle above which refraction does not exist is:

$$\theta_{critical} = \text{asin} \left(\frac{\sin(90^\circ)}{n_{\text{polymer}}} \right) \approx 39.9^\circ \quad (46)$$

The incidence angle on the mirror surface resulting from θ_m is $90^\circ - \theta_m = 48.7^\circ > 39.9^\circ$. Thus, the mirror is relying on TIR. To get more insights on the mirror placement and the theoretically achievable coupling efficiency, it is necessary to perform EM simulations.

3.2 FDTD Simulation & Modeling Methodology

EM simulations of the PIC/interposer coupling are performed using Lumerical Finite Difference Time Domain (FDTD) solver. This is a 2D/3D solver that solves Maxwell equations (3) exploiting rectangular mesh cells [85] at a moment t for a given field source. The mesh size is an extremely impactful parameter regarding the simulation time and accuracy. It mainly depends on the wavelength ($1.3 \mu\text{m}$ in our case) and the minimum dimensions of the modeled structure. The GC being a subwavelength component with minimum dimension of the order 50 nm , its simulation requires a very fine mesh and is consequently very time consuming, especially since PIC25G GCs does not allow to reduce the optimization of the coupling to a 2D problem. Indeed, the tapered form of SPGC and PSGC induces a variation of the effective index of the propagating mode and this is not easily taken into account in a 2D simulation. The 3D simulation from the SOI waveguide to the polymer taking too much time to perform detailed sweeps of the dimensional parameters of the structure, we decided to divide the simulation following the method shown in Figure 61.

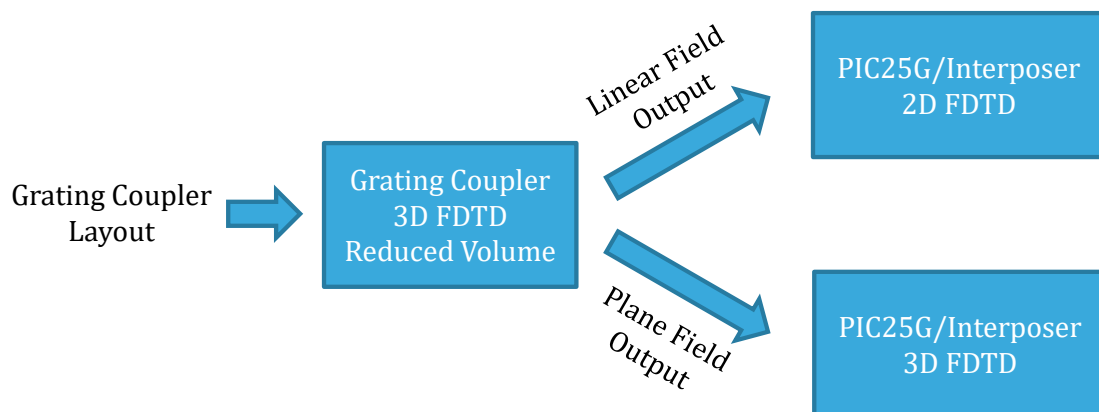


Figure 61: PIC/Interposer coupling modelling methodology

The idea is to perform the 3D simulation of a GC in a reduced simulation volume to get the fields propagating towards the interposer in both a plane and along a line. Then, the fields extracted along the line are used as a source in a 2D simulation of the PIC/Interposer coupling. This allows to optimize the mirror placement and angle while evaluating the sensitivity of the coupling efficiency to variations of these parameters. Finally, we performed a PIC/Interposer 3D simulation using the GC output fields extracted in a plane with a few selected parameters to validate the 2D approach for the rest of the structure (apart from the GC) and estimate the overall coupling efficiency.

3.3 PIC25G Grating Coupler Simulation

We started the simulation of the coupling efficiency from the SOI waveguide to the polymer waveguide by directly importing the layout of an SPGC, optimized for a wavelength of $1.31\ \mu\text{m}$, inside a volume surrounded by perfectly matched layers in Lumerical FDTD.

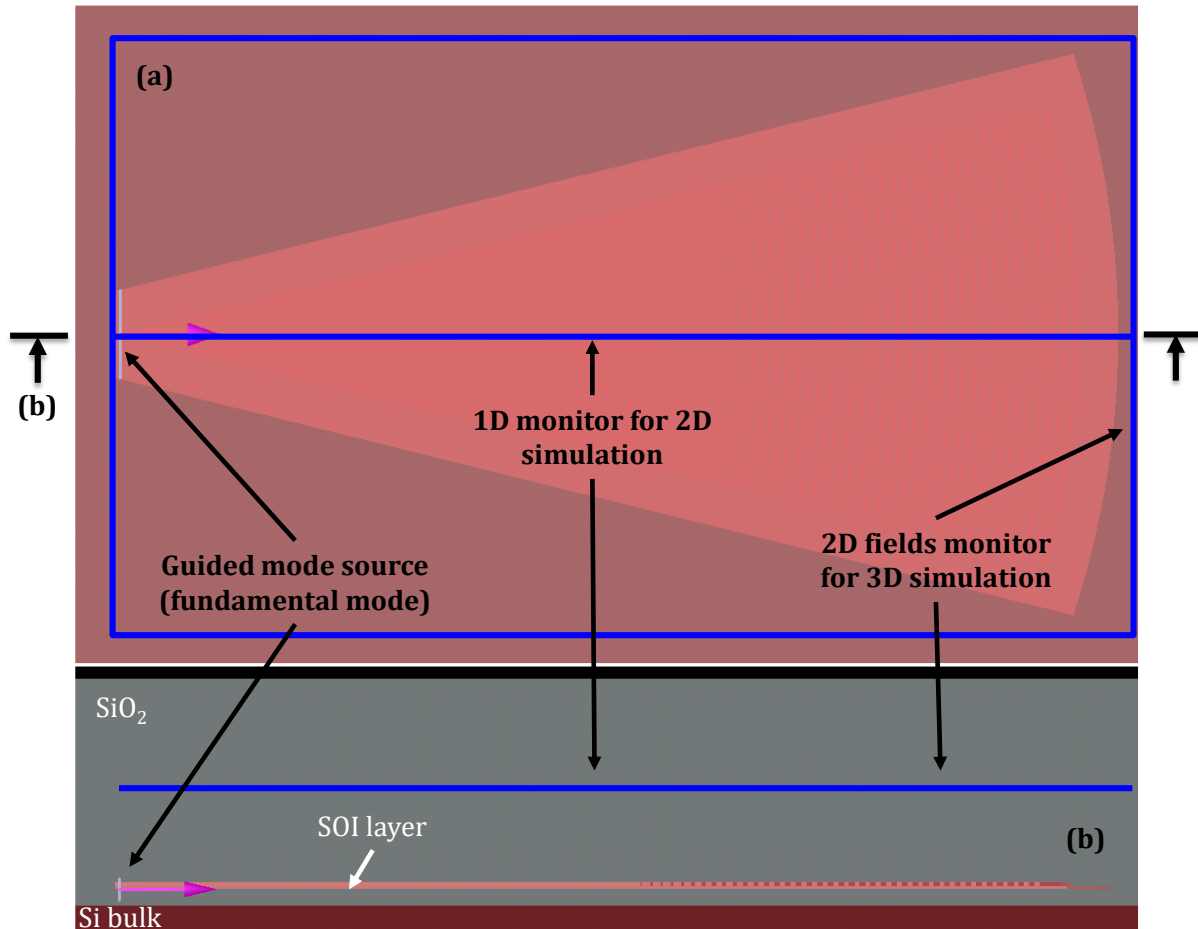


Figure 62: Schematic of the simulation setup showing (a) the top and (b) cross-section views of the modeled SPGC, the input mode source, the linear and areal output fields monitors

As depicted in Figure 62, the source is the fundamental mode of the SOI waveguide with an intensity normalized to 1. The plane and linear monitors of EM fields are placed $1\ \mu\text{m}$ above the GC. Figure 63 shows the distribution of the E field intensity above the simulated SPGC. The transmission from the source is 0.813, which correspond to a loss of 0.899 dB.

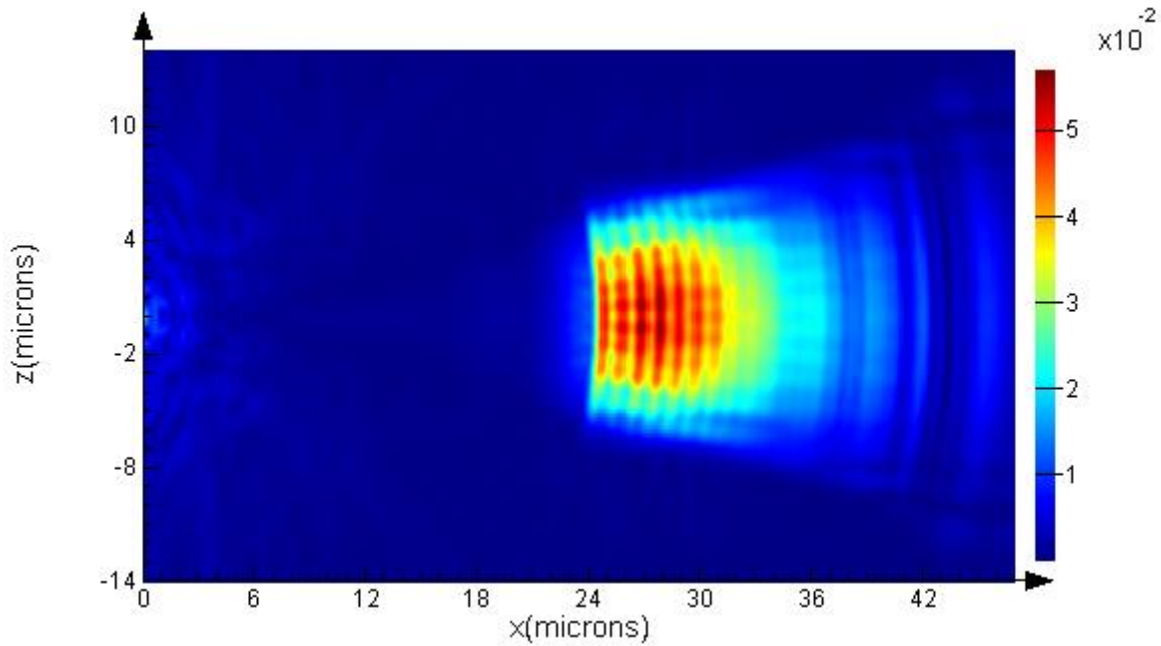


Figure 63: Distribution of the E field intensity on top of the simulated SPGC obtained using the 2D monitor of Figure 62

3.4 PIC to Interposer Coupling

3.4.1 2D Simulations

Using the linear output from the GC simulation as a source in an area delimited by PMLs, we set up a 2D FDTD simulation as described in Figure 64. The interposer is placed upside down 10 μm above the SiPh IC back-end layers. The TIR mirror is modeled by a 20 μm wide slanted air trench through the polymer layers with an angle θ_m . The interposer back-end layers are composed of four polymer layers on top of the glass substrate with the refractive indices n and thickness th summarized in Table 8.

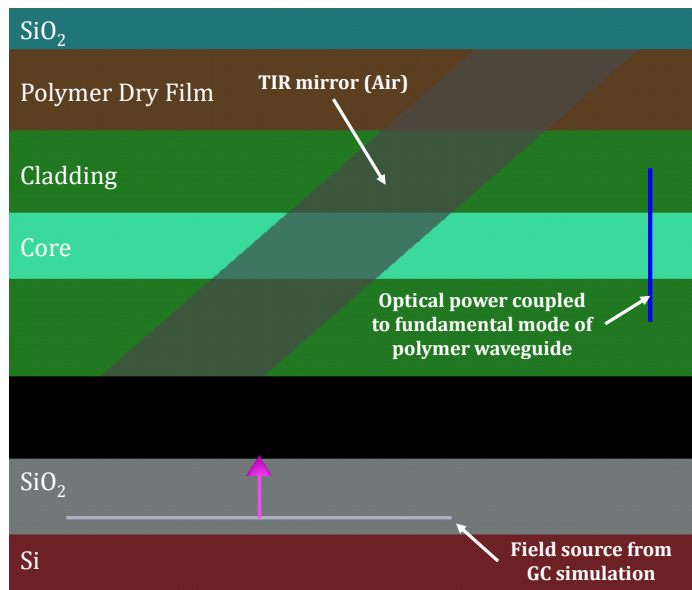


Figure 64: SiPh IC/Interposer simulation setup

Table 8: Modeled layers and their respective refractive index and thickness

Layer	Refractive index	Thickness (μm)
Glass substrate	1.4982	500
Polymer dry film	1.55	10
Cladding	1.56	10
Core	1.564	10
Cladding	1.56	20

The position X_m of the mirror was defined as the distance between the left end of the source (this corresponds to the left end of the grating coupler) and the leftmost point of the mirror. The output of this simulation is given by the association of 2 monitors: a field monitor and a mode expansion monitor. The first gives E and H fields on a specified line. The second is capable of simulating the fundamental propagation mode of the structure given in a plane (a rectangular waveguide) and calculating the coupling efficiency between the fields given by the first monitor and this fundamental (in the line) mode to give the total transmission. We performed sweeps on X_m value for 4 different values of θ_m : 39° , 40° , 41° and 42° .

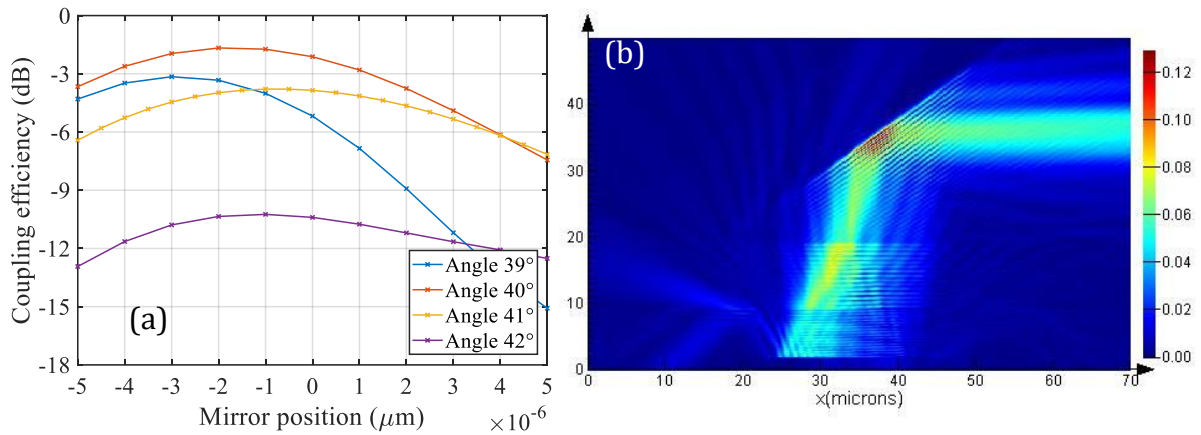


Figure 65: (a) Coupling ratio between the GC and the polymer waveguide of the glass interposer (2D simulation) and (b) E field intensity in the simulation plane

The results are given in Figure 65 (a). We can observe that the angle that gives the maximum coupling efficiency is $\theta_m = 40^\circ$ for a position $X_m = -2 \mu\text{m}$. Also, at this optimal angle, the sensitivity regarding the mirror position is 3 dB for $\pm 5 \mu\text{m}$. Similarly, the sensitivity to the angle variation is 3 dB for $\pm 1.5^\circ$.

3.4.2 3D Simulations

A 3D simulation has been set up to validate the previous 2D results. The same model was employed, the differences lying in the 3D simulation space and 2D source and field monitor. Three simulations were carried-out with $\theta_m = [39^\circ; 40^\circ; 41^\circ]$. For each angle, the mirror position with the best coupling efficiency was selected, respectively, $X_m = [-3\mu\text{m}; -2\mu\text{m}; -0.5\mu\text{m}]$. The results are presented in Figure 66. We observe the same variation compared to 2D simulation with an additional offset on the coupling efficiency. This validates our 2D approach and ultimately allows us to estimate the theoretically achievable overall coupling efficiency from the SOI to the polymer waveguide: -2.1 dB

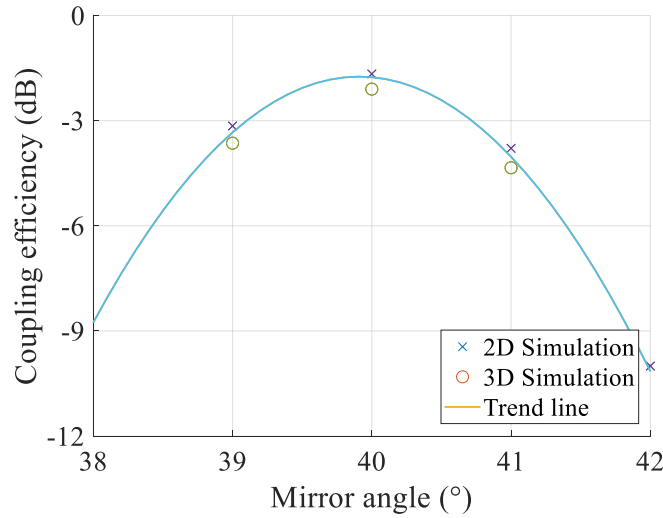


Figure 66: Coupling efficiency versus mirror angle at optimum position, 2D vs 3D

4 Conclusion

In this chapter, we first studied rectangular and rib waveguides topologies, both analytically with approximations and via FDE simulations. We determined their optimal dimensions and refractive indices to ensure single mode operation ($8\mu\text{m} \cdot 8\mu\text{m}$ for the rectangular waveguide with $\Delta n = 0.004$) and a coupling ratio to SMFs superior to -0.5 dB . Then, we chose the CPW topology for the transmission lines of the interposer and simulated several dimensional configurations to obtain a 50Ω and determine the sensitivity to variations due to the technology. Later, we optimized the transmission lines that are driving the PIC25G MZM by the addition of discrete inductors along the line. Finally, we studied by FDTD simulations the SiPh IC/Interposer coupling by means of a grating coupler and a TIR mirror. We determined optimal angle and position for the mirror and estimated the coupling losses to be 2.1 dB . These simulations, allowed to size the main components of the interposer and set objectives for their fabrication, which is detailed in the next chapter, while giving insights on their sensitivity.

III Interposer Fabrication

In the third chapter, we review the experimentations that led us to choose a particular fabrication process for the electrical and optical interposer. Firstly, three different fabrication processes for the polymer waveguides are investigated and compared, namely polymer/glass surface waveguides, rectangular waveguides by laser lithography and rectangular/rib waveguides by laser ablation. The method used to assemble the electrical and optical parts is subsequently presented. Finally, the PIC25G test chip and its functions are detailed as well as the corresponding interposer layout and the alignment strategy used for the flip-chip assembly of both chips.

<i>1 POLYMER OPTICAL WAVEGUIDES</i>	74
1.1 Polymer/Glass surface waveguides	74
1.1.1 Femtosecond Laser Direct Writing	74
1.1.2 Etching in Hydrofluoric Acid.....	76
1.1.3 Dry film lamination.....	77
1.1.4 Chemical Mechanical Polishing.....	79
1.2 Waveguides by laser lithography	80
1.2.1 Liquid resins spin-coating.....	81
1.2.2 Laser lithography.....	82
1.2.3 Dimensional Characterizations.....	83
1.2.4 Optimization for single mode operation	85
1.3 Waveguides by laser ablation	86
1.3.1 Dry films for organic stack.....	88
1.3.2 Refractive index measurements.....	88
1.3.3 Optical Transmission.....	89
1.3.4 Laser trenches.....	93
1.3.5 Rib waveguides with photosensitive resins	96
1.4 Waveguide technologies comparison.....	97
<i>2 ELECTRICAL-OPTICAL HYBRIDIZATION</i>	98
2.1 Electrical and optical glass interposer fabrication process	99
2.2 Copper deposition	100
2.2.1 Copper plating of glass substrates	100
2.2.2 Sputtered thickness calibration.....	101
2.2.2.1 Titanium buffer layer.....	101
2.2.2.2 Copper layer	101
2.3 Copper structuration	102
2.3.1 Chemical etching.....	102
2.3.2 Selective femtosecond laser ablation.....	104
2.4 Laser ablated rib waveguides	105
2.5 Laser ablation of polymer layers for flip-chip bonding and probing	106
2.6 Total Internal Reflection (TIR) mirror	107
<i>3 PIC/INTERPOSER FLIP-CHIP ASSEMBLY AND DEMONSTRATOR</i>	109
3.1 PIC25G test IC.....	109

3.2 Interposer layout & alignment strategy	110
3.3 Flip-chip bonding.....	114
4 CONCLUSION.....	116

1 Polymer optical waveguides

1.1 Polymer/Glass surface waveguides

The fabrication sequence of this first waveguide type involves four elementary steps comprising (a) a femtosecond (fs) laser modification of the glass that locally enhances the etching rate in hydrofluoric (HF) acid, (b) a smooth U-shape micro-grooving of glass in HF to delineate the optical waveguide core, (c) a dry film polymer lamination to fill the groove with a high index material and (d) a chemical-mechanical polishing (CMP) to remove the excess of core material. The different steps of the waveguide fabrication process are summarized in Figure 67.

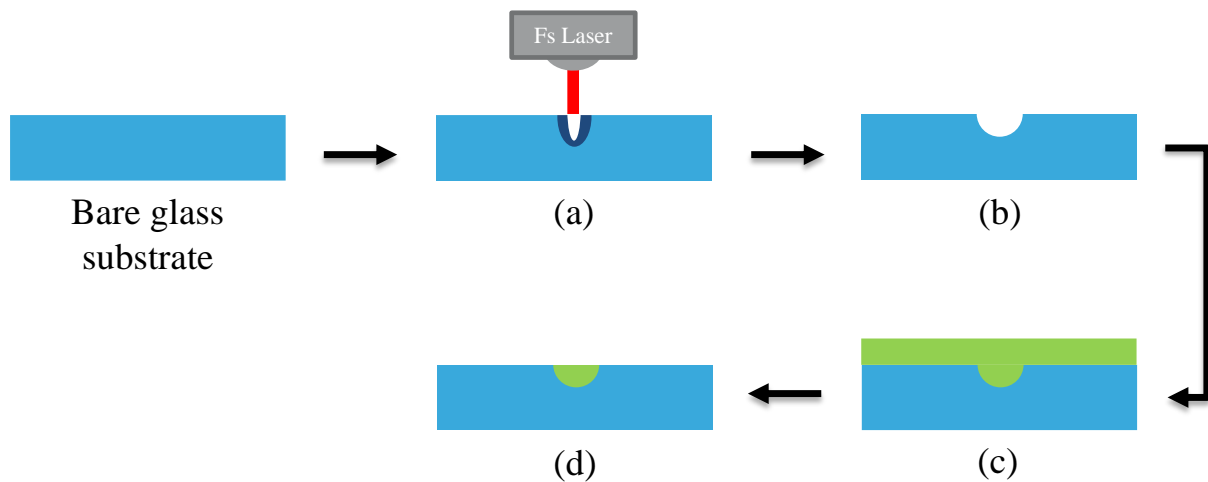


Figure 67: Fabrication sequence of surface U-shaped optical guide in a thin glass substrate: (a) localized laser-induced modification of glass microstructure, (b) U-groove etching based on locally enhanced HF etching rate, (c) dry film polymer lamination to fill the groove and (d) planarization of the core material using CMP.

1.1.1 Femtosecond Laser Direct Writing

Over the past decade, fs laser direct writing has emerged as a promising micromachining technique to locally ablate materials or to structurally change their properties [60]. Furthermore, laser direct writing holds the distinctive advantage of being a maskless technology suitable for fast prototyping loops and does not require operation in clean room conditions, thus reducing complexity and cost. When ultrashort laser pulses propagate in a transparent medium, the extremely high peak power produces spatial self-focusing resulting from the intensity dependence of the refractive index. Above a critical power, a singular wave collapse to a focal point is predicted if self-focusing overcomes

diffraction [93] thus leading to the formation of a filament [94][95]. However, as the pulse grows in intensity, an electron plasma is generated due to non-linear multi-photon and avalanche ionization. This electron gas entails a decrease of the refractive index that acts as a diverging lens. The laser pulse propagation is therefore governed by a fine balance between the Kerr focusing, diffraction and defocusing upon coupling with the electron plasma. Depending on the femtosecond laser pulse energy and duration, different types of structural modifications can take place ranging from gentle refractive index variations to material ablation resulting from optical breakdown. The material ablation occurs when the fluence (J/cm^2) of the laser beam exceeds the fluence threshold $F_{th}(N)$ of this material, which can vary depending on the number N of consecutive pulses. For a gaussian beam, the diameter of the ablated area can be related to the fluence threshold by [96]:

$$D^2 = 2w_0^2 \ln\left(\frac{F}{F_{th}(N)}\right) \quad (1)$$

where w_0 is the beam waist at $1/e^2$ of the peak intensity and F the peak fluence, defined as:

$$F = \frac{2E_p}{\pi w_0^2} \quad (2)$$

$E_p = \frac{P_{av}}{f_{rep}}$ is the energy per laser pulse calculated from the average optical power P_{av} and the laser shot repetition rate f_{rep} . The study carried out in [97] shows soda-lime, borosilicate, fused silica and sapphire glasses present fluence thresholds of 2.90, 2.98, 3.60 and 4.18 $J.cm^{-2}$, respectively, for a 500 fs laser pulse at a wavelength of 1030 nm.

Consistently with the above discussion, exposure of glass to a femtosecond laser beam is known to produce a modulation of the refractive index and a dramatic increase of the etching rate in HF acid [61]. In the present work, this last property is used to delineate the U-shaped micro-groove.

The laser setup used to inscribe micro-grooves in glass implements a Tangerine laser source (Amplitude-Systèmes) that provides ≈ 300 fs pulses at a wavelength of 343 nm after frequency tripling. The laser beam trajectory is controlled by a galvanometric scanning head equipped with a telecentric lens featuring a focal distance of 100 mm. The focused spot diameter is estimated around 10 μm at the considered wavelength. An optical attenuator comprising a half-wave plate and a polarizer allows fine tuning of the beam power independently from the laser source parameters. After running through the entire optical path, the maximum available average power amounts to 2 W at a repetition rate of 200 kHz. Glass inscription was performed under varying operating conditions for the sake of optimization: i) the laser optical attenuation was swept from 10 to 100 %, ii) the scanning speed was adjusted from 2 to 15 mm/s and iii) the repetition rate was

scanned from 10 to 200 kHz. Straight and bent waveguides as well as Y junctions were processed in 500 μm -thick AF32 Eco Thin Glass (3 inches) substrates provided by SCHOTT. As explained in chapter II section 4, the ideal waveguide core cross-section is targeted to be an $8 \times 8 \mu\text{m}^2$ square with a difference between refractive indices around $4 \cdot 10^{-3}$ to obtain single mode waveguides and an efficient coupling with optical fibers.

1.1.2 Etching in Hydrofluoric Acid

As outlined previously, several types of modifications can occur in glass exposed to femtosecond laser irradiation. The commonly observed structural changes can be classified into three families depending on the pulse energy:

- i. isotropic increase in refractive index,
- ii. birefringent modifications and
- iii. ablation resulting from micro explosions [60].

It is well established that fundamental glass properties like density and refractive index can be associated to the Si-O-Si bond angle [98]. In vitreous silica structures, the short-range order is dominated by 6- and 5-membered rings, an n-membered ring being associated to n Si-O segments contained in a closed path. From a minimum-energy standpoint, the formation of 3- and 4-membered rings is not favored because it involves a higher strain energy when compared to their higher order counterparts. A high concentration of 3- and 4-membered rings is however possible and is the signature of an out-of-equilibrium state [99] that can typically happen in a quench scenario after laser exposure. This analysis was experimentally consolidated by micro-Raman analysis of glass exposed to femtosecond laser pulses that reveals enhanced Raman peaks at 490 and 605 cm^{-1} that can be assigned to breathing modes of 3- and 4-membered rings [61]. Consistently with the previous analysis, an increased concentration of these rings leads to a global decrease of the average bond angle and, in turn, can be associated to a densified material with higher refractive index. As reported in [93], this structural modification can be accompanied with an accelerated etching rate in HF up to 1:100 with respect to the unexposed material.

In the present study, most laser exposure experiments lead to micro-explosions and local sputtering that initiated the formation of narrow channels. At high pulse energy, a channel width around $1\ \mu\text{m}$, much lesser than the spot diameter ($\approx 10\ \mu\text{m}$) suggests that filamentation occurred [100]. Immediately after laser exposure, the depth-elongated form factor resulting from filamentation and remaining glass fragments inside the micro-groove

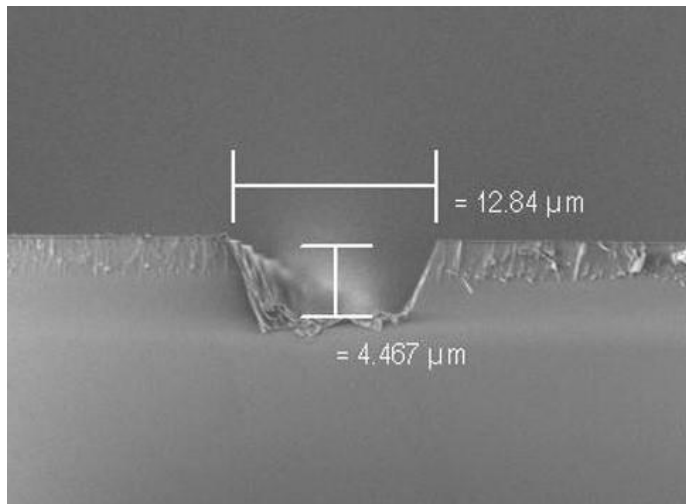
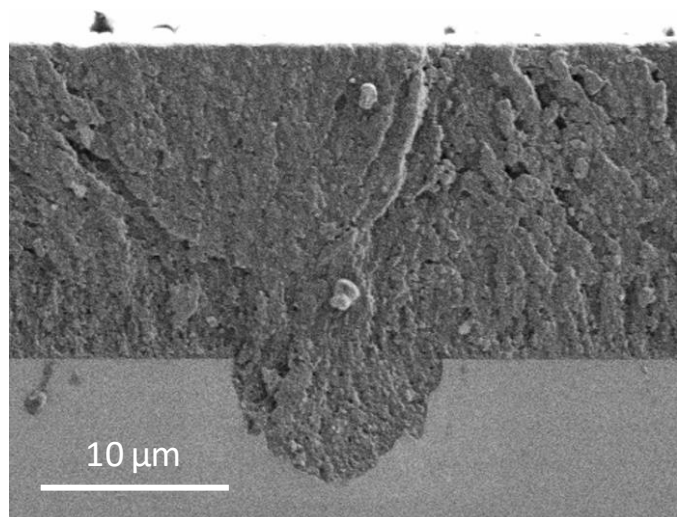


Figure 68: SEM cross-section of a micro-groove obtained by laser inscription performed with following parameters: repetition rate 30 kHz, average power of 0.12W, scanning speed of 8 mm/s and HF etching for 2.5 min.

make this structure unsuitable for wave guiding structures. Nevertheless, glass surrounding the micro-grooves in the so-called laser-affected-zone (LAZ) also features an increased refractive index and a marked modification of its microstructure. To reveal well-formed micro-grooves, the laser-exposed glass samples were dipped in a diluted solution of HF acid (10% HF/H₂O v/v) for relatively short etching times of 2.5 min and 5 min. After rinsing in deionized water, samples have been cleaned in acetone and isopropanol for 5 min each, under ultrasonic agitation. Samples were subsequently diced along a line perpendicular to the laser scan direction to observe their cross-section using scanning electron microscopy (SEM), yielding the typical picture shown in Figure 68, obtained with the following laser writing conditions: repetition frequency of 30 kHz, average power of 0.12 W, scanning speed of 8 mm/s and HF etching time of 2.5 min.

1.1.3 Dry film lamination

To fill the micro-groove with a core material, the adopted strategy consists in roll laminating a thin-film polymer available under a dry film form. Several constraints apply to the choice of the polymer base material. First, the polymer must exhibit good gap filling properties to conformally shape the geometry of the micro-grooves while remaining stable under varying ambient conditions. Thermosetting resins holds this remarkable property to be initially



viscous or soft and to further soften just above its glass transition temperature in such a way that the roll pressure efficiently fills topological inhomogeneities. Providing that the hot lamination temperature reaches glass transition, thermosetting films evolve irreversibly to a cross-linked network characterized by a high level of dimensional stability. The second selection criterion is related to the refractive index of the thermosetting dry film that must be slightly above its AF32 counterpart ($n=1.4982$ at $\lambda=1310\text{nm}$), ideally $n = 4 \cdot 10^{-3}$ as stated previously to ensure single mode propagation. Our choice focused on the ORDYL SY317 from ELGA [101] that comes in the form of a 17 μm thick dry film. Although its exact composition is not disclosed by the manufacturer, it is identified as a mix of acrylic polymer and acrylic ester containing the chemically resistant and stable epoxy group [102].

From a practical standpoint, the ORDYL SY317 dry film was laminated with a roll temperature of 110°C. Five passes of lamination were applied at a pressure corresponding to a static load of 12 kg. To improve the bond quality to the glass substrate, an adhesion promoter was applied prior to hot roll lamination. It consists in a very thin layer of Hexamethyldisilazane (HMDS) deposited by gaseous streaming on the glass substrate heated to 100°C. The final result is presented in Figure 69 showing the excellent filling of the micro-grooves as well as complete planarization of the dry film top surface.

Figure 69: SEM cross-section of a micro-groove after lamination of an ORDYL SY317 dry film with a roll temperature of 110°C. Five passes of lamination were applied at a pressure corresponding to a static load of 12 kg. A HMDS adhesion promoter was vapor-stream-deposited prior to the dry film application.

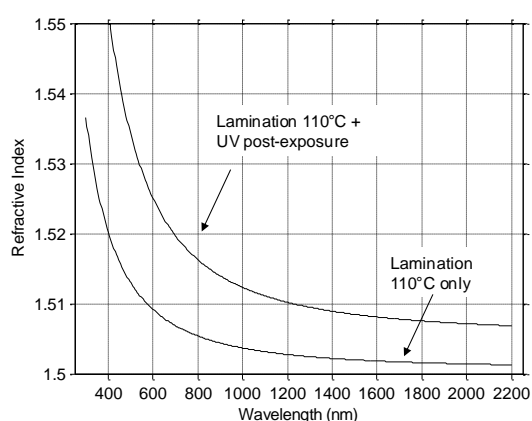


Figure 70: Refractive index of Ordyl SY317 after 5 passes of hot roll lamination performed at 110°C. The refractive index can be modulated by post-lamination UV exposure that enhances the cross-linking degree of the polymer.

The refractive index was determined by spectroscopic ellipsometry after lamination onto a non-transparent silicon to facilitate the experimental procedure. Measurements over the 350-2200 nm wavelength interval were fitted on a simple Lorentz dispersion model [103] with an excellent accuracy. Two application flavors of the dry film were tested: a simple lamination without any post-treatment and a UV post-exposure at 365nm, 10mW during 60 seconds to evaluate the capability to modulate the

refractive index by enhanced cross-linking after hot roll lamination. At a working wavelength of 1310nm, the dry film core material exhibits a refractive index of 1.503 and 1.510 without and with UV post-exposure, respectively (Figure 70). This results in a core-cladding difference of 4.8×10^{-3} without UV and 1.18×10^{-2} with UV cross-linking that does not guarantee the waveguides to be single mode. However, the immediate availability of the material and its ease of application led us to fabricate the first waveguides. Figure 5 shows a typical example of AF32 Eco glass substrate after laser inscription, HF etching and ORDYL SY317 lamination. Designed structures comprising straight, bent and Y junction waveguides can be clearly identified.

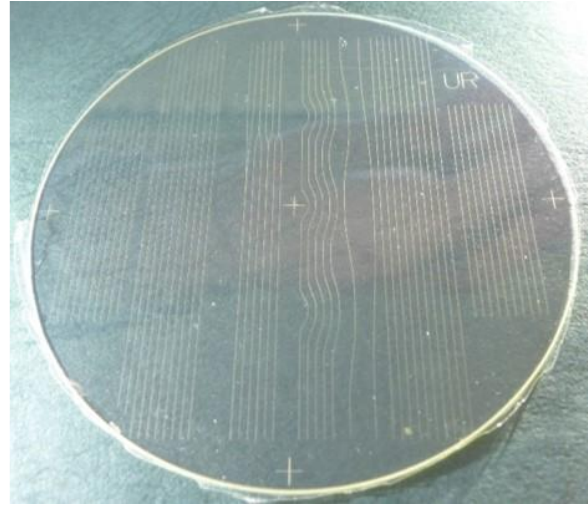


Figure 71: Picture showing a 3 inches 500 μ m thick AF32 Eco glass substrate after laser inscription, HF etching and lamination of an ORDYL SY317 dry film. The layout contains straight and bent waveguides as well as Y junctions.

1.1.4 Chemical Mechanical Polishing

As shown in Figure 69, the dry film thickness largely exceeds the depth of the processed micro-grooves which prevents proper confinement for light guiding. In order to remove the excess of polymer to delineate a surface waveguide, chemical mechanical polishing (CMP) has been used. CMP is well established in the semiconductor industry to achieve global surface planarization in complex stack of interconnection layers [104]. One major challenge of this technique is to avoid layer delamination due to the high-torque nature of the polishing mechanism [105]. This remark is all the more true as polymers have typically a lower elastic modulus and hardness when compared to metals and other inorganic dielectrics like silicon oxide or nitride. As a result, polymers are more prone to delamination, tearing and a source of scrap residues. To overcome this difficulty, ORDYL SY317 was systematically exposed to UV to produce a highly cross-linked layer that is more robust to withstand high pressures and frictions during the CMP process.

As most polymers are generally resistant to acidic and basic solutions, it can be expected that the removal rate of polymer is dominated by the mechanical action rather than the chemical one. Our choice of polishing slurry and pad was therefore guided to keep a high degree of compatibility with glass to guarantee a high removal rate contrast between the polymer and the supporting glass substrate. For that sake, a colloidal silica-based slurry with basic pH and particle size of 70 nm was used for its proven affinity with silicon dioxide that we assume to be the same with glass. A soft polyurethane impregnated polyester felt was used as polishing pad to ensure a high precision surface finishing.

Among other parameters, the pressure and rotation speed of the polishing head as well as the spinning speed of the pad plate are critical parameters that strongly conditions the quality of planarization. Figure 72 shows a typical result obtained with a carrier pressure of $1200 \text{ mdaN} \cdot \text{cm}^{-2}$, a substrate blowing back pressure of $600 \text{ mdaN} \cdot \text{cm}^{-2}$ and the same rotation speed of 60 rpm for the carrier and the pad plate. Based on this approach, we successfully managed to planarize the excess of polymer without noticeable dishing, hence creating surface waveguides.

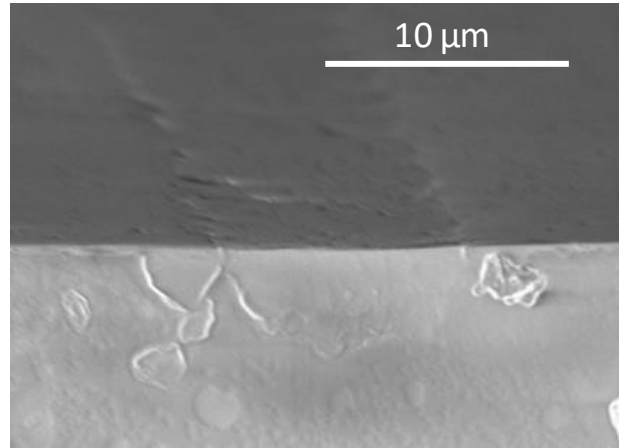


Figure 72: SEM picture showing a cross-section of a surface waveguide after the CMP step. The core hemicylinder is composed of ORDYL SY317, the bottom cladding is a glass substrate AF32 Eco.

This technique has the advantage of fabricating a waveguide with a reduced number of process steps using a polymer dry film and the glass substrate. However, it involves CMP and consequently requires wafer manufacturing. This deprives the dry film from its main asset, i.e., rectangular panel manufacturing with the constraint to use a circular substrate required by the CMP step. Moreover, in this implementation, the electrical redistribution layers have to be placed above the waveguides, which complicates the vertical coupling. Last but not least, the performance of the waveguides fabricated this way is poor, as it will be discussed in chapter IV section 1.1.2.2. Hence, we decided to investigate two other waveguide fabrication processes.

1.2 Waveguides by laser lithography

In a second approach, we have fabricated waveguides in photosensitive spin-coated resins following the fabrication process presented in chapter I section 3.2.2.4 and depicted in Figure 73 below. First (a), trenches are ablated on the back side of the glass wafer using the fs laser setup described in section 1.1.1 to ensure a good cleaving of the sample prior to measurements. After acetone and isopropanol alcohol cleaning in ultrasonic baths, a first cladding layer is spun on the wafer (b). This layer undergoes a prebake, a flood UV exposure and a post exposure bake (PEB). As recommended by the manufacturer, the sample surface is treated by a PVA TEPLA plasma system. The plasma is formed in an 8.75 standard cubic centimeters per minute (sccm) oxygen flow by an electric field generated by a 100 W generator for 1 min. The core layer is subsequently spun and prebaked (c). Continuous wave (CW) UV laser lithography is used to cross link the core of the waveguide (d) that is delineated during the development of the resins and cured (e). Another oxygen plasma surface treatment is done with the same parameters as

the previous one. The last step is the waveguide encapsulation in a second cladding layer processed identical to the first one: spin-coating, prebake, flood exposure and PEB (f).

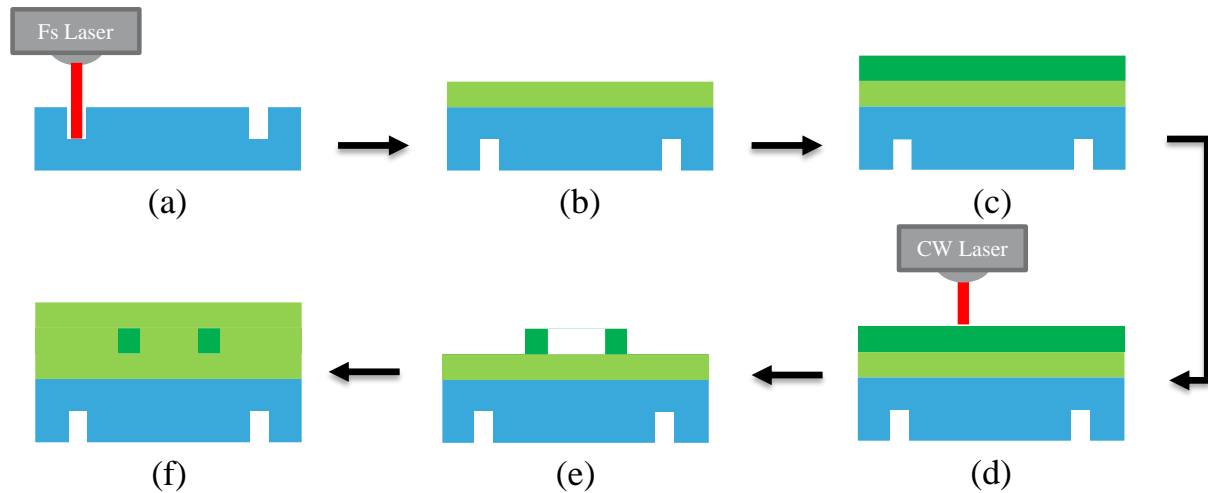


Figure 73: Fabrication steps of the waveguides: (a) trenches ablation on the back side of the wafer using the fs laser. First cladding layer pin-coating, prebake, flood exposure and PEB (b). Core layer spin-coating and prebake (c). CW UV laser lithography (d). Development and PEB of the core layer (e). Spin-coating, prebake, flood exposure and PEB of the second cladding (f).

The liquid polymer resists used in this process are from the Epocore and Epoclad series manufactured by Micro Resist Technology [106]. These resists are epoxy-based and present a high optical transmission at telecom wavelength which is essential for our application. Standard versions of these resists have refractive indices of 1.564 ± 0.002 for the cladding material Epoclad and 1.577 ± 0.002 for the core material Epocore. These values are given at a wavelength of 1310 nm. The refractive index can be tuned at fabrication so we have been supplied with specific Epocore XP with a refractive index of 1.568 ± 0.002 .

1.2.1 Liquid resins spin-coating

The resists deposition is performed by spin coating. This method consists in placing the substrate on a rotating sample holder. A small quantity of resin is deposited directly on the wafer that is rotated to spread out the resist. The deposited thickness is related to the rotation time and speed as well as the substrate material and the resist viscosity. These two last parameters being

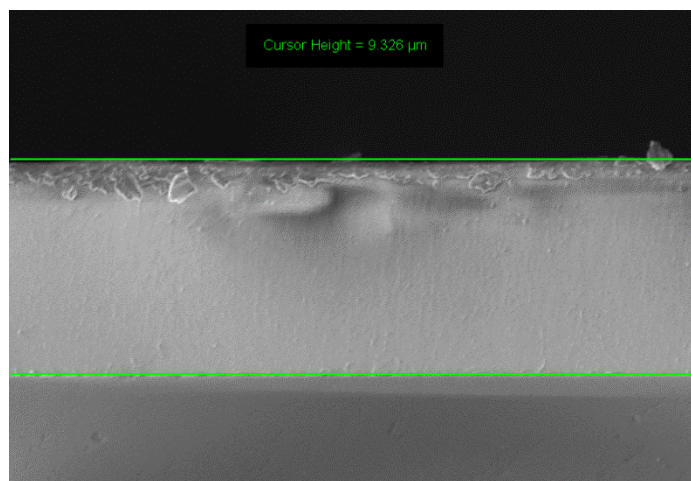


Figure 74: SEM picture of the Epocore 5 XP layer spun with a rotation speed of 1500 rpm

fixed, we performed tests to compare the deposited thickness versus rotation speed curve (also called spin curve) given in the datasheet with the one given by our setup for Epocore 5 XP in the viscosity 5. This viscosity level theoretically allows the deposition of a 5 μm thick film for a rotation speed of 3000 rpm during 30 seconds.

Two Schott AF32eco glass wafers are successively rinsed in acetone and IPA ultrasonic baths for 5 minutes each prior to spin-coating. A rotation time of 30 seconds is used for both wafers and rotation speeds of 1500 and 3000 rpm. The process sequence is completed with a prebake (3 min at 80°C), UV exposure (25 s at a fluence of 10 mW/cm²) and a PEB (3 min at 80°C). The samples are then cleaved and the polymer thickness is measured using scanning electron microscope (SEM) cross-sectional imaging as shown in Figure 74. The measured thicknesses are compared to those given in the product datasheet and both curves are interpolated with an $y = ax^b$ law as plotted in Figure 75.

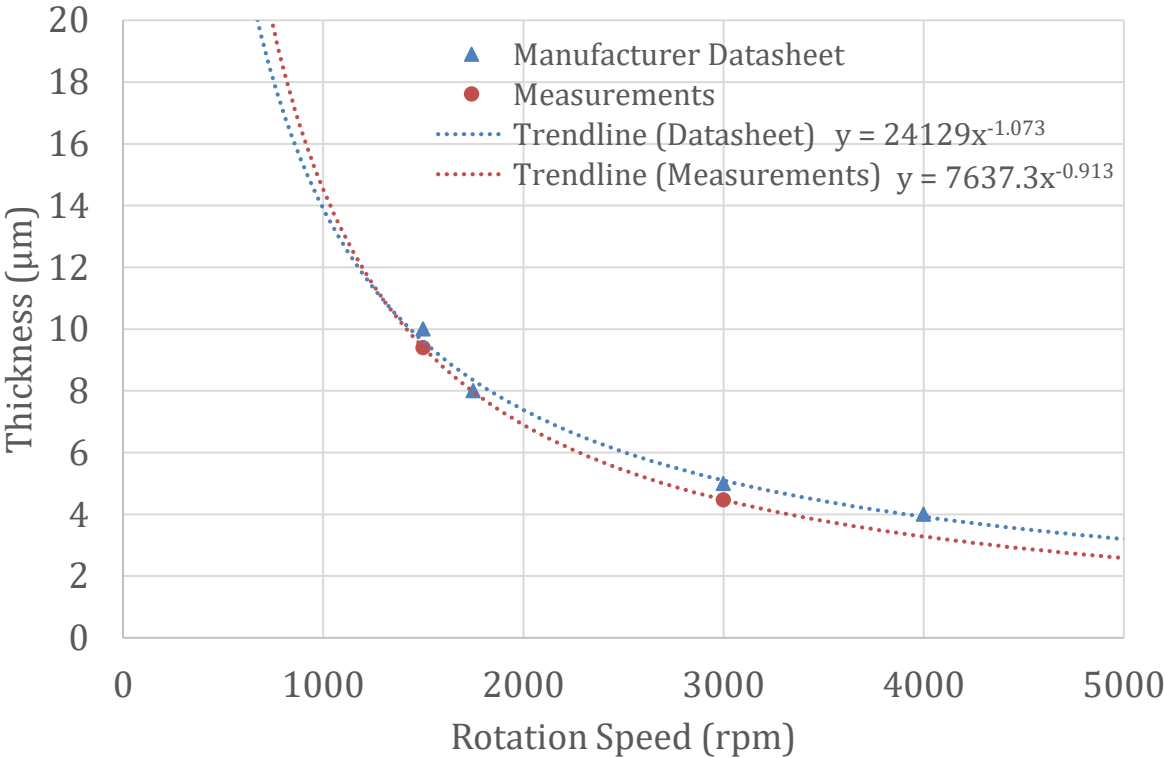


Figure 75: Measured and Datasheet spin curves of Epocore 5 XP

1.2.2 Laser lithography

Laser lithography is another maskless exposition technique that provides high flexibility at a low cost. In addition to these valuable assets for R&D, the exposure step is easily adaptable to traditional exposure through photomask for high volume production. The laser setup is a Dilase 650 (Kloé) which uses a continuous laser source at 375 nm with an average power of 63 mW and two optical paths yielding different laser spot diameters, 1

and 10 μm , respectively. The waveguide’s dimensions strongly depend on the exposition parameters. We performed variations on laser power and scanning speed to determine the optimum waveguide width and height using the layout described in Figure 76 and the 1 μm spot size. The height of the laser focal point was also scanned over 60 μm from the bottom to the top of the polymer layer. Waveguides being sensitive to roughness at the core/cladding interface, writing waveguide in one laser pass greatly limits thickness variations of the core resulting from sweep filling. With this goal in mind, we parametrized the structures with only one laser pass except for the Y-shapes structures, which are defined by overlapping S-shaped structures.

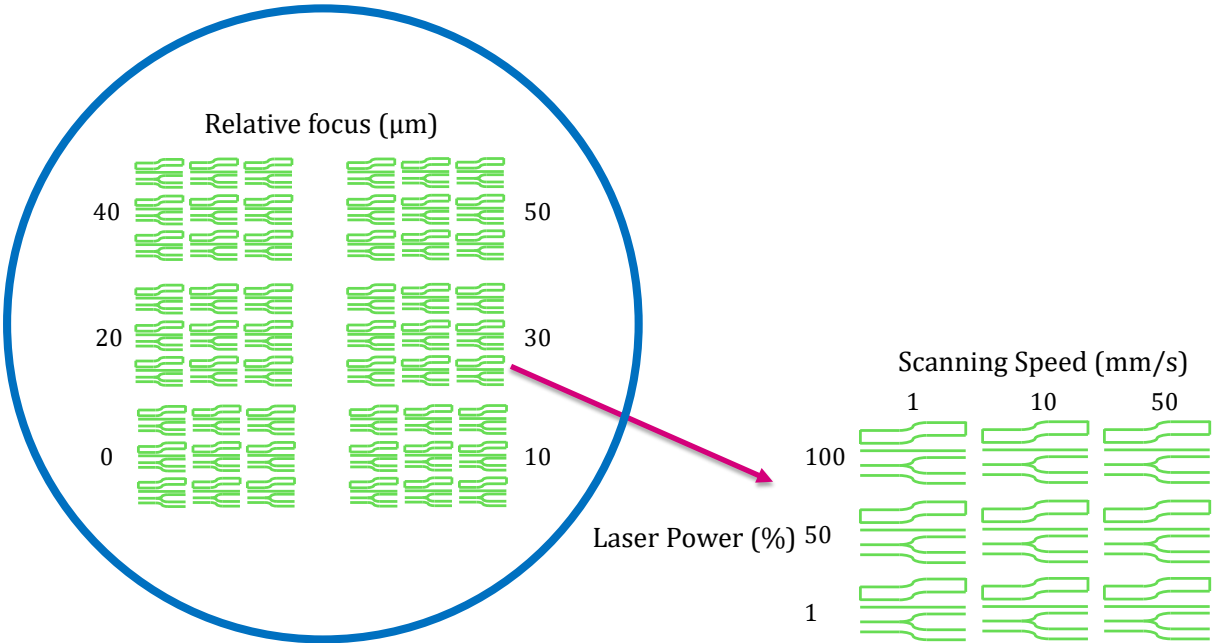


Figure 76: Schematic of the lithography calibration layout

This experiment being dedicated to dimensional characterizations, it follows the fabrication process described in Figure 73 with an additional step. Between steps (e) and (f) a 50 nm layer of titanium is deposited by sputtering for subsequent observations.

1.2.3 Dimensional Characterizations

The dimensions of the structured waveguides are characterized by optical microscopy and interferometric profilometry after step (e). The profilometer used is a Bruker ContourGT-X [107]. This tool provides topographic profiles such as the one depicted in Figure 77 using white light or green light interferometry.

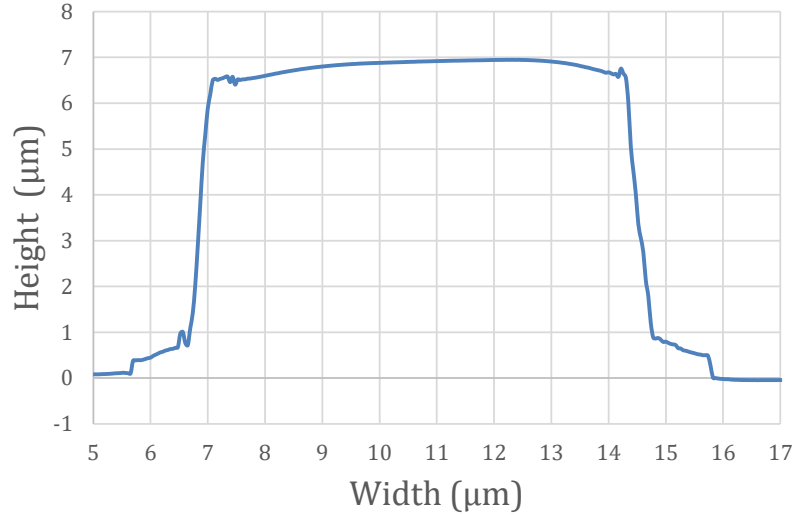


Figure 77: Elevation profile of a typical waveguide core made by laser lithography

These profiles give access to the measured width and height of the fabricated structures as a function of the laser lithography parameters. Table 9 gives the width of the measurable structures after development and also reports the presence of defects, such as unscribed or delaminated waveguides.

Table 9: Width of the fabricated structures versus laser lithography parameters

Laser Power (%)	Scanning Speed (mm/s)	Focus (mm)	Width (μm)	Defects
50	1	0	7.19	
100	1	0	9.69	
50	1	10	6.57	
100	1	10	9.11	
50	1	20	3.09	
100	1	20	4.86	
100	10	20	1.44	X
1	1	30	1.52	X
50	1	30	2	
100	1	30	2.69	
100	10	30	1.15	X
50	10	30	0.74	X
50	1	40	3.67	X
100	1	40	4.17	
100	10	40	X	X
50	1	50	6.45	
100	1	50	7.62	
100	10	50	X	X

We can observe that using a laser power above 50 % (32 mW) and a scanning speed of 1 mm/s, structures with widths of 2 μm to 9 μm are achievable by a variation of the position of the focal point relative to the polymer layer.

At the end of the process, the samples are cleaved to observe the cross-section with a SEM. Figure 78 (a) shows such a cross-section picture where the interface is clearly visible between the core and the top cladding thanks to the titanium layer whereas it is not the case for the interface between the core and the bottom cladding layer. Figure 78 (b) and (c) show optical microscope pictures of the structures (straight line and Y-shaped) in top view.

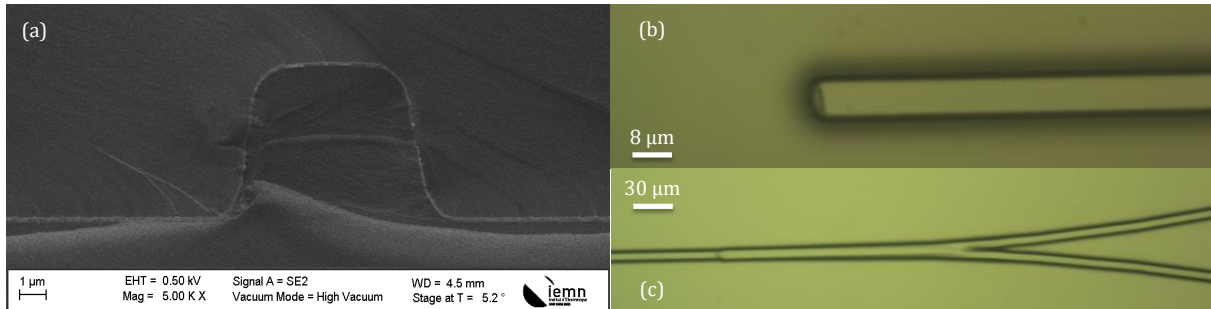


Figure 78: (a) SEM picture of a waveguide cross section, (b) optical microscope picture of the edge of a waveguide structure and (c) optical microscope picture of the Y-junction.

1.2.4 Optimization for single mode operation

After this first coarse experiment on laser lithography parameters, we progressively refined the process parameters by going back and forth from fabrication to optical characterizations to correlate dimensions to optical properties.

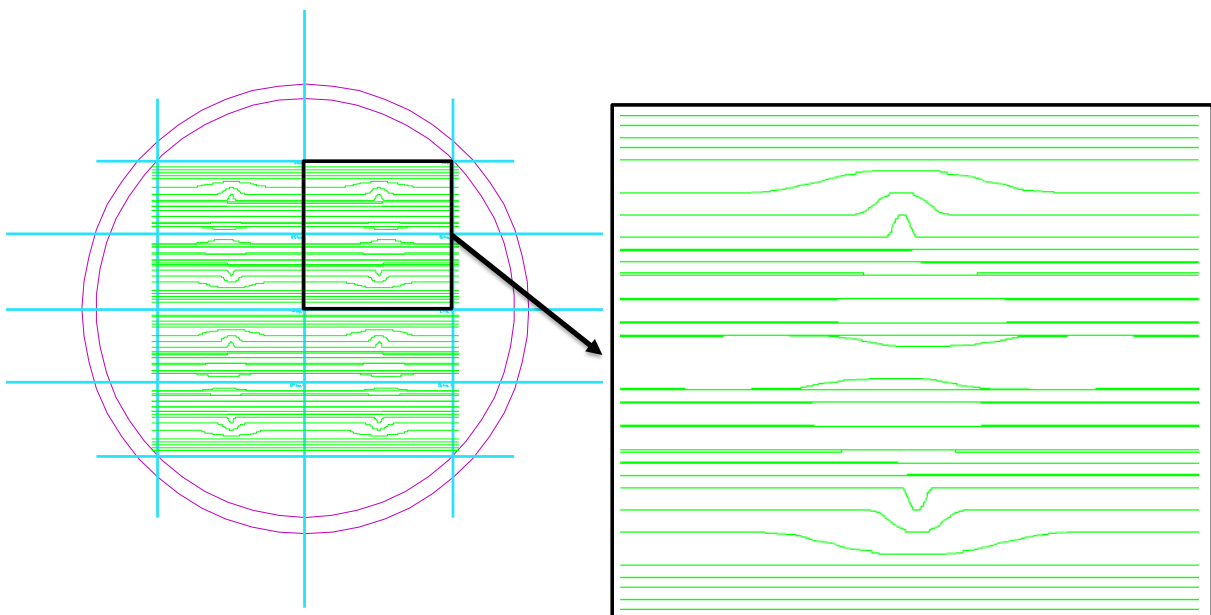


Figure 79: Superimposition of the backside cleaving trenches layout (blue lines) and laser lithography layout (green lines) for waveguides optimization. The green layout contains laser paths to fabricate straight and bent waveguides, Y junctions, directional couplers and Mach-Zehnder interferometer

The layout used to fabricate the waveguide test structures is depicted in Figure 79. Green lines represent the laser path for lithography and blue lines show the laser paths for the

ablation of the back-side cleaving trenches. The elementary cell contains: five straight waveguides, three bent waveguides formed by two connected S-shaped waveguides enabling a 500 μm vertical displacement L_{off} , two Y junctions, three directional couplers, with respective coupling sections L_c of 2, 3 and 4 mm where the waveguides paths are separated by a spacing S_c of 20 μm , and a Mach-Zehnder interferometer involving three directional couplers with coupling sections of 2 mm and a vertical offset L_{mzi} of 500 μm on one branch. These components are depicted in Figure 80. We used parametric cells from STMicroelectronics PIC25G design kit to generate the S-bent parts with a known minimum radius of curvature. We implemented the S-bent waveguides with minimum radii of 100 μm , 1 mm and 10 mm. The Y-junctions, directional couplers and Mach-Zehnder interferometer are designed with a minimum radius of 10 mm. This cell is repeated 8 times on the 3-inch glass wafer.

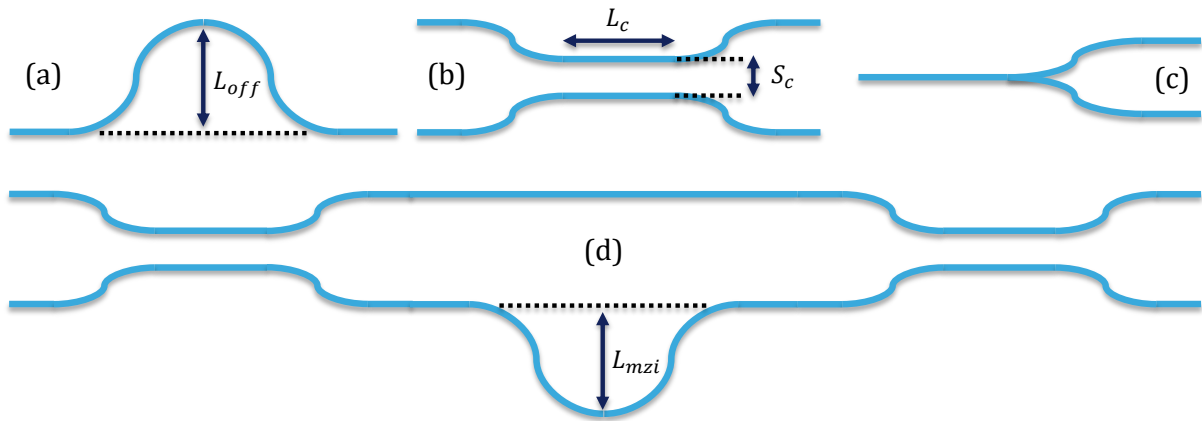


Figure 80: Schematic of the optical test structures, namely (a) bent waveguides, (b) directional couplers, (c) Y junctions and (d) Mach-Zehnder Interferometers, along with their respective characteristic dimensions

Each wafer follows a detailed process sheet, such as the one presented in annex B, and allows the testing of four different set of laser parameters. The waveguide dimensions of each set are measured by the profilometer after step (e) and at the end of the process, the wafer is cleaved along the blue lines and the optical components characterized. From a physical point of view, the dimensions are compatible with the fabrication of single mode waveguide, which we achieved. However, we encountered reproducibility and thermal stability problems using this fabrication method. This point will be addressed in the next chapter in section 1.1.1.3.

1.3 Waveguides by laser ablation

The third waveguide fabrication process involves the steps summarized in Figure 81 and detailed hereinafter. First, the glass substrate is cleaned by acetone and isopropanol ultrasonic baths and a polymer dry film resist is laminated on it to form the lower optical cladding. This is followed by the lamination of a second dry film resist which is the core

layer. Two grooves are subsequently structured by laser ablation to delineate the waveguide core while removing the core material from both sides of this structure. Finally, the waveguide core is encapsulated using lamination of the same polymer as the one used for the optical substrate.

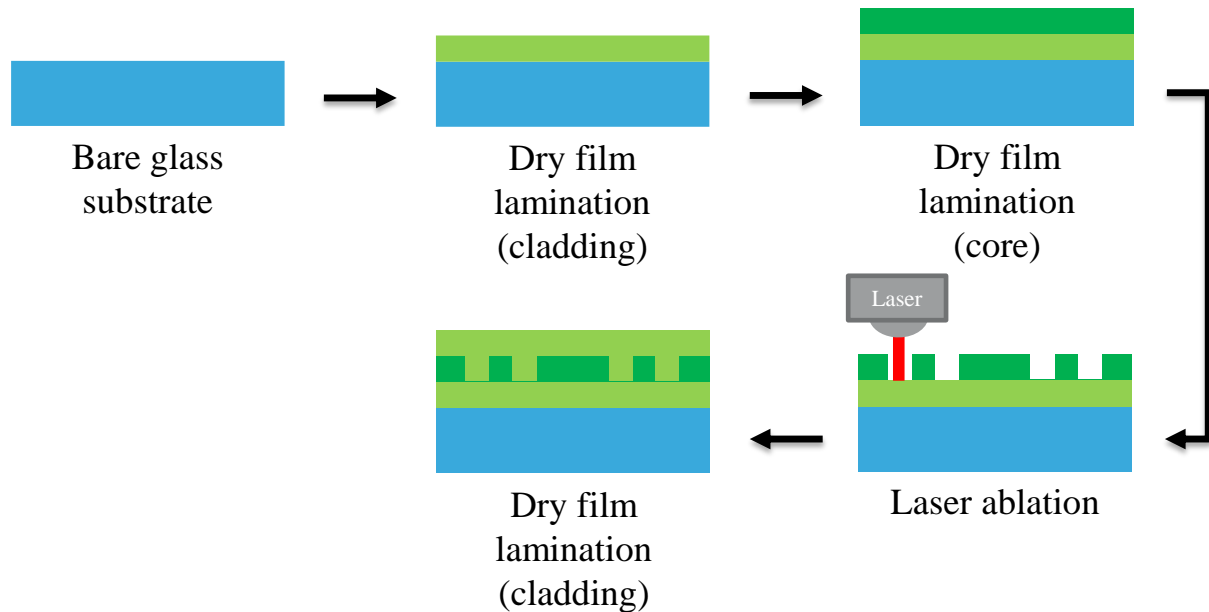


Figure 81: Fabrication process of laser ablated polymer waveguides

Similar processes have been previously described in literature. In [108], three different lasers have been compared for the purpose of waveguides manufacturing: continuous wave CO₂, pulsed UV Nd:YAG and excimer. In [109], optical waveguides have been manufactured using a nanosecond pulsed Nd:YAG laser and characterized. Propagation losses were evaluated to be 1.4 dB/cm. This confirms that waveguides made of polymer materials and fabricated using laser ablation are a viable process for the manufacturing of low-cost optical waveguides on interposers. However, in the above-cited article, only multimode waveguides at a wavelength of 850 nm were fabricated and the core and cladding materials were spin-coated.

The laser ablation of polymers is a combination of dissociation of the molecular bonds (photo-chemical ablation) and optical absorption resulting in material heating (photo-thermal ablation). It has been demonstrated in [110] that the laser pulse duration has a direct impact on the ratio between photo-thermal and photochemical ablation. Shorter pulse duration results in a reduced heat affected zone in the polymer. This heat-affected zone must be minimized in order to obtain the accuracy required for the manufacturing of single mode waveguides. As a consequence, the femtosecond laser described in section 1.1.1 seems appropriate to perform the ablation step of this process.

1.3.1 Dry films for organic stack

As discussed in chapter I section 3.2.1.3, the closer the process and materials are to conventional electrical interposers, the easier is the deployment of the technology at an industrial large-scale and low-cost. With this in mind, we initiated a collaboration with a major dry film manufacturer, Ajinomoto Fine-Techno (AFT), to evaluate the Ajinomoto Build-up Films (ABF) for the fabrication of optical polymer waveguides. This evaluation can be divided in 3 parts: physical structuration, refractive index and optical transmission evaluation. Among the line-up proposed by the supplier, the lowest dry film thickness available was 10 μm . The two selected materials, GX-T31 and GY11, are 10 μm and 35 μm thick, respectively. They feature a refractive index difference of about $\Delta n = 1 \cdot 10^{-2}$ at 800 nm and are fully compatible with electrical interposer manufacturing. Given refractive indices and thicknesses, GX-T31 can be the core and GY11 the cladding material of the polymer waveguide.

1.3.2 Refractive index measurements

In the same way as for the Ordyl dry film (section 1.1.3), we measured the refractive index of GX-T31 and GY11 by spectroscopic ellipsometry. The results given in Figure 82 show a refractive index difference of $7 \cdot 10^{-3}$ near $\lambda = 1300 \text{ nm}$. Nonetheless, the obtained refractive indices need to be confirmed as the measurements have been performed on uncured materials laminated on silicon substrates at 120°C under a pressure equivalent to a static load of 12 kg, whereas the process requires the materials to be cured after lamination.

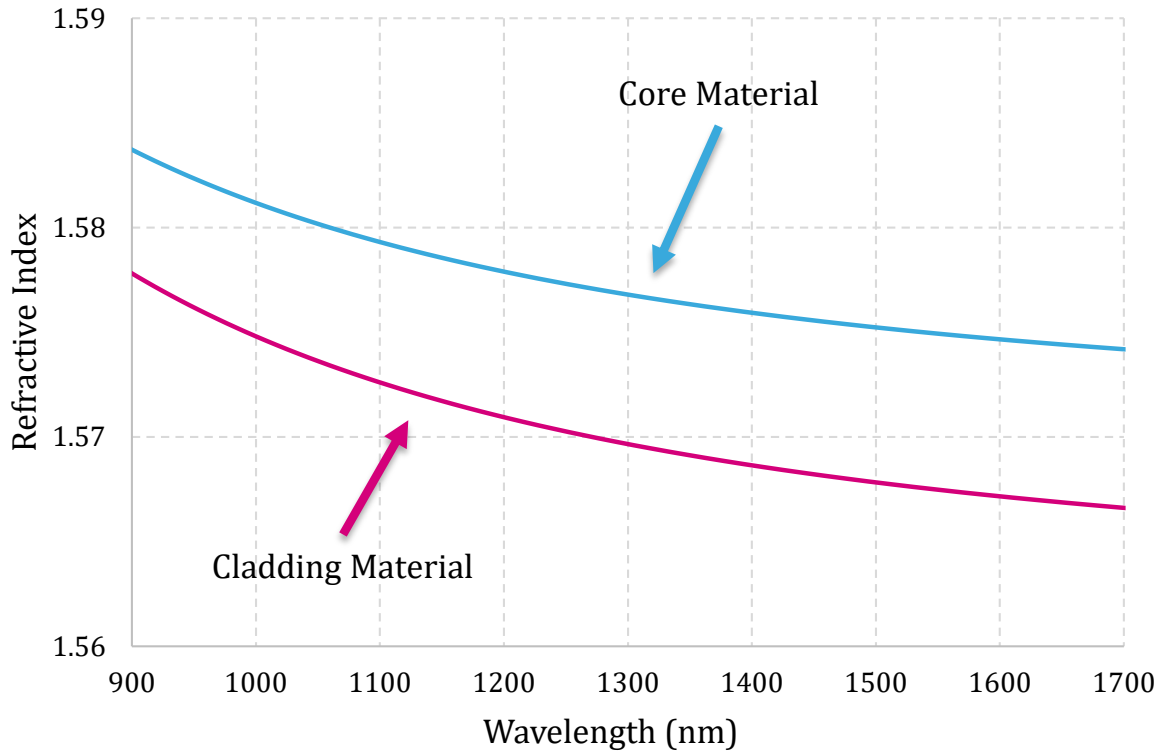


Figure 82: Refractive indexes versus wavelength of the core and cladding materials, measured by spectroscopic ellipsometry

At first glance, this refractive index difference seems too high to allow for the fabrication of single mode waveguides having an $8 \times 8 \mu\text{m}^2$ core and consequently low coupling losses with SMFs. However, this may be modified by fine tuning of the materials composition and, as it stands, does not prevent the fabrication of multimode waveguides. AFT provided four additional experimental materials but we did not measure their refractive indices.

1.3.3 Optical Transmission

The optical transmission of GX-T31 and GY11 was measured along with other experimental materials provided by AFT using a PerkinElmer Lambda 950 spectrometer covering wavelengths from 175 nm to 3300 nm. All materials were laminated onto a 500 μm thick AF32 glass panels at 120°C under a 12 kg static load and cured at 200°C for 90 minutes. The goal is to measure the transmission spectrum of each layer and determine whether the losses are compatible with waveguides fabrication. The spectrometer comprises two light sources followed by a monochromator to sweep the entire wavelength range with a resolution of 0.20 nm in the near infrared. The light is divided into two collimated beams. One is passing through the sample and travels to an integrating sphere [111] whereas the other is directly measured by a photodetector. After a calibration without samples, two methods, shown in Figure 83, were employed to obtain the transmission spectra. The equipment allows placing the sample in contact with the

integration sphere (b) or approximately 10 cm away from it (a). For simplicity, we refer to method (a) by direct transmission and (b) by total transmission.

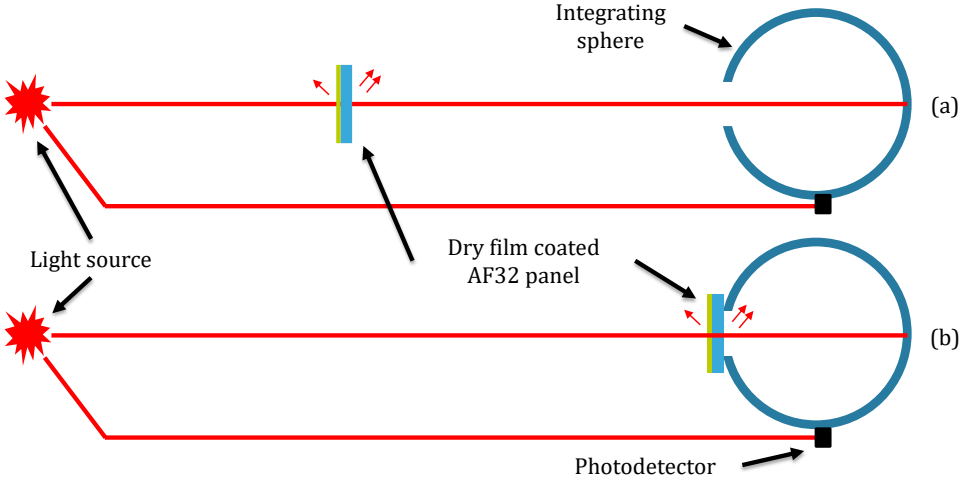


Figure 83: Transmission spectrum measurement methods: (a) direct transmission and (b) total transmission.

Performing measurements using both methods gives clues about the materials propensity to scatter light. In Figure 84, direct transmission of GX-T31 and GY11 materials laminated on 500 μm thick AF32 glass panels are reported along with four other materials deposited by the same method and a clean glass panel for reference.

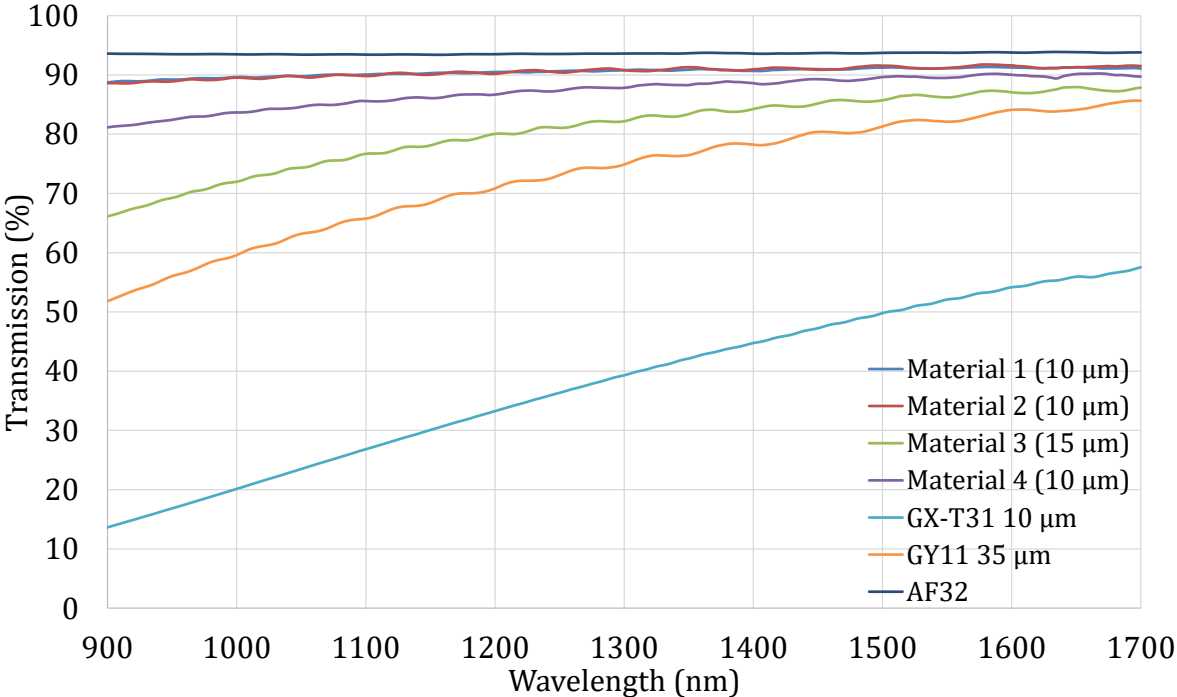


Figure 84: Direct transmission spectrum of a 10 μm thick GX-T31 film (turquoise curve), a 35 μm thick GY11 film (orange curve), the four experimental materials provided by Ajinomoto (purple, green, red and blue curves) with respective thickness of 10 μm, 15 μm, 10 μm and 10 μm, and the 500 μm thick AF32 substrate only (dark blue curve)

The analysis of these measurements indicates that the transmission of GX-T31 and GY11 around 1300 nm, 40 % and 75 % respectively, are relatively low when compared to the 94 % transmission of a glass panel alone, especially for GX-T31. It denotes, either some light absorption or light scattering due to inhomogeneities or a combination of both. To pursue the analysis deeper, we measured the direct and total transmissions of GX-T31 and GY11 for two different dry film thicknesses: 10 μm and 20 μm for GX-T31, and 35 μm and 70 μm for GY11. These additional results, presented in Figure 86, show a distinctive difference between total and direct transmission for both GX-T31 (40 % and 50 % for 10 μm and 20 μm respectively) and GY11 (10 % and 50 % for 35 μm and 70 μm respectively). We can observe that these materials suffer from strong light scattering, presumably due to their composition, which include silica nanoparticles.

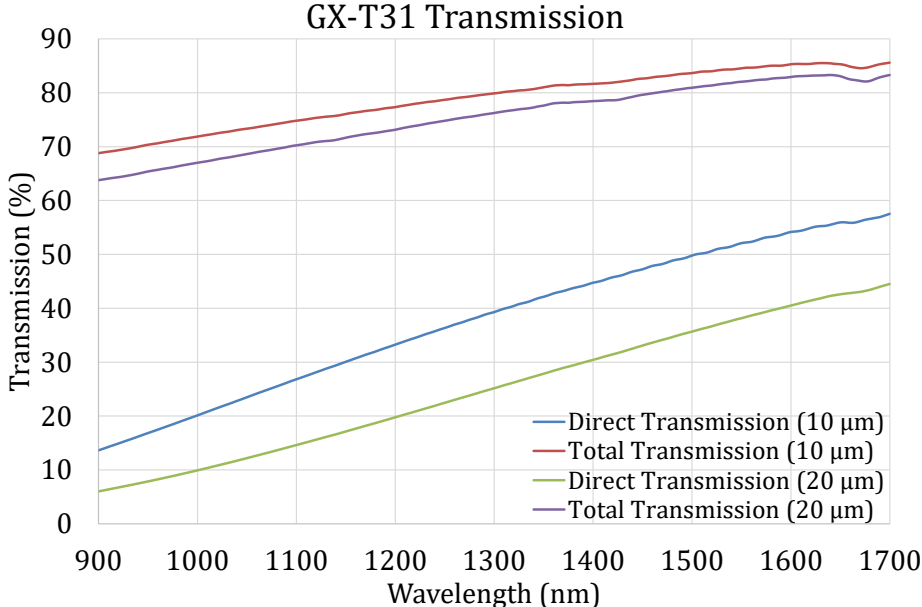


Figure 85: GX-T31 direct and total transmission spectra of 10 μm (blue curve direct transmission, red curve total transmission) and 20 μm (green curve direct transmission, purple curve total transmission) thick films

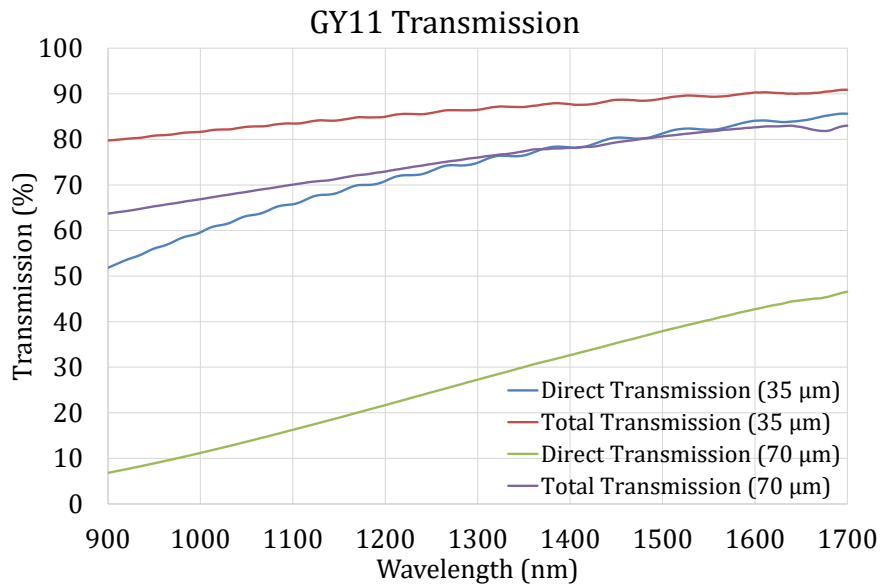


Figure 86: GY11 direct and total transmission spectra of 35 μm (blue curve direct transmission, red curve total transmission) and 70 μm (green curve direct transmission, purple curve total transmission) thick films

Moreover, there is a noticeable difference between the transmission of two different thicknesses of a same material. Thus, we expect the waveguides fabricated with these materials to have excessive propagation losses due to material composition, even for the sake of a feasibility demonstration. Nevertheless, other materials provided by AFT, such as material 1, exhibit far better total and direct transmissions (over 90 % at 1300 nm) and no noticeable difference between two thicknesses above 1400 nm, as it can be observed in Figure 87.

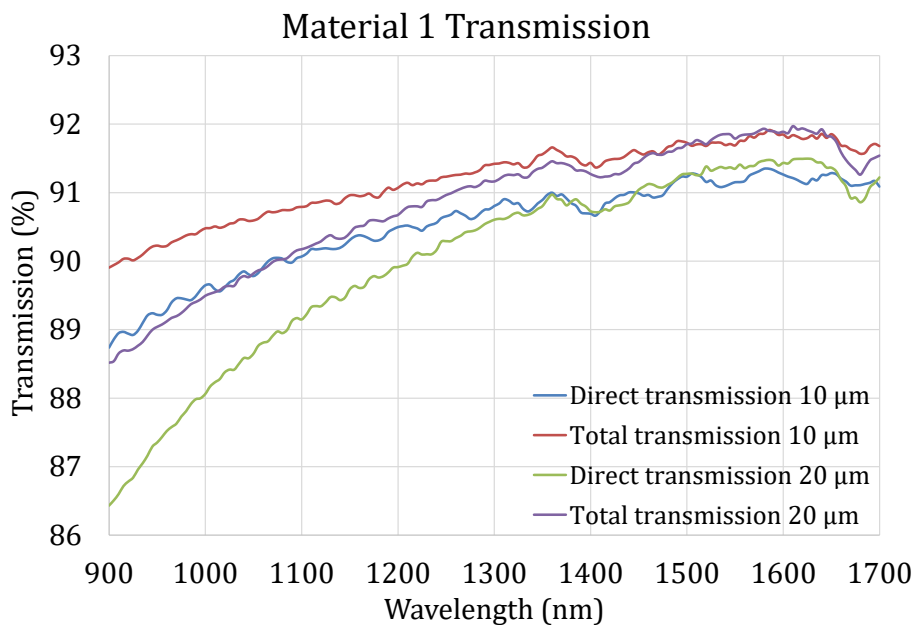


Figure 87: Material n°1 direct and total transmission spectra of 10 μm (blue curve direct transmission, red curve total transmission) and 20 μm (green curve direct transmission, purple curve total transmission) thick films

1.3.4 Laser trenches

In this section, we deal with the structuration of the waveguide core by femtosecond laser ablation using these materials. The objective was to obtain a 30 μm wide trench through the dry film layers with a high precision, a low roughness and no deformation due to heating effects. A first layer of GY11 was laminated on a 500 μm thick glass panel at 120°C and under a 12 kg static load. Then a layer of GX-T31 was laminated on top of the GY11 layer using the same parameters. Trenches were inscribed in one pass using the 343 nm wavelength, a pulse repetition frequency of 100 kHz and optical power lowering using several attenuators comprising a half waveplate and a polarizer. This yielded average optical powers of 156, 191, 226 and 261 mW at a frequency of 200 kHz. The sample was subsequently cleaved and the cross-section observed using SEM imaging. Figure 88 shows the pictures of the cross-section for each optical power. All conditions of optical power resulted in the ablation the dry films. The trenches show fine and deep cut in the layers but also deformations of the sides at the top. This effect amplifies with the increase of optical power.

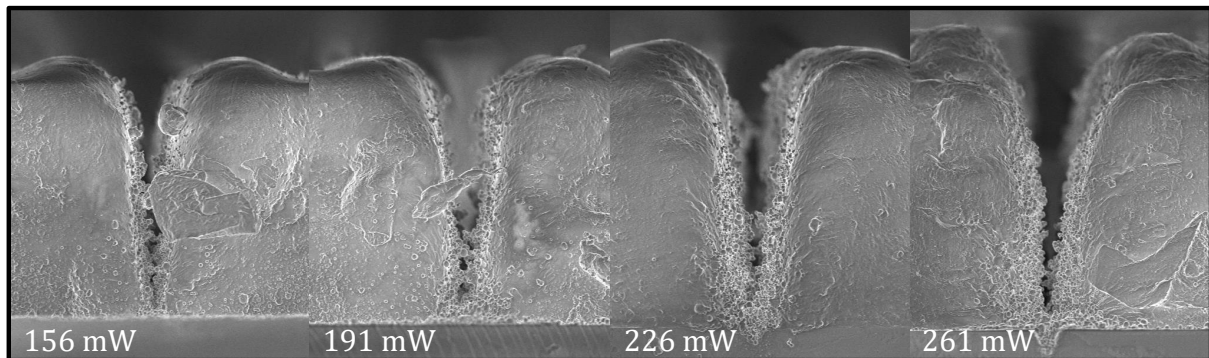


Figure 88: Cross-section of one pass laser trenches at 78, 96, 113 and 131 mW of average optical powers, at a pulse repetition frequency of 100 kHz and a scanning speed of 20 mm/s

In a second experiment, the layout of the trenches was modified and now consisted in 5 parallel laser paths separated by a pitch of 7.5 μm . We also tested a new set of laser parameters, not only based on the power modulation by attenuation, but also relying on a varying scanning speed and on the distance between two consecutive laser shots referred to as shot step defined the ratio between the scanning speed and pulse repetition rate. Table 10 summarizes all the parameters used in this design of experiment. The rest of the process was identical.

Table 10: Second set of laser parameters

Trench n°	Average power at 200 kHz (mW)	Number of pass	Shot step (nm)	Scanning speed (mm/s)
1	70	1	100	4
2	70	1	100	20
3	70	1	300	4
4	70	1	300	20
5	70	5	100	4
6	70	5	100	20
7	70	5	300	4
8	70	5	300	20
9	100	1	100	4
10	100	1	100	20
11	100	1	300	4
12	100	1	300	20
13	100	5	100	4
14	100	5	100	20
15	100	5	300	4
16	100	5	300	20

Among these operating conditions, the best result was obtained for 5 passes, a 300 nm shot step and a scanning speed of 4 mm/s, which corresponds to the lowest test frequency (13 kHz), regardless of the optical attenuation. The trenches cross-section, shown in Figure 89, feature a width of 30 μm at the top, well-defined sidewalls with a roughness comparable to that of the pristine material and no noticeable heating effect. Due to the gaussian shape of the laser beam, the trenches are slightly slanted. We measured sidewalls angles θ_{sw} of 80° and 70° relative to the glass surface for powers of 100 mW and 70 mW, respectively.

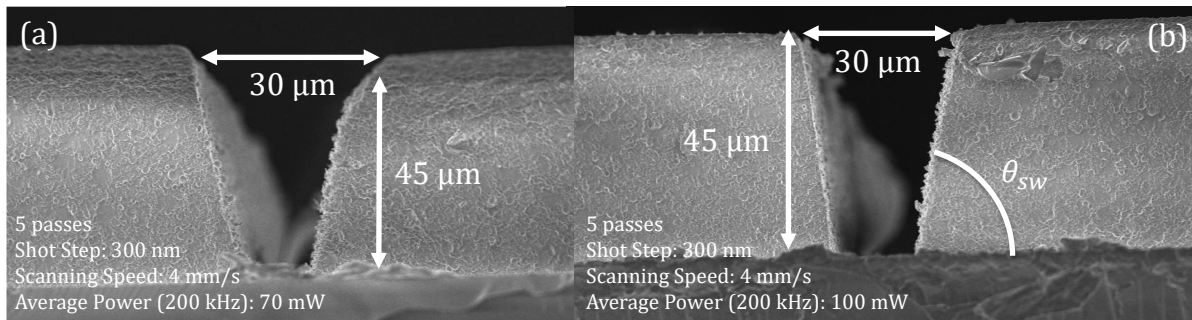


Figure 89: SEM cross-section of two 30 μm · 45 μm laser ablated trenches with optical powers of (a) 70 and (b) 100 mW at 200 kHz and respective sidewalls angle of 70° and 80°

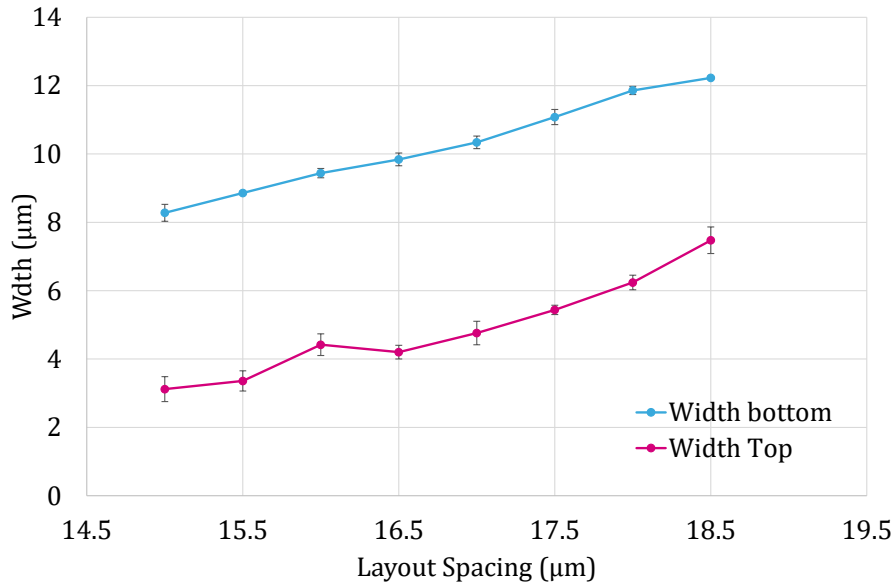


Figure 90: Width at the top and at the bottom of the core structure versus layout spacing between trenches

Keeping these parameters, we made a last iteration of this process with two trenches close to each other with a varying distance between them. The *layout spacing* is the distance between the two closest laser paths in the layout. For this experiment, we used two of the new experimental materials provided by AFT, both being 10 μm thick. The layout spacing was varied from 15 μm to 18.5 μm by steps of 0.5 μm. The width at the top and the bottom of the fabricated core structure were measured on SEM pictures. The results are reported in Figure 91. The core structure has a trapezoidal shape that is 10 μm thick with a width ranging from 2.9 μm to 7.5 μm at the top and from 8.3 μm to 12.2 μm at the bottom as shown in Figure 91 (c).

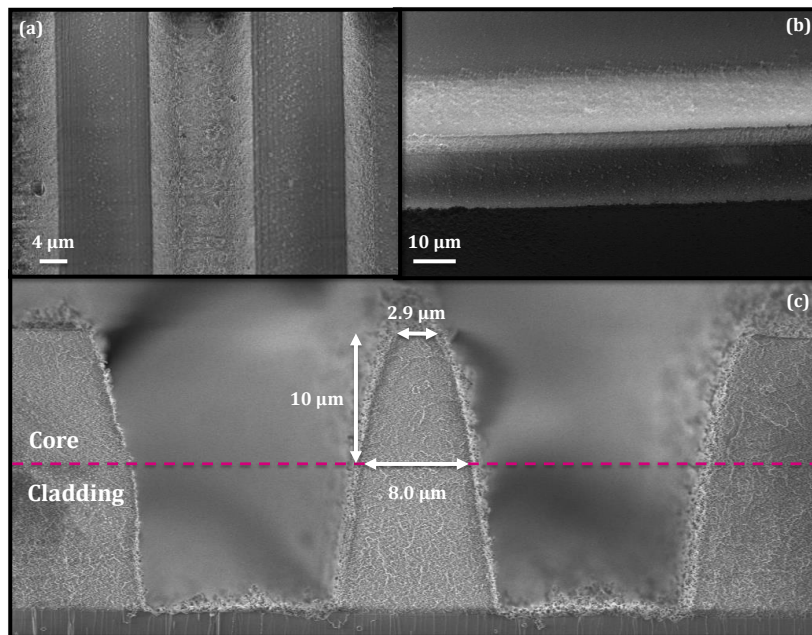


Figure 91: SEM picture of (a) the top view, (b) the angled view and (c) the cross-section of the fabricated structure

Top, perspective angled and cross-section views are given in Figure 91. We can observe that, despite the trapezoidal shape, lateral dimensions compatible with a single mode operation of waveguides are achievable with a good reproducibility. The vertical dimension is set by the thickness of the dry film provided by AFT. Since we did not measure the refractive indices of the experimental materials, we did not pursue the process to the end with these materials.

1.3.5 Rib waveguides with photosensitive resins

The last method we investigated for the fabrication of the waveguides of the interposer relied on the femtosecond laser of Micro Resist photosensitive resins used in section 1.2. The fabrication process is a modified combination using resists previously used in laser lithography and the laser ablation strategy tested on AFB dry films.

Firstly, the waveguide bottom cladding is spin-coated on a clean wafer, prebaked, exposed over the entire area and cured. Before applying the same set of steps to the core layer, the wafer surface is cleaned by O₂ plasma. Trenches are subsequently ablated with different laser parameters, starting with those defined in section 1.3.4, with the objective of reducing the time needed for structuring waveguides over an entire wafer and obtain single mode waveguides. The tested configurations are reported in Table 11 below. An isopropanol ultrasonic bath, as well as O₂ plasma were used to clear the sample from debris resulting from laser ablation. Finally, the top cladding deposited, exposed and cured.

Table 11: Summary of the materials and laser parameters tested for the fabrication of laser ablated rib waveguides

Wafer	W1	W2	W3	W4	W5
Core material	Epocore 5	Epocore 5 XP	Epocore 5	Epocore 5 XP	Epocore 5 XP
Repetition rate (kHz)	40	40-8-4-2	8	8	8
Scanning speed (mm/s)	20	20-4-2-1	4	4	4
Power @200 kHz (mW)	110	110	110	110	120
Spacing (μm)	17-18-19	20-21-22-23-24	17-18-19	18	18
Number of passes	1-2-4-6	2	2-3-4-5	2	2

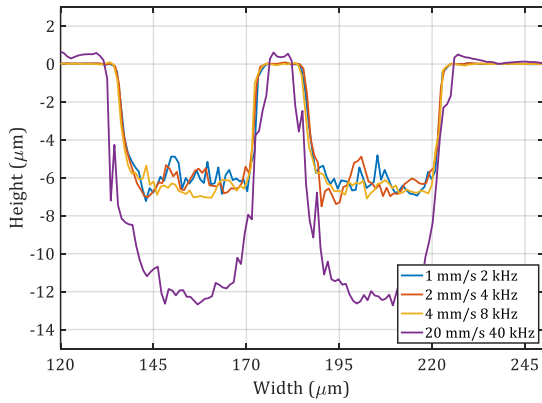


Figure 92: Ablation profile for 1 mm/s, 2 mm/s, 4 mm/s and 20 mm/s at a constant pitch of impact (Wafer $n^{\circ}2$).

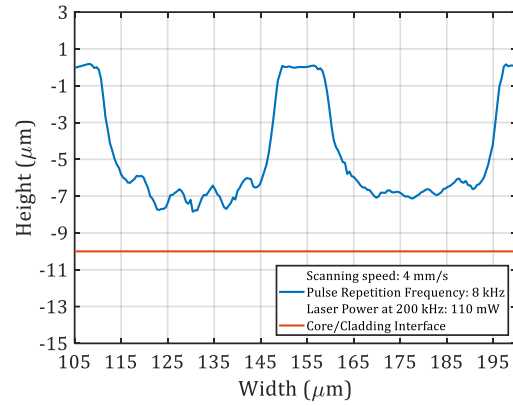


Figure 93: Ablation profile for a scanning speed of 4 mm/s, an 8 kHz pulse repetition frequency and an average power of 110 mW at 200 kHz. The core/bottom cladding interface is represented by the horizontal orange line

To reduce the ablation time, we tried to increase the scanning speed without changing the pitch of impact. This resulted, as depicted in Figure 92, in a deeper ablation depth but a higher roughness and material modification due to heating effects. We also reduced the number of laser passes and this had the effect of reducing the ablation depth while keeping the same ablation quality. As shown in Figure 92 and Figure 93, with only two laser passes, we manage to repeatedly remove between 6 μm and 7 μm of the core material. This gives a structure comparable to the rib waveguides discussed in chapter II section 1.2.2. Therefore, we validated this method to reduce ablation time and quest for obtaining single mode waveguides. To approach single mode operation, we varied the spacing between both trenches and changed the core material. The optical characterizations after the last cladding deposition are presented in chapter IV sections 1.1.1.4 and 1.1.2.4.

1.4 Waveguide technologies comparison

In the previous sections of this chapter we presented the experiments carried-out to fabricate polymer waveguides following four different fabrication methods. Each of them has advantages and drawbacks. We will summarize them in this paragraph and in Table 12 in order to choose one for the fabrication of the demonstrator.

The polymer/glass surface waveguides demonstrated light guidance at 1310 nm (Chapter IV section 1.1.1.2) but exhibited high optical losses (chapter IV section 1.1.2.2) and involve CMP, which prevents panel manufacturing. Moreover, we have not demonstrated the electrical hybridization using this technology.

Polymer waveguides defined by laser lithography presented acceptable optical properties, with respect to our objectives, but presented repeatability and thermal problems (chapter IV sections 1.1.1.3 and 1.1.2.3). In addition to that, this technology is also limited to wafer manufacturing as long as spin-coating is involved.

On the side of dry film waveguides, the processed materials have not permitted to demonstrate light guidance at 1310 nm (section 1.3.3 and chapter IV section 1.1.1.4). However, we were able to process the materials on glass panels.

The last fabrication method, namely femtosecond laser structuration combined with the dedicated optical resins from Micro Resist proved to be the most reliable way to fabricate thermally stable polymer waveguides when compared to laser lithography defined waveguides and polymer/glass surface waveguides. They present acceptable optical properties for the demonstration (chapter IV sections 1.1.1.4 and 1.1.2.4). For these reasons, we retained this last structure and combined it with an electrical redistribution layer (RDL). This hybridization is the subject of the next section. One drawback remains: the necessity to use wafers due to spin-coating.

Table 12: Polymer waveguide technologies comparison

Waveguide technology	Light guidance	Panel manufacturing	Electrical hybridization
Polymer/glass surface waveguides	Yes, High losses	Not possible CMP	Not demonstrated
Laser lithography of photosensitive resists	Yes, Losses ok	Not possible, Spin-coating	Yes, demonstrated Thermal stability issues
Fs laser structuration of polymer dry films	Not demonstrated	Yes	Not demonstrated
Fs laser structuration of photosensitive resists	Yes Losses ok	Not possible, Spin-coating	Yes, demonstrated

2 Electrical-Optical Hybridization

In this section, we detail the fabrication process that we developed in order to combine polymer waveguides on a glass substrate with an electrical RDL, as well as specific structures enabling electrical and optical coupling with a silicon photonic IC.

2.1 Electrical and optical glass interposer fabrication process

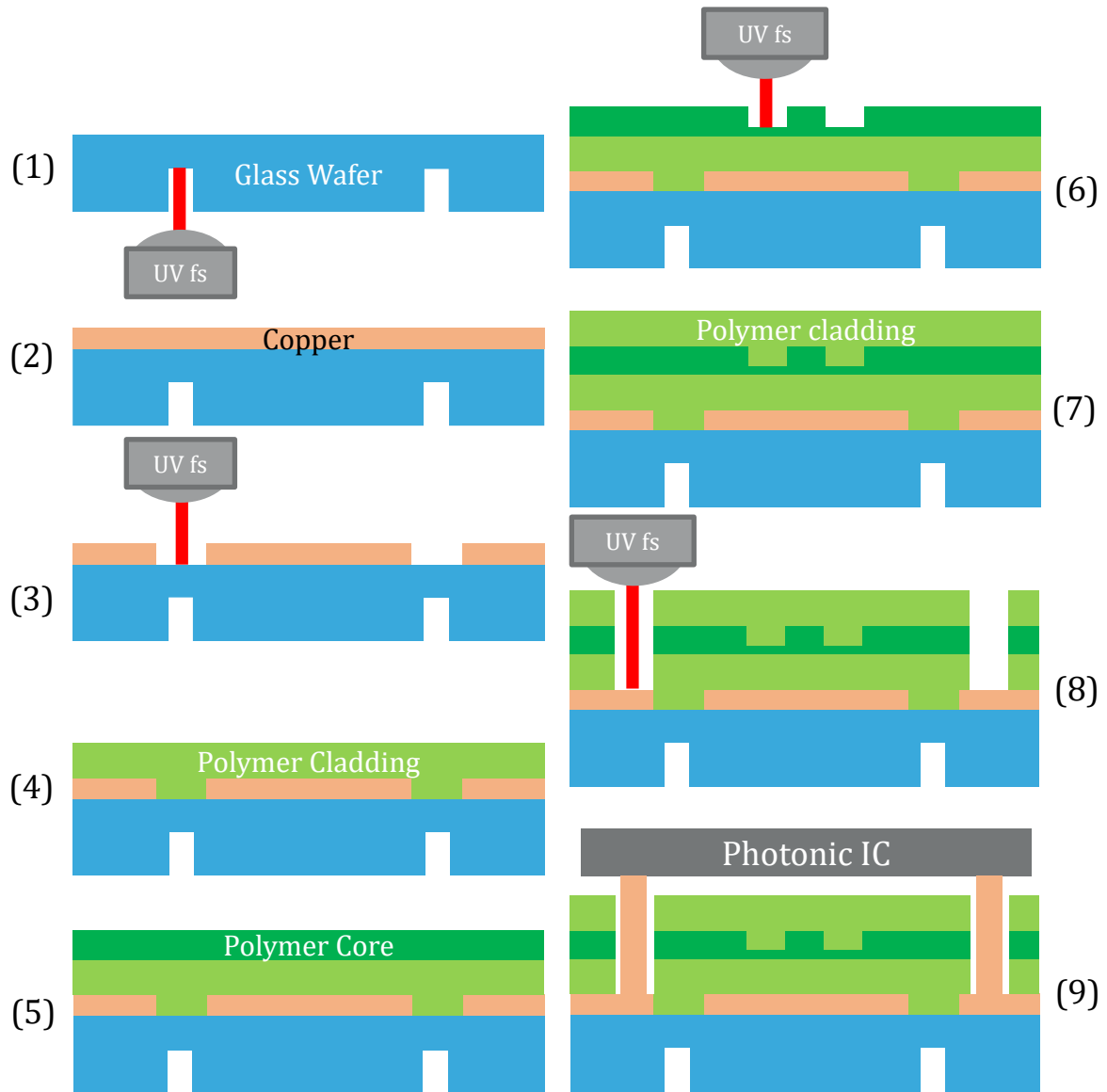


Figure 94: Complete fabrication process of the optical and electrical glass interposer involving the following steps: (1) back-side cleaving trenches ablation, (2) copper sputtering, (3) RDL structuration, (4) first waveguide cladding deposition, (5) waveguide core deposition, (6) rib waveguide structuring by fs laser ablation, (7) second waveguide cladding deposition, (8) contact holes and mirrors ablation, (9) flip-chip bonding

This process involves 9 steps that are represented in Figure 94 and described thereafter:

- Step (1): The ablation of trenches on the back-side of the glass wafer to facilitate the cutting of each chip by cleaving
- Step (2): The deposition of the copper layer. This is achieved by sputtering and is further developed in section 2.2
- Step (3): The copper layer is structured by femtosecond laser ablation to create electrical routing and RF and mmW transmission lines
- Step (4) to (7): the polymer waveguide is fabricated following the process described in section 1.3.5.
- Step (8): The femtosecond laser is used once more to perform a selective ablation of the polymer layer over the copper layer in specific areas and to ablate slanted trenches to shape integrated mirrors. These steps are addressed by section 2.5 and 2.6, respectively.
- Step (9): The PIC25G silicon photonic IC is assembled by flip-chip over the glass substrate. This is the subject of section 3.3.

2.2 Copper deposition

2.2.1 Copper plating of glass substrates

Copper plating of glass wafers and panels is a big challenge to face for the industrialization of glass interposers. Indeed, the CTE mismatch and low adhesion strength between copper and glass can induce delamination. Several methods have been used in the literature to solve this problem. Two of them stand out: sputtering and electroless plating. Both rely on the deposition of a copper seed layer followed by electroplating but the deposition method of the seed layer differs. The first method uses sputtering to cover the glass substrate with decananometric layer of titanium followed by a thicker copper seed layer [112]. The titanium layer acts as a buffer layer to mitigate the CTE mismatch and to improve adhesion. The second method relies on electroless copper plating, also referred as autocatalytic plating, to deposit the seed layer. This is largely preferred to sputtering from an economical point of view. However, seed layers with strong adhesion are more difficult to obtain. Once again, a buffer layer is needed. Such a layer can be coated using a liquid solution deposited by dip-coating, as discussed in [113].

In our case, only the sputtering method was available. Thus, we implemented the seed layer using the first method. Furthermore, we observed, as detailed in the next section, that several micrometers of copper can be sputtered within reasonable processing times (less than one hour). Together with the fact that the resolution of copper wet etching depends on copper thickness and the performance of CPW simulated in chapter II section

2.1.2, we decided to deposit about 3 μm of copper by sputtering only, i.e. without electrolytic plating.

2.2.2 Sputtered thickness calibration

Sputtering consists in removing atoms from a solid source material by exposing it to highly energetic ionized particles [114]. Usually, this is achieved by the ionization of an inert gas, e.g. argon, through the application of a strong electric field, either DC or RF, in an ultra-vacuum chamber under cryogenic pumping (typical pressures of the order of $1 \times 10^{-2} \text{ Pa}$). Sputtering can be used to deposit different materials. In the case of metals, the source material is the cathode material used to apply the electric field. The deposition rate, in nm/min, varies following the electric field intensity, the gas flow and chamber pressure. The thickness of sputter-deposited Cu layers associated to three different sputtering times was performed to determine the deposition rate for both titanium and copper. For the sake of commodity, silicon samples were used for coating with metals and cleaved to measure the metal thickness by SEM cross-sectional analysis.

2.2.2.1 Titanium buffer layer

For the titanium layer, we applied the electric field using a RF generator delivering 250 W and an argon flow of 70 sccm. Samples were coated during 100, 200 and 300 s. The measured thicknesses are presented in Figure 95. We determined an average deposition rate of 11 nm/min and kept 200 s of deposition as a standard parameter for the rest of the process, which results in a 38 nm titanium layer.

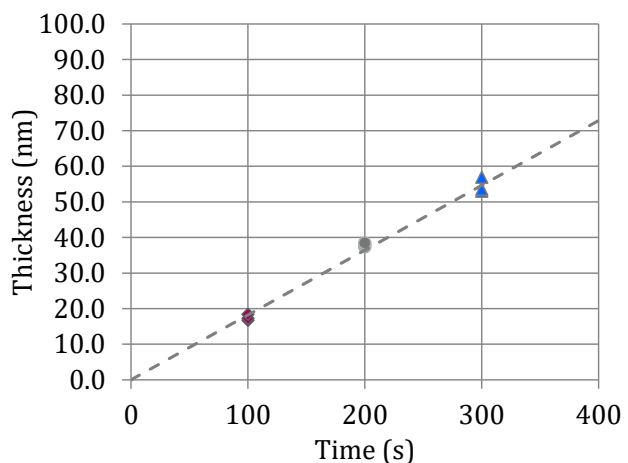


Figure 95: SEM measured thicknesses of Ti coated silicon samples for 100, 200 and 300 s.

2.2.2.2 Copper layer

For copper, we used a DC generator delivering 400 W of average power and an argon flow of 70 sccm. Samples were coated during 100, 200 and 300 s. The SEM pictures of the cross-sections are presented in Figure 96. We can observe that the deposited layers have a columnar structure and identical deposition rates for 100 s and 200 s deposition times, whereas,

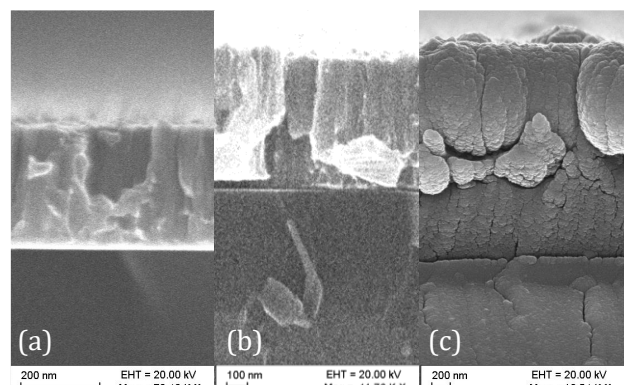


Figure 96: SEM cross-section of the copper coated silicon samples for (a) 100 s, (b) 200 s and (c) 300 s.

for 300 s, the layer shows an agglomerated morphology with cracks that denote high residual stresses [115]. The deposition rate is also higher.

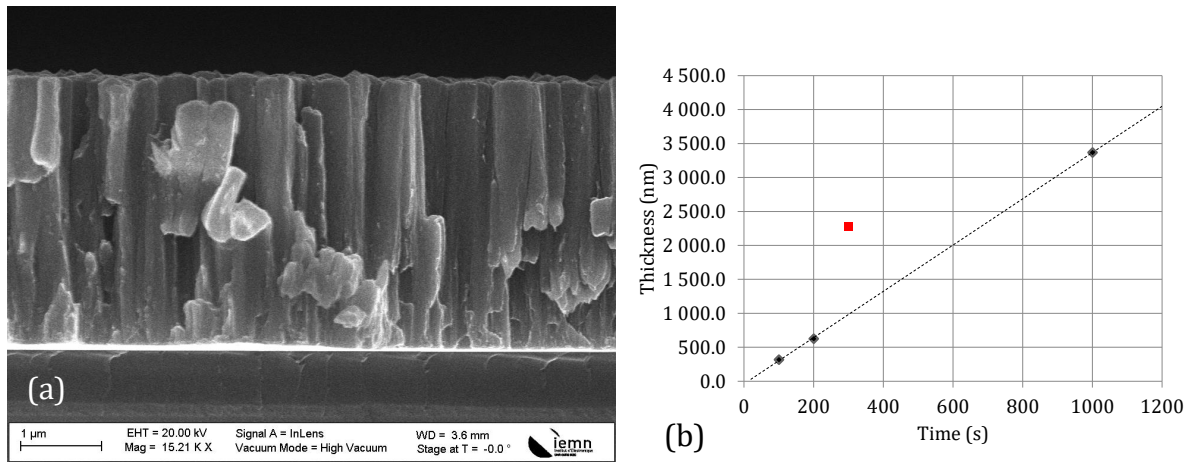


Figure 97: (a) SEM cross-section of the 3.3 μm copper layer obtained performing 5 cycles of deposition during 200s with a 300s pause to avoid sample heating. (b) Thickness versus deposition time for 100 s, 200 s, 300 s and 5 · 200 s durations

To cope with this heating effect, the process is split in five deposition steps of 200 s separated by 300 s cooling steps. This resulted in a 3.3 μm thick copper layer with the same columnar shape and deposition rate as 100 s and 200 s layers. The cross section of the 3.3 μm layer is shown in Figure 97 (a) and the thickness versus deposition time is presented in Figure 97 (b).

The adopted sputtering method consisted in associating a 38 nm thick layer titanium to promote the adhesion of the 3.3 μm thick copper layer.

2.3 Copper structuration

Two methods for structuring the copper RDL of the interposer were investigated: the chemical etching of copper through a mask and the femtosecond laser ablation.

2.3.1 Chemical etching

The structuration of copper traces using photolithography and wet etching, also known as the subtractive method, has been used for a very long time in the industry of printed circuit boards. Given that the electrical and optical interposer demonstrator did not need, a priori, the wiring density enabled by the semi-additive process presented in chapter I section 3.2.1.2, we applied the subtractive method to the copper layer sputtered by following the steps described in Table 13.

Table 13: Tested subtractive process for the glass interposer

Step n°	Step name	Substep n°	Substep name	Substep content
1	Positive tone photoresin deposition Megaposit SPR220	1.1	Spin-coating	Spinning Speed: 2500 rps Acceleration: 1000 rps ² Time: 20 s
		1.2	Prebake	Temperature: 110°C Time: 1min30s
2	Laser Lithography	2.1	UV laser exposure	Power: 20 % Scanning speed: 20mm/s
		2.2	PEB	Temperature: 110°C Time: 1min30s
		2.3	Development	Developer: Microposit MF319 Time: 20s Deionized water rinse
3	Wet chemical etching of copper	3.1	Copper etching	Technietch CR-01 (Chromium etchant) Time: 9 min Agitation Deionized water rinse
		3.2	Titanium etching	Titanium etchant (HNO ₃ + HF + Deionized water) Time: ~5s Deionised water rinse
4	Resin removal	4.1	Flood exposure	Fluence: 10mW/cm ² Time: 30s
		4.2	Development	Developer: Microposit MF319 Time: until wafer optically clean with mild agitation Deionised water rinse

With this process, the fabrication of CPW transmission lines was easily achieved as well as the complete interconnection routing required to connect the PIC25G IC using flip-chip bonding pads. However, the fabricated structures suffered from a strong over-etching below the photomask, as it can be seen in Figure 98. In the case of flip-chip bonding pads, the structure is 20 μm wider at the bottom than at the top. Moreover, the compensation of the width difference at layout level results in thin openings in the resin and to an inhomogeneous etching of copper.

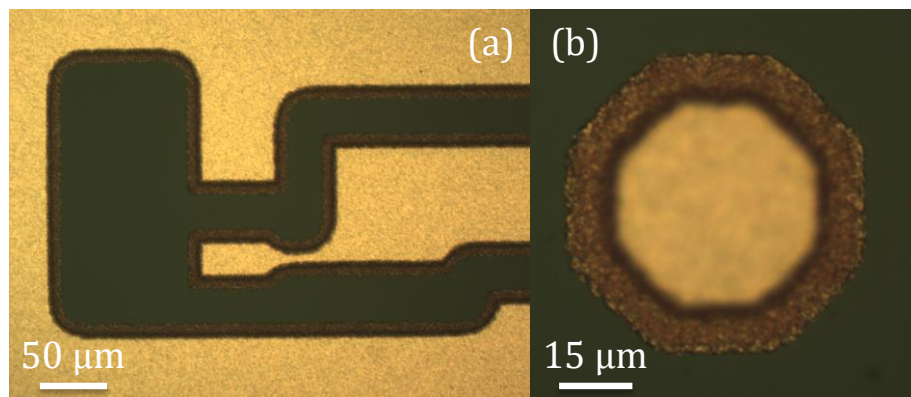


Figure 98: Optical microscope pictures of the fabricated structures: (a) on-wafer RF characterization pads and (b) flip-chip bonding pads

In parallel, we developed a process to selectively ablate copper on the glass substrate which yields better results. It is described in the next section.

2.3.2 Selective femtosecond laser ablation

According to the experiment carried out in [96], the ablation fluence threshold of copper for one 550 fs laser pulse at a wavelength of 800 nm is 0.95 J.cm^{-2} . This is at least 3 times lower than the fluence threshold of all the glasses tested in [97]. This contrast in the threshold fluence of both materials offers a large window to perform a selective ablation. The determination of the laser parameters needed to ablate the $3 \mu\text{m}$ thick copper was carried-out by Kathia Harrouche in her master traineeship and is succinctly presented thereafter. The objective was to find the laser parameters enabling the highest resolution possible at high speed.

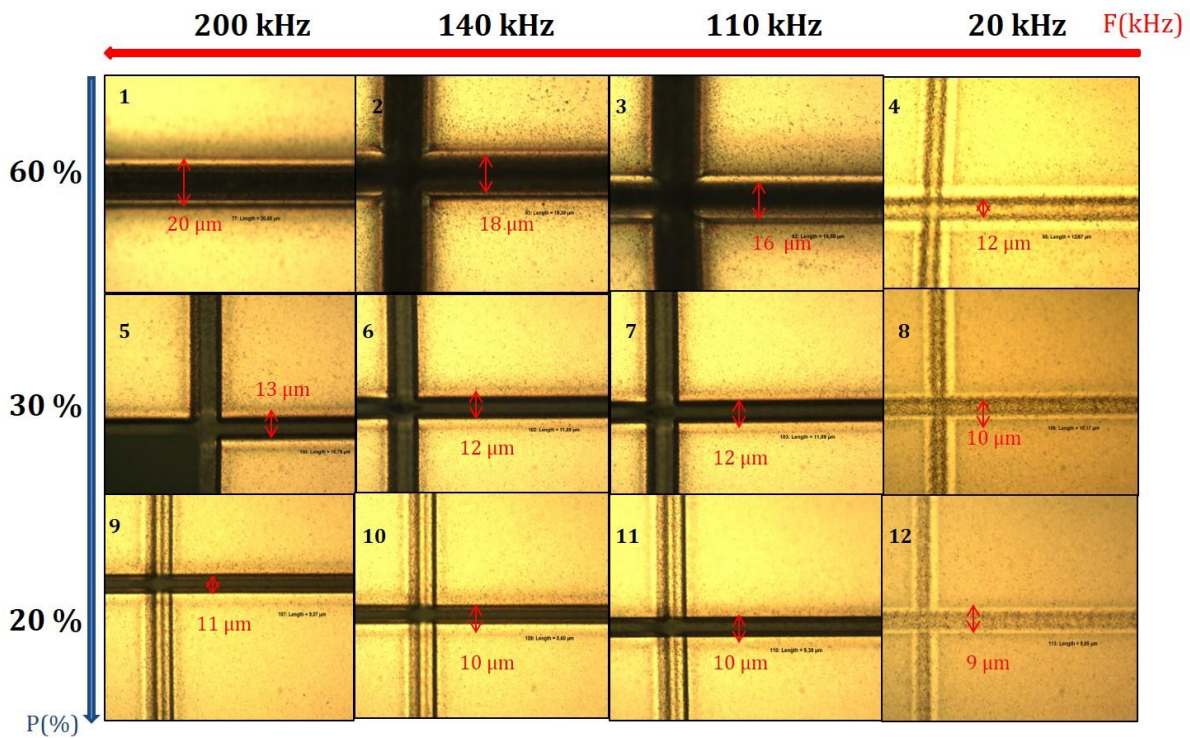


Figure 99: Optical microscope pictures of the grid test structures for laser powers of 20, 30 and 60 % and pulse repetition frequencies of 20, 110, 140 and 200 kHz giving ablation widths ranging from 10 to 20 μm .

Firstly, laser attenuation and pulse repetition frequency were swept across the 20-60 % and 20-200 kHz ranges, respectively, at a scanning speed of 15 mm/s. Test structures were fabricated for each parameter and measured by both optical microscope pictures and optical profilometry. The results are presented in Figure 99. The best results were obtained for the operating condition (110 kHz, 20%) which corresponds to an energy per pulse $E_p = 0.0045 \text{ mJ}$. The ablation is homogeneous, the sidewalls are tapered resulting in a trapezoidal profile, 12 μm wide at the top and 8 μm wide at the bottom for an ablation depth of 3 μm .

Secondly, we designed the electrical redistribution layer of the interposer and its components, namely CPW, DC routing, flip-chip bonding pads, alignment crosses, RF and DC on-wafer characterization pads.

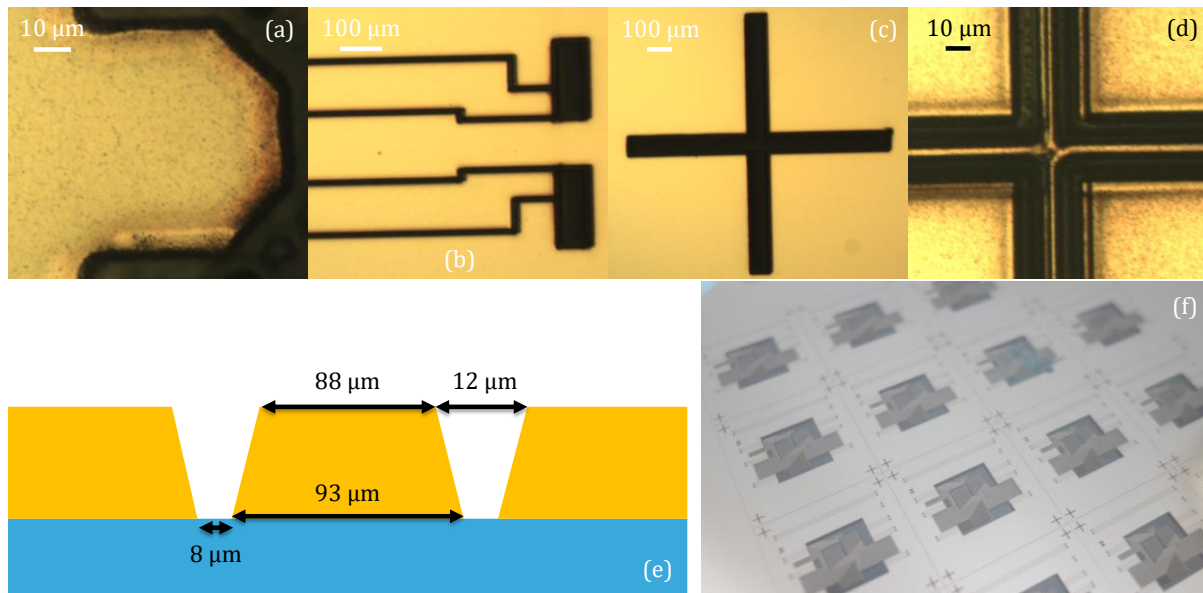


Figure 100: Optical microscope pictures of (a) a flip-chip bonding pad, (b) 2 parallel CPWs and their characterization pads on the right, (c) 100 μm wide alignment cross and (d) 5 μm wide inverted alignment cross. (e) Schematic of the fabricated CPW cross section. (f) macroscopic picture the interposer RDL.

CPWs are fabricated in a single laser pass that delineates them from the ground plane which basically corresponds the rest of the chip. Three different line widths were drawn at the layout level: 100 μm , 75 μm and 30 μm . The fabricated lines exhibit a trapezoidal shape such as the one depicted by Figure 100 (e) with 85, 60 and 10 μm of respective widths at half height. At the place where the PIC25G will be bonded, the DC routing is shaped while the rest of the copper is removed by milling. The flip-chip bonding pads (Figure 100 (a)) are $60 \times 60 \mu\text{m}^2$ octagons connected either at the ground plane, at a CPW for RF functions or at DC traces for the functions of the same type. The purpose of each path is detailed in section 3.2. Finally, two types of alignment crosses are structured, 100 μm wide crosses of $1 \times 1 \text{ mm}^2$ for automatic flip-chip bonding (Figure 100 (c)) and 5 μm wide inverted crosses of $0.5 \times 0.5 \text{ mm}^2$ for manual alignment (Figure 100 (d)). The resolution of femtosecond laser ablation allows a minimum spacing of 12 μm . It is compatible with the fabrication of high frequency CPW, such as those simulated in chapter II section 2.1.2, and also allows enough wiring density to interconnect every functionality of the demonstrator. The next step consists in fabricating the polymer waveguides.

2.4 Laser ablated rib waveguides

The fabrication of the polymer waveguides on top of the metallic layer follows exactly the process described in section 1.3.5. The rib waveguides have been characterized by optical

microscopy (Figure 101) and profilometry before encapsulation. Thanks to the planarization effect of spin coating and the low copper thickness, we did not observe a step in the waveguide height at the interface between copper ground plane areas and copper-free areas. After this step, we have both the electrical and optical functions integrated on the same substrate.

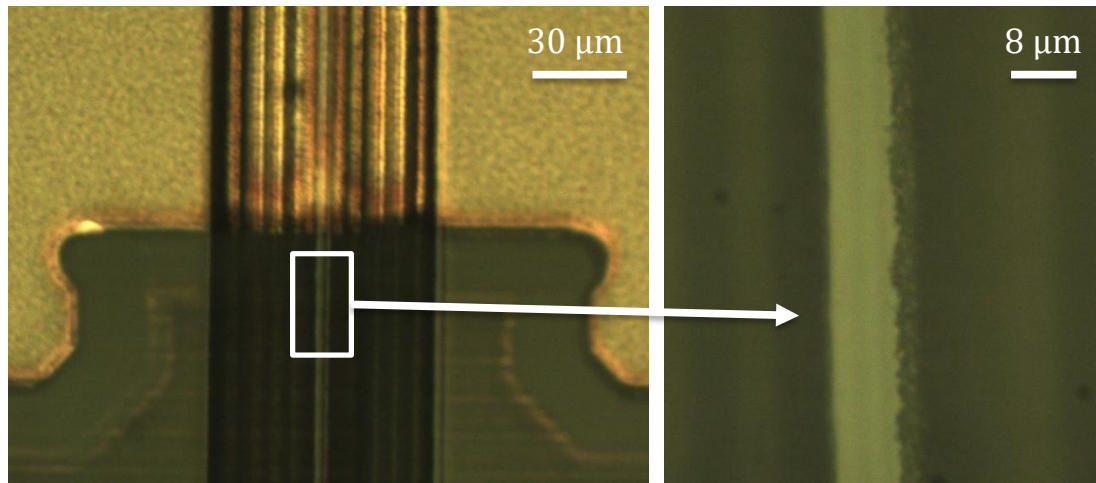


Figure 101: Optical microscope pictures of the polymer rib waveguide on top of the copper layer

2.5 Laser ablation of polymer layers for flip-chip bonding and probing

The next step (step (8)) has a twofold objective. It first consists in selectively ablating the polymer layer over specific areas to accommodate electrical connections as well as ablating slanted trench to enable optical coupling with the photonic IC by redirecting upwards the optical signal carried by the optical waveguides. The first point is detailed in this section while the second will be discussed in section 2.6.

The electrical connections, and thus openings in the polymer layer, are required for both on-wafer tests and flip-chip bonding. The on-wafer tests using DC and RF probes necessitate the removal of large areas whereas connections for flip-chip bonding only require opening of the order of the size of the bonding pads. It is important to notice, as shown in Figure 101, that waveguides travel between the pads and, consequently, that the ablation of the opening may cause damage to the waveguides if it is not carried out carefully. Flip-chip bonding pads openings were obtained by milling 120 μm wide circularly shaped

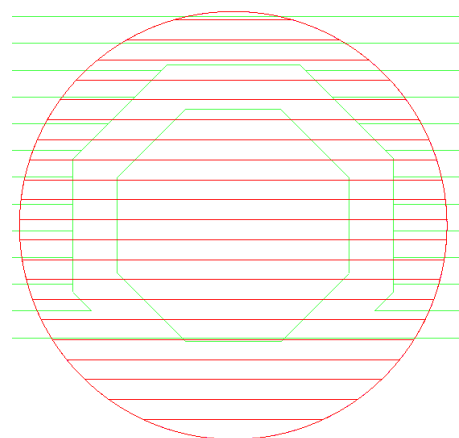


Figure 102: Layout of the laser path for the ablation of flip-chip bonding pads openings (red lines)

surfaces (Figure 102) with the following laser parameters: scanning speed 5 mm/s, laser power 110 mW at 200 kHz, pulse repetition frequency 10 kHz and 8 passes. This produces 97 μm wide openings at the copper level. As it can be observed in Figure 103 (a) and (b), the polymer above and around the pad is removed while the pad itself remains intact. Removing the polymer over large areas of up to $1 \times 5 \text{ mm}^2$ is more time consuming but necessitates less laser passes at higher speed and higher removal rate. In this case, the used parameters are: scanning speed 20 mm/s, laser power 110 mW at 200 kHz, pulse repetition frequency 40 kHz and 7 passes.

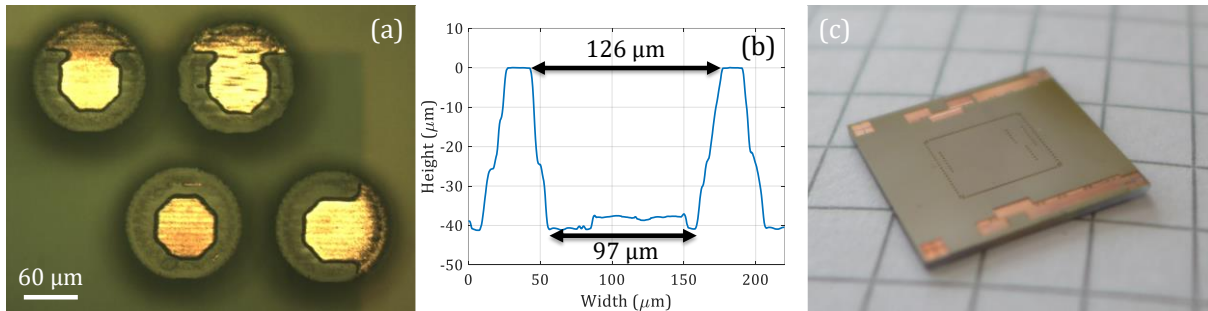


Figure 103: (a) Optical microscope picture of the flip-chip bonding pads openings. (b) Profile of a flip-chip bonding pad opening. (c) Macroscopic picture of a cleaved interposer with openings.

After these two laser ablation steps, the sample is cleaned from debris by an isopropanol ultrasonic bath to ensure a good electrical contact.

2.6 Total Internal Reflection (TIR) mirror

The mirror used to redirect the signal vertically toward the grating coupler of the PIC is based on the total internal reflection (TIR) of the beam. The ablation of this mirror is based on ablation parameters similar to those used previously, but on a sample placed on a slanted holder by an angle θ_h , as depicted in Figure 104. In chapter II section 3.4.1, we determined by simulations that the mirror angle offering the maximum coupling is 40° . We evaluated six sample holders with the following angles: 49° , 51° , 53° , 59° , 60° and 61° .

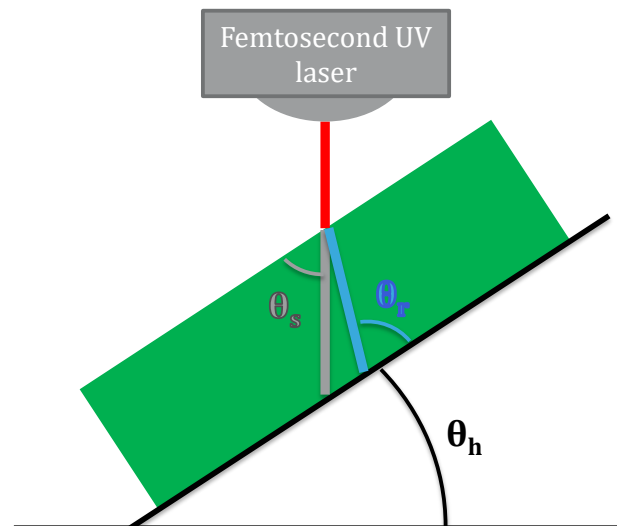


Figure 104: Schematic of the TIR mirror laser ablation setup

The layout determining the laser trajectory is composed of a multipass step involving 5 parallel lines separated by 7 μm . Then the layout is scaled by $\cos(\theta_h)$ to account for the

sample tilt. The laser parameters are: scanning speed 4 mm/s, pulse repetition frequency 8 kHz, 8 laser passes and a laser power of 200 mW at 200 kHz. The power was raised compared to openings made in the previous section since the required ablation depth is larger as well as the laser beam reflection coefficient.

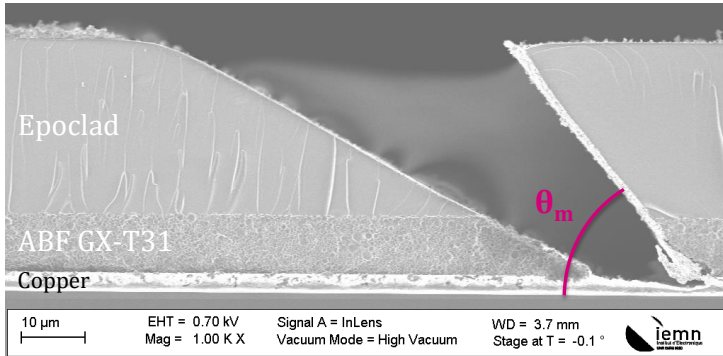


Figure 105: SEM picture of the cleaved edge of a sample in which the TIR mirror is structured. The ABF layer was implemented in the first tests but subsequently removed to reduce the stack height.

Once the laser process is complete, the sample is cleaned by an isopropanol ultrasonic bath, cleaved and the mirror angle θ_m is measured on SEM pictures of the cleaved edge, as depicted in Figure 105. The measured mirror angles as a function of sample holder tilt are shown in Figure 106 and

compared to the theoretical angles θ_r and θ_s , which are respectively the refracted and straight rays displayed in Figure 104.

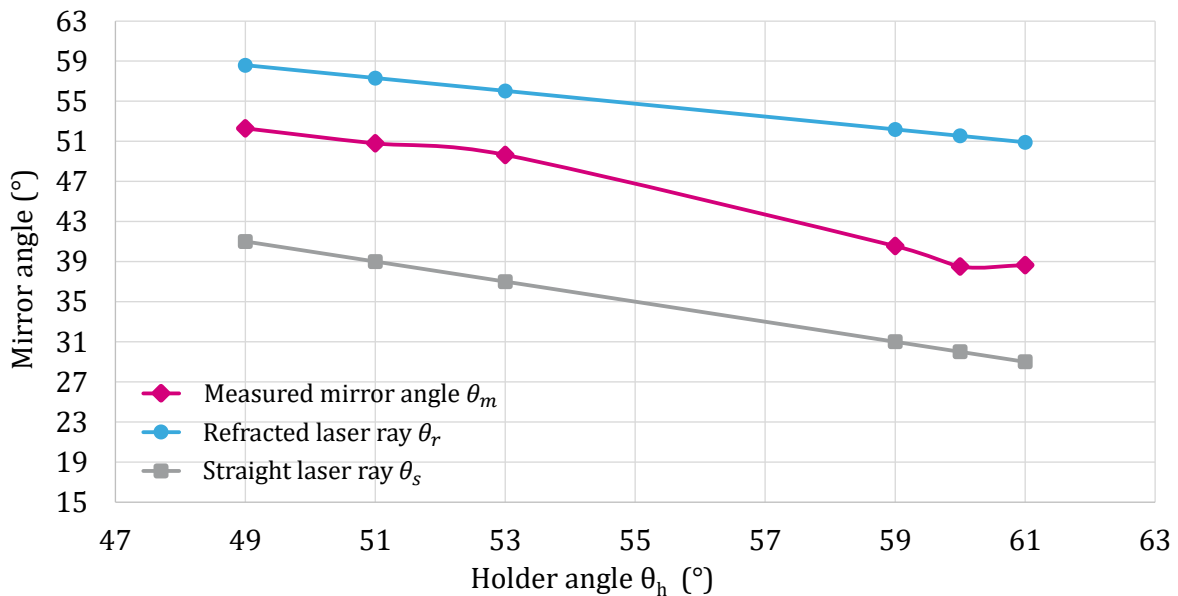


Figure 106: TIR mirror angle versus holder angle compared to a theoretical refracted ray in the polymer layer and a theoretical straight ray

We can observe that the measured mirror angle sits between the refracted and straight angles and that we obtain a 40° mirror angle for a holder angle of 59° . At this point, the last remaining step towards the fabrication of the electrical and optical glass interposer demonstrator is the flip-chip bonding of the PIC25G IC.

3 PIC/Interposer Flip-Chip Assembly and Demonstrator

In this section, details are given on the silicon photonic IC used for the demonstration, its functions and the interposer layout developed to allow the testing of its functionality. Finally, the flip-chip step is presented.

3.1 PIC25G test IC

The PIC25G chip presented in this section has essentially been designed during the PhD work of Folly-Eli Ayi-Yovo [40]. Figure 108 depicts its layout. It is composed of: (1) photodiodes test structures, (2) single mode waveguides connecting one side of the chip (a) to the other (b), (3) more photodiodes test structures, two Mach-Zehnder modulators (6) and (7) and their optical I/O (4), as well as two RF/mmW transmission lines (5).

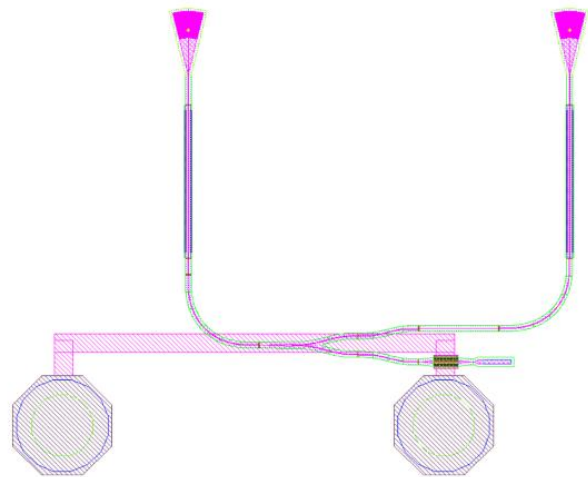


Figure 107: Layout of a single photodiode test structure.

Each of the photodiode test structures involves, an input grating coupler, a Y junction, one branch goes to the photodiode while the other is routed to an output grating coupler, as depicted in Figure 107. Four of them are present on each side of the chip. All of them make use of SPGCs but the peak wavelength of each test structure is different: 1270 nm, 1290 nm, 1310 nm and 1330 nm.

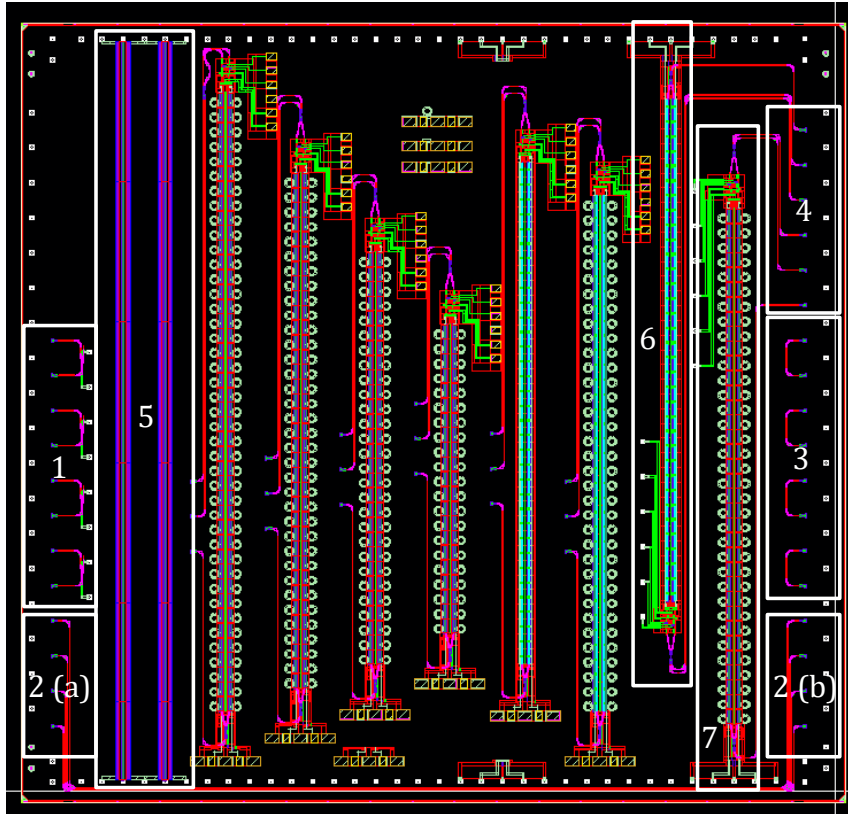


Figure 108: Layout of the PIC25G test chip. It includes: (1) photodiodes test structures, (2) single mode waveguides connecting one side of the chip (a) to the other (b), (3) more photodiodes, two Mach-Zehnder modulators, (6) and (7), and their optical I/O grating couplers (4) as well as two RF/mmW transmission lines (5).

The same single polarization grating coupler (SPGC) peak wavelength specificity applies to the 4 single mode waveguides crossing the chip. The modulators are 3.5 mm long devices such as the one described in chapter II section 2.2.

The transmission lines are 50 Ω , 5.7 μm wide and 5.3 mm long aluminum microstrip lines with a ground plane and sidewalls. The electrical connections of the previously described electrical and electro-optical functions are terminated by 60 \times 60 μm^2 flip-chip bonding pads identical to those of the interposer. A pad ring is also present. This chip was fabricated by STMicroelectronics on a 300 mm multi-project wafer. For the requirements of flip-chip bonding, the dedicated pads received, at foundry level, 30 μm thick copper pillars covered by SnAg soldering balls.

3.2 Interposer layout & alignment strategy

The layout of the interposer directly results from the PIC layout described in the previous section. As mentioned earlier in this chapter, the base substrate of the interposer is a 500 μm thick 3 inches glass wafer. We divided the wafer into 16 interposers delineated by the back-side cleaving grooves. Figure 109 represents macroscopic pictures of the wafers at different fabrication steps, namely, after the RDL structuration (a), after the ablation of

the rib waveguides (b) and after the ablation of the probing and bonding areas in the polymer layer (c).

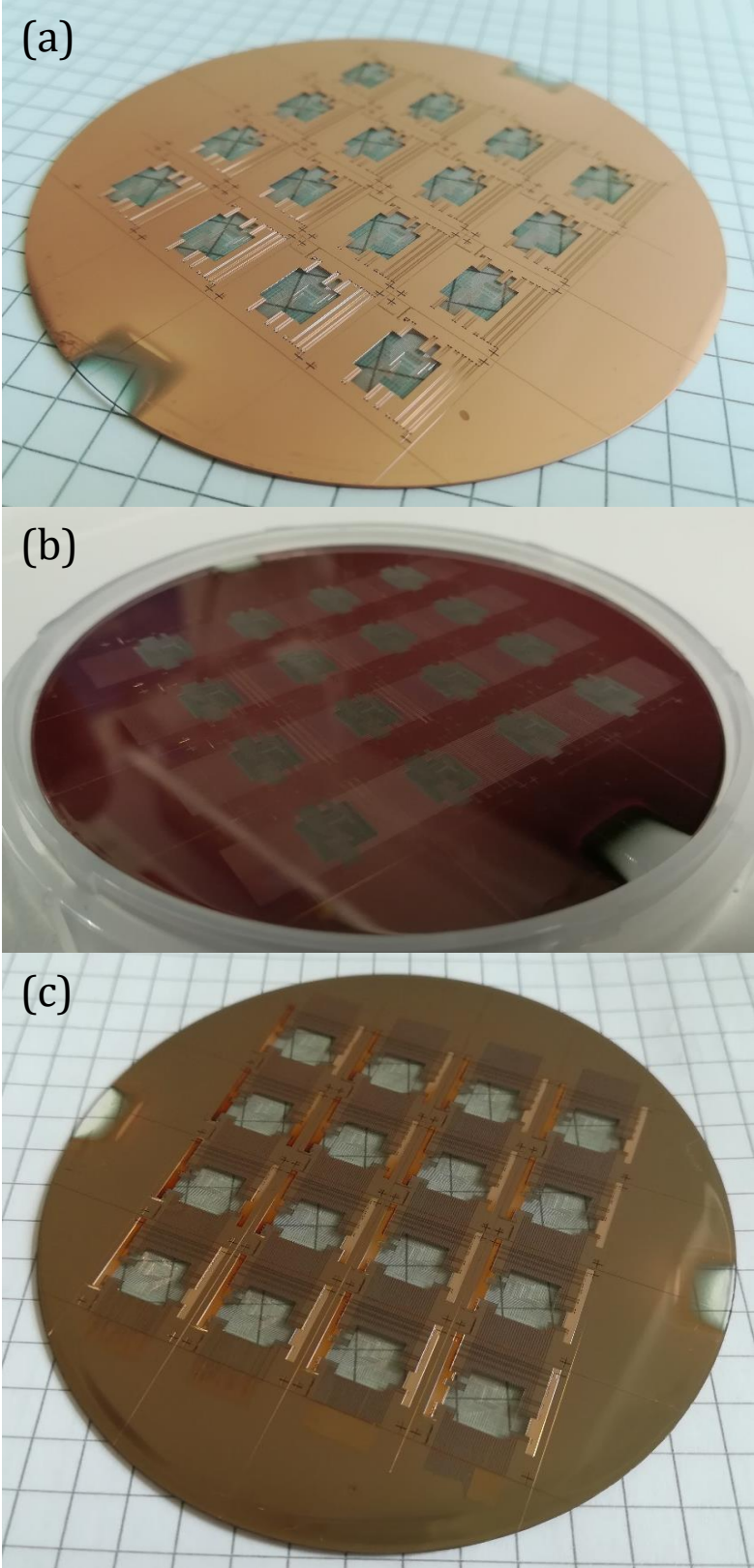


Figure 109: Macroscopic pictures of the wafers at different fabrication steps: after the RDL structuration (a), after the ablation of the rib waveguides (b) and after the ablation of the probing and bonding areas in the polymer layer (c)

We can distinguish 5 different laser masks for the interposer, namely, i) back-side trenches, ii) copper RDL, iii) rib waveguides, iv) surface opening in resist and v) mirror trenches. For the last four, the masks of a single interposer are presented in Figure 110 (the copper RDL, rib waveguides and mirror trenches) and Figure 111 (copper RDL and openings).

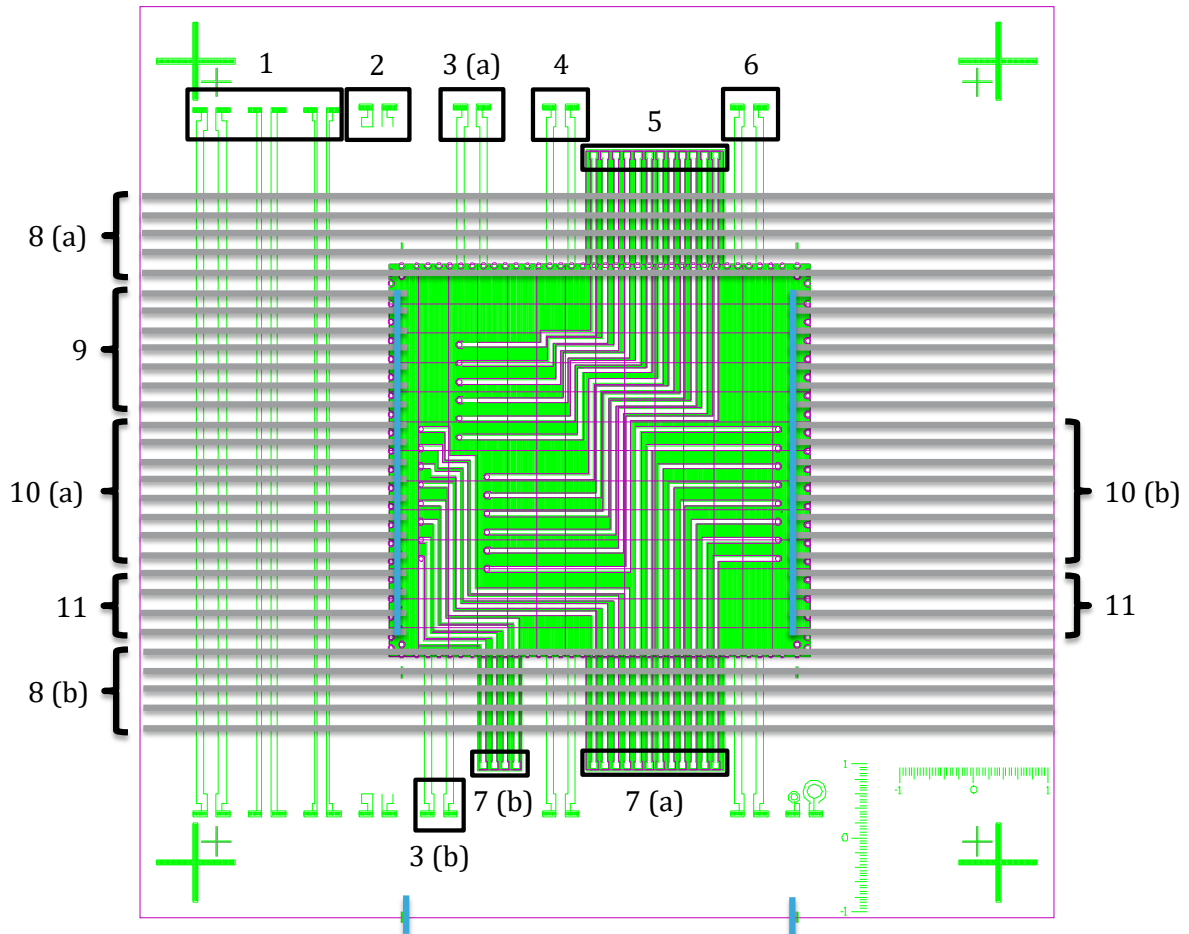


Figure 110: Superimposed layouts of the copper RDL mask (green lines), the rib waveguides (grey lines) and mirror trenches (blue lines)

All electrical functions can be measured using probes placed at the north and south of the chip. The following functions are measurable:

- (1) 6 CPWs with 3 different widths
- (2) open and short deembedding structures
- (3) (a) and (b) the RF paths to HSPMs of the MZMs,
- (4) PIC25G deembedding structures
- (5) DC pads for the PIN phase modulators of both MZM,
- (6) RF paths passing through the SiPh IC
- (7) (a) and (b) DC paths to the anodes and cathodes of the PIC25G photodiodes.

From the optical point of view, we have:

- (8) (a) and (b) 10 straight polymer rib waveguides passing through the interposer,
- (9) optical I/Os of the MZMs,
- (10) Optical I/Os of the photodiodes test structures and
- (11) 4 optical paths through the PIC25G IC.

Each mask has to be precisely aligned with respect to the others. The first one is the back-side trenches mask. It does not implement any specific alignment fiducials because it is the less alignment-sensitive, in terms of impact on the performance of the assembly. Then, the RDL mask is aligned relatively to the back-side trenches using a laser mounted camera. Since the sample is placed manually in the laser equipment at each step, the reference point of the wafer changes as well as the angular position of the wafer. The laser coordinate system is compensated by measuring the angle between a horizontal back-side trench relative to the aforementioned coordinate system horizontal axis. This can be done thanks to a marking on the copper layer on the front side due to the ablation back-side trenches despite the copper layer being sputtered afterward. As discussed in section 2.3.2, this mask embeds crosses dedicated to alignment. All subsequent masks, except the mirrors, are aligned using these crosses as a reference owing to the transparency of the polymer.

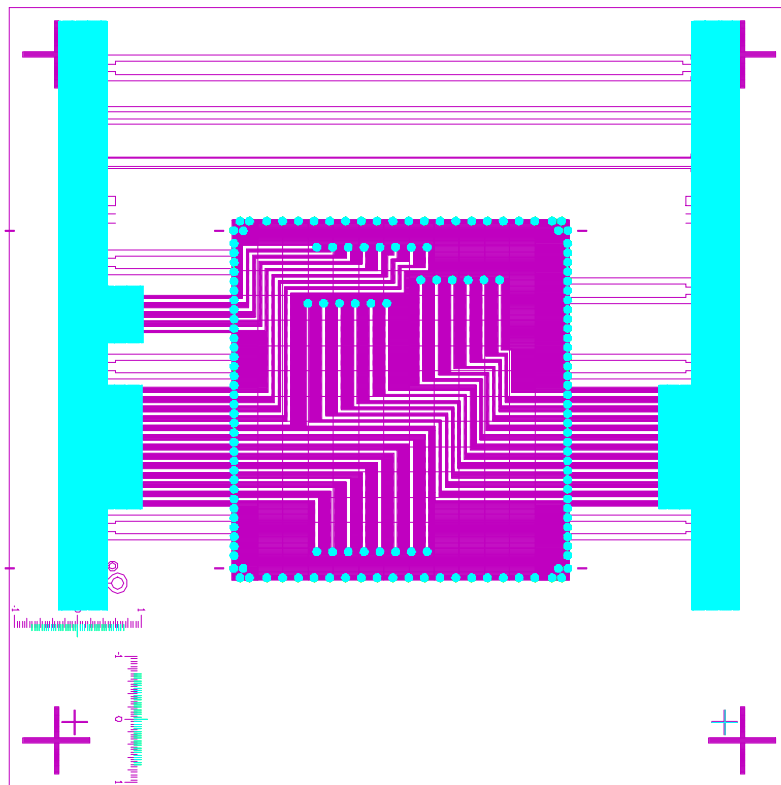


Figure 111: Superimposed layouts of the Copper RDL (purple lines), probing areas and wholes for flip-chip bonding (blue areas)

The mirrors require specific alignment structures placed at the same abscissa. They are formed by two close trenches at each corner of the pad ring, as illustrated in Figure 112.

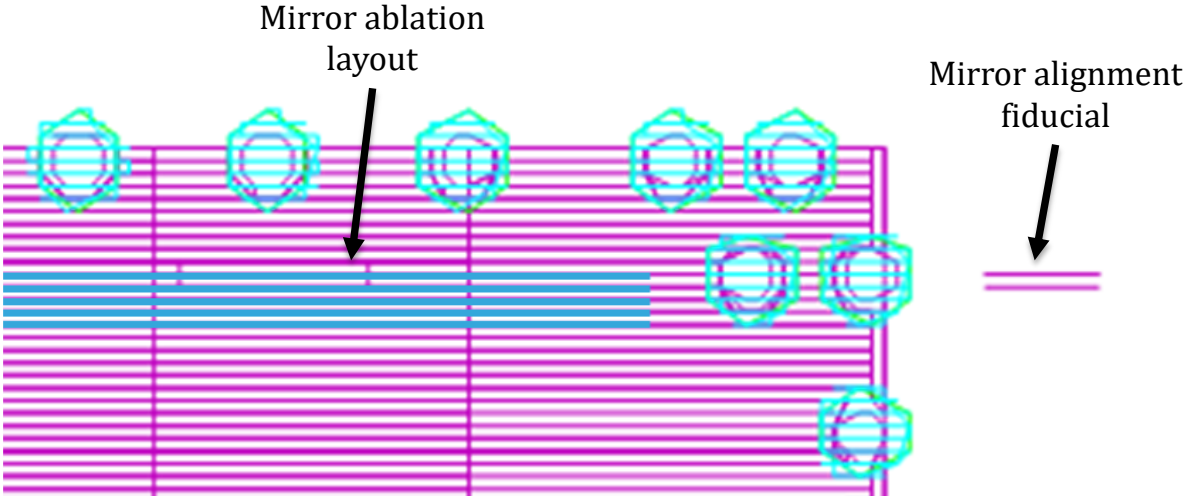


Figure 112: Superimposed layouts of the mirror alignment fiducial and mirrors ablation paths in the top right corner.

Thanks to the femtosecond laser high depth of focus and these fiducials, we can structure the mirrors using the same focus elevation as the one found for the fiducial. This is represented by the schematic in Figure 113. A compensation of rotation is also performed using the right and left alignment structures of each mirror.

Despite this convenience, the alignment of the mirrors remains a tricky operation since each mirror of each interposer involves the manual placement of the chip on the holder. This lack of mechanical stop often results in a height difference between both extremities of the mirror and affects the laser ablation. This ends the fabrication of the interposer that is now ready for assembly.

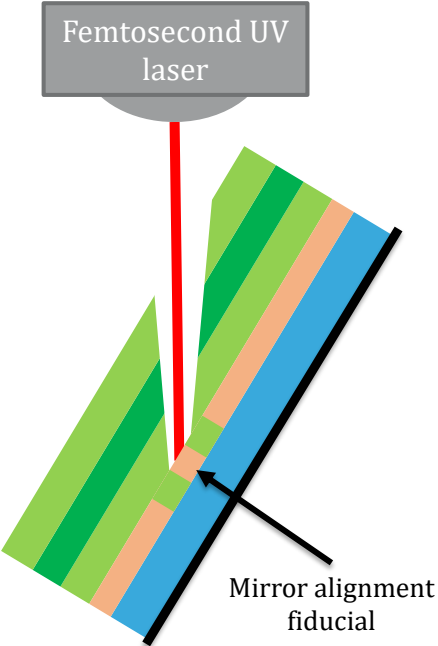


Figure 113: Schematic of the alignment method for the ablation of mirrors

3.3 Flip-chip bonding

The flip-chip bonding of silicon ICs onto interposer and organic substrates is a quite common procedure in the semiconductor industry. This consists in depositing melted soldering balls on the I/O contacts of a silicon IC. The IC is cooled down and flipped on the receiving substrate. The solders balls are melted once again to perform soldering. As explained in section 3.1, the soldering structure deposited on the PIC25G chip is composed of a copper pillar and a SnAg ball. SnAg solder balls exhibit a melting

temperature of 221°C [116]. From this knowledge, we developed the eutectic cycle presented in Figure 114 (a), which involves both temperature rise and compression cycles. However, and unlike a typical process, we placed the upside of the PIC25G chip standing on the hotplate while the interposer is flipped, picked and placed over the SiPh IC, as depicted in Figure 114 (b). This, together with the transparency of glass, allows to directly align both chips using the same top camera. Once the interposer is placed, the vacuum suction of the handling tool is switched off but the tool itself is left in place. The assembly is first heated to 50°C before a pressure corresponding to a static load of 500 g is applied and the assembly is heated to 250°C. Once this temperature is reached, it is maintained for 1 minute before the pressure and placing tool are removed. Finally, the assembly is cooled down to room temperature. The machine used to perform the assembly is the semi-automatic pick-and-place equipment PP7 from JFP Microtechnic.

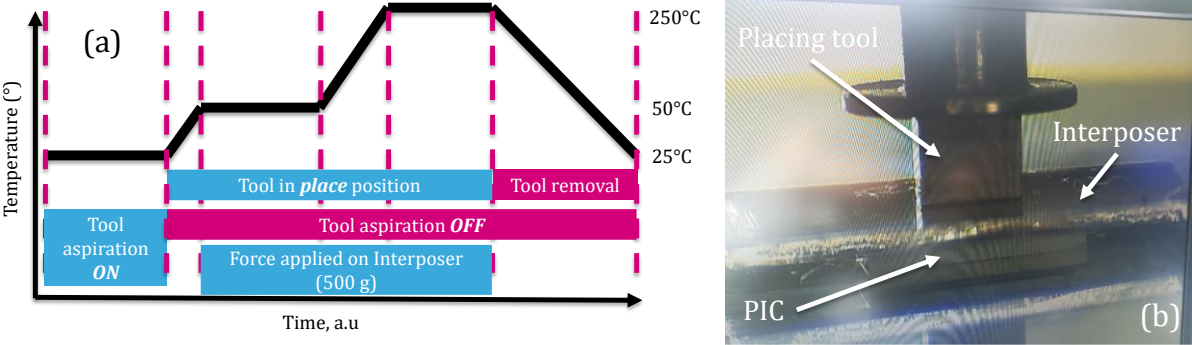


Figure 114: Eutectic cycle of the flip-chip assembly (a) and side camera picture of the interposer and PIC25G IC during assembly (b)

After the bonding, the assembly is observed by optical microscopy through the glass interposer to obtain the pictures of Figure 116. In (a), the focus is adjusted at the surface of the PIC25G chip whereas in (b), it is set at the copper RDL level. From these pictures, we evaluate the misalignment between the pads of both chips to be about 5 μm.

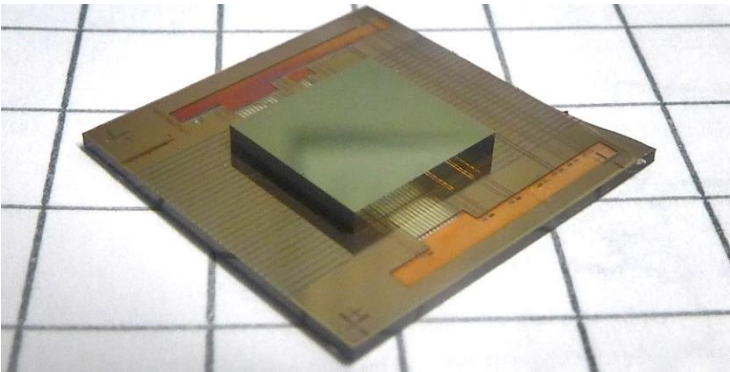


Figure 115: Macroscopic picture of the PIC25G assembled with the electrical and optical glass interposer

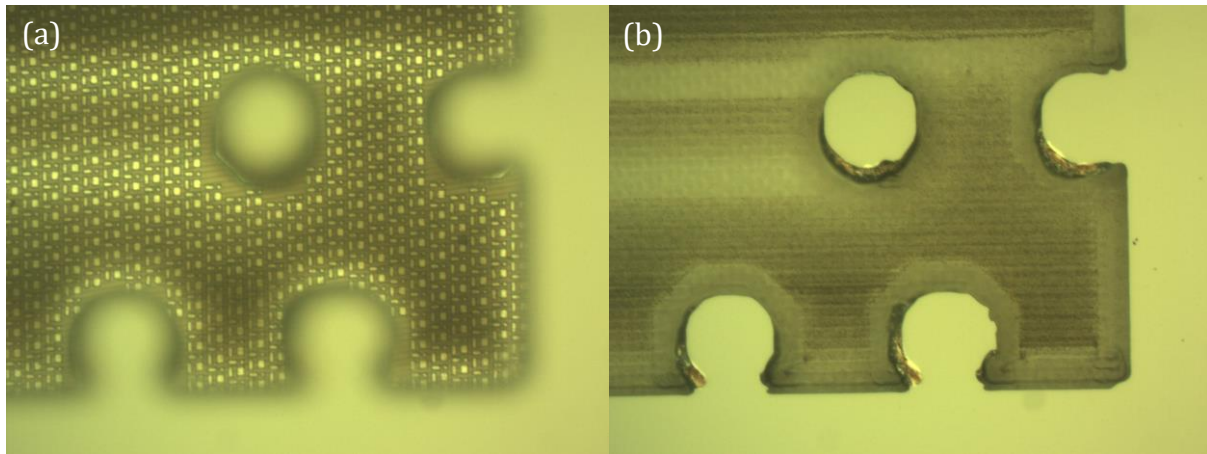


Figure 116: Optical microscope pictures of the back-side of the assembly, focus being done at the SiPh IC surface (a) and the interposer RDL level (b)

4 Conclusion

In this chapter, we have first presented the process development work associated with three different fabrication methods to integrate polymer optical waveguides on a glass interposer: polymer/glass surface waveguides, then laser lithography of photosensitive resists and finally femtosecond laser ablation of both dry films used in the organic substrate industry and photosensitive resists. We have retained the solution based on laser ablation of photosensitive resists for the fabrication of the electrical and optical glass interposer. In a second time, we have developed a fabrication process to combine the aforementioned optical waveguide technology with a RF/mmW copper RDL. This process also involves the fabrication of optical and electrical coupling interfaces. It is worth noting that all structuration steps use the femtosecond laser. In a third and final time, we designed the interposer layout to be assembled with a previously fabricated SiPh test chip from STMicroelectronics PIC25G technology and performed the flip-chip bonding of the latter with the electrical and optical glass interposer.

IV Characterizations

Chapter IV presents the characterizations carried out during and after the fabrication of the interposer. In the first part, we review the optical characterizations of the three polymer waveguide technologies studied in sections 1.1 1.2 1.3 of chapter III, the RF/mmW characterization of the interposer transmission lines (Chapter III section 2.3.2) and the optical characterizations of the total internal reflection mirror (Chapter III section 2.6). The second part is dedicated to the characterizations performed on the assembled demonstrator, namely, the validation of RF/mmW paths and the demonstration of the optical coupling by a characterization involving both the optical path and integrated photodetectors, thanks to the test structures presented in chapter III sections 3.1 and 3.2.

<i>1 INTERPOSER</i>	118
1.1 Polymer waveguides characterization.....	118
1.1.1 Mode profile	118
1.1.1.1 Principle.....	118
1.1.1.2 Polymer/glass surface waveguides	119
1.1.1.3 Waveguides by laser lithography.....	120
1.1.1.4 Waveguides by laser ablation.....	124
1.1.2 Propagation & coupling losses	126
1.1.2.1 Principle.....	126
1.1.2.2 Polymer/glass surface waveguides	127
1.1.2.3 Waveguides by laser lithography.....	128
1.1.2.4 Waveguides by laser ablation.....	128
1.2 RF/mmW characterizations	129
1.2.1 Characterization setup.....	129
1.2.2 CPW measurements and deembedding structures.....	130
1.3 Total internal reflection mirror.....	133
1.3.1 Measurement bench.....	133
1.3.2 Angle measurement.....	134
<i>2 ASSEMBLY</i>	136
2.1 RF/mmW characterizations	136
2.1.1 RF/mmW path	136
2.1.2 Modulators reflection coefficient.....	137
2.2 Optical path characterization.....	139
2.2.1 Mode Profile	139
2.2.2 Losses	140
2.3 Optical coupling measurement through embedded photodetector.....	141
2.3.1 Principle.....	141
2.3.2 Results.....	143
<i>3 CONCLUSION</i>	144

1 Interposer

1.1 Polymer waveguides characterization

In this section, we present the mode profile, wavelength spectrum and loss characterizations performed on the polymer waveguides that we fabricated (chapter III sections 1.1, 1.2, 1.3) with the objective to determine if the waveguides are single mode and their optical loss.

1.1.1 Mode profile

1.1.1.1 Principle

Characterization of the mode profile is one of the first steps to determine if a structure is guiding light and determine the characteristics of the guided modes. As emphasized in chapter II sections 1.2.1 and 1.3.2, we set the goal to obtain a single mode waveguide and showed that its dimension and shape have a direct impact on the coupling efficiency with SMFs. The measurement bench involves (Figure 117): a laser source, a single mode fiber SMF-28 placed in front of a waveguide at the sample edge using a 3-axis micro-positioner. At the output of the waveguide, a microscope objective (typically with a $\times 20$ or $\times 50$ magnification) is placed in front of a camera. Another camera is placed above the sample to ease the alignment of the fiber and the inspection of the sample.

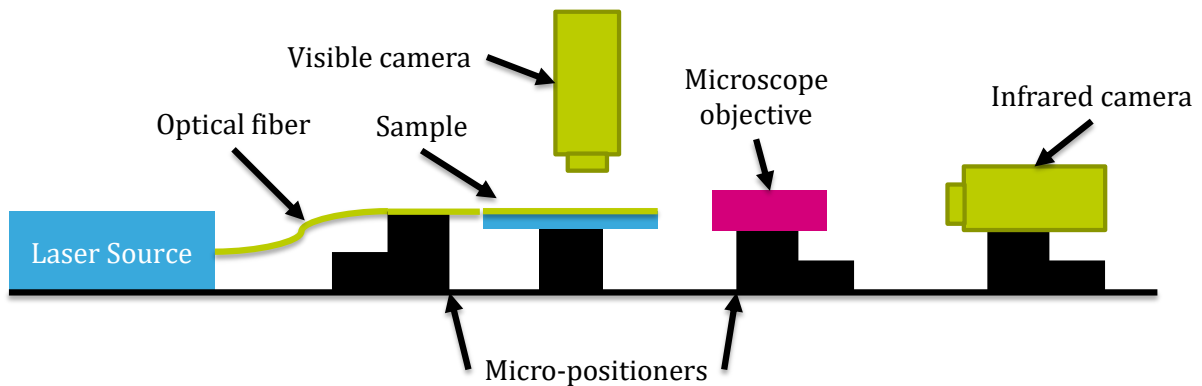


Figure 117: Schematic of the mode profile measurement bench

The in-line camera provides an image of the infrared light at the output facet of the sample, focused by means of the microscope objective. For a multimode waveguide, the image is given by the sum of the light carried by the guided modes at the waveguide output. The waveguide in this situation supports several guided modes, whose excitation depends on the position of the optical fiber with respect to the sample. Indeed, as we change the position of the fiber, the coupling efficiencies between the fiber mode and the waveguides modes vary. As a consequence, the optical power coupled to each mode changes and so is the distribution of light intensity at the waveguide output. In the case of

a single mode waveguide, the light intensity varies but its overall distribution remains insensitive to the fiber position, since it is set by the fundamental mode and the fiber mode/waveguide mode coupling efficiency. This major difference helps determining whether the waveguide is multimode or single mode. In the following paragraphs, we discuss results obtained with surface waveguides made with the polymer/glass process discussed in chapter III section 1.1, waveguides obtained by means of laser lithography, as discussed in paragraph 1.2 of chapter III and laser-ablated waveguides, as discussed in paragraph 1.3 of the same chapter.

1.1.1.2 Polymer/glass surface waveguides

The polymer/glass surface waveguides (chapter III section 1.1) were characterized first. In order to facilitate the alignment and determine the location of defects in the waveguide, the first acquisitions were made using a visible source, operating at a wavelength of 630 nm.

Figure 118, shows the top view of the sample during the mode profile characterization of a waveguide in the visible spectrum. The injection fiber is placed on the left side of the picture. We can observe two bright spots. The leftmost, at the edge of the sample, is characteristic of a reflection at the waveguide input due to the scattering associated to the facet. The second one, just to the right, denotes a second discontinuity. We observed it on several

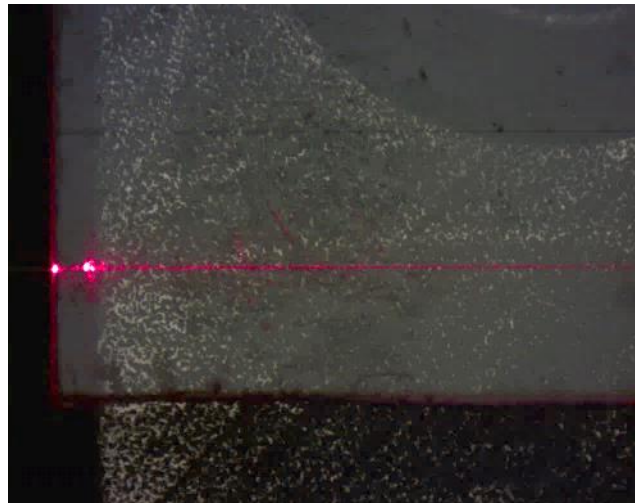


Figure 118: Picture taken from the top camera during the mode profile measurement of a waveguide at 630 nm

waveguides at similar locations. Possible causes maybe related to the cleaving of the sample. The ablation of cleaving trenches with the femtosecond laser on the back-side of the sample, as described in chapter III section 1.2 or the cleaving itself may have deteriorated the waveguide. After these bright spots, we can see that scattered light decreases in intensity as long as the signal propagates in the waveguide. This is characteristic of the waveguide roughness, affecting the visible light propagation much more than in the infrared range.

Then, the mode profiles were characterized at 1550 nm and 1310 nm, using the in-line infrared camera. The pictures of Figure 119 were obtained.

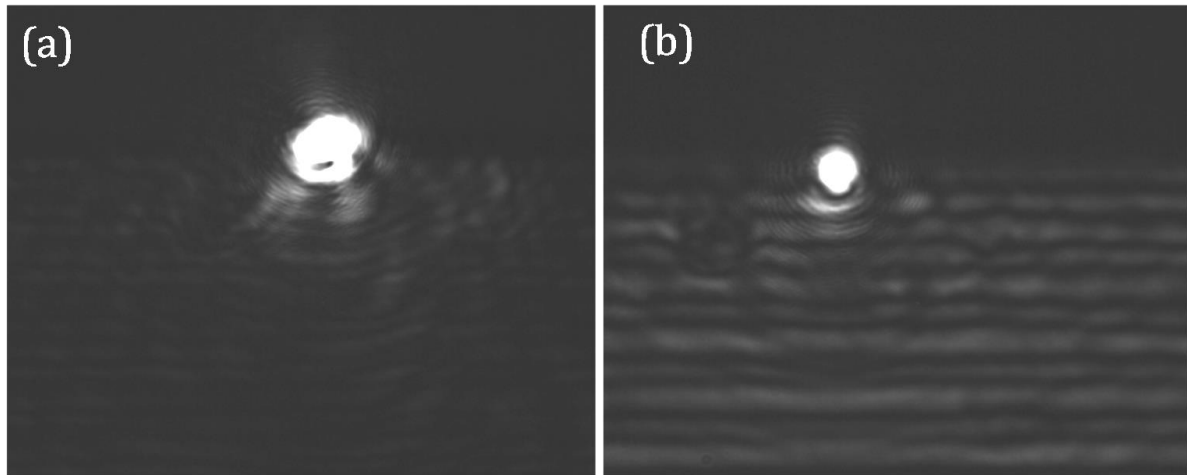




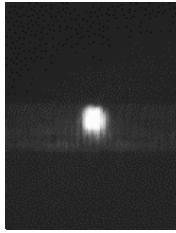
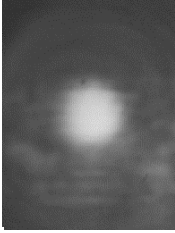
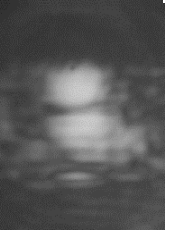
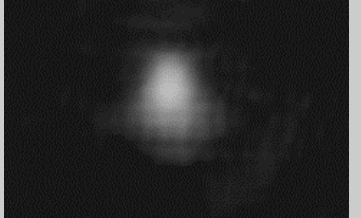
Figure 119: Mode profiles of a polymer/glass waveguide at (a) 1310 nm and (b) 1550 nm

On these pictures, it can be observed that light is guided through the waveguide. When moving the injection fiber, the shape of the output profile changes, demonstrating that the waveguides are multimode at both wavelengths. As explained in chapter III section 1.1.3, we expected that the refractive index difference between the polymer and the glass together with the core dimension would lead to multimode waveguides.

1.1.1.3 Waveguides by laser lithography

Following waveguide theory and simulations discussed in the paragraph 1 of chapter II, we set the objective to obtain a waveguide with cross-section dimensions of $7 \mu\text{m} \times 7 \mu\text{m}$ and a refractive index $\Delta n = 4 \cdot 10^{-3}$.

Table 14: Relevant waveguides configurations and mode profiles

Core material	Focus Height (mm) Laser Power (%)	Width · Height (μm^2)	Mode Profile (650 nm)	Mode Profile (1310nm)	N°
Epocore 5 XP $\Delta n = 4 \cdot 10^{-3}$	10 mm 100 %	8.9×8.9		No observable mode profile	1
	0 mm 50 %	5.3×8.1	No observable mode profile	No observable mode profile	2
Epocore 5 $\Delta n = 1 \cdot 10^{-2}$	15 mm 100 %	6.7×4.8		No observable mode profile	3
	10 mm 100 %	8.7×10.0		 	4
	10 mm 75 %	7.9×7.0	Not measured		5

Therefore, we tried to fabricate waveguides of these dimension using MicroResist photosensitive resins. The most relevant waveguide configurations measured are compiled in Table 14. We achieved the fabrication of $8.9 \times 8.9 \mu\text{m}^2$ waveguides using Epocore 5 XP via the process described in chapter III section 1.2. However, we did not observe any mode profile at 1310 nm. The characterization of the waveguide at 650 nm showed a mode profile (Configuration n°1). Having measured the waveguides dimensions beforehand, we supposed that the refractive index difference was lower than expected. We therefore changed the core resin for a higher refractive index Epocore 5 and progressively refined the laser parameters to obtain a single mode waveguide. As shown in Table 14, configuration n°3, waveguides with a thickness of $4.8 \mu\text{m}$ do not guide light

at 1310 nm. Thicker waveguides of 10 μm clearly show a multimode behavior when the injection fiber is moved vertically. In configuration n°4, two pictures of the same waveguide were shot at 1310 nm and two different output profiles are observable. In between, we characterized a 7 μm thick and 7.9 μm wide waveguide (configuration n°5) that did not show modifications of the mode profile following a displacement of the injection fiber. Yet, the mode profile is neither circular nor elliptical, which differs from eigenmode simulations performed in chapter II section 1.2.3. It is possible that this modal shape results from the trapezoidal shape of the waveguide but also from an unanticipated distribution of the refractive index that does not match the physical shape of the core.

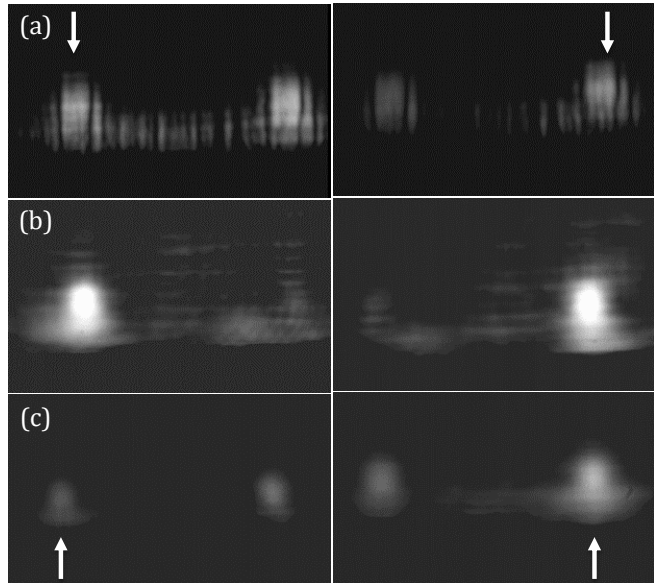


Figure 120: Mode profiles of directional couplers with coupling lengths of (a) 2 mm, (b) 3 mm and (c) 4 mm. White arrows point the waveguides where light is injected.

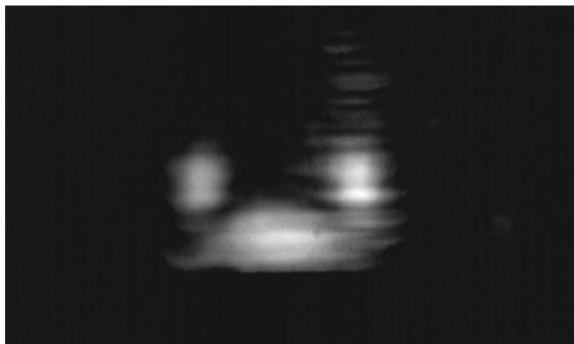


Figure 121: Mode profile of a Y junction

Aside straight waveguides, we characterized the other optical components, described in section 1.2.4 of chapter III, embedded in the test sample of configuration n°5, namely the directional couplers and Y junctions described in chapter III section 1.2.4. Figure 120, shows the mode profiles of the directional couplers at 1310 nm with light injected to the right input (right picture) and the left input (left picture) for (a), (b) and (c). We can observe the profiles of both waveguides of each coupler but also light between them. A similar phenomenon appears for the Y-junction. The mode profile presented in Figure 121 shows the two output waveguides profiles as well as stray light in the bottom central area.

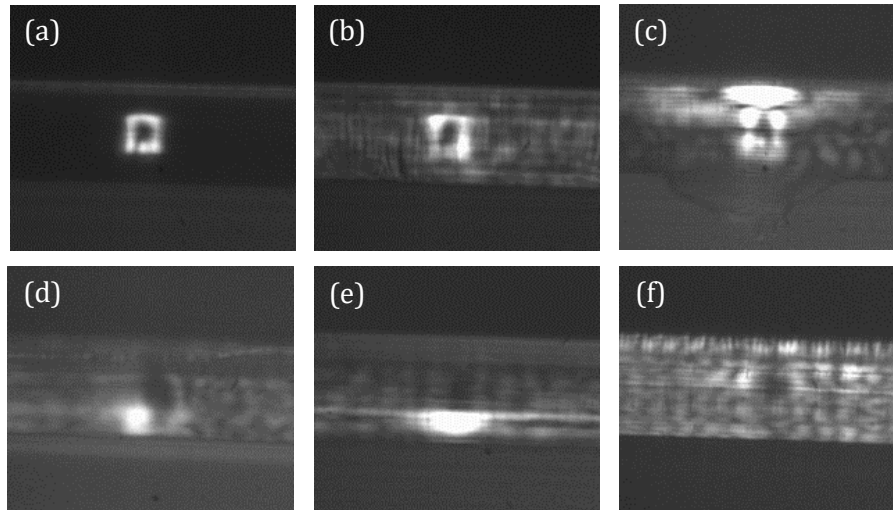


Figure 122: Examples of typical laser lithography waveguides defects. Epocore 5 waveguide mode profiles at 658 nm (a) after 120°C 10 min final post exposure bake (PEB), (b) after 140°C 30 min hard bake and (c) after 250°C 5 min flip-chip simulation. Waveguides presenting defects with the following process specificities: (d) uncovered core exposed to a 140°C 60 min hard bake and 250°C 5 min final hard bake, 120°C 5 min final PEB (e) before and (f) after 250 °C min flip- chip simulation.

Despite the first encouraging results, we faced reproducibility and thermal stability issues. As depicted in Figure 122, we observed several defects using the 658 nm laser source. In the case of the mode profiles (a), (b) and (c) from the same waveguide after different consecutive baking steps at the end of the process, we observe a dark area in the central part of the waveguide in the first measurement. It persists until the last baking step at 250°C where we notice a displacement of the guided light to the upper part of the resin layers. (d), (e) and (f) are three different waveguides mode profiles at 658 nm associated to different baking steps. We observe the same dark area and light is guided in the lower part of the resin for waveguides (d) and (e), whereas only stray light is observable for waveguide (f).

Two possible causes, among others, for these defects and thermal instability may be related to the photolithographic exposure by means of a continuous UV laser. Epocore resists are effective for broadband and i-line exposure, i.e. a 365 nm wavelength, while the UV laser wavelength that we used is 375 nm. The spectral purity of the laser associated to the low absorption of the resin, in addition to the need to obtain large waveguides compared to the laser spot diameter ($\approx 1 \mu\text{m}$), result in the use of high optical energies compared to the recommended values. On one hand, the waveguide may not be sufficiently cross-linked, yielding a lower than expected refractive index contrast despite good results from a dimensional point of view. On the other hand, the high laser power may heat the material and modify its chemical, mechanical and optical properties, namely thermal stability and refractive index. These assumptions may be validated or

unvalidated by the use of a conventional lithographic mask and i-line light source, however we could not carry out these in the time allotted.

1.1.1.4 Waveguides by laser ablation

As detailed in chapter III section 1.3, we studied the fabrication of waveguides by femtosecond laser ablation of both dry films from Ajinomoto and photosensitive resins from MicroResist. Despite not bringing the process to its end with the first materials because of their transmission issue (q.v. chapter III section 1.3.4), we performed mode profile characterizations of the fabricated core structure, with air being used as top and side cladding material. In Figure 123 (a), the 1550 nm laser source allowed to see a confinement of light in the core structure as well as in the rest of the core material. However, we could not confine light inside the core layer using the 1310 nm laser source, as observed in Figure 123 (b)

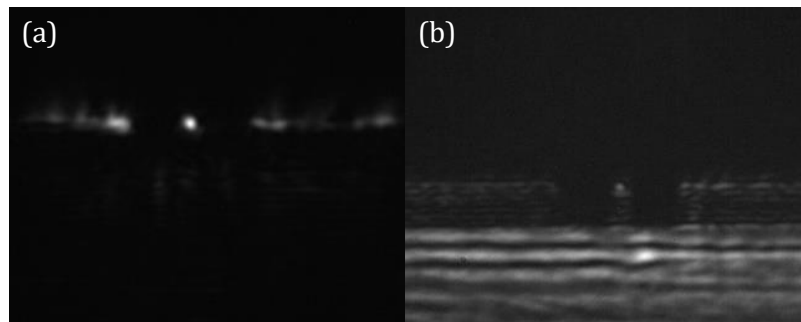


Figure 123: Mode profiles of the core structure fabricated by the laser ablation of two trenches inside Ajinomoto dry films at (a) 1550 nm and (b) 1310 nm

Laser ablated waveguides based on Epocore and Epoclad resins, on their side, demonstrated mode profiles at 1310 nm. Figure 124 illustrates three mode profiles recorded for the configurations tested during the development of these waveguide. The acquired profiles were shot using a 1310 nm laser with a relatively high optical power first (left picture), then reducing the optical power (right picture), to avoid camera saturation. These waveguides were structured with a laser power attenuation equivalent to an optical power of 110 mW at 200 kHz. The other fabrication parameters are recalled in the right part of the figure.

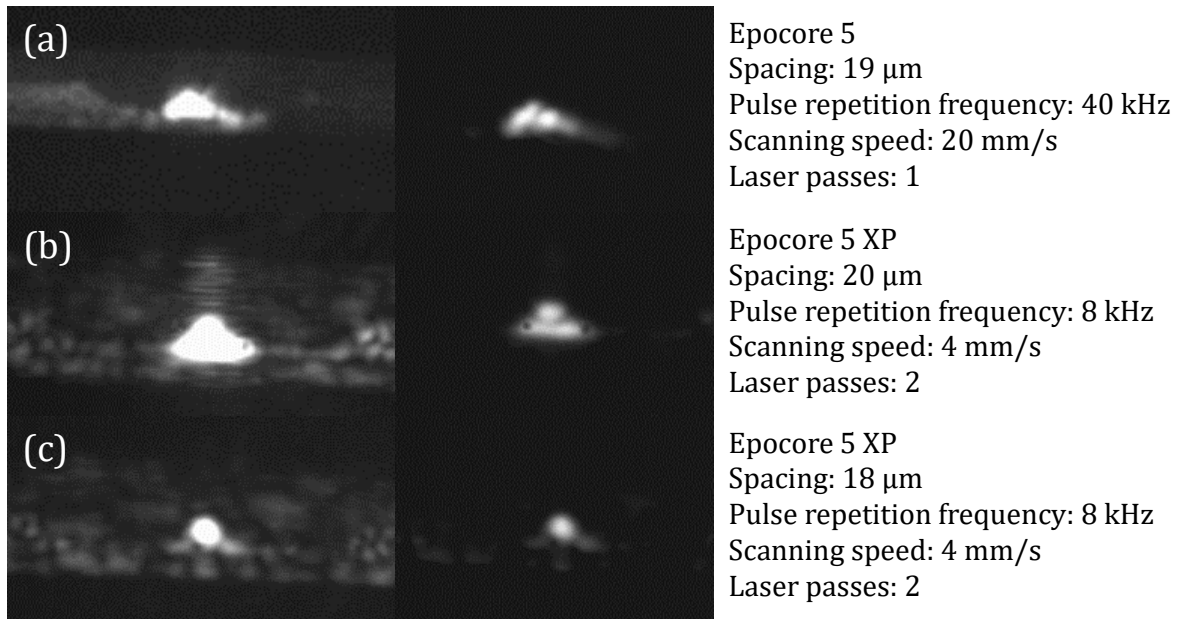


Figure 124: Mode profiles (left column) at high optical power and (right column) at low optical power of three waveguides at 1310 nm, representative of the tested configurations (a), (b) and (c) whose parameters are shown on the right part of the figure.

At high optical powers, we can observe the mode (that saturates the camera), as well as each resin layer thanks to the presence of stray light. This confirms that the mode is guided inside the rib waveguide. At low optical powers, we can see the progressive reduction of the mode profile size using smaller waveguide width thanks to a lower spacing. We also used the lower index contrast offered by Epocore 5 XP try to obtain a SMWG. These tests were not performed on electrically functionalized interposers.

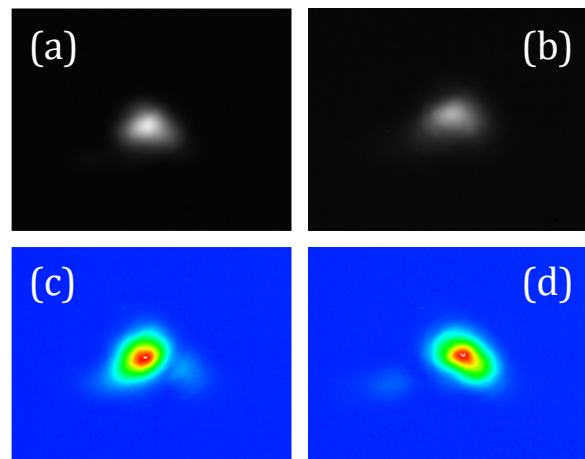


Figure 125: Mode profile at 1310 nm of waveguides integrated with the electrical RDL (a) before and (b) after flip-chip bonding of the PIC25G. Colorized mode profiles of a waveguide before flip-chip with a slight displacement of the injection fiber to the left (c) and to the right (d)

Other test waveguides were then fabricated using the complete process described in section 2.1 of chapter III and the laser parameters of configuration (c) of Figure 124. They also underwent mode profile characterizations before and after flip-chip. The results are presented in Figure 125. No major mode profile differences were observed between the waveguides before, Figure 125 (b), and after, Figure 125 (a), flip-chip bonding. However, and despite the decrease of the spacing trenches, Figure 125 (c) and (d) reveal that the waveguide is multimode.

1.1.2 Propagation & coupling losses

1.1.2.1 Principle

After determining the mode profile and spectral response of the polymer waveguides, it is necessary to determine the waveguide losses. They can be divided into two parts: coupling losses, resulting mainly from mode mismatch and Fresnel reflections at both ends of the waveguide, as well as propagation losses, which are mainly attributed to three physical mechanisms: radiation, scattering and absorption [117]. Reliably measuring the sum of these contributions and determining the proportion of each is not trivial. Several methods can be employed to achieve a first separation between coupling and propagation losses.

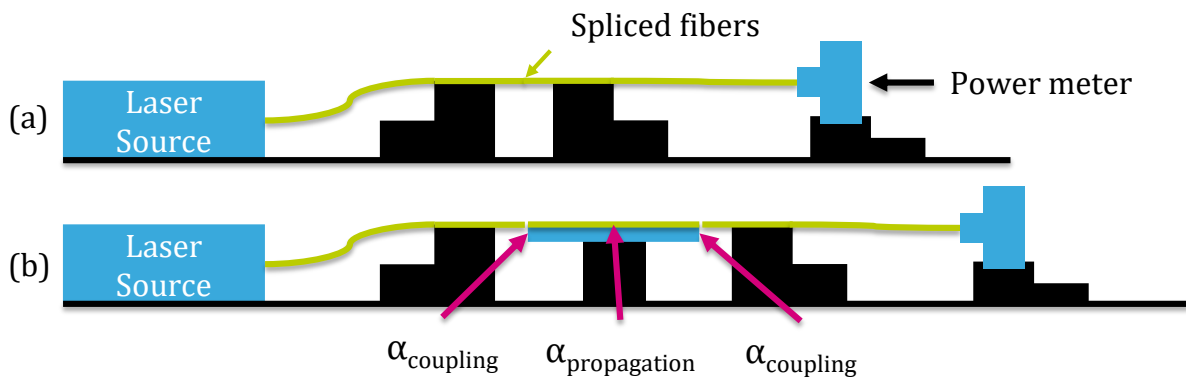


Figure 126: Schematics of the measurement setups for measuring (a) the reference power using spliced fibers, a laser source, a power meter, as well as micro positioners, and (b) the waveguide losses using the same equipment with the fibers cleaved.

One commonly used technique consists in feeding a waveguide with a known optical power and measuring the output power [117]. First of all, a reference optical power is obtained by the setup depicted by the schematic (a) of Figure 126, which makes use of a fiber splicer to connect the cleaved edges of both fibers. Then, as described in the schematic (b) of Figure 126, a laser source at the wavelength of interest is connected to a single mode fiber that is cleaved at the other end. The fiber is aligned in front of the waveguide using a v-grooved holder mounted onto a micro-positioner. A similar setup is used at the output of the waveguide to collect light and measure the optical power using a power meter. In our case, the setup involves 0 dBm optical sources at 1310 and 1550 nm and a power meter capable of detecting optical signal down to -80 dBm. Then, the waveguide is cut to a different length and the same measurement is repeated. This destructive method relies on the length dependence of propagation losses and assumes that the coupling losses at the input and output of both the full-length and cut waveguide are equal. For two waveguides of respective length l_{g_1} and l_{g_2} , and respective optical powers P_{g_1} and P_{g_2} measured using the setup of Figure 126 (b) and expressed in dBm, as

well as a reference power P_{ref} obtained by the setup of Figure 126 (a), we have the propagation losses ($dB \cdot unit\ length^{-1}$) equal to:

$$\alpha_{propagation} = \frac{P_{g_2} - P_{g_1}}{l_{g_2} - l_{g_1}}, l_{g_2} < l_{g_1} \quad (1)$$

However, this method involves the cutting of the sample after a first series of measurements and the cleaving of our samples was not reliable enough to obtain reproducible facet planarity. This is why we decided not to cut the samples twice. Therefore, we could only evaluate the sum of the propagation and coupling loss. The measured power P_g deembedded from the reference power P_{ref} can be expressed as:

$$P_g - P_{ref} = 2\alpha_{coupling} + \alpha_{propagation} \cdot l_g \quad (2)$$

From there, a pessimistic approach consists in considering that the waveguide is long and lossy enough to completely neglect the coupling losses. This gives an estimation of the maximum propagation losses for the waveguide. To push the analysis a little bit further, we simulated a theoretical waveguide with the dimensions measured by the profilometer using the same method as in chapter II section 1.2.3 and used the theoretical power coupling ratio between the fundamental mode of the waveguide and the fiber plus Fresnel's power transmission coefficient T of an air/polymer diopter to approximately evaluate the coupling loss. This coefficient, for a normal incidence, is given by the following formula: $T = \frac{4n_1n_2}{(n_1+n_2)^2}$, where n_1 is the refractive index of the material in which light is incident (presently air) and n_2 the index of the material in which light is transmitted (presently the polymer material) [75]. This method is used in upcoming sections 1.1.2.2 and 1.1.2.3.

1.1.2.2 Polymer/glass surface waveguides

We measured the total loss of 2 cm long polymer/glass surface waveguides. The best result we obtained was $P_{ref} - P_g = -26\ dB \pm 1\ dB$ at 1550 nm. Given the large amount of loss, we did not push the measurement further. If we were to improve the performance of these waveguides, two main points are to be studied:

- The trench shape has to be refined or the polymer refractive index lowered in order to obtain single-mode waveguides reliably. In fact, the waveguide dimensions obtained coupled to the measured index difference do not make it possible to obtain a single mode waveguide at 1310 nm as discussed in chapter III section 1.1.3.
- The roughness of the bottom of the trench, which is currently $1 \pm 0.5\ \mu m$, must be improved to reduce the propagation losses of the waveguide, in order to lower the propagation losses to $1\ dB \cdot cm^{-1}$

1.1.2.3 Waveguides by laser lithography

Among the polymer waveguides fabricated by laser lithography, the best results were obtained on the waveguides of configuration n°5 (Table 14 section 1.1.1.3). The 24.7 mm long waveguides were measured using the losses measurement benches described previously. We obtained:

$$P_{ref} = -2.7 \text{ dBm} \pm 0.2 \text{ dB}$$

$$P_g = -8.2 \text{ dBm} \pm 0.2 \text{ dB}$$

The $7.9 \times 7.0 \mu\text{m}^2$ waveguides exhibit down to $5.5 \text{ dB} \pm 0.4 \text{ dB}$ of total losses. As discussed in section 1.1.2.1, a retro-simulation using the measured waveguide dimensions allows to compute the power coupling ratio between the waveguide and fiber fundamentals modes. This ratio is 0.2 dB for each interface. Moreover, a first approximation of the Fresnel reflections coefficient can be derived from an air/polymer diopter loss at normal incidence. The approximated coefficient is 0.36 dB. Assuming that the waveguide facets are flat and the fibers perfectly aligned, we determine theoretical propagation loss of $1.92 \text{ dB} \cdot \text{cm}^{-1} \pm 0.4 \text{ dB} \cdot \text{cm}^{-1}$.

1.1.2.4 Waveguides by laser ablation

For the loss characterization of laser ablated waveguides in photosensitive resins, we had a tunable laser source in the range 1260 nm to 1340 nm. As shown in chapter 3 section 3.2, four 1.23 cm long straight waveguides have been fabricated on both sides of the interposer for this purpose. We measured the total losses

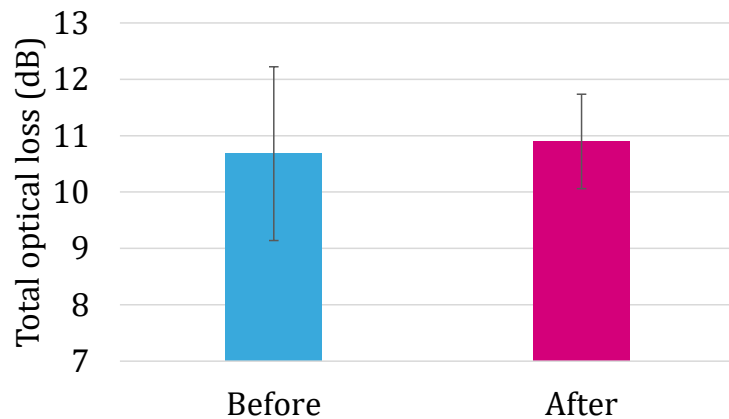


Figure 127: Average and standard deviation of the total optical loss of eight laser ablated polymer waveguides before and after flip-chip bonding at 1310

of eight waveguides on an interposer where the flip-chip bonding was performed and eight others on an interposer without the PIC25G chip at 1310 nm. The results are summed up by Figure 127. We can observe an average total optical loss of 10.7 dB before and 10.9 dB after flip-chip bonding. However, the standard deviation is almost two times higher for the waveguides of the first category compared to the second (3.1 vs 1.7). This may be due to the temperature elevation occurring during flip-chip.

The waveguide with the lowest losses before flip-chip bonding was measured in the full range of the laser source. The results are shown in Figure 128. A minimum loss of $7.2 \text{ dB} \pm$

0.4 dB is obtained at 1310 nm while, the loss variation between 1260 nm and 1340 nm stays below 1 dB.

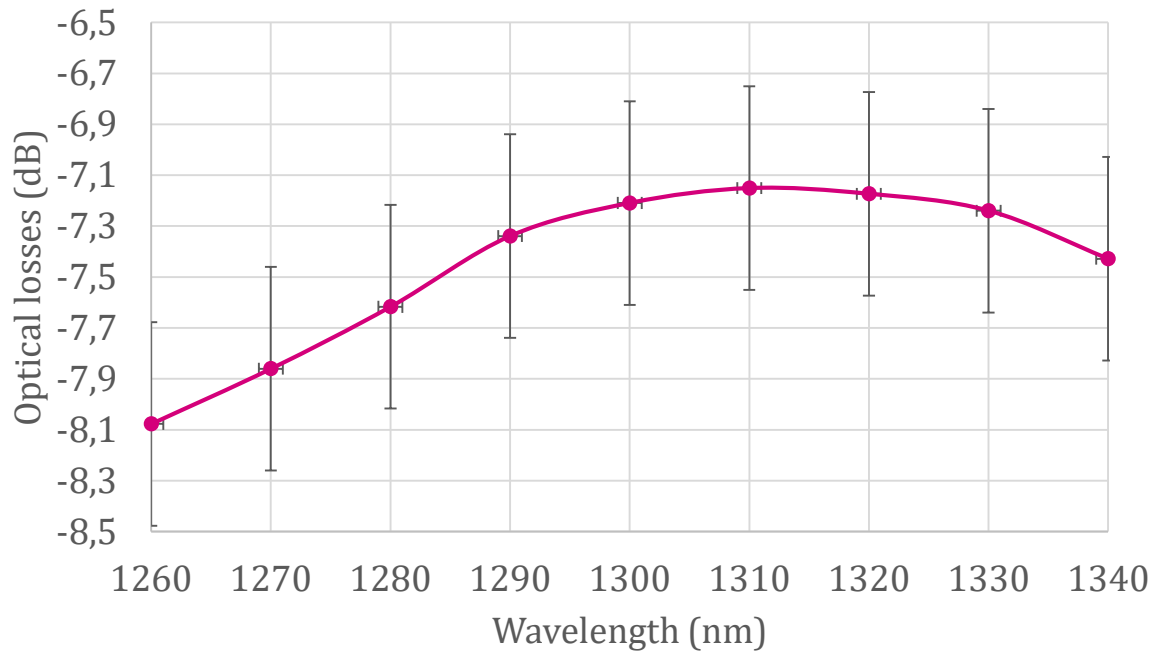


Figure 128: Total optical loss of the best laser ablated waveguide between 1260 nm and 1340 nm

Similarly to what we did with laser lithography defined waveguides, we backwardly simulated the waveguide with the measured dimensions and computed the power coupling ratio between the waveguide and fiber fundamental modes. This ratio is -0.7 dB for each interface. Together with the approximation of Fresnel reflections loss calculated in the previous section, we obtain theoretical propagation loss of $4.42 \pm 0.25 \text{ dB} \cdot \text{cm}^{-1}$. Despite being higher than those of waveguides by laser lithography, these propagation losses are low enough to measure a communication between the interposer and the PIC25G chip, given our measurement methods.

1.2 RF/mmW characterizations

1.2.1 Characterization setup

The characterization of the interposer CPWs was carried-out using the measurement bench depicted by Figure 129. The two ports of the Power Network Analyzer (PNA) E8361A from Agilent are connected to ground – signal – ground (GSG) Infinity Probe probes. This PNA also implements polarization tees connected to a two-channel Source Monitor Unit (SMU) E5263A, from the same manufacturer, as well as a GPIB interface connected to a PC. This bench allows the measurement of S parameters of a two-port device between 0.1 GHz and 67 GHz. The whole is calibrated via the Line-Reflect-Reflect-

Match (LRRM) method to bring the measurement plane from the PNA to the RF probes by taking into account an eight-term error model for the cables and probes [118].

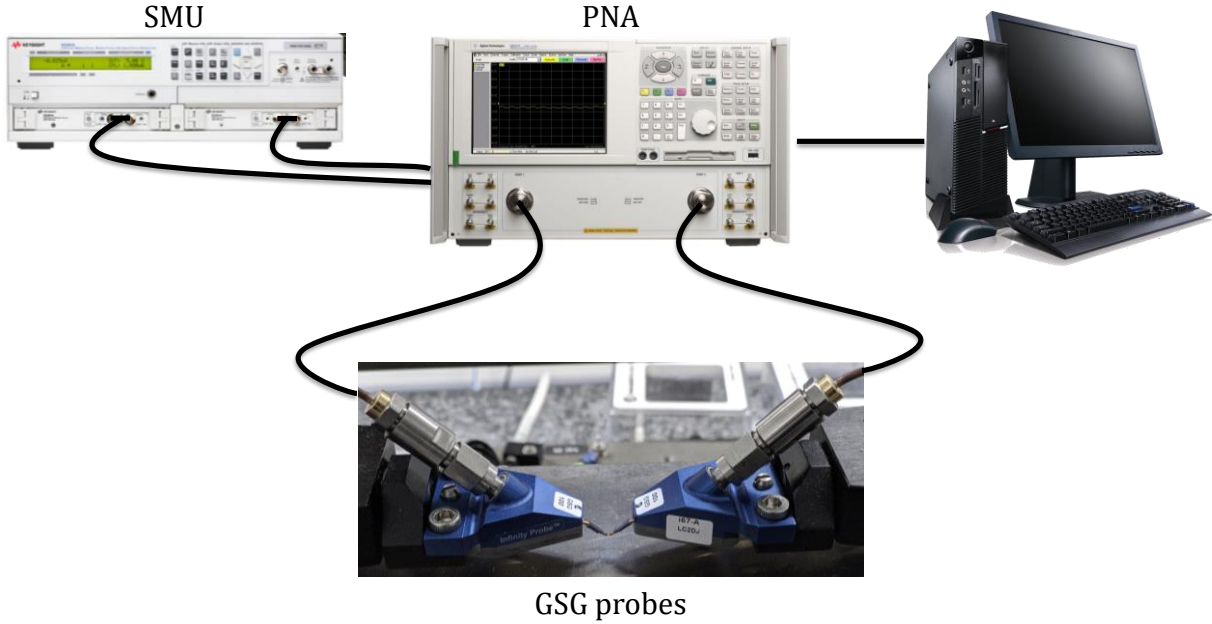


Figure 129: Schematic of the 0.1 - 67 GHz S parameters measurement bench

1.2.2 CPW measurements and deembedding structures

In this section, we present the characterization results of the CPWs and deembedding structures described in chapter 3 section 2.3.2 and section 3.2.

The deembedding structures are 1-port components formed by open and short circuits created from the probing pads and accesses to CPW. Figure 130 presents the measured S-parameters of these devices. As standard RF/mmW probes feature tips separated by 100 μm , a short transition is used to pass from 60 μm wide probing pads to 85 μm wide CPW. These transitions can impact the measurement of the line. As for calibration of the PNA, the deembedding of these accesses brings the measurement plane to the device under test itself. A simple 2-term error model can be taken into account using open and short circuit structures. In our case,

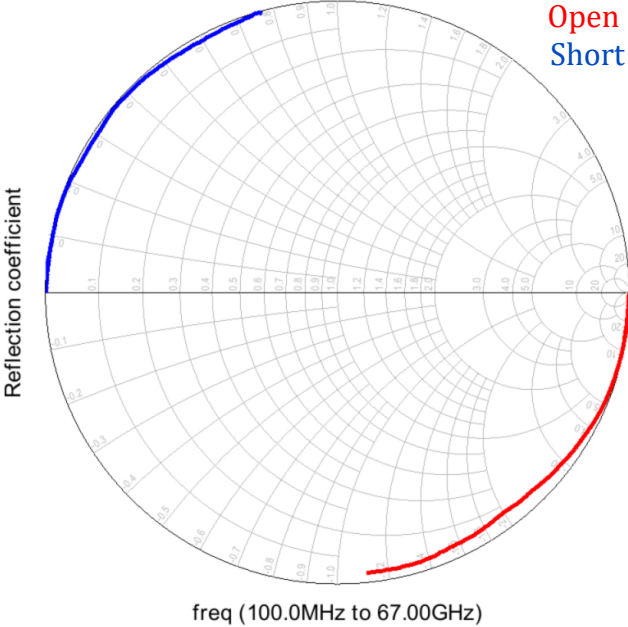


Figure 130: Open and Short deembedding structures fabricated on the interposer.

we found that the impact of the transitions is minor, since the short circuit resistance and open circuit capacitance are relatively low with respect to the line resistance and capacitance. If the short-circuit and open-circuit structures are considered as perfect resistance R_{short} and capacitance C_{open} with respective impedances Z_{short} and Z_{open} , their values are given by, respectively, $R_{short} = \Re(Z_{short})$ and $C_{open} = -\frac{1}{\Im(Z_{open})\omega}$. Both impedances are obtained from their measured S parameter by: $Z = \frac{1+S}{1-S}$. These equations give an R_{short} of 0.04Ω at 100 MHz and $36 \text{ fF} < C_{open} < 43 \text{ fF}$. As we will show thereafter, the corresponding values resistance and capacitance for the transmission lines are one or two orders of magnitude higher. Thus, we did not deembedded the accesses.

The PNA gave the S parameters matrix of each CPW. Then, we determined the attenuation coefficient and characteristic impedance of each line following the calculation described in chapter 2 section 2.1.2. The results are depicted by Figure 131. The lowest attenuation coefficient is obtained for 85 μm wide CPWs that reach $3 \text{ dB} \cdot \text{cm}^{-1}$ at 58 GHz for a real part of the characteristic impedance of 46Ω .

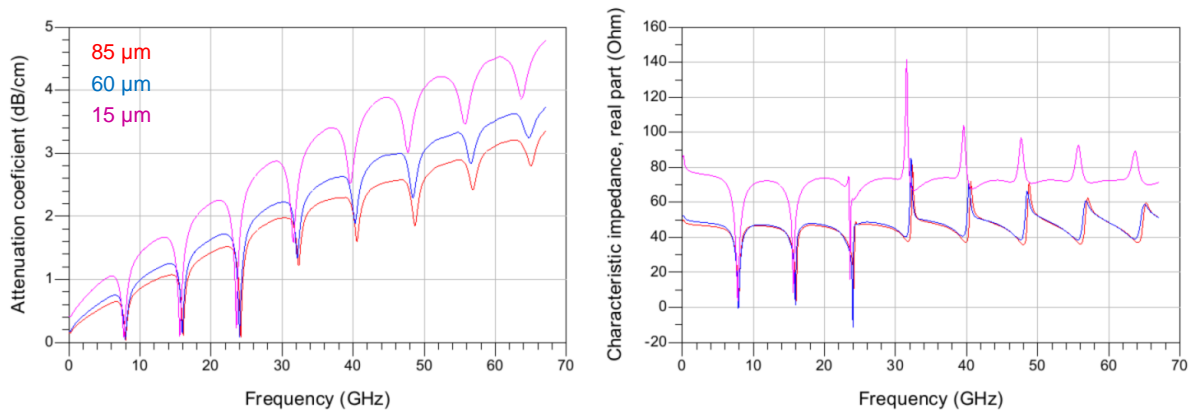


Figure 131: Attenuation coefficient (a) and real part of the characteristic impedance of the 938 mm long interposer CPWs with widths of (red line) 85 μm , (blue line) 60 μm , (purple line) 15 μm .

The 60 μm wide CPW exhibits a slightly higher impedance of 47Ω (real part) that results in a better adaptation but at the expense of the attenuation coefficient, which is $0.4 \text{ dB} \cdot \text{cm}^{-1}$ higher at the same frequency. The 15 μm wide line shows an impedance of 74Ω and an attenuation coefficient of $4.5 \text{ dB} \cdot \text{cm}^{-1}$ at 58 GHz. The goal of these transmission lines being to carry $25 \text{ Gb} \cdot \text{s}^{-1}$ digital signals driving the PIC25G Mach-Zehnder modulators, the performance of 60 μm and 85 μm CPWs is sufficient to perform this task. Furthermore, and since the PIC25G design has been optimized at 50Ω , we seek a transmission line presenting an identical characteristic impedance to minimize reflected waves. We can observe that the attenuation coefficient drops at each multiple of 8 GHz. This is due to standing wave appearing at these specific frequencies, making the

measurement of the attenuation coefficient more difficult. Measuring shorter line reduces this phenomenon.

We modeled the 85 μm CPW using the RLCG model presented in chapter II section 2.1.1. Consistently with the definition of the propagation constant γ and the characteristic impedance Z_0 given in the aforementioned section, we computed each per unit length parameter of the measured line:

$$R_{meas} = \Re(\gamma_{meas} \cdot Z_{0_{meas}}) \quad (2)$$

$$L_{meas} = \Im(\gamma_{meas} \cdot Z_{0_{meas}}) \quad (3)$$

$$C_{meas} = \Im\left(\frac{\gamma_{meas}}{Z_{0_{meas}}}\right) \quad (4)$$

$$G_{meas} = \Re\left(\frac{\gamma_{meas}}{Z_{0_{meas}}}\right) \quad (5)$$

The modeled component is instantiated in the form a 2-port component taking into parameter the line length l and determined by its ABCD matrix parameters, namely:

$$A = \cosh(\gamma_{mod} \cdot l) \quad (6)$$

$$B = Z_{0_{mod}} \cdot \sinh(\gamma_{mod} \cdot l) \quad (7)$$

$$C_{param} = \frac{1}{Z_{0_{mod}}} \sinh(\gamma_{mod} \cdot l) \quad (8)$$

$$D = \cosh(\gamma_{mod} \cdot l) \quad (9)$$

γ_{mod} and $Z_{0_{mod}}$ are defined by the linear capacitance C_{mod} , inductance L_{mod} and conductance G_{mod} of the model, which are approximated by constant values and the resistance R_{mod} , which is modeled by the following equation: $R_{mod} = R_{dc} + k_1 \cdot (\text{frequency} \cdot 10^{-9})^{k_2}$, where R_{dc} is the extracted resistance R_{meas} value at 100 MHz and k_1 and k_2 arbitrary determined by fitting the curves of the extracted resistances of the measured line and the simulated component with the same length as the measured line. The modeled conductance G_{mod} is also determined by the value of the conductance value at 100 MHz extracted from the measurement. The model capacitance C_{mod} and inductance L_{mod} are obtained by a fit of the extracted curves. Table 15 summarizes the model parameters, their value and extraction method. Figure 132 presents the RLCG curves of both the measured CPW and the simulated two-port component.

Table 15: Value and extraction method of CPW model component parameters

Parameter	Value	Extraction method
R_{dc}	$166 \Omega \cdot mm^{-1}$	Measured value 100 MHz
L_{mod}	$301 pH \cdot mm^{-1}$	Curve fit
C_{mod}	$144 fF \cdot mm^{-1}$	Curve fit
G_{mod}	$0.004 S \cdot mm^{-1}$	Measured value 100 MHz
k_1	$125 \Omega \cdot mm^{-1} \cdot Hz^{-1}$	Curve fit
k_2	0.8	Curve fit

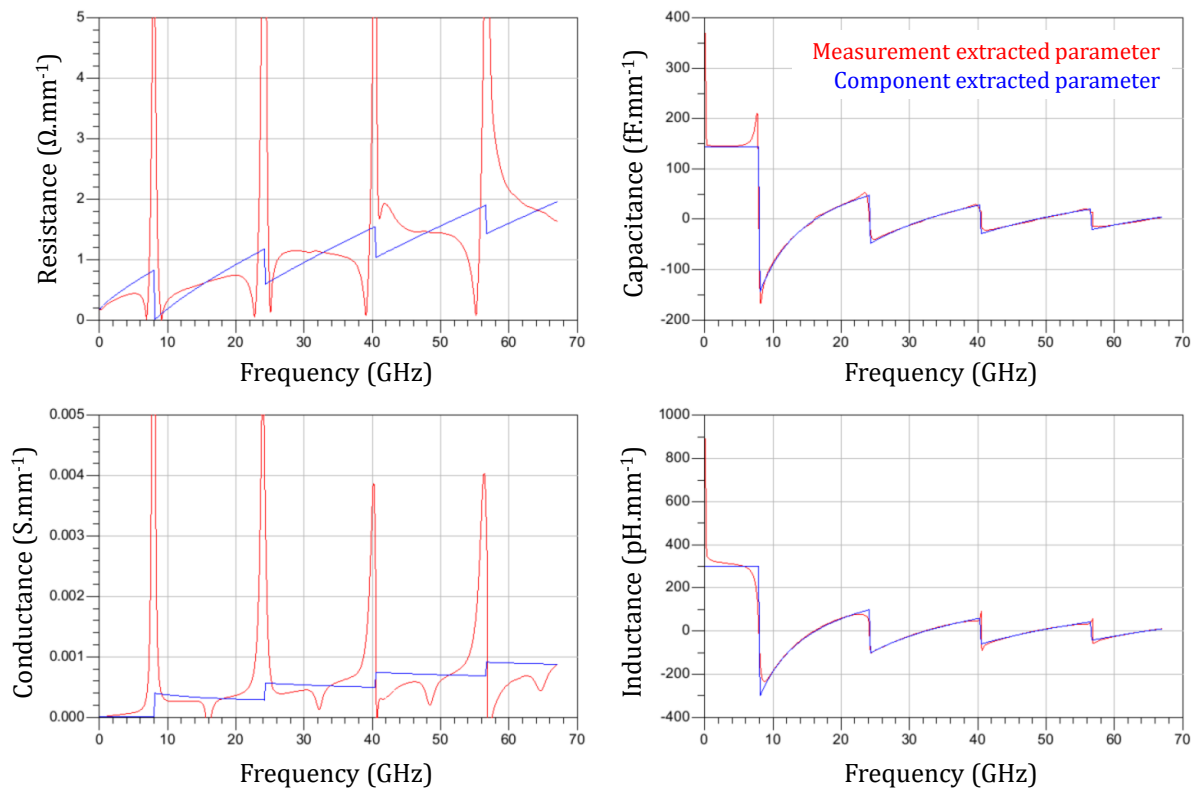


Figure 132: RLCG parameters extracted from the measured S parameters of the $85 \mu m$ (red curves) and from the simulated S parameters of the 2-port component parametrized with the same length (blue curves)

This component can naturally be used to model CPWs of a length that differs from the 9.38 mm long measured line. Therefore, it is helpful in the analysis of other test structures involving the $85 \mu m$ CPW or in the design of future chips using this technology.

1.3 Total internal reflection mirror

1.3.1 Measurement bench

The characterization of the mirror angle is an important step, since we expect its value to strongly impact light coupling performance, as detailed in chapter II section 3.4. To this

purpose, we developed a measurement bench by modifying the loss measurement bench described previously in section 1.1.2.1.

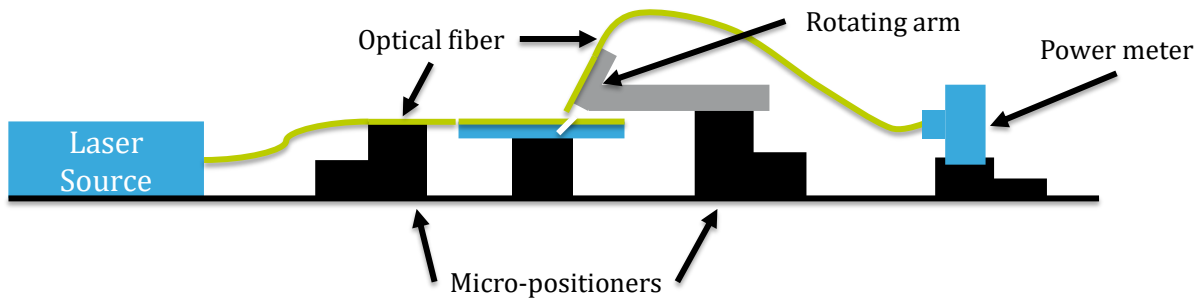


Figure 133: Schematic of the mirror angle measurement bench

On the left part of the schematic presented in Figure 133, the bench is similar in every point to the loss measurement bench: a laser source is connected to a SMF cleaved at the other end and aligned in front of the waveguide thanks to a micro-positioner. On the right side, on the contrary, the SMF is aligned above the mirror using a V-groove holder mounted on a custom-made rotating arm whose detailed schematic is presented in Figure 134. The rotation is performed by a graduated rotation stage that we adjusted vertically using a spirit level. The same adjustment was done for the sample holder.

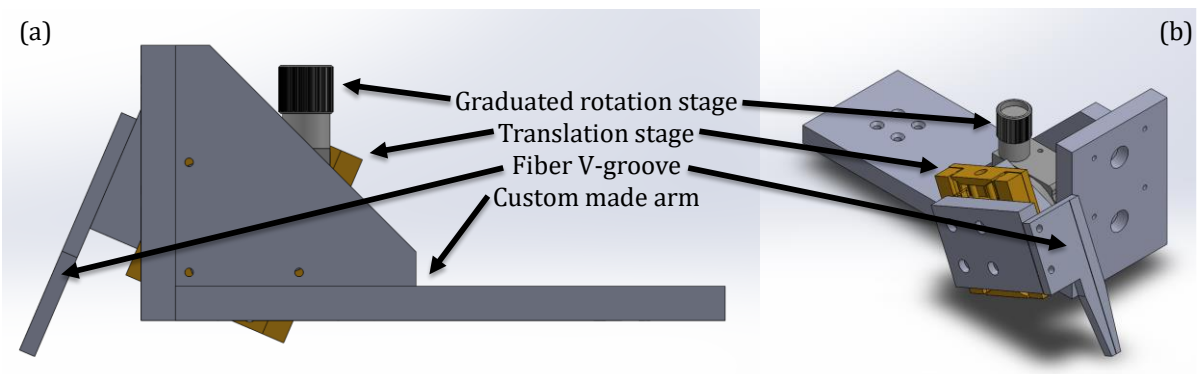


Figure 134: SolidWorks schematic of the rotating arm, (a) front view and (b) isometric view

1.3.2 Angle measurement

Following the schematic presented in Figure 135, we varied the fiber angle θ_{fiber} from 10° to 16° by steps of 1° and re-aligned the fiber using the translations of the micro-positioner to obtain the maximum power. This optical power recorded for each angle was normalized using a reference power measured using the measurement bench Figure 126 (a). The results are summarized in Figure 136. We observe a minimum loss for an angle of 14° , however we do not observe a strong angular selectivity, in agreement to the simulation performed in chapter II section 3.4.2.

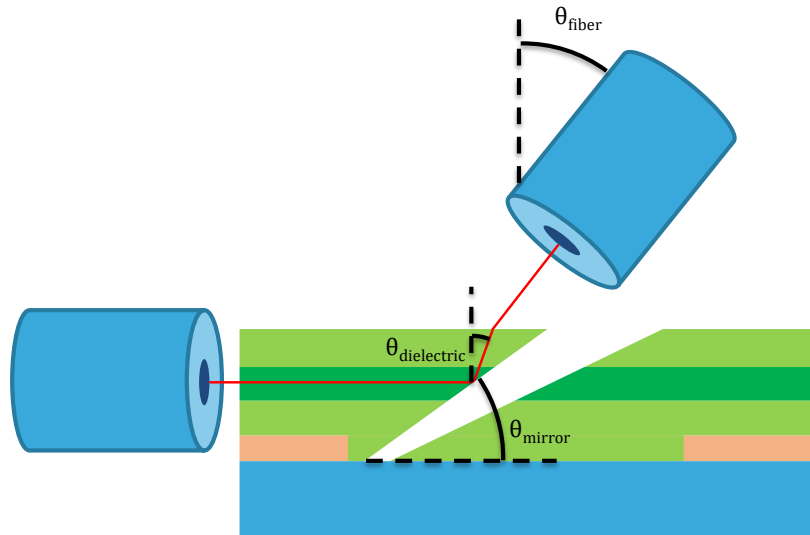


Figure 135: Schematic of the mirror angle measurement principle

Supposing that the maximum power coupling ratio is obtained when the output beam is aligned with the fiber, the fiber angle can be related to the mirror angle using ray optics. For $0^\circ < \theta_{mirror} < 90^\circ$, the reflected ray angle to the vertical in the dielectric is $\theta_{dielectric} = 90 - 2\theta_{mirror}$ and is also directly linked to the refracted ray angle to the vertical in the air by Snell-Descartes's law. Following this method, the 14° angle of the fiber corresponds to a mirror angle of 40.5° .

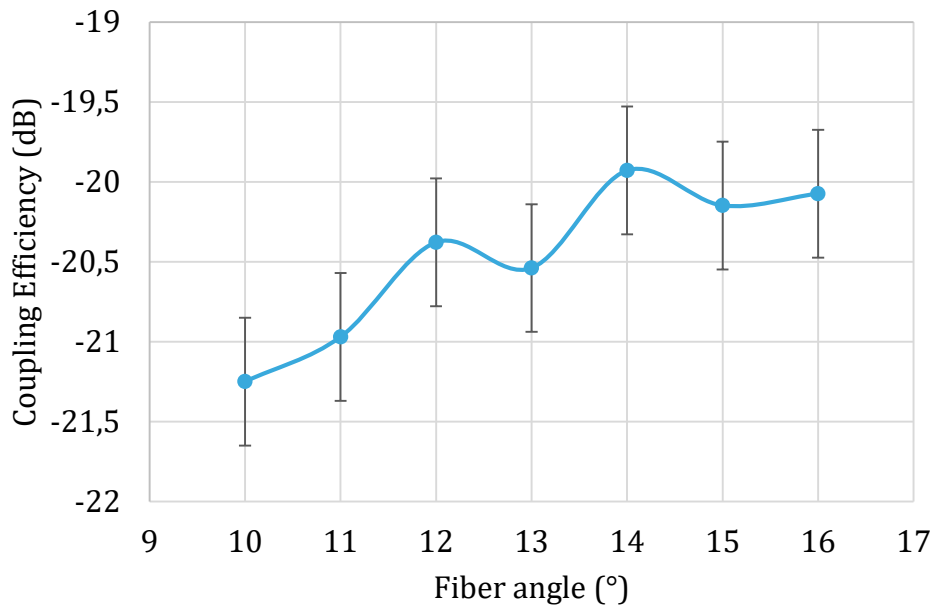


Figure 136: Total loss measured versus fiber angle

In chapter II section 3.4.2, we determined by simulations that the optimum angle is 40° . A mirror angle of 40.5° theoretically leads to less than 1 dB additional loss. Parallely, this angle correlates to the SEM measurement of the mirror angle on the sample cross-section.

2 Assembly

In this section, we present the characterization results of the test structures enabled by the assembly of the SiPh IC and the glass interposer described in chapter III section 3.

2.1 RF/mmW characterizations

2.1.1 RF/mmW path

The first test structure of the assembly is dedicated to the performance evaluation of transmission of high frequency signals. The structure involves, as depicted in Figure 137, a 5.3 mm microstrip transmission line in the SiPh IC connected at both ends to two 2.1 mm long and 85 μm wide CPWs in the interposer through 30 μm thick copper pillars. Two structures of this type are present in the demonstrator.

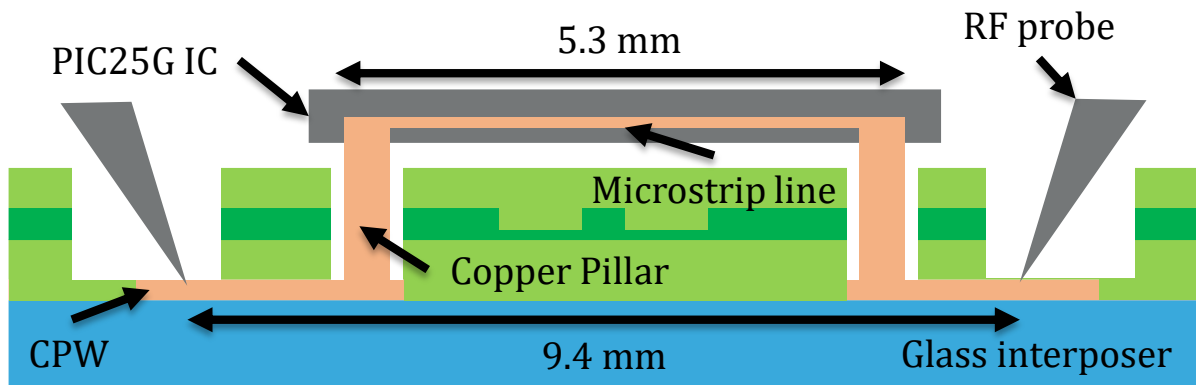


Figure 137: Schematic of the RF/mmW test structure

We used the same measurement bench as for the interposer CPWs measurements. Figure 138, shows the return loss and insertion loss of both test structures. We can observe that the frequency response of the two structures are almost identical. They show return loss below 13 dB over the entire frequency range (0 – 67 GHz), as well as insertion loss of 7.1 dB at 50 GHz. These results are consistent with the implementation of a $25 \text{ Gb} \cdot \text{s}^{-1}$ transceiver but also with higher data rate applications.

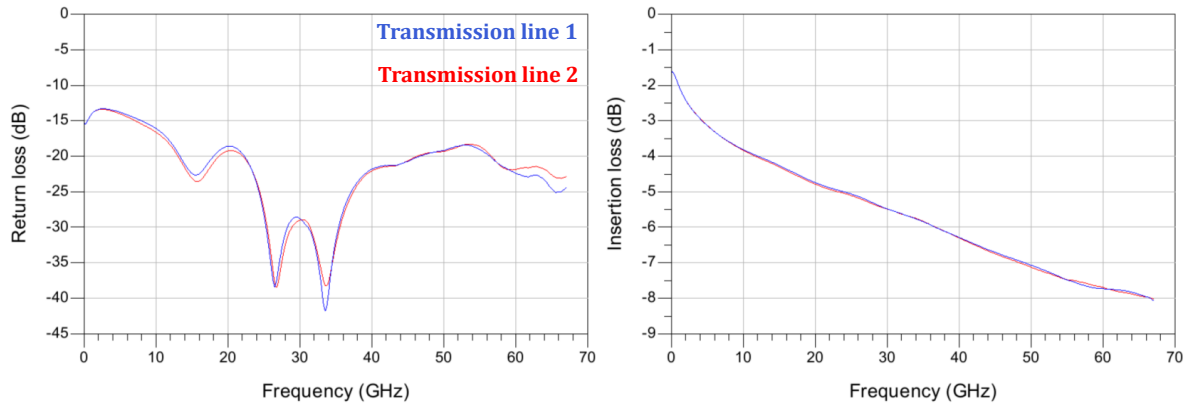


Figure 138: Return loss and insertion loss of the RF/mmW path through the assembly

In section 1.2.2, we measured the attenuation coefficient of the interposer CPWs. Parallely, the PIC25G microstrip attenuation coefficient was measured by STMicroelectronics. At 50 GHz, the 85 μm wide CPWs exhibits an attenuation coefficient of $0.27 \text{ dB} \cdot \text{mm}^{-1}$ while the 5.7 μm wide PIC25G microstrip lines show an attenuation coefficient of $1.2 \text{ dB} \cdot \text{mm}^{-1}$. Accounting for the respective CPW and microstrip length, we can easily calculate 1.1 dB of loss for the CPWs and 6.4 dB of loss for the PIC25G, at 50 GHz. The sum of these contribution being higher than the measured insertion loss, we expect process variations from both the interposer and the PIC25G chip to account for the 0.4 dB difference. Another option to explain this incoherence comes from the measurement. Indeed, on-wafer measurements generates an additional contact resistance that varies each time the probes are placed. When the measured devices exhibit a low resistance, the impact of this contact resistance becomes significant. For instance, the extracted resistance of the current device, following the method used in section 1.2.2, is 20.44Ω while the sum of the theoretical resistances of the different metallic rods is 19.54Ω . The latter is calculated using the formula $R = \frac{\rho L}{W \cdot Th}$, where ρ is the resistivity of the metal, L the length of the line, W its width and Th its thickness. This results in a 4% difference. In the case of the 85 μm standalone CPW of section 1.2.2, the extracted resistance is 1.56Ω and the theoretical resistance is 0.63Ω , which leads to a 60% difference.

2.1.2 Modulators reflection coefficient

The two MZM designed in chapter II section 2.2 have been implemented as test structures in their 3.5 mm long variant as one port components. Therefore, we could measure their respective reflection coefficients, still using the same test bench. Figure 139 and Figure 140 present the return loss and reflection coefficient of respectively, the 3.5 mm long MZM without inductors and its counterpart with inductors.

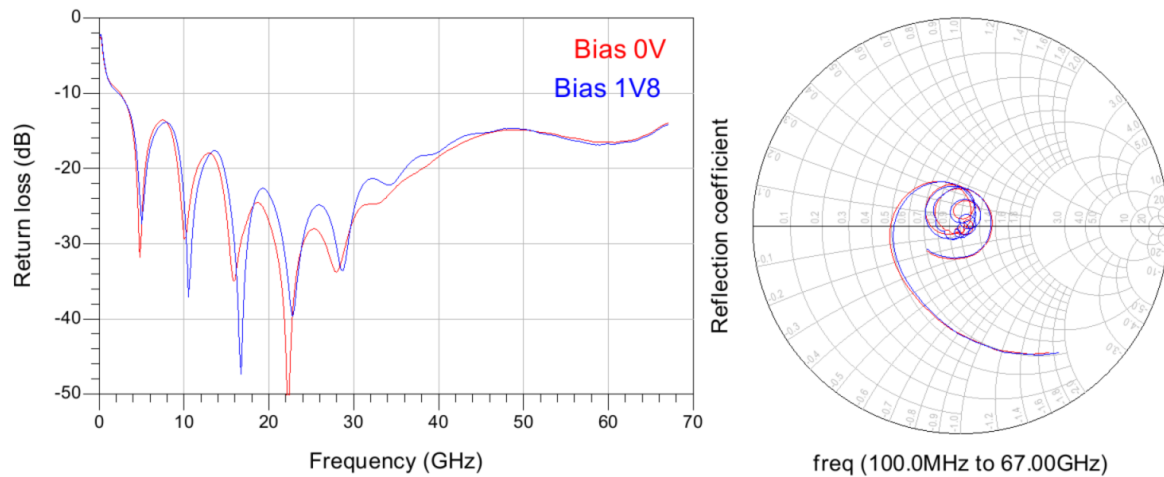


Figure 139: Return loss and reflection coefficient of the 3.5 mm long MZM without inductors

Without inductors, the return loss of the modulator is below -10 dB from 2.5 GHz to 67 GHz with a portion of the spectrum below -20 dB between 15 GHz and 35GHz.

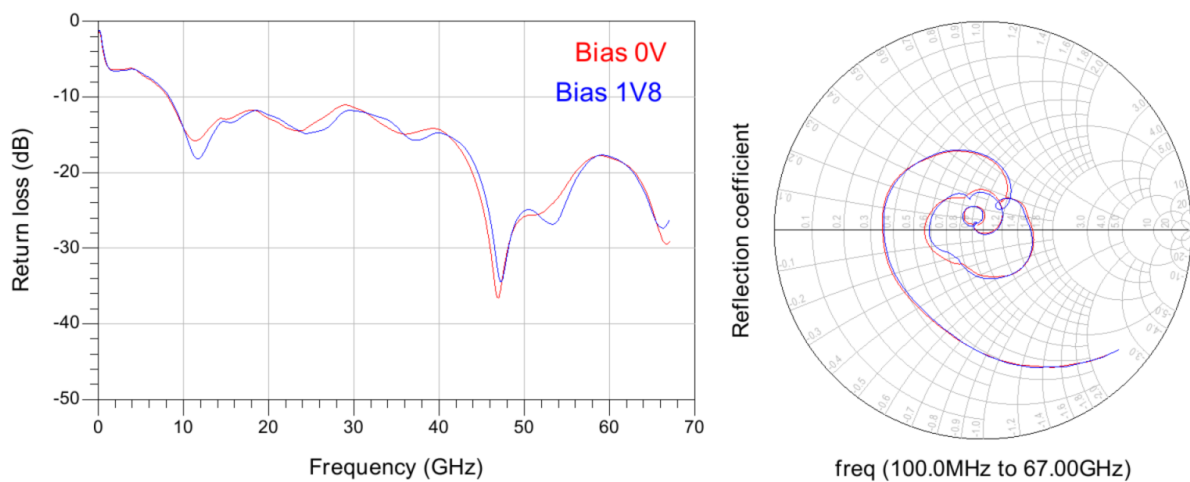


Figure 140: Return loss and reflection coefficient of the 3.5 mm long MZM with inductors

In the case of the modulator with inductors, the return loss reaches the same acceptable level over 8.5 GHz and until 67 GHz while the most adapted part of the spectrum, below -17 dB, is shifted between 45 GHz and 67 GHz.

We expected both test structure to show less return loss, especially at lower frequencies, when compared to the simulations of chapter II. To understand this major difference, we have deembedded the interposer CPW using the model created in section 1.2.2. Considering that the test structure is equivalent to the schematic of Figure 141, a 2.1 mm long CPW is simulated using the model and the inverse of its ABCD matrix is computed

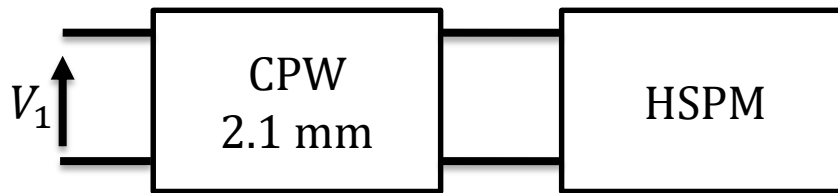


Figure 141: Simplified schematic of the HSPM test structure

Multiplying the inverse of the ABCD matrix of the CPW with the ABCD matrix of the HSPM is equivalent to removing the CPW component in the schematic of Figure 141. The result of this operation is compared in Figure 142 with the simulations performed previously. Additionally, we performed a new simulation of the HSPM without inductors with the 35Ω terminating load removed.

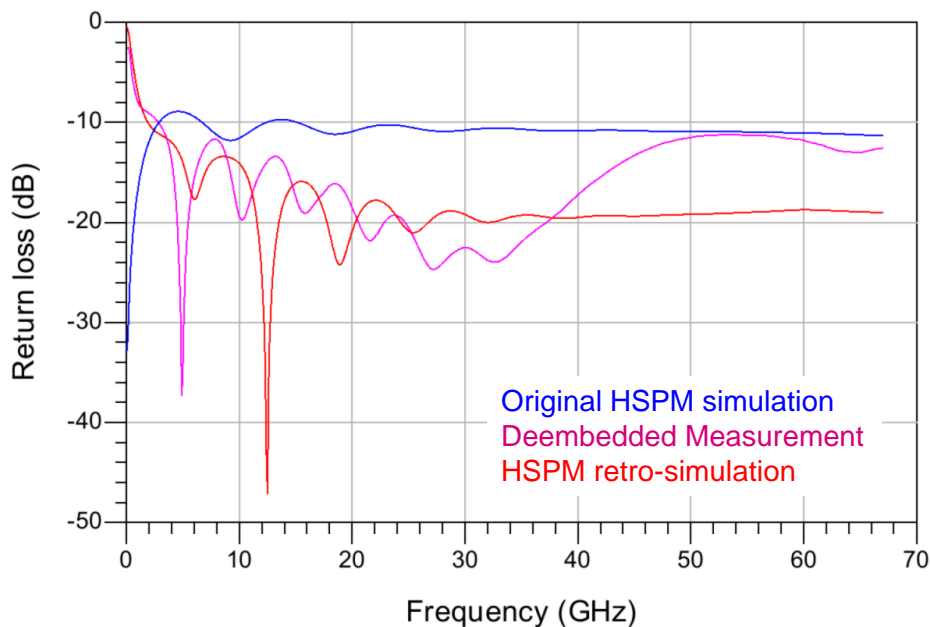


Figure 142: Return loss of the original HSPM simulation without inductors using spice models (blue curve), the measurement deembedded from the interposer CPW (pink curve) and the HSPM retro-simulation using spice models with an open circuit in the place of the 35Ω load at the end of the circuit. (red curve).

We can observe a similar behavior between the deembedded measurement and the retro-simulation using an open circuit at the end of the circuit. Both exhibit lower return loss over the entire frequency range than the loaded circuit simulation except below 2 GHz. They also show a minimum loss peak at 4 GHz and 12 GHz respectively. This analysis allowed us to identify a mistake in the HSPM design at layout level.

2.2 Optical path characterization

2.2.1 Mode Profile

The second test structure is a full optical path passing through both the PIC25G and the interposer. It is composed of two 3.5 mm long polymer waveguides in the interposer and

a 5.2 mm SOI rib waveguide connected together by two TIR mirror/GC coupling structures, as depicted in Figure 143.

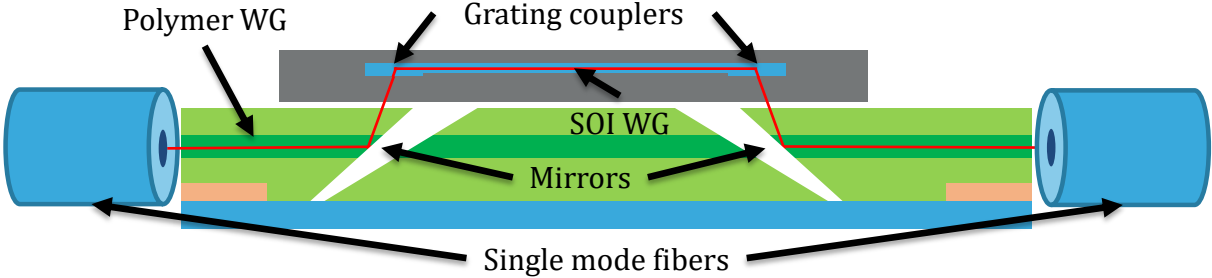


Figure 143: Schematic of the optical path test structure

We characterized the mode profile at the output of the second polymer waveguide. Thanks to a tunable laser source, we observed a strong variability in the mode profile and output power depending on the wavelength. Figure 144 shows the mode profiles of the structure at wavelengths ranging from 1277 nm (a) to 1282 nm (f), spaced by 1 nm. This characterization confirms that we achieved light coupling from the interposer to the PIC25G chip and conversely. The multimode behavior of the polymer waveguides is also confirmed.

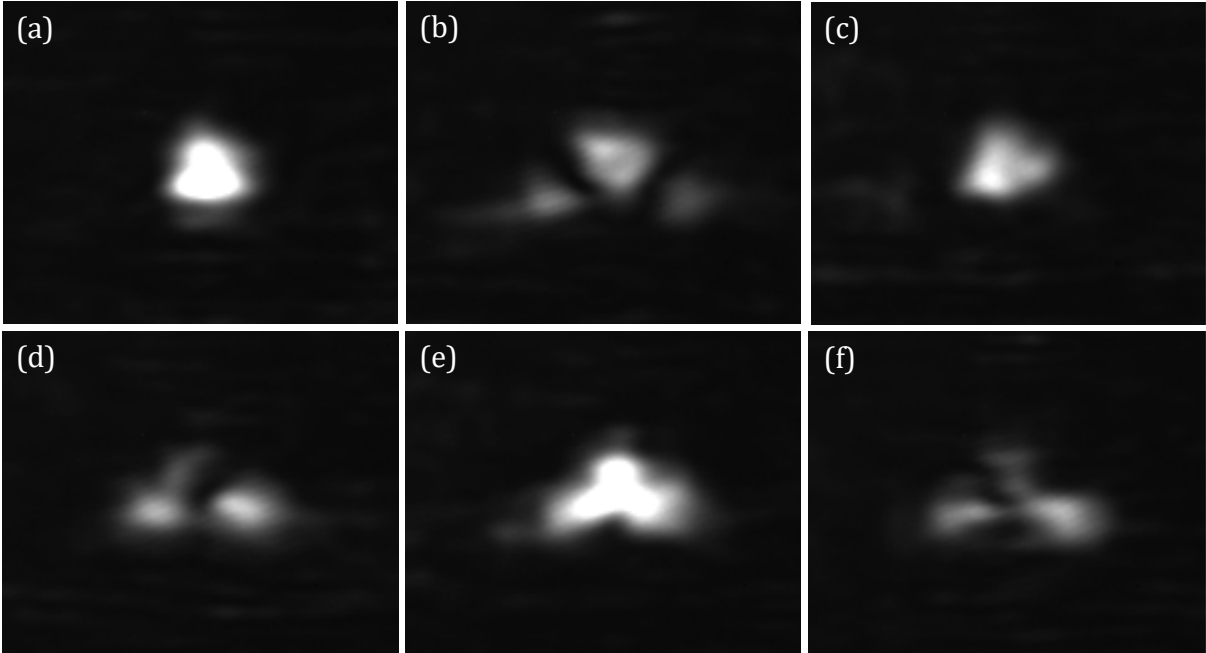


Figure 144: Mode profiles of the optical path test structure at (a) 1277 nm, (b) 1278 nm, (c) 1279 nm, (d) 1280 nm, (e) 1281 nm and (f) 1282 nm

2.2.2 Losses

We also measured the total losses of this structure from 1260 nm to 1340 nm every 10 nm. As it can be observed in Figure 145, we could measure a minimum loss of 63 dB at

1320 nm, which is 17 dB higher than the -80 dBm noise threshold of our measurement setup.

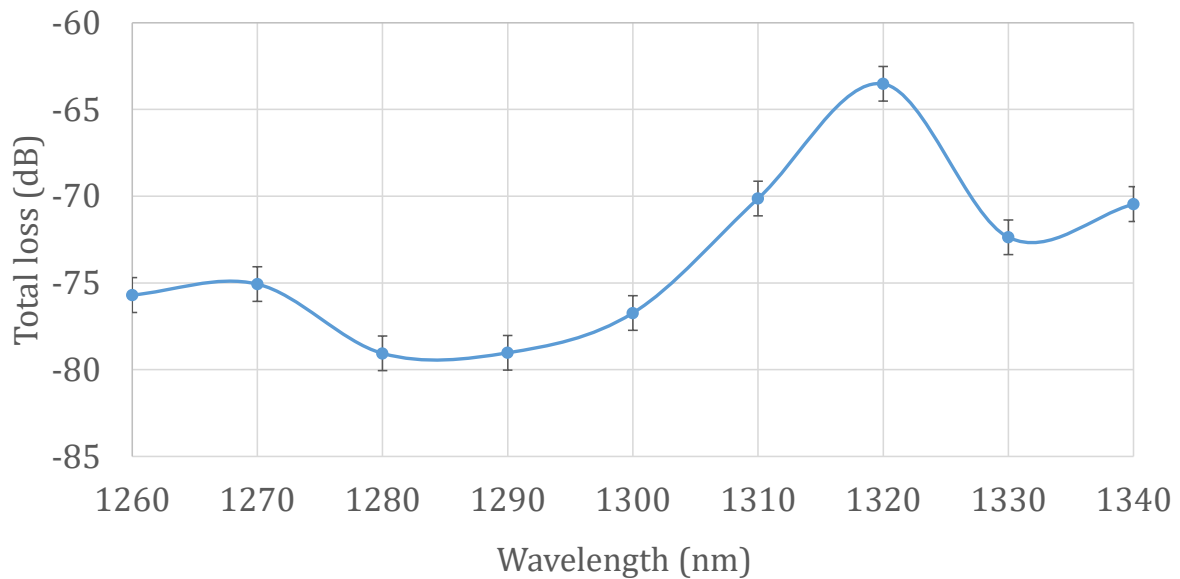


Figure 145: Total loss of the optical path test structure versus wavelength associated to the optical path described in Figure 143

Several sources may be the cause of such high losses. Among them, we expect the misalignment between the TIR mirrors and the GCs to play an important role. Moreover, GCs are sensitive to the presented mode profile and wavelength, the latter being directly related to diffraction angle by Bragg's law. The combination of these three factors with the multimode behavior of polymer waveguides may result in such a high loss and wavelength sensitivity. After demonstrating and evaluating the optical coupling between both chips, we wanted to demonstrate the association of electrical and optical coupling. This also allows to consider only one optical coupling structure at a time whereas the all optical test structure involve two of them. This opto-electrical characterization is described in the next section.

2.3 Optical coupling measurement through embedded photodetector

2.3.1 Principle

The last characterization we performed makes use of the photodiode test structures described in chapter III section 3.1. As depicted in Figure 146, it consists in illuminating the photodiode through the polymer waveguides of the interposer, the TIR mirror/GC coupling structure and the SOI waveguide of the PIC25G IC. At the input, the polymer waveguide is illuminated by a SMF aligned to the edge by butt-coupling. The photodiode

is also probed through the interposer electrical RDL. Figure 147 shows a macroscopic picture of the demonstrator during this characterization where both the electrical probes and the SMF can be seen.

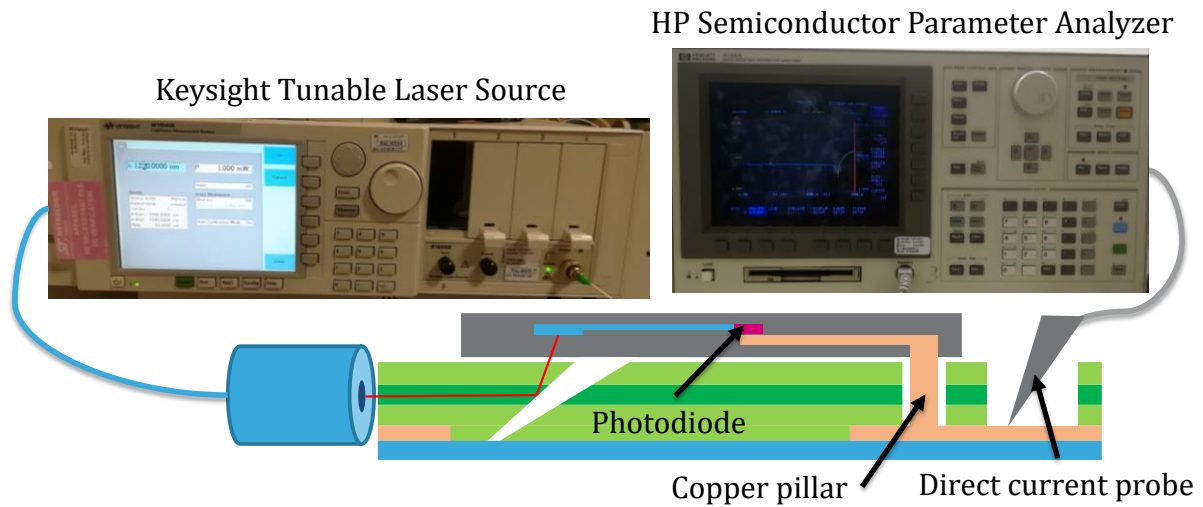


Figure 146: Schematic of the principle of the optical coupling measurement through embedded photodiodes.

Then, the photodiode I-V characteristic is measured by a semiconductor parameters analyzer with the tunable laser source turned on and off. PIC25G photodiodes are well known components showing a typical responsivity of $0.98 \text{ A} \cdot \text{W}^{-1}$ at $\lambda=1310 \text{ nm}$ and under a 1 V reverse bias. Therefore, we can determine the static optical power at the photodiode level by probing their output current.

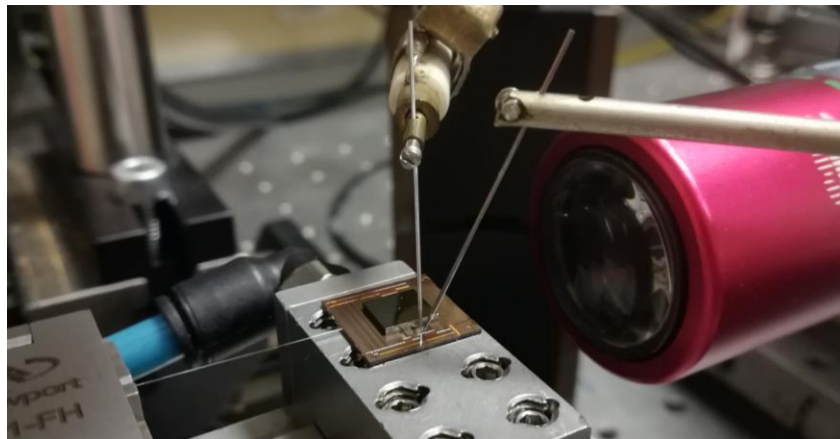


Figure 147: Macroscopic picture of a demonstrator during the optical coupling measurement through embedded photodiodes

We measured the I-V characteristic of four photodiodes with a 1 mW laser source between a wavelength of 1260 nm and 1340 nm every 10 nm. Reference curves were obtained in obscurity, with the input laser switched off. When appropriate, the wavelength interval has been reduced. Each photodiode test structure involves a GC with a specific optimal frequency: 1270 nm, 1290 nm, 1310 nm and 1330 nm.

2.3.2 Results

Figure 148 shows the $I(V)$ characteristic of the 1290 nm test structure with the laser source turned on at 1265 nm and turned off. We can clearly observe the photocurrent generated by light exposure. However, the light on measurement is noisy. As we did not remark strong power variation of the source (thanks to a built-in power meter), we expect the noise to come from vibrations of the injection fiber, which is sensitive because of the length between the V-groove and the sample edge. To attenuate this phenomenon, we computed an average photocurrent I_{on} using all the values between -1.25 V and -0.75 V, for each structure and at each wavelength point.

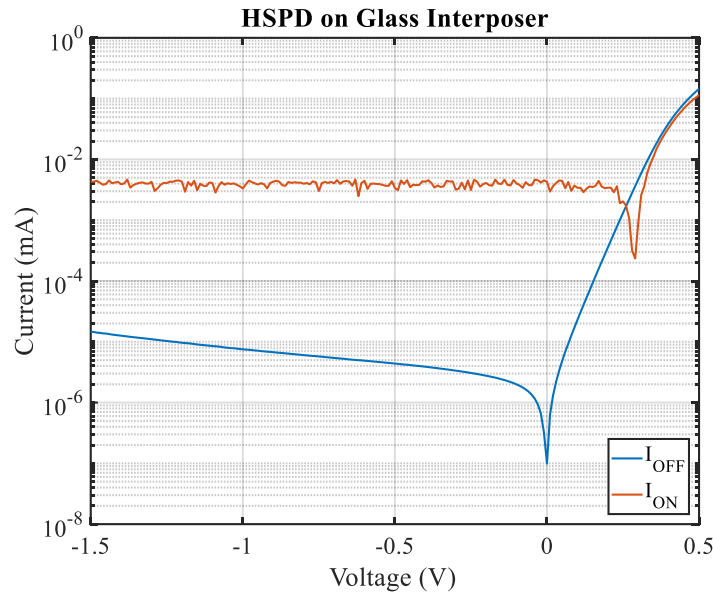


Figure 148: $I(V)$ characteristic of the 1290 nm test structure illuminated with a 1 mW laser source at 1265 nm (red) and without light (blue)

The optical loss $OptLoss$ of these test structures, from the laser source to the photodiode, is calculated using the following formula:

$$OptLoss = 10 \log \left(\frac{I_{on} - I_{off}}{Responsivity \times 1 \text{ mW}} \right) + 3 \text{ dB} \quad (3)$$

I_{off} is the current measured without light exposure at -1 V. The currents are expressed in mA and the laser source is 1 mW. It is noteworthy that equation (3) compensates by 3 dB for the presence of a Y junction in the optical path

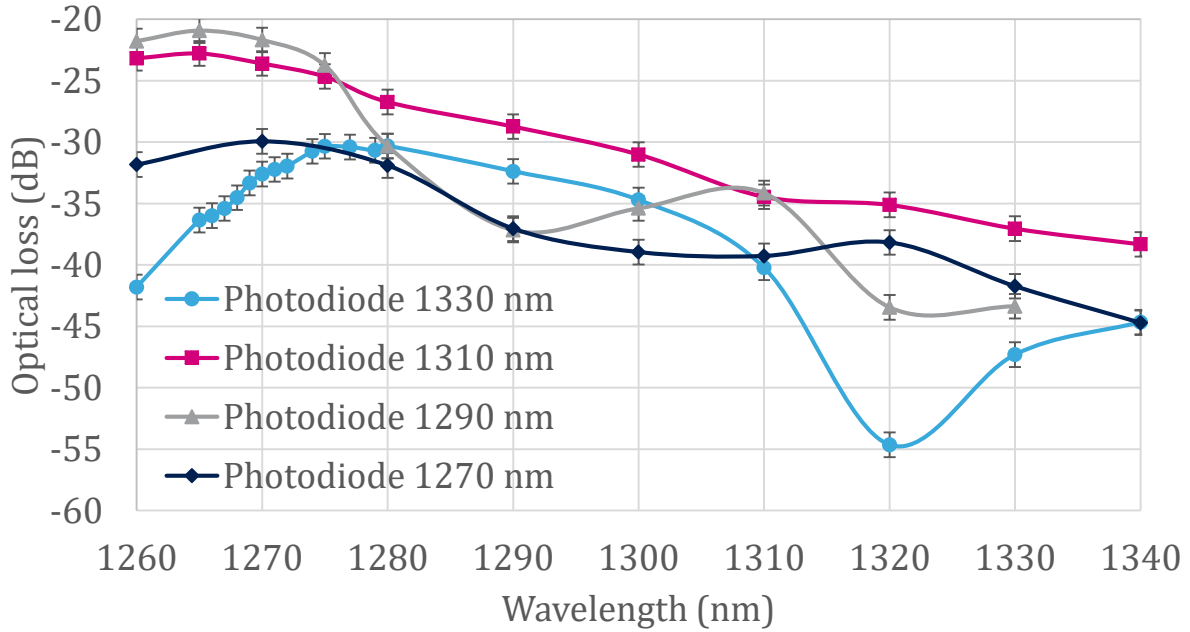


Figure 149: Loss of the optical path from the laser source to the photodiode of photodiode test structures 1270 nm, 1290 nm, 1310 nm, 1330 nm

Based on our estimate of the polymer waveguides propagation and coupling losses, we evaluate their contribution to 2.24 dB. On the silicon side, the SOI optical waveguides length is approximately 340 μm . Thus, we can simply neglect their contribution. Finally, a first estimation of the TIR mirror/GC coupling structure loss in the best case is 18.7 dB. This is high compared to the simulated structure and cannot compete with other solution for the time being. Nonetheless, we expect to reduce this loss with a better alignment of the layers and ICs.

3 Conclusion

In this chapter, we have presented the different types of optical and electrical characterizations performed on the interposer, the assembled demonstrator and their individual components. Firstly, we have determined that the laser ablation of photosensitive resins for the polymer waveguides fabrication was the best trade-off for our demonstrator since this technology handles the flip-chip bonding and offers reasonable waveguide losses for the demonstrator, i.e. $4.42 \text{ dB} \cdot \text{cm}^{-1}$. We have also showed that the glass interposer CPW lines are of no concern regarding the transmission of high-speed signals, exhibiting $3 \text{ dB} \cdot \text{cm}^{-1}$ at 58 GHz. We have validated the electrical, RF and mmW connection between the PIC25G chip and the interposer. Last but not least, we have demonstrated the optical coupling between the aforementioned photonic circuits and evaluated the coupling loss to be 18.7 dB.

V General Conclusion & Perspectives

This work proposed to assess the feasibility of a new approach to the packaging of optical transceivers based on silicon photonic technologies. In the first chapter, we have placed silicon photonic technologies in the context of data centers optical communications, firstly from a general perspective and secondly from the standpoint of STMicroelectronics' PIC25G technology. We showed that this technology is capable of light modulation and detection in the 50 Gb/s range, but the coupling with SMFs suffers from high assembly costs and a bandwidth narrower than the bandwidth required in CWDM systems. We subsequently compared different electrical interposers technologies and optical technologies to highlight that a passive, low-cost, electrical/optical glass interposer has the potential to provide 4×100 Gb/s CWDM 4λ transceivers based on SiPh. Finally, we defined objectives to achieve during this work in terms of design, fabrication and characterization of an assembly capable of demonstrating the interfacing between a fiber, an interposer and a SiPh IC.

1 Achievements versus Objectives

As stated in the first chapter, our objectives can be boiled down to:

- i. Develop a polymer-based optical technology allowing the fabrication of single mode waveguides with low coupling losses to butt-coupled SMFs and low insertion losses at 1310 nm (1 dB/cm each) on a glass substrate.
- ii. Design and fabricate a slanted mirror solution for interposer/SiPh IC coupling with an efficiency equivalent to a fiber/grating coupler coupling scheme.
- iii. Integrate, along with the optical technology, a copper RDL involving RF/mmW transmission lines able to transmit 50 Gb/s signals over a few millimeters. We targeted insertion losses below 3-dB/mm at 75 GHz.
- iv. Assemble an existing PIC25G IC with this electrical and optical interposer by flip-chip bonding and demonstrate both optical coupling and electrical continuity between the interposer and the SiPh IC.

Along chapter II, III and IV, we presented the corresponding results that are described thereafter:

- i. We investigated three different fabrication methods of polymer waveguides. One of them could be used in the final process. It consists in laser-ablated rib waveguides in photosensitive polymer resists. The fabricated waveguides are functional but they turned out to be multimode and exhibit $4.42 \text{ dB} \cdot \text{cm}^{-1}$ of

propagation losses at 1310 nm. We suspect this level of losses to come from both the sidewalls roughness and the laser impact on the core material. Despite being far from our objective, such propagation losses do not compromise our objectives on the other topics. Also, simulations allow to expect coupling losses with fiber equivalent to 0.7 dB

- ii. Thanks to FDTD simulations, we determined that a slanted mirror with an angle of 40° and relying on TIR could theoretically allow a 2.1 dB coupling efficiency at 1310 nm between an SOI waveguide and a polymer waveguide. In practice, the mirror was fabricated by a femtosecond laser ablation on a tilted sample. This component was characterized in standalone by SEM characterizations and optical measurements. The angle obtained was determined to be 40.5° , which theoretically accounts for less than 1 dB of additional losses.
- iii. The copper RDL was implemented below the optical layer by titanium-copper sputtering and by selective laser ablation structuring while electrical contacts were ensured thanks to the local removal of the optical layer, once again by selective femtosecond laser micromachining. This RDL involves CPW transmission lines characterized between 0.1 and 67 GHz. They exhibit a characteristic impedance of 46Ω throughout the measured range and an attenuation constant of $3 \text{ dB} \cdot \text{cm}^{-1}$ at 58 GHz, which is already better than PIC25G transmission lines and therefore suitable for the application as long as comparable lengths are involved. The layer also involves the routing required by the PIC25G IC for of its embedded test structures.
- iv. The PIC25G chip was flip-chip bonded to the interposer using a semi-automatic pick-and-place equipment allowing a $\pm 5 \mu\text{m}$ alignment tolerance. Subsequently, we characterized the electrical connection by measuring a transmission line passing through both the interposer and the SiPh IC and demonstrated the optical coupling thanks to the characterization of an all-optical path, also passing through both circuits. We measured 7.1 dB of insertion losses at 50 GHz and return losses below 10 dB over the entire frequency range for the electrical path. The mode profile of the output polymer WG is observable at 1310 nm and we measured total optical losses of 63 dB at 1320 nm. Finally, we demonstrated that this assembly is capable of light detection, since we measured up to 4 μA of photocurrent while illuminating a polymer WG and probing a PIC25G photodiode through the interposer. This last measurement allows us to estimate the coupling efficiency of the mirror/GC coupling structure to 18.7 dB

As a conclusion, it can be said that the objectives of this work have been achieved, at least partially, but enough to carry out the main demonstration of an optical coupling between an electrical and optical interposer and a silicon photonic integrated circuit through flip-chip assembly. This leaves plentiful of perspectives that are discussed in the next section.

2 Perspectives

2.1 Short-term perspectives

From short-term perspective, performance improvements of the components can be foreseen.

- i. The polymer WG have to be made single mode in order to be fully compatible with silicon photonic technologies. If the same fabrication method is kept, the influence of the laser exposure on the refractive index the waveguide core has to be taken into account. As demonstrated in [119], femtosecond laser exposure can induce a positive refractive index change in polymers. This change may occur in our case near the ablated areas and may be the cause of the multimode behavior that we observed. Parallely, the waveguides propagation losses have to be reduced and this goes by the reduction of sidewalls roughness. Both issues may be addressed by a nanometric etching/smoothing of the waveguide core using one or several techniques, such as, descum, plasma ashing or surface polishing by vapor phase solvent [120]. Once low-loss single mode waveguides are obtained and the effective index of the propagation mode tightly controlled, the design of the integrated multiplexer can be feasible.
- ii. Despite showing potential low losses in FDTD simulations, the estimated coupling efficiency through measurements is more than 16 dB higher than fiber/GC coupling efficiency. The causes of this difference have to be investigated in order to determine whether the glass interposer approach is competitive with respect to lateral coupling solutions through spot size converters. Three axes of development are to be considered. The first one is the optimal mirror placement. Being critical regarding coupling efficiency, the position, in every dimension, of the flip-chip bonded IC relative to the interposer has to be determined with a precision of one micrometer. The second axis is the improvement the placement precision of the mirror at fabrication level through, for example, 3D alignment and the compensation of focus variations. This goes hand in hand with a better flip-chip bonding precision, also of the order of one micrometer, that may be achievable with a

more advanced alignment methodology and optionally a more accurate machine. Last but not least, the reflective surface also plays a critical role. The impact of roughness and of a potential curvature have to be studied. This surface can undergo treatments similar to those of the waveguide core to improve its reflectivity.

- iii. The interposer CPWs are probably the most mature component of this work. However, there is still room for further improvements given the intrinsic properties of the glass substrate, especially using a thicker metal layer. A multilayer back-end would also be beneficial to enhance the redistribution capabilities.
- iv. Regarding characterizations, a few points should be taken into account. We characterized RF/mmW interconnects, all-optical coupling and light detection; the latter being done only using a constant optical input. As we were not able to validate the modulation of light by high-speed digital signals through the interposer, this point is still to be demonstrated. Also, optical characterizations still require the active alignment of the fiber. Passive alignment structures etched in the interposer could solve this drawback.

2.2 Long-term perspectives

Given the performance improvement of the interposer, this work paves the path towards lower-cost packaging of silicon photonic-based transceivers. The demonstration of a fully assembled transceiver in a small form factor pluggable is yet to be achieved. Given the multiplexing capability, this interposer technology could offer an additional candidate for the next generation of $400 \text{ Gb} \cdot \text{s}^{-1}$ transceivers. On an even longer term, the glass interposer technology is also valuable to go from the small form factor pluggable approach, which involves the separate packaging of the transceiver and the networking equipment, to the transceiver integrated on the same board as the networking equipment, as it envisioned by the Consortium for On-Board Optics (COBO) [121].

Annex A: Matlab Script for Rectangular Waveguide Modes Computation

```
clear all;
close all;
clc;
format long
% Single Mode Propagation Conditions

% Parameters
Dn = 0.008;

d = 8e-6;
Ncl = 1.56;

lambda = 1310e-9;
n0_all = [];
cmptr = 0;

for Dn = 0.0001:0.0001:0.008
    Dn
    Nco = Ncl + Dn;
    peff = 0;
    dneff = 1e-7;
    neff = Nco;
    r_1 = 1;
    r = 1e-13;
    neffs = [];
    peffs = [];

    % Planar waveguide modes
    imag(r);
    neff;
    abs(r);

    while imag(r) == 0 && neff > Ncl && abs(r) < 1e-11

        while abs(dneff) > 1e-16
```

```

        r = 2*atan(sqrt(neff*neff-Ncl*Ncl)/sqrt(Nco*Nco - neff*neff)) -
2*pi*d/lambda*sqrt(Nco*Nco - neff*neff) + peff*pi;
        if r*r_1 < 0
            dneff = -dneff/2;
            neff = neff-dneff;
        else
            neff = neff-dneff;
        end

        r_1 = r;
        dneff;
        neff;
        r;
        %cmptr = cmptr+1;
    end
    dneff;
    peff;
    neff;
    r;
    if imag(r) == 0 && neff > Ncl && abs(r) < 1e-11
        neffs = [neffs, neff];
        peffs = [peffs, peff];
        peff = peff+1;
        dneff = 1e-7;
        neff = neff-dneff;
    end
    neff;
    r;
end

r;
% neff
% cmptr

% 2D waveguide modes with effective index method

q = 0;
n0 = Nco;
dn0 = 1e-7;

n0s = [];
qs = [];
rs = [];
numel(neffs);
neffs;

for i = 1:numel(neffs)

```

```

i;
neffs;
neffs(i);
q = 0;
n0 = neffs(i);
n0s_neff_i = [];
r_1 = 1;
r = 1e-13;
dn0 = 1e-7;

while imag(r) == 0 && n0 > Ncl && abs(r) < 1e-11

    %cmptr = 0;
    while abs(dn0) > 1e-16

        r = 2*atan(sqrt(n0*n0-Ncl*Ncl)/sqrt(neffs(i)*neffs(i) -
n0*n0)) - 2*pi*d/lambda*sqrt(neffs(i)*neffs(i) - n0*n0) + q*pi;
        if r*r_1 < 0
            dn0 = -dn0/2;
            n0 = n0-dn0;
        else
            n0 = n0-dn0;
        end

        r_1 = r;
        %cmptr = cmptr+1;
    end

    n0;
    numel(n0s_neff_i);
    if imag(r) == 0 && n0 > Ncl && abs(r) < 1e-11
        n0s = [n0s, n0];
        n0s_neff_i = [n0s_neff_i, n0];
        qs = [qs, q, i];
        rs = [rs, r];
        q = q+1;
        dn0 = 1e-7;
        n0 = n0-dn0;
    end

end

n0s;
end

numel(n0s);
n0s;

```

```

qs;

if numel(n0s)<size(n0_all,1)
    n0s = [n0s, 0];
end

if numel(n0s) == 0
    n0_all = [n0_all, 0];
else
    n0s = sort(n0s, 'descend');
    Matrix_temp = zeros(numel(n0s), length(n0_all)); % The new matrix
(with zeros)
    Matrix_temp(1:size(n0_all,1), 1:length(n0_all)) = n0_all; % Overlap
the original matrix in the new matrix
    n0_all = [Matrix_temp, transpose(n0s)];
    cmptr = cmptr+1;
end

end

%n0_all = [zeros(size(n0_all,1), 3) n0_all];
Delta_n = 0.0001:0.0001:0.008;
n0_all(n0_all==0) = nan;

plot (Delta_n, n0_all, 'LineWidth', 1.5)
axis([0 0.008 1.56 1.562])
%xticks(0:0.005:0.02)
%yticks(1.5:0.005:1.52)
xlabel('\Deltan') % x-axis label
ylabel('n_0') % y-axis label
legend('TE00','TE10','TE01','TE11','Location','northwest')
set(gca, 'FontSize', 16, 'fontName','Times', 'LineWidth', 1.5);
grid on

    %r
    %n0
    %cmptr

```


Annex B: Example of a Detailed Process Sheet

Wafer name : 2017-10-17-Essai-litho-laser-Try8

Process steps		Steps	Recipe
1	Cleaning	1.1	Acetone rinse Acetone 3 min ultrasonic bath
		1.2	IPA rinse IPA 3 min ultrasonic bath
		1.3	N2 drying N2 drying
2	Back Side Ablation	2.1	Fs laser back side ablation Back side ablation for cleaving lines and alignment marks See alphacam file: 2017-10-30-Basic-devices-V3-cutting.ald
3	Spin Coating Epoclad 10	3.1	Substrate preparation Oven 30 min 200°C
		3.2	Resist spin 1 Cover: open Speed: 0 rpm Acceleration: 1000 rpm/s Time: resist deposition
		3.3	Resist spin 2 Cover: Closed Speed: 2000 rpm Acceleration: 1000 rpm/s Time: 30s
		3.4	Prebake Hotplate Temperature: 120°C Time: 5 mn
		3.5	UV Exposure Full Wafer Fluence: 10 mW/cm ² Time: 35s
		3.6	PEB Hotplate Temperature: 120°C Time: 5 min
4	Spin Coating Epocore 5	4.1	Substrate preparation Oxygen Plasma 2 min 525 mL/h 100W
		4.2	Resist spin 1 Cover: open Speed: 0 rpm Acceleration: 1000 rpm/s Time: resist deposition

		4.3	Resist spin 2	Cover: Closed Speed: 1750 rpm Acceleration: 1000 rpm/s Time: 30s
		4.4	Prebake	Hotplate Temperature: 70°C => 90°C over 4 min
5	Lithography & development	5.1	Litho laser Kloé	DXF file: 2017-10-30-Basic-Devices-V8-Litho.dxf
		5.2	resin development	Time: 60s Developer: mrDev-600 (PGMEA)
		5.3	IPA rinse	IPA rinse
		5.4	Post Exposure Bake	Temperature: 70°C => 85°C Time: 4 min
6	Spin Coating Epoclad 20	6.1	Substrate preparation	Oxygen Plasma 2 min 525 mL/h 100W
		6.2	Resist spin 1	Cover: open Speed: 0 rpm Acceleration: 1000 rpm/s Time: resist deposition
		6.3	Resist spin 2	Cover: Closed Speed: 2000 rpm Acceleration: 1000 rpm/s Time: 30s
		6.4	Prebake	Hotplate Temperature: 120°C Time: 5 mn
		6.5	UV Exposure	Full Wafer Fluence: 10 mW/cm ² Time: 60s
		6.6	PEB	Hotplate Temperature: 120°C Time: 5 min

References

- [1] Cisco, "Cisco Visual Networking Index: Forecast and Trends, 2017–2022," 2019.
- [2] Cisco, "Cisco Global Cloud Index: Forecast and Methodology, 2016–2021," 2018.
- [3] G. P. Agrawal, *Fiber-Optic Communication Systems*. Hoboken, NJ, USA: John Wiley & Sons, Inc., 2010.
- [4] T. H. Maiman, "Stimulated optical radiation in Ruby," *Nature*, 1960.
- [5] I. Hayashi, M. B. Panish, P. W. Foy, and S. Sumski, "JUNCTION LASERS WHICH OPERATE CONTINUOUSLY AT ROOM TEMPERATURE," *Appl. Phys. Lett.*, vol. 17, no. 3, pp. 109–111, Aug. 1970.
- [6] M. W. Jones and K. C. Kao, "Spectrophotometric studies of ultra-low loss optical glasses II: Double beam method," *J. Phys. E.*, 1969.
- [7] H. Kogelnik, "High-capacity optical communications: personal recollections," *IEEE J. Sel. Top. Quantum Electron.*, vol. 6, no. 6, pp. 1279–1286, Nov. 2000.
- [8] R. J. Sanferrare, "Terrestrial Lightwave Systems," *AT&T Tech. J.*, vol. 66, no. 1, pp. 95–107, Jan. 1987.
- [9] R. J. Mears, L. Reekie, I. M. Jauncey, and D. N. Payne, "Low-noise erbium-doped fibre amplifier operating at 1.54 μm ," *Electron. Lett.*, vol. 23, no. 19, p. 1026, 1987.
- [10] H. Isono, "Latest standardization trends for client and networking optical transceivers and its future directions," in *Metro and Data Center Optical Networks and Short-Reach Links*, 2018, p. 23.
- [11] ITU-T, "ITU-T G.694.2 Spectral grids for WDM applications: CWDM wavelength grid," *Telecommun. Stand. Sect. ITU*, p. 12, 2003.
- [12] ITU-T, "G.694.1 (02/2012), Spectral grids for WDM applications: DWDM frequency grid," 2012.
- [13] Corning, "How to Order Corning® SMF-28® Ultra Optical Fiber Product Information Optical Specifications," 2014.
- [14] Corning, "Corning® HI 1060 & RC HI 1060 Specialty Optical Fibers High Index / Bend Insensitive," 2010.
- [15] Corning, "Fiber Selection and Standards Guide for Premises Networks," 2013.
- [16] IEEE, "802.3-2018 - IEEE Standard for Ethernet," 2018.
- [17] Z. Zhou, R. Chen, X. Li, and T. Li, "Development trends in silicon photonics for data centers," *Opt. Fiber Technol.*, vol. 44, pp. 13–23, Aug. 2018.
- [18] D. Mahgerefteh *et al.*, "Techno-Economic Comparison of Silicon Photonics and Multimode VCSELs," *J. Light. Technol.*, vol. 34, no. 2, pp. 233–242, Jan. 2016.
- [19] C. Schinke *et al.*, "Uncertainty analysis for the coefficient of band-to-band absorption of crystalline silicon," *AIP Adv.*, 2015.

- [20] I. H. Malitson, "Interspecimen Comparison of the Refractive Index of Fused Silica*,†," *J. Opt. Soc. Am.*, vol. 55, no. 10, p. 1205, 1965.
- [21] F. Boeuf *et al.*, "Silicon Photonics R&D and Manufacturing on 300-mm Wafer Platform," *J. Light. Technol.*, vol. 34, no. 2, pp. 286–295, 2016.
- [22] F. Boeuf *et al.*, "A multi-wavelength 3D-compatible silicon photonics platform on 300mm SOI wafers for 25Gb/s applications," in *2013 IEEE International Electron Devices Meeting, 2013*, vol. 25, pp. 13.3.1-13.3.4.
- [23] L. Zehnder, *Ein neuer Interferenzrefraktor*. Springer, 1891.
- [24] R. Soref and B. Bennett, "Electrooptical effects in silicon," *IEEE J. Quantum Electron.*, vol. 23, no. 1, pp. 123–129, Jan. 1987.
- [25] P. Chevalier *et al.*, "A 55 nm triple gate oxide 9 metal layers SiGe BiCMOS technology featuring 320 GHz fT / 370 GHz fMAX HBT and high-Q millimeter-wave passives," in *2014 IEEE International Electron Devices Meeting, 2014*, vol. 2015-Febru, no. February, pp. 3.9.1-3.9.3.
- [26] G. Denoyer, A. Chen, B. Park, Y. Zhou, A. Santipo, and R. Russo, "Hybrid Silicon Photonic Circuits and Transceiver for 56Gb / s NRZ 2 . 2km Transmission over Single Mode Fiber," *Ecoc 2014*, no. 1, pp. 4–6, 2014.
- [27] S. M. Sze and K. K. Ng, *Physics of Semiconductor Devices*. Hoboken, NJ, USA: John Wiley & Sons, Inc., 2006.
- [28] L. Virot *et al.*, "Integrated waveguide PIN photodiodes exploiting lateral Si/Ge/Si heterojunction," *Opt. Express*, 2017.
- [29] Z. Lu, P. Yin, and K. Shi, "Bent Metal-Clad Waveguides for Fiber-to-Waveguide and 3D Chip-to-Chip Light Coupling Applications," in *Frontiers in Optics 2016, 2016*, p. JTh2A.161.
- [30] R. Marchetti, C. Lacava, L. Carroll, K. Gradkowski, and P. Minzioni, "Coupling strategies for silicon photonics integrated chips [Invited]," *Photonics Res.*, vol. 7, no. 2, p. 201, Feb. 2019.
- [31] F. E. Ayi-Yovo *et al.*, "Enablement of advanced silicon photonics optical passive library design leveraging silicon based RF passive development methodology," *SiRF 2016 - 2016 IEEE 16th Top. Meet. Silicon Monolith. Integr. Circuits RF Syst.*, pp. 88–90, 2016.
- [32] T. Shoji, T. Tsuchizawa, T. Watanabe, K. Yamada, and H. Morita, "Low loss mode size converter from 0.3 [micro sign]m square Si wire waveguides to singlemode fibres," *Electron. Lett.*, 2002.
- [33] G. Roelkens, P. Dumon, W. Bogaerts, D. van Thourhout, and R. Baets, "Efficient silicon-on-insulator fiber coupler fabricated using 248-nm-deep UV lithography," *IEEE Photonics Technol. Lett.*, 2005.
- [34] S. McNab, N. Moll, and Y. Vlasov, "Ultra-low loss photonic integrated circuit with membrane-type photonic crystal waveguides," *Opt. Express*, vol. 11, no. 22, p. 2927, 2003.
- [35] T. Tsuchizawa *et al.*, "Microphotonics devices based on silicon microfabrication

- technology," *IEEE J. Sel. Top. Quantum Electron.*, 2005.
- [36] B. Ben Bakir *et al.*, "Low-Loss (< 1 dB) and polarization-insensitive edge fiber couplers fabricated on 200-mm silicon-on-insulator wafers," *IEEE Photonics Technol. Lett.*, vol. 22, no. 11, pp. 739–741, Jun. 2010.
- [37] T. Barwicz *et al.*, "An O-band Metamaterial Converter Interfacing Standard Optical Fibers to Silicon Nanophotonic Waveguides," in *Optical Fiber Communication Conference*, 2015, p. Th3F.3.
- [38] T. Barwicz *et al.*, "Photonic Packaging in High-Throughput Microelectronic Assembly Lines for Cost-Efficiency and Scalability," 2015.
- [39] W. D. Sacher, T. Barwicz, B. J. F. Taylor, and J. K. S. Poon, "Polarization rotator-splitters in standard active silicon photonics platforms," *Opt. Express*, vol. 22, no. 4, p. 3777, Feb. 2014.
- [40] F. E. Ayi-yovo, "Évaluation d'un module électro-optique hybride combinant la photonique sur silicium et sur verre pour des applications de multiplexage en longueur d'onde (WDM)," UNIVERSITÉ GRENOBLE ALPES, 2017.
- [41] L. Soldano *et al.*, "Multi-wavelength 100Gb/s silicon photonics based transceiver with silica mux/demux and MEMS-coupled InP lasers," in *2017 Optical Fiber Communications Conference and Exhibition (OFC)*, 2017, pp. 1–3.
- [42] C.-C. Lee *et al.*, "An Overview of the Development of a GPU with Integrated HBM on Silicon Interposer," in *2016 IEEE 66th Electronic Components and Technology Conference (ECTC)*, 2016, vol. 2016-Augus, pp. 1439–1444.
- [43] S. Ramalingam, "3D IC Development and Key Role of Supply Chain Collaboration," 2011.
- [44] M. Sunohara, A. Shiraishi, Y. Taguchi, K. Murayama, M. Higashi, and M. Shimizu, "Development of silicon module with TSVs and global wiring (L/S=0.8/0.8 μ m)," in *Proceedings - Electronic Components and Technology Conference*, 2009.
- [45] C. W. Kaanta *et al.*, "Dual Damascene: a ULSI wiring technology," in *1991 Proceedings Eighth International IEEE VLSI Multilevel Interconnection Conference*, 1991, pp. 144–152.
- [46] M. Sunohara, H. Sakaguchi, A. Takano, R. Arai, K. Murayama, and M. Higashi, "Studies on electrical performance and thermal stress of a silicon interposer with TSVs," in *2010 Proceedings 60th Electronic Components and Technology Conference (ECTC)*, 2010, pp. 1088–1093.
- [47] S. W. Ho, S. W. Yoon, Q. Zhou, K. Pasad, V. Kripesh, and J. H. Lau, "High RF performance TSV silicon carrier for high frequency application," in *Proceedings - Electronic Components and Technology Conference*, 2008.
- [48] T. Kang and A. Yee, "A comparison of Low Cost Interposer Technologies," in *IEEE/CPMT Luncheon Meeting Contents*, 2013.
- [49] J. Dukovic *et al.*, "Through-silicon-via technology for 3D integration," in *2010 IEEE International Memory Workshop*, 2010, pp. 1–2.

- [50] R. Furuya *et al.*, "Demonstration of 2 μ m RDL wiring using dry film photoresists and 5 μ m RDL via by projection lithography for low-cost 2.5D panel-based glass and organic interposers," *Proc. - Electron. Components Technol. Conf.*, vol. 2015-July, pp. 1488–1493, 2015.
- [51] Rogers Corporation, "RO4000 ® Series High Frequency Circuit Materials," #92-004, 2006. [Online]. Available: <http://www.rogerscorp.com>.
- [52] H. Lee, K. Cho, H. Kim, S. Choi, J. Lim, and J. Kim, "Electrical performance of high bandwidth memory (HBM) interposer channel in terabyte/s bandwidth graphics module," in *2015 International 3D Systems Integration Conference, 3DIC 2015*, 2015.
- [53] H. Lu *et al.*, "Demonstration of 3-5 μ m RDL line lithography on panel-based glass interposers," in *Proceedings - Electronic Components and Technology Conference*, 2014.
- [54] Y.-H. Chen *et al.*, "Low Cost Glass Interposer Development," *Int. Symp. Microelectron.*, vol. 2014, no. 1, pp. 000397–000401, Jan. 2014.
- [55] B. R. West, "Ion-exchanged glass waveguide technology: a review," *Opt. Eng.*, vol. 50, no. 7, p. 071107, 2011.
- [56] J. Grelin, A. Bouchard, E. Ghibaudo, and J.-E. Broquin, "Study of Ag⁺/Na⁺ ion-exchange diffusion on germanate glasses: Realization of single-mode waveguides at the wavelength of 1.55 μ m," *Mater. Sci. Eng. B*, vol. 149, no. 2, pp. 190–194, Mar. 2008.
- [57] A. Tervonen, "Analysis of symmetric directional couplers and asymmetric Mach-Zehnder interferometers as 1.30- and 1.55- μ m dual-wavelength demultiplexers/multiplexers," *Opt. Eng.*, vol. 32, no. 9, p. 2083, 1993.
- [58] B. Buchold and E. Voges, "Polarisation insensitive arrayed-waveguide grating multiplexers with ion-exchanged waveguides in glass," *Electron. Lett.*, vol. 32, no. 24, p. 2248, 1996.
- [59] L. Brusberg, H. Schroder, M. Queisser, and K.-D. Lang, "Single-mode glass waveguide platform for DWDM chip-to-chip interconnects," in *2012 IEEE 62nd Electronic Components and Technology Conference*, 2012, pp. 1532–1539.
- [60] R. Osellame, G. Cerullo, and R. Ramponi, *Femtosecond Laser Micromachining*, vol. 123. Berlin, Heidelberg: Springer Berlin Heidelberg, 2012.
- [61] J. W. Chan, T. Huser, S. Risbud, and D. M. Krol, "Structural changes in fused silica after exposure to focused femtosecond laser pulses," *Opt. Lett.*, vol. 26, no. 21, p. 1726, Nov. 2001.
- [62] L. Tong, R. R. Gattass, I. Maxwell, J. B. Ashcom, and E. Mazur, "Optical loss measurements in femtosecond laser written waveguides in glass," *Opt. Commun.*, vol. 259, no. 2, pp. 626–630, Mar. 2006.
- [63] G. Douglass, F. Dreisow, S. Gross, and M. J. Withford, "Femtosecond laser written arrayed waveguide gratings with integrated photonic lanterns," *Opt. Express*, vol. 26, no. 2, p. 1497, Jan. 2018.
- [64] Q. Hivin *et al.*, "Femtosecond Pulsed Laser for Advanced Photonic Packaging," in

- 2018 7th Electronic System-Integration Technology Conference (ESTC), 2018, pp. 1–5.
- [65] A. Himeno, K. Kato, and T. Miya, “Silica-based planar lightwave circuits,” *IEEE J. Sel. Top. Quantum Electron.*, 1998.
- [66] Y. Hida, Y. Hibino, H. Okazaki, and Y. Ohmori, “10 m long silica-based waveguide with a loss of 1.7 dB/m,” in *Integrated Photonics Research*, 1995, p. IThC6.
- [67] H.-H. Hsu and S. Nakagawa, “Dry-film polymer waveguide for silicon photonics chip packaging,” *Opt. Express*, vol. 22, no. 19, p. 23379, Sep. 2014.
- [68] A. Elmogi, E. Bosman, J. Missinne, and G. Van Steenberge, “Comparison of epoxy- and siloxane-based single-mode optical waveguides defined by direct-write lithography,” *Opt. Mater. (Amst.)*, vol. 52, pp. 26–31, Feb. 2016.
- [69] E. Zraggen *et al.*, “Laser Direct Writing of Single-Mode Polysiloxane Optical Waveguides and Devices,” *J. Light. Technol.*, vol. 32, no. 17, pp. 3036–3042, Sep. 2014.
- [70] S. S. Zakariyah, “Laser Ablation for Polymer Waveguide Fabrication,” in *Micromachining Techniques for Fabrication of Micro and Nano Structures*, InTech, 2012.
- [71] K. Watanabe, A. Leinse, D. Van Thourhout, R. Heideman, and R. Baets, “Silica-based optical interposer for Si photonics,” *CLEO/Europe - EQEC 2009 - Eur. Conf. Lasers Electro-Optics Eur. Quantum Electron. Conf.*, 2009.
- [72] M. Mirshafiei, J.-P. Bérubé, S. Lessard, R. Vallée, and D. V. Plant, “Glass interposer for short reach optical connectivity,” *Opt. Express*, vol. 24, no. 11, p. 12375, 2016.
- [73] M. Immonen, M. Karppinen, and J. K. Kivilahti, “Fabrication and Characterization of Polymer Optical Waveguides With Integrated Micromirrors for Optical Interconnects,” *Electron. Packag. Manuf. IEEE Trans.*, vol. 28, no. 4, pp. 304–311, 2005.
- [74] Ik-Bu Sohn, Man-Seop Lee, and Jeong-Yong Chung, “Fabrication of optical splitter and passive alignment technique with a femtosecond laser,” *IEEE Photonics Technol. Lett.*, 2005.
- [75] M. Born, E. Wolf, and A. B. Bhatia, *Principles of Optics: Electromagnetic Theory of Propagation, Interference and Diffraction of Light*. Cambridge University Press, 2000.
- [76] E. A. J. Marcatili, “Dielectric Rectangular Waveguide and Directional Coupler for Integrated Optics,” *Bell Syst. Tech. J.*, vol. 48, no. 7, pp. 2071–2102, Sep. 1969.
- [77] A. Kumar, K. Thyagarajan, and A. K. Ghatak, “Analysis of rectangular-core dielectric waveguides: an accurate perturbation approach,” *Opt. Lett.*, vol. 8, no. 1, p. 63, Jan. 1983.
- [78] R. M. Knox and P. P. Toulous, “Integrated circuits for the millimeter through optical frequency range,” in *Symposium on Submillimeter Waves*, 1970, vol. 42, no. 4, pp. 497–516.

- [79] Corning, "Corning SMF-28e+ Optical Fiber," 2014. [Online]. Available: www.corning.com/opticalfiber.
- [80] L. Vivien *et al.*, "Comparison between strip and rib SOI microwaveguides for intra-chip light distribution," *Opt. Mater. (Amst.)*, vol. 27, no. 5, pp. 756–762, Feb. 2005.
- [81] R. A. Soref, J. Schmidtchen, and K. Petermann, "Large single-mode rib waveguides in GeSi-Si and Si-on-SiO₂," *IEEE J. Quantum Electron.*, vol. 27, no. 8, pp. 1971–1974, 1991.
- [82] S. P. Pogossian, L. Vescan, and A. Vonsovici, "The single-mode condition for semiconductor rib waveguides with large cross section," *J. Light. Technol.*, vol. 16, no. 10, pp. 1851–1853, 1998.
- [83] A. G. Rickman, G. T. Reed, and F. Namavar, "Silicon-on-Insulator Optical Rib Waveguide Loss and Mode Characteristics," *J. Light. Technol.*, vol. 12, no. 10, pp. 1771–1776, 1994.
- [84] Z. Zhu and T. Brown, "Full-vectorial finite-difference analysis of microstructured optical fibers," *Opt. Express*, vol. 10, no. 17, p. 853, Aug. 2002.
- [85] Kane Yee, "Numerical solution of initial boundary value problems involving maxwell's equations in isotropic media," *IEEE Trans. Antennas Propag.*, vol. 14, no. 3, pp. 302–307, May 1966.
- [86] D. M. Pozar, *Microwave Engineering, 4th Edition*. Wiley, 2011.
- [87] C. VEYRES and V. FOUAD HANNA, "Extension of the application of conformal mapping techniques to coplanar lines with finite dimensions," *Int. J. Electron.*, vol. 48, no. 1, pp. 47–56, Jan. 1980.
- [88] S. B. Cohn, "Thickness Corrections for Capacitive Obstacles and Strip Conductors," *IEEE Trans. Microw. Theory Tech.*, vol. 8, no. 6, pp. 638–644, Nov. 1960.
- [89] H. A. Wheeler, "Formulas for the Skin Effect," *Proc. IRE*, vol. 30, no. 9, pp. 412–424, Sep. 1942.
- [90] R. A. Matula, "Electrical resistivity of copper, gold, palladium, and silver," *J. Phys. Chem. Ref. Data*, vol. 8, no. 4, pp. 1147–1298, Oct. 1979.
- [91] SCHOTT AG, "Electrical Properties of SCHOTT Thin Glasses," 2019. [Online]. Available: <https://www.schott.com/d/corporate/6a54c237-f03d-4699-987e-3edd56dd66a7/row-schott-electrical-properties-datenflyer-view-2019-05-24.pdf>. [Accessed: 13-Sep-2019].
- [92] F. E. Ayi-Yovo *et al.*, "Enablement of advanced silicon photonics optical passive library design leveraging silicon based RF passive development methodology," in *SiRF 2016 - 2016 IEEE 16th Topical Meeting on Silicon Monolithic Integrated Circuits in RF Systems*, 2016.
- [93] C. B. Schaffer, A. Brodeur, and E. Mazur, "Laser-induced breakdown and damage in bulk transparent materials induced by tightly focused femtosecond laser pulses," *Meas. Sci. Technol.*, vol. 12, no. 11, pp. 1784–1794, Nov. 2001.
- [94] K. D. Moll, A. L. Gaeta, and G. Fibich, "Self-Similar Optical Wave Collapse: Observation of the Townes Profile," *Phys. Rev. Lett.*, vol. 90, no. 20, p. 203902, May

2003.

- [95] Y. Bellouard, A. Said, M. Dugan, and P. Bado, "Fabrication of high-aspect ratio, microfluidic channels and tunnels using femtosecond laser pulses and chemical etching," *Opt. Express*, vol. 12, no. 10, p. 2120, 2004.
- [96] C. S. R. Nathala *et al.*, "Ultrashort laser pulse ablation of copper, silicon and gelatin: effect of the pulse duration on the ablation thresholds and the incubation coefficients," *Appl. Phys. A*, vol. 122, no. 2, p. 107, Feb. 2016.
- [97] D. Nieto, J. Arines, G. M. O'Connor, and M. T. Flores-Arias, "Single-pulse laser ablation threshold of borosilicate, fused silica, sapphire, and soda-lime glass for pulse widths of 500 fs, 10 ps, 20 ns," *Appl. Opt.*, vol. 54, no. 29, p. 8596, Oct. 2015.
- [98] A. Masuno, N. Nishiyama, F. Sato, N. Kitamura, T. Taniguchi, and H. Inoue, "Higher refractive index and lower wavelength dispersion of SiO₂ glass by structural ordering evolution via densification at a higher temperature," *RSC Adv.*, vol. 6, no. 23, pp. 19144–19149, 2016.
- [99] A. Pasquarello and R. Car, "Identification of Raman Defect Lines as Signatures of Ring Structures in Vitreous Silica," *Phys. Rev. Lett.*, vol. 80, no. 23, pp. 5145–5147, Jun. 1998.
- [100] L. Bergé, S. Skupin, R. Nuter, J. Kasparian, and J.-P. Wolf, "Ultrashort filaments of light in weakly ionized, optically transparent media," *Reports Prog. Phys.*, vol. 70, no. 10, pp. 1633–1713, Oct. 2007.
- [101] Elga Europe, "Ordyl Sy 300," 2014.
- [102] P. Vulto *et al.*, "Microfluidic channel fabrication in dry film resist for production and prototyping of hybrid chips," *Lab Chip*, vol. 5, no. 2, p. 158, Feb. 2005.
- [103] M. Born *et al.*, *Principles of Optics*, 7th ed. Cambridge: Cambridge University Press, 1999.
- [104] P. B. Zantye, A. Kumar, and A. K. Sikder, "Chemical mechanical planarization for microelectronics applications," *Mater. Sci. Eng. R Reports*, vol. 45, no. 3–6, pp. 89–220, Oct. 2004.
- [105] S. Balakumar *et al.*, "Peeling and delamination in Cu/SiLK™ process during Cu-CMP," *Thin Solid Films*, vol. 462–463, no. SPEC. ISS., pp. 161–167, Sep. 2004.
- [106] Micro Resist Technology GmbH, "EpoCore & EpoClad Serien." [Online]. Available: <https://www.microresist.de/en/products/negative-photoresists/uv-lithography-broadband-and-i-line-exposure/epocore-epoclad-serien>. [Accessed: 01-Jun-2018].
- [107] Bruker, "ContourGT-X 3D Optical Microscope," 2013. [Online]. Available: https://www.bruker.com/fileadmin/user_upload/8-PDF-Docs/SurfaceAnalysis/3D-OpticalMicroscopy/DataSheets/DS552-RevA0-ContourGTK_3D_Optical_Microscope-Datasheet.pdf.
- [108] S. S. Zakariyah *et al.*, "Polymer Optical Waveguide Fabrication Using Laser Ablation," 2009.
- [109] S. S. Zakariyah *et al.*, "Fabrication of Polymer Waveguides by Laser Ablation Using

- a 355 nm Wavelength Nd:YAG Laser," *J. Light. Technol.*, vol. 29, no. 23, pp. 3566–3576, Dec. 2011.
- [110] A. A. Serafetinides, M. I. Makropoulou, C. D. Skordoulis, and A. K. Kar, "Ultra-short pulsed laser ablation of polymers," *Appl. Surf. Sci.*, vol. 180, no. 1–2, pp. 42–56, Aug. 2001.
- [111] J. A. Jacquez and H. F. Kuppenheim, "Theory of the Integrating Sphere," *J. Opt. Soc. Am.*, vol. 45, no. 6, p. 460, Jun. 1955.
- [112] K. Demir, A. Armutlulu, J. Tong, R. Pucha, V. Sundaram, and R. Tummala, "First demonstration of reliable copper-plated 30 μm diameter through-package-vias in ultra-thin bare glass interposers," in *2014 IEEE 64th Electronic Components and Technology Conference (ECTC)*, 2014, pp. 1098–1102.
- [113] Z. Liu *et al.*, "Electroless and Electrolytic Copper Plating of Glass Interposer Combined with Metal Oxide Adhesion Layer for Manufacturing 3D RF Devices," in *2016 IEEE 66th Electronic Components and Technology Conference (ECTC)*, 2016, vol. 2016-Augus, pp. 62–67.
- [114] R. Behrisch and W. Eckstein, "Introduction and Overview," in *Sputtering by Particle Bombardment*, vol. 110, Berlin, Heidelberg: Springer Berlin Heidelberg, 2007, pp. 1–20.
- [115] J. A. Thornton, "The microstructure of sputter-deposited coatings," *J. Vac. Sci. Technol. A Vacuum, Surfaces, Film.*, vol. 4, no. 6, pp. 3059–3065, Nov. 1986.
- [116] L. Zhang, C. He, Y. Guo, J. Han, Y. Zhang, and X. Wang, "Development of SnAg-based lead free solders in electronics packaging," *Microelectron. Reliab.*, vol. 52, no. 3, pp. 559–578, Mar. 2012.
- [117] R. G. Hunsperger, *Integrated Optics: Theory and Technology*, vol. 33. Berlin, Heidelberg: Springer Berlin Heidelberg, 1991.
- [118] F. Purroy and L. Pradell, "New theoretical analysis for the LRRM calibration technique for vector network analyzers," *IEEE Trans. Instrum. Meas.*, vol. 50, no. 5, pp. 1307–1314, Oct. 2001.
- [119] W. Watanabe, S. Sowa, T. Tamaki, K. Itoh, and J. Nishii, "Three-Dimensional Waveguides Fabricated in Poly(methyl methacrylate) by a Femtosecond Laser," *Jpn. J. Appl. Phys.*, vol. 45, no. No. 29, pp. L765–L767, Jul. 2006.
- [120] C. Matellan and A. E. del Río Hernández, "Cost-effective rapid prototyping and assembly of poly(methyl methacrylate) microfluidic devices," *Sci. Rep.*, vol. 8, no. 1, p. 6971, Dec. 2018.
- [121] Consortium For On-Board Optics, "The Use of On-Board Optic Compliant Modules in Coherent Applications," 2019.
- [122] W. Bogaerts, "Lecture: Coupling light to silicon photonic circuits," *Helios*, no. November, 2009.
- [123] H. Schröder and L. Brusberg, "Thin glass based electro-optical circuit board (EOCB): Waveguide process, PCB technology, and coupling interfaces," 2015 IEEE CPMT Symposium Japan (ICSJ), 2015

List of Related Publications

J.M. Boucaud, F.E. Ayi-Yovo, Q. Hivin, C. Durand, F. Giancesello, D. Bucci, J.E. Broquin, G. Ducournau, J.F. Robillard, E. Dubois, "Cost Effective Integration of Optical Waveguides on Thin Glass Interposer", *5th Micro/Nano-Electronics Packaging and Assembly, Design and Manufacturing Forum (MINAPAD)*, Grenoble, France, 2017

J.M. Boucaud, Q. Hivin, C. Durand, F. Giancesello, D. Bucci, J.F. Robillard, F. Vaurette, J.E. Broquin, E. Dubois, "Single Mode Polymer Optical Waveguides and Out-of-plane Coupling Structure on a Glass Substrate", *2018 7th Electronic System-Integration Technology Conference (ESTC)*, Dresden, Germany, 2018

Q. Hivin, J.M. Boucaud, F. Braud, C. Durand, F. Giancesello, D. Bucci, J.F. Robillard, J.E. Broquin, C. Gaquière, E. Dubois, "Femtosecond Pulsed Laser for Advanced Photonic Packaging," *2018 7th Electronic System-Integration Technology Conference (ESTC)*, Dresden, 2018, pp. 1-5.

J.M Boucaud; F.E. Ayi-Yovo; Q. Hivin; M. Berthomé; C. Durand; F. Giancesello; D. Bucci; G. Ducournau; J.F. Robillard; J.E. Broquin; E. Dubois, "Cost Effective Laser Structuration of Optical Waveguides on Thin Glass Interposer", *Journal of Lightwave Technology*, Volume: 35, Issue: 20, 2017

List of Figures

Figure 1: Exponential growth of the bit rate · distance product [7]	15
Figure 2: Schematic diagram of a generic optical link	17
Figure 3: Block Diagram of optical transmitters using (a) a Directly Modulated Laser (DML) and (b) an Externally Modulated Laser (EML) [3]	17
Figure 4: NRZ (a) and PAM4 (b) modulation formats.....	18
Figure 5: Core and cladding layers of an optical fiber.....	18
Figure 6: Block diagram of an optical receiver [3]	19
Figure 7: Application space in current data centers based on (a) transmission reach and fiber type, (b) loss budget, or (c) technology [18].....	21
Figure 8: Manufacturing process of SOI rib waveguides [Boeuf et al. 2016]	22
Figure 9: TEM cross section of a SOI rib waveguide	23
Figure 10: Schematic of (a) a directional coupler and (b) a Y junction.....	23
Figure 11: Fabrication process of high-speed phase modulators [Boeuf et al. 2016]	24
Figure 12: TEM cross section of a HSPM [21].....	24
Figure 13: Fabrication process of an integrated waveguides Ge photodiode [Boeuf et al. 2016]	25
Figure 14: TEM cross section and top view of a Ge HSPD	25
Figure 15: Schematic of a SOI rib waveguide in front of an SMF core	26
Figure 16: Grating coupler – SMF coupling scheme [122]	26
Figure 17: SEM top views of (a) an SPGC and (b) a PSGC [22].....	27
Figure 18: Schematic of a standard SOI EC for coupling light between an SOI waveguide and a tapered single-mode fiber. The waveguide is tapered down to a small tip to allow mode expansion in the horizontal direction, whereas an overlay of polymer, Si ₃ N ₄ , SiON, or	28
Figure 19: Optical design of the metamaterial fiber interface. (a) Schematic top view of the three sections of the mode size convertor. (b) Cross-sectional diagram of the metamaterial waveguide. PECVD stands for plasma-enhanced chemical vapor deposition. The refractive index of the fluid or adhesive must be under 1.445 at 1310 nm. (c) Detailed top view of the metamaterial fiber coupler. (d) Detailed top view of the transition from a metamaterial to a hybrid waveguide.[37]	28
Figure 20: Assembly strategy of a 100G PSM4 silicon photonic transceiver [22]	29
Figure 21: CWDM Transceiver in housing without lid (a). Enlargement of the optical engine (b) [41].....	30
Figure 22: Generic schematic of an electrical interposer	31
Figure 23: Dual Damascene process [45].....	32

Figure 24: TSV fabrication process [49]	33
Figure 25: Semi-additive process on organic substrate [50]	33
Figure 26: Ion-exchanged waveguides process.....	35
Figure 27: Silica PLC fabrication process [65]	36
Figure 28: Fabrication of polymer waveguides by photolithography	37
Figure 29: Fabrication process of polymer waveguides by laser ablation.....	37
Figure 30: Electrical and Optical Interposer Approach for silicon photonic transceivers	40
Figure 31: 3D view of the electrical and optical interposer proposed approach	40
Figure 32: Schematic of the refraction principle.....	44
Figure 33: Schematic of a 2D slab WG cross-section	45
Figure 34: 3D Rectangular waveguide cross section.....	48
Figure 35: Effective index method for a rectangular waveguide with a unique cladding material	49
Figure 36: Computation of modes index n_0 vs refractive index difference Δn in an $8 \mu\text{m} \times$ $8 \mu\text{m}$ waveguide using the effective index method	50
Figure 37: Rib waveguide cross-section.....	50
Figure 38: Effective index method applied to a rib waveguide topology	51
Figure 39: r and t parameters in function of WG slab part h . Single mode conditions are verified for $r > 0.5$ equation (18) and eq (19) whose lower limit is represented by the green line.	52
Figure 40: Cross section of the simulated rectangular waveguide in the simulation plane with PML boundaries.....	52
Figure 41: (a) TE_{00} , (b) TE_{01} , (c) TE_{10} modes E field distribution across the waveguide cross section	53
Figure 42: Cross section of the simulated rib waveguide in the simulation plane with PML boundaries	53
Figure 43: (a) TE_{00} , (b) TE_{01} , (c) TE_{10} modes E field distribution across rib waveguides cross section with a height H of $8 \mu\text{m}$, a width a of $8 \mu\text{m}$ and respective slab thicknesses h of 4 , 2.9 and $6.4 \mu\text{m}$	54
Figure 44: Fundamental mode E field distribution (a) of the simulated SMF28 fiber (b)56	
Figure 45: Power coupling ratio vs (a) WG width and height for a rectangular waveguide and (b) slab thickness for a rib waveguide. Values represented by a cross indicate a multimode behavior	56
Figure 46: 3D schematic of (a) a stripline, (b) a microstrip and (c) a CPW.....	57
Figure 47: Voltage and current definitions and equivalent circuit for an incremental length of transmission line. (a) Voltage and current definitions. (b) Lumped-element equivalent circuit. [86].....	58

Figure 48: A transmission line terminated in a load impedance ZL [86]	59
Figure 49: Cross-section schematic of a CPW with ADS CPW model parameters	60
Figure 50: Attenuation coefficient in dB/cm (a) and real part of the characteristic impedance (b) of 4 CPWs simulated using ADS model with widths varying from 15 μm to 85 μm	61
Figure 51: Cross section of the CPW with polymer layers.	62
Figure 52: Attenuation coefficient and real part of the characteristic impedance of the ADS model (blue line) and HFSS simulated (red line) CPWs.....	63
Figure 53: MZM differential travelling wave electrodes (TWE) and differential drive [26]	63
Figure 54: Modeling a line section of the form modulator electrode.....	64
Figure 55: Modeling of a line section of the modulator with an inductor	64
Figure 56: Return loss (a) and insertion loss (b) of MZM electrodes terminated by a 35 Ω load with and without discrete inductors.....	65
Figure 57: Simulation of an optical eye diagram at the output of a 2.8 mm long modulator with inductors in response to a 25 Gb · s – 1 PRBS with 2.5 V between the 1 and 0 state.	65
Figure 58: Elementary cell of the MZM with inductors	66
Figure 59: 2.1mm MZM with inductors	66
Figure 60: Coupling scheme between a polymer waveguide and a silicon-on-insulator waveguide	67
Figure 61: PIC/Interposer coupling modelling methodology.....	68
Figure 62: Schematic of the simulation setup showing (a) the top and (b) cross-section views of the modeled SPGC, the input mode source, the linear and areal output fields monitors.....	69
Figure 63: Distribution of the E field intensity on top of the simulated SPGC obtained using the 2D monitor of Figure 62.....	70
Figure 64: SiPh IC/Interposer simulation setup	70
Figure 65: (a) Coupling ratio between the GC and the polymer waveguide of the glass interposer (2D simulation) and (b) E field intensity in the simulation plane	71
Figure 66: Coupling efficiency versus mirror angle at optimum position, 2D vs 3D	72
Figure 67: Fabrication sequence of surface U-shaped optical guide in a thin glass substrate: (a) localized laser-induced modification of glass microstructure, (b) U-groove etching based on locally enhanced HF etching rate, (c) dry film polymer lamination to fill the groove and (d) planarization of the core material using CMP.	74
Figure 68: SEM cross-section of a micro-groove obtained by laser inscription performed with following parameters: repetition rate 30 kHz, average power of 0.12W, scanning speed of 8 mm/s and HF etching for 2.5 min.....	77

Figure 69: SEM cross-section of a micro-groove after lamination of an ORDYL SY317 dry film with a roll temperature of 110°C. Five passes of lamination were applied at a pressure corresponding to a static load of 12 kg. A HMDS adhesion promoter was vapor-stream-deposited prior to the dry film application.	78
Figure 70: Refractive index of Ordyl SY317 after 5 passes of hot roll lamination performed at 110°C. The refractive index can be modulated by post-lamination UV exposure that enhances the cross-linking degree of the polymer.....	78
Figure 71: Picture showing a 3 inches 500µm thick AF32 Eco glass substrate after laser inscription, HF etching and lamination of an ORDYL SY317 dry film. The layout contains straight and bent waveguides as well as Y junctions.	79
Figure 72: SEM picture showing a cross-section of a surface waveguide after the CMP step. The core hemicylinder is composed of ORDYL SY317, the bottom cladding is a glass substrate AF32 Eco.....	80
Figure 73: Fabrication steps of the waveguides: (a) trenches ablation on the back side of the wafer using the fs laser. First cladding layer pin-coating, prebake, flood exposure and PEB (b). Core layer spin-coating and prebake (c). CW UV laser lithography (d). Development and PEB of the core layer (e). Spin-coating, prebake, flood exposure and PEB of the second cladding (f).....	81
Figure 74: SEM picture of the Epocore 5 XP layer spun with a rotation speed of 1500 rpm	81
Figure 75: Measured and Datasheet spin curves of Epocore 5 XP	82
Figure 76: Schematic of the lithography calibration layout.....	83
Figure 77: Elevation profile of a typical waveguide core made by laser lithography.....	84
Figure 78: (a) SEM picture of a waveguide cross section, (b) optical microscope picture of the edge of a waveguide structure and (c) optical microscope picture of the Y-junction.	85
Figure 79: Superimposition of the backside cleaving trenches layout (blue lines) and laser lithography layout (green lines) for waveguides optimization. The green layout contains laser paths to fabricate straight and bent waveguides, Y junctions, directional couplers and Mach-Zehnder interferometer	85
Figure 80: Schematic of the optical test structures, namely (a) bent waveguides, (b) directional couplers, (c) Y junctions and (d) Mach-Zehnder Interferometers, along with their respective characteristic dimensions	86
Figure 81: Fabrication process of laser ablated polymer waveguides	87
Figure 82: Refractive indexes versus wavelength of the core and cladding materials, measured by spectroscopic ellipsometry	89
Figure 83: Transmission spectrum measurement methods: (a) direct transmission and (b) total transmission.....	90

Figure 84: Direct transmission spectrum of a 10 μm thick GX-T31 film (turquoise curve), a 35 μm thick GY11 film (orange curve), the four experimental materials provided by Ajinomoto (purple, green, red and blue curves) with respective thickness of 10 μm , 15 μm , 10 μm and 10 μm , and the 500 μm thick AF32 substrate only (dark blue curve)	90
Figure 85: GX-T31 direct and total transmission spectra of 10 μm (blue curve direct transmission, red curve total transmission) and 20 μm (green curve direct transmission, purple curve total transmission) thick films	91
Figure 86: GY11 direct and total transmission spectra of 35 μm (blue curve direct transmission, red curve total transmission) and 70 μm (green curve direct transmission, purple curve total transmission) thick films	92
Figure 87: Material n°1 direct and total transmission spectra of 10 μm (blue curve direct transmission, red curve total transmission) and 20 μm (green curve direct transmission, purple curve total transmission) thick films	92
Figure 88: Cross-section of one pass laser trenches at 78, 96, 113 and 131 mW of average optical powers, at a pulse repetition frequency of 100 kHz and a scanning speed of 20 mm/s	93
Figure 89: SEM cross-section of two 30 μm · 45 μm laser ablated trenches with optical powers of (a) 70 and (b) 100 mW at 200 kHz and respective sidewalls angle of 70° and 80°	94
Figure 90: Width at the top and at the bottom of the core structure versus layout spacing between trenches	95
Figure 91: SEM picture of (a) the top view, (b) the angled view and (c) the cross-section of the fabricated structure	95
Figure 92: Ablation profile for 1 mm/s, 2 mm/s, 4 mm/s and 20 mm/s at a constant pitch of impact (Wafer n°2)	97
<i>Figure 93: Ablation profile for a scanning speed of 4 mm/s, an 8 kHz pulse repetition frequency and an average power of 110 mW at 200 kHz. The core/bottom cladding interface is represented by the horizontal orange line</i>	<i>97</i>
Figure 94: Complete fabrication process of the optical and electrical glass interposer involving the following steps: (1) back-side cleaving trenches ablation, (2) copper sputtering, (3) RDL structuration, (4) first waveguide cladding deposition, (5) waveguide core deposition, (6) rib waveguide structuring by fs laser ablation, (7) second waveguide cladding deposition, (8) contact holes and mirrors ablation, (9) flip-chip bonding.....	99
Figure 95: SEM measured thicknesses of Ti coated silicon samples for 100, 200 and 300 s.	101
Figure 96: SEM cross-section of the copper coated silicon samples for (a) 100 s, (b) 200 s and (c) 300 s.....	101

Figure 97: (a) SEM cross-section of the 3.3 μm copper layer obtained performing 5 cycles of deposition during 200s with a 300s pause to avoid sample heating. (b) Thickness versus deposition time for 100 s, 200 s, 300 s and 5 · 200 s durations.....	102
Figure 98: Optical microscope pictures of the fabricated structures: (a) on-wafer RF characterization pads and (b) flip-chip bonding pads.....	103
Figure 99: Optical microscope pictures of the grid test structures for laser powers of 20, 30 and 60 % and pulse repetition frequencies of 20, 110, 140 and 200 kHz giving ablation widths ranging from 10 to 20 μm	104
Figure 100: Optical microscope pictures of (a) a flip-chip bonding pad, (b) 2 parallel CPWs and their characterization pads on the right, (c) 100 μm wide alignment cross and (d) 5 μm wide inverted alignment cross. (e) Schematic of the fabricated CPW cross section. (f) macroscopic picture the interposer RDL.	105
Figure 101: Optical microscope pictures of the polymer rib waveguide on top of the copper layer.....	106
Figure 102: Layout of the laser path for the ablation of flip-chip bonding pads openings (red lines).....	106
Figure 103: (a) Optical microscope picture of the flip-chip bonding pads openings. (b) Profile of a flip-chip bonding pad opening. (c) Macroscopic picture of a cleaved interposer with openings.....	107
Figure 104: Schematic of the TIR mirror laser ablation setup	107
Figure 105: SEM picture of the cleaved edge of a sample in which the TIR mirror is structured. The ABF layer was implemented in the first tests but subsequently removed to reduce the stack height.....	108
Figure 106: TIR mirror angle versus holder angle compared to a theoretical refracted ray in the polymer layer and a theoretical straight ray.....	108
Figure 107: Layout of a single photodiode test structure.....	109
Figure 108: Layout of the PIC25G test chip. It includes: (1) photodiodes test structures, (2) single mode waveguides connecting one side of the chip (a) to the other (b), (3) more photodiodes, two Mach-Zehnder modulators, (6) and (7), and their optical I/O grating couplers (4) as well as two RF/mmW transmission lines (5).	110
Figure 109: Macroscopic pictures of the wafers at different fabrication steps: after the RDL structuration (a), after the ablation of the rib waveguides (b) and after the ablation of the probing and bonding areas in the polymer layer (c).....	111
Figure 110: Superimposed layouts of the copper RDL mask (green lines), the rib waveguides (grey lines) and mirror trenches (blue lines).....	112
Figure 111: Superimposed layouts of the Copper RDL (purple lines), probing areas and wholes for flip-chip bonding (blue areas)	113

Figure 112: Superimposed layouts of the mirror alignment fiducial and mirrors ablation paths in the top right corner.	114
Figure 113: Schematic of the alignment method for the ablation of mirrors	114
Figure 114: Eutectic cycle of the flip-chip assembly (a) and side camera picture of the interposer and PIC25G IC during assembly (b)	115
Figure 115: Macroscopic picture of the PIC25G assembled with the electrical and optical glass interposer	115
Figure 116: Optical microscope pictures of the back-side of the assembly, focus being done at the SiPh IC surface (a) and the interposer RDL level (b)	116
Figure 117: Schematic of the mode profile measurement bench	118
Figure 118: Picture taken from the top camera during the mode profile measurement of a waveguide at 630 nm	119
Figure 119: Mode profiles of a polymer/glass waveguide at (a) 1310 nm and (b) 1550 nm	120
Figure 120: Mode profiles of directional couplers with coupling lengths of (a) 2 mm, (b) 3 mm and (c) 4 mm. White arrows point the waveguides where light is injected.	122
Figure 121: Mode profile of a Y junction	122
Figure 122: Examples of typical laser lithography waveguides defects. Epocore 5 waveguide mode profiles at 658 nm (a) after 120°C 10 min final post exposure bake (PEB), (b) after 140°C 30 min hard bake and (c) after 250°C 5 min flip-chip simulation. Waveguides presenting defects with the following process specificities: (d) uncovered core exposed to a 140°C 60 min hard bake and 250°C 5 min final hard bake, 120°C 5 min final PEB (e) before and (f) after 250 °C min flip- chip simulation.	123
Figure 123: Mode profiles of the core structure fabricated by the laser ablation of two trenches inside Ajinomoto dry films at (a)1550 nm and (b) 1310 nm	124
Figure 124: Mode profiles (left column) at high optical power and (right column) at low optical power of three waveguides at 1310 nm, representative of the tested configurations (a), (b) and (c) whose parameters are shown on the right part of the figure.....	125
Figure 125: Mode profile at 1310 nm of waveguides integrated with the electrical RDL (a) before and (b) after flip-chip bonding of the PIC25G. Colorized mode profiles of a waveguide before flip-chip with a slight displacement of the injection fiber to the left (c) and to the right (d).....	125
Figure 126: Schematics of the measurement setups for measuring (a) the reference power using spliced fibers, a laser source, a power meter, as well as micro positioners, and (b) the waveguide losses using the same equipment with the fibers cleaved.....	126
Figure 127: Average and standard deviation of the total optical loss of eight laser ablated polymer waveguides before and after flip-chip bonding at 1310 nm	128

Figure 128: Total optical loss of the best laser ablated waveguide between 1260 nm and 1340 nm	129
Figure 129: Schematic of the 0.1 - 67 GHz S parameters measurement bench	130
Figure 130: Open and Short deembedding structures fabricated on the interposer.....	130
Figure 131: Attenuation coefficient (a) and real part of the characteristic impedance of the 938 mm long interposer CPWs with widths of (red line) 85 μm , (blue line) 60 μm , (purple line) 15 μm	131
Figure 132: RLCG parameters extracted from the measured S parameters of the 85 μm (red curves) and from the simulated S parameters of the 2-port component parametrized with the same length (blue curves).....	133
Figure 133: Schematic of the mirror angle measurement bench	134
Figure 134: SolidWorks schematic of the rotating arm, (a) front view and (b) isometric view.....	134
Figure 135: Schematic of the mirror angle measurement principle	135
Figure 136: Total loss measured versus fiber angle	135
Figure 137: Schematic of the RF/mmW test structure.....	136
Figure 138: Return loss and insertion loss of the RF/mmW path through the assembly	137
Figure 139: Return loss and reflection coefficient of the 3.5 mm long MZM without inductors	138
Figure 140: Return loss and reflection coefficient of the 3.5 mm long MZM with inductors	138
Figure 141: Simplified schematic of the HSPM test structure	139
Figure 142: Return loss of the original HSPM simulation without inductors using spice models (blue curve), the measurement deembedded from the interposer CPW (pink curve) and the HSPM retro-simulation using spice models with an open circuit in the place of the 35 Ω load at the end of the circuit. (red curve).....	139
Figure 143: Schematic of the optical path test structure	140
Figure 144: Mode profiles of the optical path test structure at (a) 1277 nm, (b) 1278 nm, (c) 1279 nm, (d) 1280 nm, (e) 1281 nm and (f) 1282 nm.....	140
Figure 145: Total loss of the optical path test structure versus wavelength associated to the optical path described in Figure 143.....	141
Figure 146: Schematic of the principle of the optical coupling measurement through embedded photodiodes.	142
Figure 147: Macroscopic picture of a demonstrator during the optical coupling measurement through embedded photodiodes.....	142
Figure 148: I(V) characteristic of the 1290 nm test structure illuminated with a 1 mW laser source at 1265 nm (red) and without light (blue)	143

Figure 149: Loss of the optical path from the laser source to the photodiode of photodiode test structures 1270 nm, 1290 nm, 1310 nm, 1330 nm.....144

List of Tables

Table 1: Main characteristics of three different optical fibers.....	19
Table 2: 100Gb/s Ethernet Standards [16]	20
Table 3: 400 Gb/s Ethernet Standards.....	20
Table 4: 100 Gb/s Multi-Source Agreement standards for short-reach interconnects	21
Table 5: Summary of the main SiPh IC coupling strategies.....	29
Table 6: Comparison of interposer core materials.....	39
Table 7: Comparison of optical technologies on a glass substrate.....	40
Table 8: Modeled layers and their respective refractive index and thickness	71
Table 9: Width of the fabricated structures versus laser lithography parameters	84
Table 10: Second set of laser parameters	94
Table 11: Summary of the materials and laser parameters tested for the fabrication of laser ablated rib waveguides	96
Table 12: Polymer waveguide technologies comparison	98
Table 13: Tested subtractive process for the glass interposer.....	103
Table 14: Relevant waveguides configurations and mode profiles	121
Table 15: Value and extraction method of CPW model component parameters.....	133

List of Acronyms

ABF	Ajinomoto Build-up Film
ADS	Advanced Design System
AFT	Ajinomoto Fine Techno
BEOL	Back-End of Line
CE	Coupling Efficiency
CMOS	Complementary Metal Oxide Semiconductor
CMP	Chemical Mechanical Polishing
CTE	Coefficient of Thermal Expansion
CW	Continuous Wave
CWDM	Coarse Wavelength Division Multiplexing
DC	Data Center
DFB	Distributed Feedback
DML	Directly Modulated Laser
DWDM	Dense Wavelength Division Multiplexing
EC	Edge Coupler
EIC	Electronic Integrated Circuit
EM	Electromagnetic
EML	Externally Modulated Laser
ER	Extinction Ratio
FDE	Finite Difference Eigenmode
FDTD	Finite Difference Time Domain
FHD	Flame Hydrolysis Deposition
FPGA	Field Programmable Gate Array
GC	Grating Coupler

GPU	Graphics Processing Unit
HDI	High Density Interposer
HF	Hydrofluoric
HMDS	Hexamethyldisilazane
HSPD	High Speed Photodiode
HSPM	High Speed Phase Modulator
IC	Integrated Circuit
InP	Indium Phosphide
I/O	Input/Output
LAZ	Laser Affected Zone
LRRM	Line Reflect Reflect Match
MEMS	Micro Electro-Mechanical System
MFD	Mode Field Diameter
MMF	Multimode Fiber
mmW	Millimeter Wave
MSA	Multi-Source Agreement
MZM	Mach-Zehnder Modulator
NRZ	Non-Return to Zero
OFC	Optical Fiber Communication
OSAT	Out-source Semiconductor Assembly and Test
PAM4	4-Level Pulse Amplitude Modulation
PCB	Printed Circuit Board
PEB	Post Exposure Bake
PIC	Photonic Integrated Circuit
PLC	Planar Lightwave Circuit
PML	Perfectly Matched Layer
PNA	Power Network Analyzer

PRBS	Pseudo Random Binary Sequence
PSGC	Polarization Splitting Grating Coupler
PSM4	Parallel Single Mode 4
RDL	Redistribution Layer
RF	Radio Frequency
SAP	Semi-Additive Process
SEM	Scanning Electron Microscope
SDM	Space Division Multiplexing
SiPh	Silicon Photonic
SMF	Single Mode Fiber
SMU	Source/Measurement Unit
SMWG	Single Mode Waveguide
SOI	Silicon on Insulator
SPGC	Single Polarization Grating Coupler
SSC	Spot Size Converter
TIR	Total Internal Reflection
TPV	Through Package Via
TSV	Through Silicon Via
UHNA	Ultra High Numerical Aperture
VCSEL	Vertical Cavity Surface Emitting Laser
WDM	Wavelength Division Multiplexing
WG	Waveguide

Résumé

Le trafic de données interne aux *datacenters* a connu une croissance exponentielle ces dernières années avec une mise sous pression permanente de la capacité de stockage, du débit et du temps de latence. Une conséquence directe de cette course à la performance est l'amélioration inexorable des technologies d'interconnexion pour répondre à cette demande. Dans la recherche de communications à fibre optique à faible coût pour les *datacenters*, la photonique sur silicium, une technologie électro-optique dérivée des technologies CMOS standard, apparaît comme une solution prometteuse pour réduire la consommation d'énergie, améliorer les débits de données des liaisons optiques tout en restant économiquement rentable. Bien que les procédés technologiques associés aux plateformes CMOS puissent être judicieusement exploités pour l'intégration monolithique de fonctions optiques extrêmement denses et performantes, la photonique sur silicium présente néanmoins des contraintes de packaging supplémentaires liées à l'interfaçage avec les fibres optiques d'entrée/sortie. Ces contraintes d'assemblage entraînent un accroissement substantiel du coût des émetteurs-récepteurs optiques à base de puces photoniques silicium et compliquent la mise en œuvre de technologies telles que le multiplexage en longueur d'onde à bas coût (CWDM).

L'objectif premier de cette thèse est d'étudier et développer une version bas coût d'interposeur embarquant des fonctions électriques et optiques intégrés à un substrat de verre. L'ambition consiste à réaliser l'assemblage passif complet d'un émetteur-récepteur CWDM basé sur la technologie photonique sur silicium PIC25G de STMicroelectronics.

En premier lieu, ce travail propose la conception des principales fonctions élémentaires intégrée à l'interposeur, à savoir, des guides d'ondes monomodes, des structures de couplage vertical et des lignes de transmission hautes fréquences. Dans un second temps, un procédé de fabrication, principalement basé sur l'ablation laser femtoseconde, a été développé afin d'intégrer ces fonctions sur un substrat de verre sur lequel une puce PIC25G peut être interfacées. Enfin, la fonctionnalité de l'interposeur et de l'assemblage complet a été démontrée au travers d'un travail détaillé de caractérisations électriques, optiques et mixtes.

Nous avons fabriqué un interposeur intégrant des guides d'ondes multimodes avec des pertes de propagation <6 dB / cm à 1310 nm, des lignes de transmission coplanaires avec des pertes d'insertion de 3 dB / cm à 60 GHz, des miroirs de redirection du signal optique et l'ensemble du routage électrique et optique permettant de tester la détection et la modulation de la lumière par la puce PIC25G. Nous avons réalisé l'assemblage de la puce

PIC25G sur l'interposeur en utilisant une technique classique de *flip-chip* et avons validé le couplage optique entre les guides d'ondes en polymère de l'interposeur et les guides d'ondes sur substrat silicium-sur-isolant (SOI) de la puce PIC25G grâce à la mesure du photo-courant d'une photodiode SiGe intégrée dans la puce photonique.

Abstract

Data traffic inside data centers has grown exponentially in recent years, with a constant pressure storage capacity, data rate and latency. A direct consequence of this race for performance is the persistent improvement in interconnect technologies to meet this demand. In the search for higher data rate and lower cost optical fiber communications for data centers, silicon photonics, an electro-optical technology derived from standard CMOS technologies, appears as a promising solution to reduce power consumption and enhance data rates of optical links while remaining economically viable. Despite leveraging most of the developments around the CMOS platform, Silicon photonics presents additional packaging constraints related to the interfacing of input/output optical fiber. These packaging constraints induce a substantial increase of silicon photonics based optical transceivers cost and complicates the implementation of technologies such as coarse wavelength division multiplexing (CWDM).

The purpose of this thesis is to study and develop a low-cost interposer made on a glass substrate implementing both electrical and optical functions with the ambition to perform a complete passive assembly of a CWDM transceiver based on STMicroelectronics PIC25G silicon photonic technology.

Firstly, this work proposes to design the interposer main components, namely, single mode waveguides, vertical coupling structures and high frequency transmission lines. Then, a fabrication process mainly relying on femtosecond laser ablation that allow to implement these components on a glass substrate as well as the assembly with an existing PIC25G chip is developed. Finally, the interposer and the complete assembly functions are demonstrated through detailed electrical, optical and hybrid characterizations.

We fabricated an interposer implementing multimode waveguides with propagation losses $< 6\text{dB/cm}$ at 1310 nm, coplanar transmission lines with insertion losses of 3 dB/cm at 60 GHz, slanted TIR mirrors and all the electrical and optical routing allowing to test the detection and modulation of light by the PIC25G chip. We achieved the assembly of the PIC25G chip over the interposer using the conventional flip-chip technique and demonstrated an optical coupling between the polymer waveguide interposer and the silicon-on-insulator waveguide of the PIC25G chip through the measurement of the photo-current of an SiGe photodiode embedded in the silicon photonic chip.